Antenna Calibration and Energy Measurement of Ultra-High Energy Cosmic Rays with the Auger Engineering Radio Array

Von der Fakultät für Mathematik, Informatik und Naturwissenschaften der RWTH Aachen University zur Erlangung des akademischen Grades eines Doktors der Naturwissenschaften genehmigte Dissertation

vorgelegt von

Diplom-Physiker

Klaus Frank Weidenhaupt

aus Aachen

Berichter: Universitätsprofessor Dr. Martin Erdmann
Universitätsprofessor Dr. Christopher Wiebusch

Tag der mündlichen Prüfung: 17. November 2014

Contents

1. Introduction

Even more than a century after their discovery, fundamental questions about cosmic rays remain unanswered. It is still not clear which astrophysical objects accelerate cosmic rays to extreme energies of more than 10^{20} eV and what is their chemical composition.

Vast ground based detectors such as the Pierre Auger Observatory address these questions by measuring the arrival direction, energy and mass of the cosmic ray particles up to the highest energies. They utilize the Earth's atmosphere to detect cosmic rays indirectly by means of extensive air showers initiated by inelastic collisions of the cosmic ray with air nuclei in the upper atmosphere. The air showers are commonly registered either by sampling secondary shower particles at ground level or by telescopes which track fluorescence light emitted when the shower particles propagate through the atmosphere.

Besides these established detection techniques, a promising innovative approach is the detection of cosmic ray air showers by means of electromagnetic radiation emitted during the shower development. The emission becomes coherent at MHz frequencies and can be detected by arrays of radio antennas at ground level. The ultra-short broadband radio pulses carry information about the shower development and the properties of the primary cosmic ray particle. Besides the measurement of the comic rays arrival direction and energy, it is especially interesting to exploit the radio technique for complementary measurements of the chemical composition of cosmic rays. Furthermore, the radio technique could provide a cost effective alternative to established detection techniques for the instrumentation of large areas in the scope of next generation cosmic ray detectors.

A pathfinder experiment to explore the potential of radio detection for large scale applications is the Auger Engineering Radio Array (AERA). Its co-location with the baseline detectors of the Pierre Auger observatory in Argentina allows for complementary studies of cosmic rays and provides unique opportunities for the calibration of the radio emission.

AERA currently consists of 124 autonomous radio detector stations covering an area of about six square kilometers. The sensitive component of the detector stations are two different types of radio antennas.

In this thesis we aim for the measurement of one of the fundamental cosmic ray parameters with the radio technique, the energy of the primary cosmic ray. This task requires two major steps. First, the calibration of the antenna response is vital as it provides the basis for the reconstruction of the electric field emitted by cosmic ray air showers. Second, a radio energy estimator needs to be developed based on the calibrated electric field data obtained from the radio detector stations. Consequently, this thesis is subdivided into two main sections.

As a basis for the antenna calibration we introduce the theoretical concepts to describe antennas and adapt them to enable a full characterization of antennas for the application in cosmic ray radio detection. We describe the development and design of the radio antennas used at AERA as a consequence of multiple demands imposed by the nature of the radio emission and environmental conditions at AERA. The design of the antennas is evaluated by various measurements of their electrical properties and extensive testing of the mechanical structure in dedicated test benches. We apply the experience gained in these studies to develop an improved mechanical structure for the so called Butterfly antenna which is currently deployed in 100 of the AERA radio detector stations.

We conduct in situ calibrations of the AERA antennas by measurements of the vector effective length which describes the antenna response depending on the frequency and incoming direction of the radio signals and furthermore includes signal dispersion effects which occur within the antenna structure. For this purpose we develop novel methods based on calibrated signal sources which are placed either by a balloon or a GPS-controlled flying drone in the far-field region of the radio stations. We compare the antenna calibration measurements with simulations and develop the antenna simulation models of the Butterfly antenna station which are currently used for the radio reconstruction at AERA.

Having achieved a calibration of the AERA stations we can reconstruct the vectorial electric field emitted by air showers. We select radio events which are confirmed as cosmic ray events by coincidences with the surface detector of the Pierre Auger Observatory. We probe the dominating radio emission mechanisms present in the AERA data by comparisons of the polarization of the measured electric field with model predictions.

Based on the identified emission mechanisms, we formulate geometrical corrections on the radio signal amplitude. We parameterize the lateral distribution of the signal amplitude and define a unified energy estimator at a certain lateral distance. Finally, we calibrate the radio energy estimator with the corresponding energy measurement of the Auger surface detector and enable an energy measurement of cosmic rays with the AERA radio detector.

2. Physics of Ultra-High Energy Cosmic Rays

The term 'cosmic rays' refers to charged particles originating from space. With an energy density comparable to the one of visible starlight or the microwave background [1] cosmic rays form a major fraction of radiation reaching the earth from outside our solar system.

Cosmic rays were discovered in conjunction with early investigations of radioactivity. The fact that statically charged bodies lose their charge in the course of time was first explained with the discovery of radioactivity by A. H. Bequerel in 1986. Radioactive isotopes in the Earth's crust were believed to ionize the air which then discharges the body. Following this theory the air ionization would thus decrease with growing height above the surface of the earth.

In 1912 Victor Hess found using balloon flights that beyond 1000 m, the intensity of the ionizing radiation increases with increasing altitudes, rather than decreases as is expected for sources on the earth's surface [2]. He concluded that at least a part of the ionizing radiation is of extraterrestrial origin. Further dedicated balloon ascents up to 9 km of altitude by W. Kohlhörster [3] confirmed Hess's findings. For the discovery of cosmic radiation Hess was awarded the Nobel Price in Physics in 1936.

In 1937 Pierre Auger investigated cosmic rays with arrays of particle detectors at ground level. Thereby he was able to observe coincidences between spatially separated detectors. He concluded that extensive particle showers are generated by high-energy primary cosmic rays that interact with air nuclei high in the atmosphere, initiating a cascade of interactions that ultimately yield a shower of secondary particles that reach ground level. His further studies suggested that the energy of these cosmic ray induced air showers vary over several orders of magnitude extending up to 10^{15} eV.

2.1 Energy Spectrum

After Hess's discovery multiple experiments have been dedicated to the exploration of cosmic rays at various energies. They complementary cover a range of approximately 12 orders of magnitude in energy. The resulting energy spectrum of cosmic rays is depicted in Fig.2.1. It is expressed in terms of the differential flux

$$J(E) = \frac{d^4N}{dE\,dA\,d\Omega\,dt}, \tag{2.1}$$

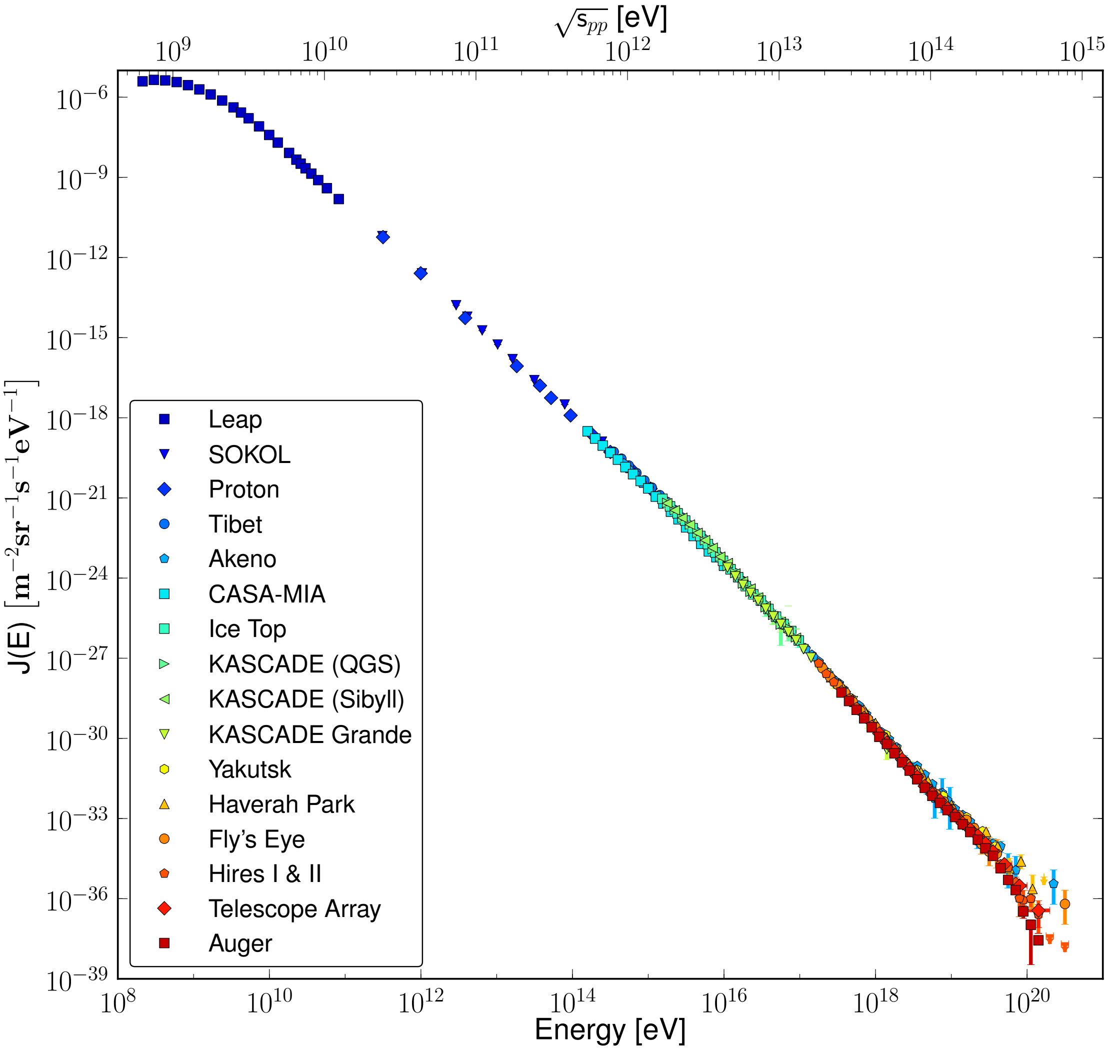

Figure 2.1: Energy Spectrum of cosmic rays as measured with the denoted experiments. The references to the experiments in the order of appearance in the legend [4, 5, 6, 7, 8, 9, 10, 11, 12, 13, 14, 15, 16, 17]

where N denotes the number of observed cosmic rays per energy E, sensitive area A, solid angle Ω and exposure time t.
Below energies of $\approx$ 10 GeV the cosmic ray flux is modulated by magnetic fields in our solar system depending on the activity of the sun [18]. Towards higher energies the flux decreases steeply. The spectrum can be approximated by a power law

$$J(E) \propto E^{\gamma} \quad \text{with} \quad \gamma \approx -2.7. \tag{2.2}$$

On closer inspection the spectrum features small changes in the power law's spectral index γ. Above energies of $\approx$ 10^{15} eV, the so called 'knee' of the spectrum, the spectral index changes from $\gamma = -2.7$ to $\gamma = -3.1$. The region around 10^{18} eV is called 'ankle' of the spectrum, where the spectral index changes back to $\gamma = -2.7$. Cosmic rays above the 'ankle' with energies exceeding 10^{18} eV are referred to as ultra-high energy cosmic rays (UHECRs). Above 4×10^{19} eV a strong suppression of the flux has recently been observed [15, 19]. The measured spectrum ends at energies of around 10^{20} eV, the so far highest energetic particle was observed at an energy of 3×10^{20} eV [20].

Within the broad energy range of the cosmic ray spectrum the flux drops about 33 orders of magnitude. As a consequence two fundamentally different detection techniques are being applied. At energies below $\approx$ 100 TeV the flux is sufficiently high to allow for a direct detection of the primary cosmic rays with balloon borne or satellite experiments such as LEAP [4] and PROTON [21]. At higher energies large detectors are necessary to gather sufficient statistics in a reasonable time of observation as e.g. at energies of 10^{20} eV only one particle per square kilometer and century is expected. At these energies vast ground based detectors measure cosmic rays indirectly via their induced air showers.

2.2 Composition

In the energy region below $\approx$ 100 TeV, where a direct detection of cosmic rays is possible, the chemical composition is well known [1, 23]. It matches roughly the element distribution in our solar system consisting of 79% protons, 15% helium and 1% heavier nuclei. Also small fractions of leptons are present, with a suppressed flux towards higher energies due to synchrotron radiation losses in magnetic fields.

With the transition to indirect measurements the composition has to be determined from the properties of the measured air shower such as its longitudinal development in the atmosphere. From the point of the first interaction of the cosmic ray with the atmosphere, the number of shower particles grows due to subsequent interactions until it reaches a maximum at a certain depth in the atmosphere. This point of the longitudinal shower development is referred to as shower maximum. With further increasing depth, the number of shower particles decreases again mainly due to the absorption of low-energetic shower particles in the atmosphere. The corresponding depth of the shower maximum in the atmosphere X_{max} is sensitive to the mass of the primary particle[1]. Due to large fluctuations in the development of air showers, the identification of the primary particle's mass is challenging on an event by event basis. Instead, the mean mass in terms of the mean depth of the shower maximum $\langle X_{max} \rangle$ and its fluctuation RMS(X_{max}) are usually investigated to characterize the composition.

For an interpretation of the data, air shower simulations are indispensable. In particular, the dependency of $\langle X_{max} \rangle$ and RMS(X_{max}) on the primary particles energy is simulated for specific atomic masses or mass groups and compared to the measurements.

Composition measurements in the energy range from the 'knee' to 10^{17} eV have been performed by the KASCADE experiment [24]. The measurements suggest an

---

[1] For a detailed description of the air shower development please refer to the next chapter.

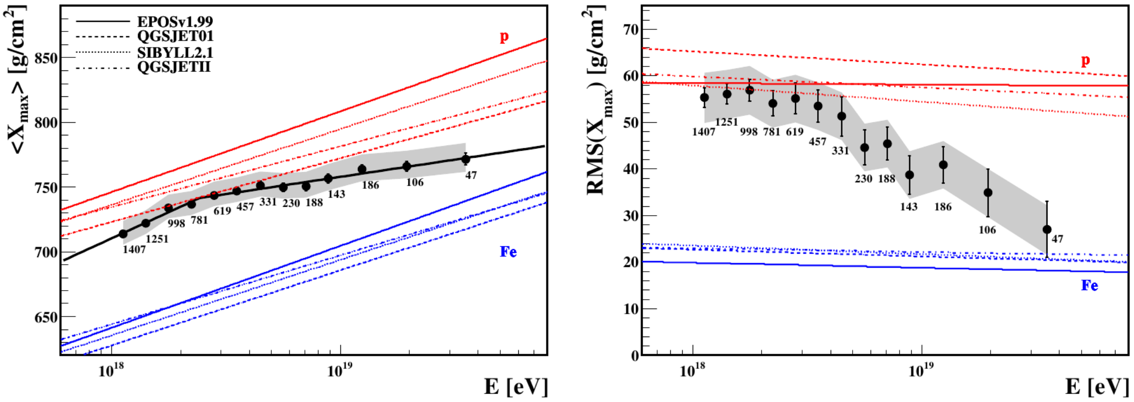

Figure 2.2: Measurement of the mean depth of the shower maximum $\langle X_{max} \rangle$ (left) and its fluctuation RMS(X_{max}) (right) as a function of the primary cosmic rays energy. Systematic uncertainties are represented by the gray bands, the number of events is denoted for each energy bin. Predictions from simulations for both a pure proton and a pure iron composition based on four different interaction models are depicted as lines [22].

increase of the mean mass with energy. The 'knee' feature in the all-particle spectrum can thus be interpreted with the decreasing flux of the light elements [25].
In the subsequent decade in energy, studies based on HiRes data show that the composition is changing again from a heavy to a lighter mix of nuclei as the energy increases [26].

A composition measurement in the ultra-high energy region as performed by the Pierre Auger Collaboration is depicted in Fig.2.2. The respective expectations from simulations for proton and iron nuclei are denoted for comparison. The measurement indicates a transition from a predominantly light composition to a composition dominated by heavier elements at the highest energies. However, composition measurements in the ultra-high energy range appear not consistent yet between different experiments. Corresponding results by the Telescope Array [27] and HiRes Collaboration [28] indicate a composition dominated by protons also at the highest energies.

2.3 Propagation

On their way from the source to the observer, cosmic rays are subjected to galactic or intergalactic magnetic fields respectively. Magnetic fields in the Milky Way disk and halo can be determined to a few μG from observations of Faraday rotation measures, e.g. [29]. Intergalactic magnetic fields can be constrained based on the observation of the CMB to be weaker then a few nG [30]. If an inhomogeneous structure of magnetic fields as provided by large scale structure simulations is assumed, the interpretation of rotation measure yields upper limits for the field strength in cosmic filaments and sheets in the order of μG [31, 32].

The implications of magnetic fields for the propagation of cosmic rays can be understood in a simplified picture. A particle with charge $Z \cdot e$ and energy E will rotate in a homogeneous magnetic field with field strength B on a circle with the Larmor radius r_L:

$$r_L[pc] = 1.08\,pc\,\frac{E[PeV]}{Z \cdot B[\mu G]}, \tag{2.3}$$

With increasing energy the Larmor radius will exceed the thickness of the galactic disk and a confinement of the particle within the galaxy becomes more and more unlikely. Consequently a leakage from particles out of our galaxy occurs (leaky-box model). In this context the 'knee' in the all-particle spectrum can be understood as a propagation effect [1]. Due to the dependency on the atomic number $r_L \propto 1/Z$, the leakage will first occur for protons, sequentially followed by the heavier elements. The resulting rigidity dependent cut-off of the flux for individual elements thus causes the steepening of the spectrum above the knee and the associated change towards a heavier composition. For a review of astrophysical models regarding the knee feature refer to [33].

A further implication of Eq. 2.3 is that cosmic rays below approximately the energy of the ankle are presumably of galactic origin. Assuming galactic magnetic fields of a few μG, the gyro radius of a proton reaches the order of the thickness of the galactic disk of a few kpc at an energy of $\approx$ 1 EeV. Thus cosmic rays with energies $\ll$ 1 EeV are bound to the galactic magnetic field. Vice versa, cosmic rays with energies below $\approx 10^{18}$ eV originating from other galaxies and subjected to similar magnetic fields would not be able to escape their galaxy and would thus never reach us. Hence, a popular interpretation for the spectral slope around the ankle and the corresponding change in composition is the onset of an extragalactic component of cosmic rays.

Cosmic rays with energies above the ankle can not be confined by magnetic fields within our galaxy anymore as implied by Eq. 2.3. Furthermore, the arrival directions of cosmic rays with energies from the ankle up to several 10^{19} eV are observed to be isotropic [1]. Galactic UHECR sources are thus disfavored as they would result in an observable anisotropy. Consequently it is likely that cosmic rays above the ankle are of extragalactic origin. Hence, a popular interpretation for the spectral slope around the ankle and the corresponding change in composition is the onset of an extragalactic component of cosmic rays.

Besides the deflection in magnetic fields, the flux of cosmic rays at the highest energies will be attenuated due to interactions with background photons during the propagation. Protons with energies above $6 \cdot 10^{19}$ eV should be attenuated by photoproduction processes [34] while heavier elements with similar energies are broken up due to photodisintegration e.g. [35].
A prime example of the former process is the production of a $\Delta^+(1232)$ - resonance if the center of mass energy of a cosmic ray proton together with a photon of the

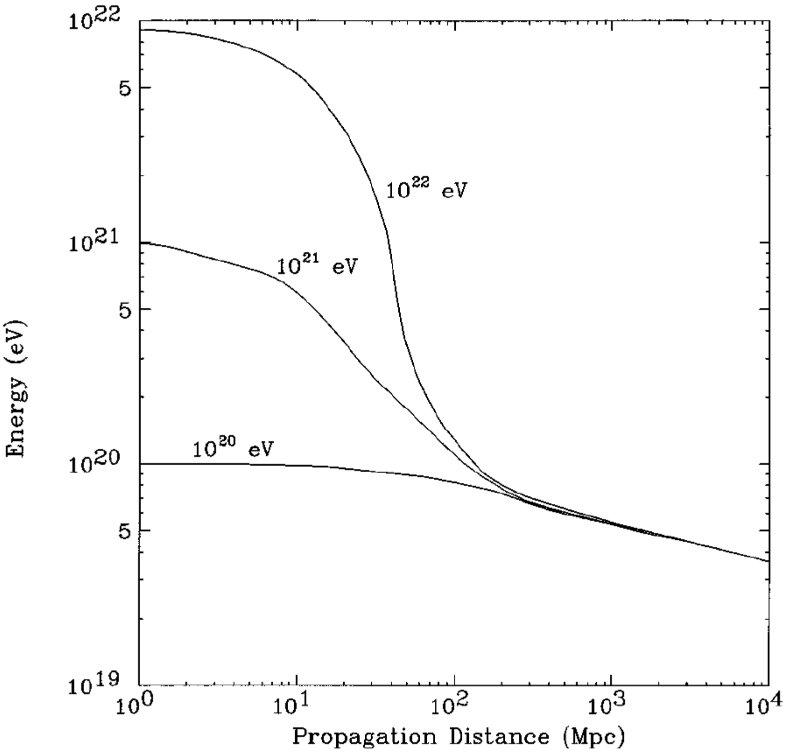

Figure 2.3: Simulated decrease of the proton energy with traveled distance for different initial energies according to the GZK-effect [37].

CMB exceeds the rest mass of the Δ^+. This implies proton energies above $6 \cdot 10^{19}$ eV with increasing interaction probability towards higher energies. The Δ^+ will decay in two dominant channels:

$$\begin{aligned} p \;+\; \gamma_{CMB} \;&\rightarrow\; \Delta^+ \;\rightarrow n + \pi^+ \\ p \;+\; \gamma_{CMB} \;&\rightarrow\; \Delta^+ \;\rightarrow p + \pi^0. \end{aligned} \tag{2.4}$$

The proton will loose a fraction of its primary energy to produce the mass of the pion. If the proton energy is still sufficient to produce another Δ^+ the process will repeat, yielding a successive energy loss.

Assuming these processes, the propagation of protons over large distances can be simulated for different initial energies. This is shown in Fig. 2.3 for 10^{20} eV, 10^{21} eV and 10^{22} eV. In all cases the proton will be decelerated below energies of 10^{20} eV after about 100 Mpc traveled distance. Hence, cosmic rays reaching the earth with energies above 10^{20} eV must come from sources closer than $\approx$ 100 Mpc. This effect should lead to a suppression of the flux at the highest energies. The effect is called GZK-Cutoff after Greizen, Zatsepin and Kuzmin [34, 36] who predicted it in 1966. A suppression of the flux above $4 \cdot 10^{19}$ eV was recently observed with the Pierre-Auger Observatory and the HiRes experiment is consistent with the GZK-Cutoff [19, 15].

2.4 Origin and Anisotropy

The question of the sources of cosmic rays is strongly related to the question of which mechanism is responsible for the acceleration of cosmic rays. The variety of

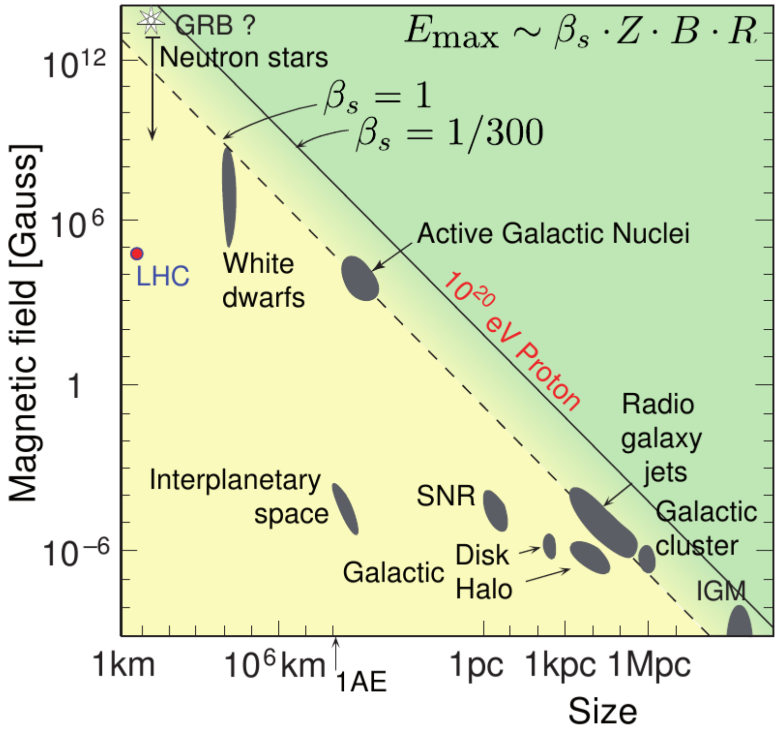

Figure 2.4: Extension and magnetic field strength of potential sources of UHECRs (Hillas Plot). Adopted from [1], originally based on [38].

acceleration mechanisms currently discussed (for an overview see e.g. [39]) can be classified into 'direct' acceleration in electric fields and 'stochastic' acceleration in magnetic fields.

Sufficiently high electric field gradients for a direct acceleration can be found in the proximity of neutron stars or near black holes. However, models of direct acceleration are disfavored as they lack a consistent explanation of the observed energy spectrum [39].

The favored models rely on stochastic acceleration in magnetic fields based on a model by Enrico Fermi [40]. In the 'first-order' Fermi mechanism, particles gain energy by diffuse scattering in magnetized plasma. Such an environment is e.g. provided by supernova explosions which emit shock fronts that propagate from a supernova remnant (SNR) into the interstellar medium. A charged particle passing the shock front back and forth will gain an amount of energy $\Delta E \propto E$ at each cycle. At each cycle, there is a probability that the particle leaves the shock region. Assuming an energy-independent escape probability, a power law energy spectrum is generated [41].

An upper limit for the maximum energy attainable by a source can be estimated with the Larmor radius (cf. 2.3). The acceleration is stopped when the Larmor radius of a particle exceeds the size of the acceleration region. A.M. Hillas adapted this consideration to diffusive shock acceleration and formulated the following constraint [38]:

$$E_{max} \simeq 10^{18} eV \, Z \, \beta_s \left(\frac{R}{kpc}\right) \left(\frac{B}{\mu G}\right). \tag{2.5}$$

Sources with size R and magnetic fields of strength B are thus able to accelerate particles with charge $Z \cdot e$ up to energies E_{max}. Further, β_s denotes the velocity of the scattering centers, respectively the speed of the supernova shock front in units of the vacuum velocity of light c.
Typical values of Type II supernovae yield maximum energies of $E_{max} \approx Z \cdot 10^{14}$ eV [42] and $E_{max} \approx Z \cdot 3 \cdot 10^{15}$ eV for special types of supernovae [43] respectively. The dependence of E_{max} on the charge of the nucleus $Z \cdot e$ introduces consecutive cut-offs for the spectra of the individual elements contributing to the cosmic ray composition. The steepening in the all particle spectrum and the associated shift towards heavier elements at the knee can thus be interpreted by the increasing acceleration efficiency towards heavier elements. In section 2.3 the knee feature was discussed as a propagation effect. In [33] a combination of both effects is favored as it leads to a better agreement with recent observations in the knee region.

For the origin of galactic cosmic rays SNR are widely accepted (for a review of galactic cosmic rays refer to [44]). Models of diffusive shock acceleration in SNR can explain the observed power law energy spectrum. Furthermore supernovae can provide the total energy input needed to generate the overall cosmic ray flux [45]. Direct evidence that protons are accelerated in SNR has recently been found by observations of γ-rays. High-energy γ-rays are considered a tracer for cosmic ray sources as they partly originate from decays of neutral pions produced in collisions of cosmic rays with background plasma [46]. For some of the observed SNR the emitted γ-rays are of hadronic origin, giving evidence that cosmic rays are accelerated in the SNR [47].

For UHECRs the situation seems less clear. A compilation of various astrophysical objects with respect to typical values of their magnetic field strengths and extensions is shown in Fig. 2.4. Eq. 2.5 is evaluated for protons with a maximum energy of 10^{20} eV and plotted as diagonal lines for $\beta_s = 1$ and $\beta_s = 1/300$ respectively. Considering the Hillas constraint, protons can only be accelerated up to energies of 10^{20} eV by sources that touch or lie above the diagonals. Thus, for UHECRs only a few source candidates remain: gamma ray bursts (GRBs), neutron stars, active galactic nuclei (AGNs), radio galaxy lobes and clouds of intergalactic matter.

An additional constraint on potential sources of UHECRs is imposed by the GZK effect discussed in section 2.3. The GZK-horizon of a 10^{20} eV proton surrounds a sphere around earth with a radius of about 100 Mpc. Within this sphere only a limited number of possible sources exist which fulfill the Hillas criteria (cf. Eq. 2.5).

These source candidates are distributed anisotropically. For the highest energies, the deflection of cosmic rays during their propagation becomes relatively small. Simulations assuming realistic galactic and intergalactic magnetic fields (cf. section 2.3) predict that cosmic rays point back to their source for proton energies exceeding about $4 \cdot 10^{19}$ eV [48]. Thus, the anisotropy of the sources should be reflected in the arrival directions of UHECRs observed at Earth.

A correlation of arrival directions of cosmic rays at the highest energies with the direction of nearby astrophysical objects is being probed by the Pierre Auger Observatory. In particular, the correlation with AGNs as obtained from the Véron-Cetty and Véron (VCV) catalogue [49] has been studied as they are considered one of the most promising source candidates. The analysis published in [50] is influenced by three parameters listed below.

First, the maximum angular deviation Φ from an AGN is defined. If the observed arrival direction has a angular deviation smaller than Φ to one of the considered AGNs, the event is counted as correlated. This cut takes the detector resolution and the fact that even the most energetic cosmic rays are slightly deflected into account.
Second, the minimum energy from which cosmic rays are expected to point back to their sources is considered with the threshold energy E_{th}.
Third, the distance D_{max} up to which AGNs are taken into account. This constrain reduces the number of eligible AGNs due to the implications of the GZK-Cutoff.

In an exploratory scan using an initial dataset, these parameters have been optimized to minimize the probability that the correlation with AGNs in the VCV catalog could occur by chance if the flux was isotropic. The scan yields: $\Phi = 3.1°$, $E_{th} = 55$ EeV and $D_{max} = 75$ Mpc. In an analysis of a subsequent dataset using the prescribed parameters, 8 out of 13 events were correlated with AGNs. Under the hypothesis that the flux is isotropic, only a fraction of 21% is expected to correlate. The isotropic hypothesis could thereby be rejected with a least 99% confidence level. It should be mentioned that the observed correlation with AGNs does not necessarily imply that AGNs are the sources of cosmic rays.
With increased statistics the AGN-correlation has been updated [51]. A total of 69 events has been detected in excess of 55 EeV until December 2009. The arrival directions of these events are mapped in Fig. 2.5 together with AGNs closer than 75 Mpc. From 55 events (14 out of 69 are excluded as they have been used for the exploratory scan), 21 correlate with AGNs. This gives a degree of correlation of $(38^{+7}_{-6})\%$, to be compared with 21% for an isotropic expectation.
In a current report of the Pierre Auger Collaboration, the degree of correlation with AGNs decreased to $(33 \pm 5)\%$ (28 of 84 events correlate) [52]. However, the chance probability of observing such a correlation from a random distribution remains below 1%.
Equivalent analyses from the HiRes [53] and Telescope Array Collaborations [54] indicate a compatibility with an isotropic flux. The differences between these observations and the Auger data is currently under discussion. Possible causes are

differences in the energy scale of the experiments and the fact that they operate on opposite hemispheres [1].

Besides the presented correlation of arrival directions with AGNs, the Auger collaboration has performed further extended analysis of the UHECR arrival direction distributions in several energy ranges and different angular scales. For a overview of the latest results of these analysis please refer to [55].

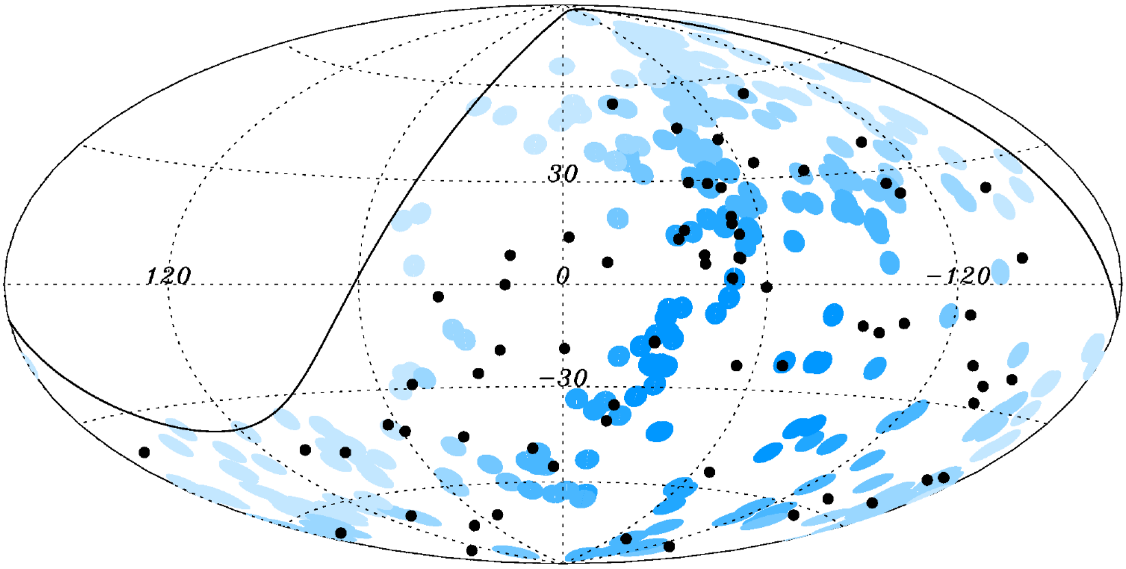

Figure 2.5: Map of the of the sky in galactic coordinates (Aitoff-Hammer projection) showing the arrival direction of 69 UHECRs in excess of 55 EeV (black dots) as measured by the Pierre Auger Observatory until December 2009. The solid line represents the border of the field of view of the Observatory for zenith angles smaller than 60°. The blue circles of radius 3.1° are centered around AGNs in the VCV catalog closer than 75 Mpc and within the field of view of Auger. Darker blue indicates larger relative exposure. Taken from [51].

3. Extensive Air Showers

Cosmic rays hitting the atmosphere of our earth will collide with an air nucleus at a certain height above ground. In this collision, particles are produced which themselves carry enough energy to initiate further inelastic processes. The result is a cascade of particles propagating through the atmosphere with almost the speed of light. UHECRs can induce air showers consisting of billions of particles. The particles partly reach ground level and can spread over several km^2. This justifies the commonly used term Extensive Air Shower (EAS).

In the first section of this chapter we focus on a theoretical description of EAS. Based on simplified models, fundamental air shower properties are introduced and their correlation to the nature of the primary cosmic ray is deduced. Furthermore, simulations of EAS are briefly discussed.

In the second section we consider the fact that today's UHECR detector systems utilize the earth's atmosphere as a giant calorimeter to detect cosmic rays indirectly via their induced EAS. Quantities of EAS accessible through measurements with recent detection techniques are emphasized.

3.1 Theory of Air Showers

The earth's atmosphere acts as a calorimeter with variable density and an integrated column density of 1033 g/cm^2 (at sea level) in vertical direction. Considering the mean path lengths in air, this corresponds to a thickness of $\approx$11 hadronic interaction lengths and $\approx$26 electromagnetic radiation lengths [56].

EAS are usually grouped into three components according to their respective particle content, a hadronic, an electromagnetic and a muonic cascade. A schematic overview of an air shower subdivided into these cascades is presented in Fig. 3.1. The hadronic cascade, consisting at rough approximation of 90% pions and 10% kaons, evolves directly from the first interaction of the primary cosmic ray with an air nucleus. The charged pions and kaons extend the hadronic cascade through further hadronic interactions. Finally they decay into muons and neutrinos forming the muonic cascade. As muons and neutrinos are unlikely to interact further in the atmosphere, they do not contribute significantly to the further shower development. Due to their high γ-factor most of the muons reach ground level before they decay [1] and thus contribute a major fraction of the particles that can be observed with

---

[1] For very inclined showers (showers with zenith angles exceeding 60°) the muon decay can not be neglected anymore. Very inclined showers are not discussed here as they will not be part of the analysis within this thesis. For a detailed discussion see [57].

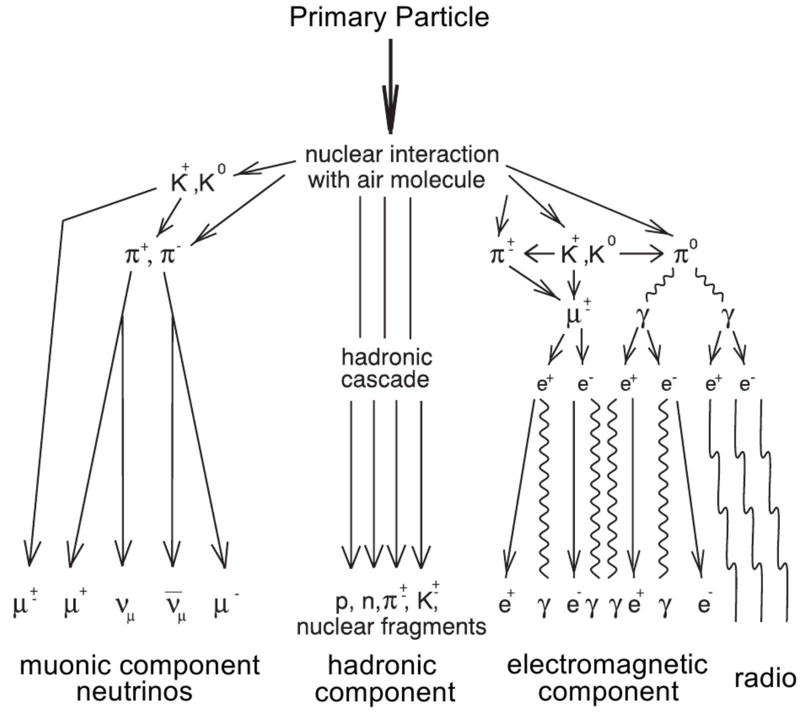

Figure 3.1: Schematic overview of an air shower divided into a hadronic, electromagnetic and muonic sub cascade [58].

ground based detectors.
The electromgnetic cascade is initiated by the decay of neutral pions. With a lifetime of $\tau \approx 10^{-16}$ s they decay into two photons. Consecutive pair production and Bremsstrahlung processes constitute the electromagnetic component consisting of photons, electrons and positrons. As approximately 1/3 of all produced pions are neutral, at each hadronic interaction length, about 1/3 of the energy of the hadronic cascade is transferred into photons. For a typical vertical air shower of 10^{19} eV observed at sea level, the electromagnetic component contains about 99% of the total shower particles and carries about 85% of the total energy [56].
In the following we discuss a simplified model of electromagnetic showers suitable to derive basic shower properties. Hadronic showers are reconsidered by an extension of the electromagnetic model in the subsequent section.

3.1.1 The Heitler Model of Electromagnetic Showers

Within the Heitler model [60], electromagnetic showers are approximated by a perfect binary tree as depicted in Fig. 3.2, left. The tree is initiated by a photon or electron (a photon is shown in Fig. 3.2) of energy E_0. At each node an interaction occurs which produces two secondaries. Photons interact by pair production, creating an electron and a positron of equal energy. Electrons emit a single photon via Bremsstrahlung and survive with half of the initial energy. The cross section of both processes are assumed energy independent and equal. Consequently at each level of the binary tree, the number of shower particles is doubled, yielding $N = 2^n$ particles

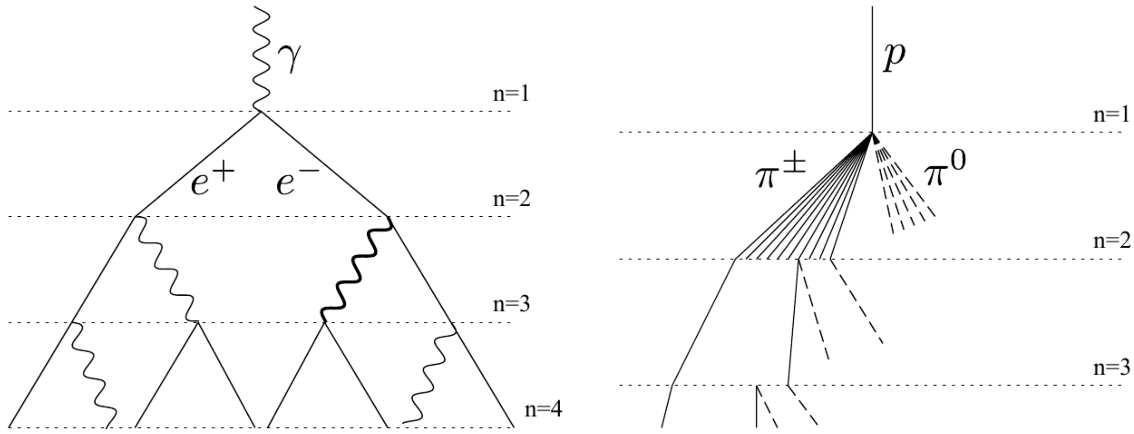

Figure 3.2: Schematic views of an electromagnetic cascade (left) and a hadronic cascade (right). In the hadron shower, not all pion lines are shown after the $n = 2$ level. Diagram is not to scale. From [59].

of energy $E = E_0/N$ at depth n. The splitting length d is then associated with the radiation length λ_r of the medium as

$$d = \lambda_r \ln 2 \quad \text{with} \quad \lambda_r = 37 \text{ g/cm}^2. \tag{3.1}$$

in air. The shower development continues until the individual energy of the shower particles drops below a critical energy E_c. Below E_c energy losses are dominated by ionization processes rather then pair production and Bremsstrahlung. In air, E_c amounts to $\approx$ 85 MeV [59]. At this point the shower evolution has reached a maximum, by means of the maximum number of particles which is then given as

$$N_{max} = E_0/E_c = 2^n = e^{n\,ln2} \tag{3.2}$$

An important result is thus that the number of particles at the shower maximum is proportional to the energy of the primary particle.
The integrated slant depth of the shower maximum X_{max} corresponds to n steps of length d and is thus given by

$$X_{max} = X_0 + n\,d, \tag{3.3}$$

with the depth of the first interaction X_0. Solving Eq. 3.2 for n yields

$$n = \ln(E_0/E_c)/\ln 2 \tag{3.4}$$

Insertion of Eq. 3.1 and Eq. 3.4 in Eq. 3.3 yields

$$X_{max} = X_0 + \lambda_r \ln(E_0/E_c). \tag{3.5}$$

The depth of the shower maximum in the atmosphere hence scales logarithmically with the cosmic ray's energy.

Comparison of measurements with detailed simulations indicate that N_{max} is overestimated by a factor of 2 – 3 in the Heitler model. Furthermore it predicts an electron to photon ratio of two, whereas simulations give a ratio of about 1/6 [56]. These differences can be attributed to an underestimation of the electron cross section and to the fact that multiple photons can be emitted due to Bremsstrahlung.
Despite these restrictions, the general dependencies derived in Eq. 3.2 and Eq. 3.5 hold true also for the development of real air showers and are confirmed by measurements and simulations.

3.1.2 Extension to Hadronic Showers

An extension of Heitler's model from electromagnetic to hadronic showers has been developed by Matthews [59]. Therein, the hadronic cascade of an air shower is also modeled as a tree as depicted in Fig. 3.2, right. The splitting length d is given by the hadronic interaction length λ_I as

$$d = \lambda_I \ln 2, \quad \text{with} \quad \lambda_I = 120 \text{ g/cm}^2 \quad \text{in air} \tag{3.6}$$

which is assumed to be constant. The cascade is started with a proton of energy E_0. At every node, a hadronic interaction produces N_{ch} charged pions and 1/2 N_{ch} neutral ones of equal energy. The pion multiplicity as a model parameter is set to $N_{ch} = 10$ in agreement with laboratory experiments [2]. The neutral pions decay and extend the electromagnetic cascade. In this way, 1/3 of the energy is transferred to the electromagnetic component whereas the total energy of the hadronic cascade decreases with every step as

$$E_\pi^{tot} = (2/3)^n \, E_0. \tag{3.7}$$

With the number of charged pions extending the hadronic cascade, $N_\pi = {N_{ch}}^n$, the energy of a single pion after n steps can be calculated as

$$E_\pi = \frac{E_\pi^{tot}}{N_\pi} = \frac{E_0}{(\frac{3}{2} N_{ch})^n}. \tag{3.8}$$

The cascade progression ceases when a decay of the pions becomes more likely than a next hadronic interaction. For pions in air, this is the case for $E_c^\pi = 20$ GeV. At this point, all pions are assumed to decay into muons. The number of muons thus equals the number of charged pions at the final stage n_c of the shower development, $N_\mu^p = {N_{ch}}^{n_c}$. The depth n_c is obtained by solving Eq. 3.8 for n,

$$n_c = \frac{\ln(E_0/E_c^\pi)}{\ln(\frac{3}{2} N_{ch})}. \tag{3.9}$$

---

[2] In fact, the pion multiplicity changes as a function of energy. The adopted value is accurate to within a factor of two for pion kinetic energies from about 1 GeV to 10 TeV and provides a simplification for the model [59].

We can now express the number of muons as a function of the primary proton's energy,

$$\begin{aligned} N_\mu^p &= {N_{ch}}^{n_c} && (3.10)\\ \Leftrightarrow \ln N_\mu^p &= n_c \ln N_{ch} \overset{eq.3.9}{=} \ln(E_0/E_c^\pi)\,\underbrace{\frac{\ln N_{ch}}{\ln(\frac{3}{2}N_{ch})}}_{\equiv\beta} && (3.11)\\ \Leftrightarrow \quad N_\mu^p &= (E_0/E_c^\pi)^\beta. && (3.12) \end{aligned}$$

Unlike the particle number in an electromagnetic cascade (cf. Eq. 3.2), the muon number does not scale linearly with the primary particles energy but grows at a smaller rate depending on the pion multiplicity N_{ch}. With $N_{ch} = 10$ we obtain $\beta \approx 0.85$.

So far we have only considered proton primaries. An air shower initiated by a nucleus with atomic number A can be modeled as a superposition of A proton showers of energy E_0/A starting at the same point. This is valid as the binding energy of the nucleus can be neglected compared to the cosmic rays energy. For Eq. 3.12 this implies

$$N_\mu^A = A\left(\frac{E_0/A}{E_c^\pi}\right)^\beta = (E_0/E_c^\pi)^\beta\, A^{1-\beta} = N_\mu^p\, A^{1-\beta}. \qquad (3.13)$$

The muon number for a given initial energy depends on the mass of the primary cosmic ray. Showers of heavier primaries produce more muons. The sensitivity of the muon number to the composition is exploited by air shower experiments. As electron number and muon number scale differently with the primary mass, usually the electron-to-muon ratio is used as a robust composition estimator.

By applying energy conservation we obtain that the cosmic ray's energy is distributed between the electromagnetic and the hadronic component, $E_0 = E_{em} + E_H$. At the final stage of the shower development, the energy of the hadronic component is carried by the muons, $E_H = N_\mu E_c^\pi$. With Eq. 3.13 the fraction of energy in the electromagnetic component reads

$$\frac{E_{em}}{E_0} = 1 - \left(\frac{E_0}{E_c^\pi}\right)^{\beta-1} A^{1-\beta}. \qquad (3.14)$$

For a proton shower of 10^{18} eV and the previously used values of β and E_c^π, more than 90 % of the cosmic rays's energy end in the electromagnetic component.

As likewise the particle content of the air shower is dominated by the electromagnetic component, the maximum of the air shower is given by the maximum of the electromagnetic cascade. In the first interaction $N_{ch}/2$, neutral pions are produced which decay into a total of N_{ch} photons. These initiate electromagnetic cascades of energy $E_0/(3\,N_{ch})$. Hence, the depth of the shower maximum can be estimated by X_{max} of an electromagnetic shower of enegy $E_0/(3\,N_{ch})$ starting at X_0 with

$$X^p_{max} = X_0 + \lambda_r \ln\left(\frac{E_0}{3\,N_{ch}\,E_c}\right). \tag{3.15}$$

A shower started by a nucleus is treated as a superposition of proton showers of energy E_0/A. For X^A_{max} follows

$$X^A_{max} = X^p_{max} - \lambda_r \ln A. \tag{3.16}$$

Showers induced by heavier primaries thus develop higher in the atmosphere than proton showers. The depth of the shower maximum is a widely used composition estimator for detectors that are able to measure the shower development within the atmosphere. For instance, the data shown in Fig. 2.2 are obtained with this method. Furthermore it is intuitive that the superposition of A proton showers averages the fluctuations in the individual showers. The variation of the shower maximum $RMS(X_{max})$ (also shown in Fig. 2.2) thus decreases with increasing primary mass.

The qualitative dependencies of EAS derived in the model are in agreement with observations. However, the introduced simplifications impose some restrictions. The pion multiplicity N_{ch} and the critical energy E^{π}_c, implemented as constant factors, change as a function of energy. Furthermore, in high energy hadron interactions only constituents of the hadron interact, yielding a significant fraction of energy carried away by a single 'leading' particle. This effect can be taken into account by introducing the inelasticity of a hadron interaction in the above model.

Such simplifications can be omitted by air shower simulations. They provide a helpful tool for direct comparisons with experimental data.

3.1.3 Simulations of Air Showers

Recent air shower simulation programs such as CORSIKA [61] and AIRES [63] allow to individually track each shower particle. Possible interactions or decays of each particle can then be applied according to its individual species and energy. For the description of these processes, interaction models from particle physics are adapted. While the electromagnetic and weak interactions are well described within the standard model, the hadronic interactions introduce the dominating uncertainties in air shower simulations [64]. As the energies in EAS collisions exceed the energies accessible in man-made accelerators, the relevant cross-sections have to be extrapolated from experimental data at lower energies.

The features of CORSIKA are briefly discussed here as they become relevant in the scope of simulations of radio signals from air showers in the following chapter. As input CORSIKA accepts primaries of different species specified by their energy and

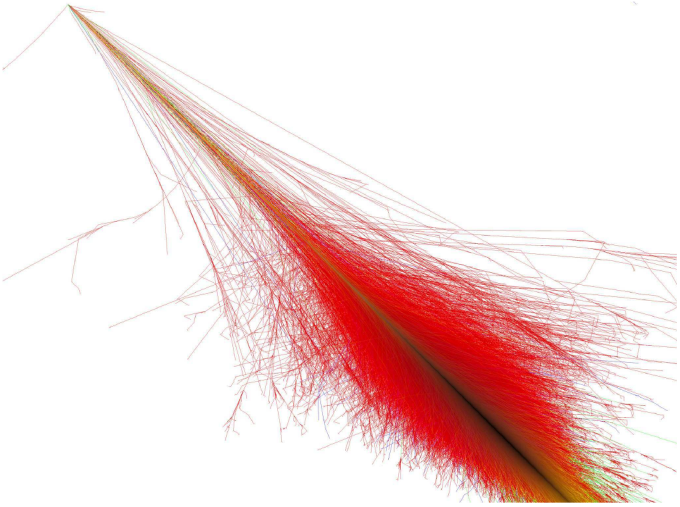

Figure 3.3: Image of a 10^{15} eV proton shower simulated with CORSIKA [61]. Electron, positron and photon tracks are red, muon tracks green and hadron tracks blue. Taken from [62].

incoming direction. CORSIKA recognizes 50 different elementary particles which can be tracked through the atmosphere, are able to interact, annihilate or decay, and produce secondary particles. Access to the shower particles is provided by defining observation levels, for instance the ground level containing the detector. All particles penetrating these levels with an energy exceeding a predefined cutoff will be stored together with their kinematics and provide the output of the simulation. An image of a CORSIKA shower simulated for a 10^{15} eV proton is shown in Fig. 3.3. For the high-energy hadronic interactions one of five different interaction models can be selected and their influence on the air shower development can be compared. Furthermore, the environmental conditions, such as models of the atmosphere and the geomagnetic field can be adjusted by the user. This allows to study systematic effects as for example the influence of the seasons.

Air shower simulations have become essential for the interpretation of data from modern UHECRs experiments (cf. Fig. 2.2 and the corresponding discussion). They provide a link between the primary cosmic rays properties and the quantities observed by experiments discussed in the following.

3.2 Shower Profiles and Methods of Observation

For the detection of UHECRs, two technical approaches have been well established: Arrays of particle detectors and flourescence detectors. The former method is based on the observation of the lateral shower profile at ground level. Fluorescence telescopes measure the longitudinal profile of an air shower by tracking fluorescence light emitted during the shower development in the atmosphere. Both techniques are visualized together with the geometry of an air shower in Fig. 3.4.

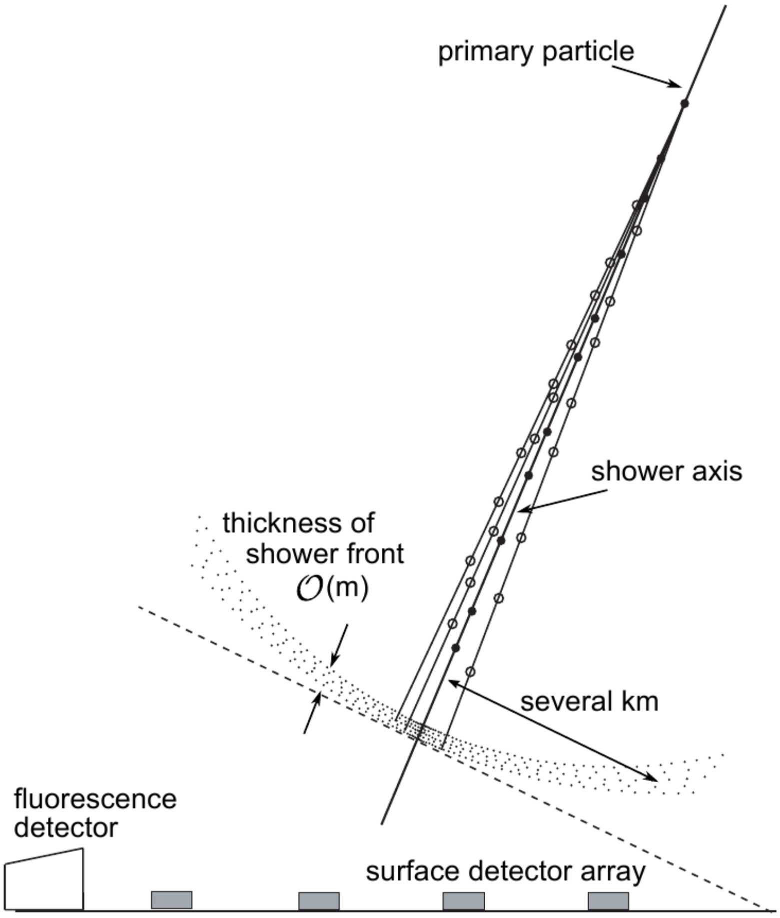

Figure 3.4: Geometry of an air shower. The shower propagates along the shower axis defined by the incoming direction of the primary cosmic ray. Secondary shower particles are located within a curved shower disk of a few meters longitudinal extension. Common measurement techniques are depicted. From [58].

3.2.1 Lateral Shower Profile

After the first interaction, the newly produced hadrons will carry a transverse momentum with respect to the direction of the inducing cosmic ray. This transverse momentum is transferred in further interactions and yields a lateral spreading of the shower particles with increasing shower age. The resulting shower disk reaches a few kilometers lateral extension for typical UHECR showers at ground level [65]. The geometry of an air shower is visualized in Fig. 3.4.

The lateral profile is observed by registering secondary shower particles at ground level in particle detectors employed with a certain spacing. As the size of the air shower scales with the primary energy, the detector spacing implies a lower energy threshold of the array. For UHECR arrays, a typical spacing is in the order of 1 km. The total instrumented area is chosen with respect to the cosmic ray flux and reaches several 1000 km^2 for an effective observation at the highest energies.

If an air shower is detected in at least three non-collinear stations, the shower axis can be reconstructed by adjusting a planar wavefront (cf. Fig. 3.4), to the arrival

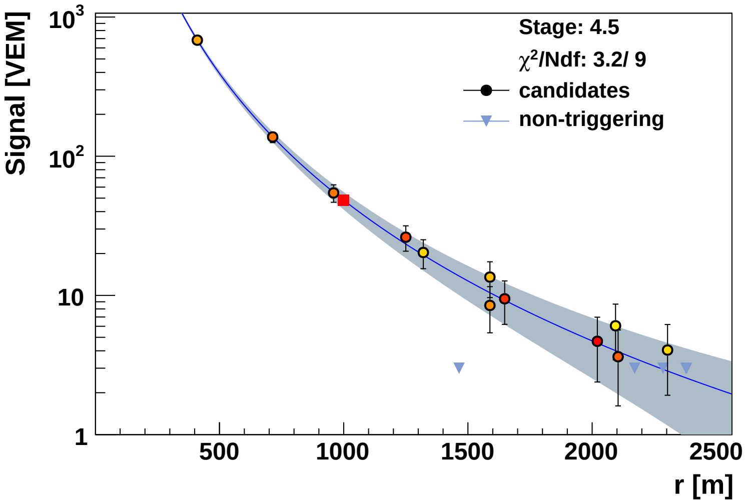

Figure 3.5: Lateral profile of an air shower measured with the surface detector of the Pierre-Auger Observatory. The response of the individual stations is given in units of a vertical incident muon (VEM). The color indicates the timing of the signals from early (yellow) to late (red). A fit of the LDF is shown as solid line with its uncertainties as gray band. The red square marks the energy estimator at a distance of 1000 m to the shower axis. The cosmic rays energy was reconstructed to $(1.43 \pm 0.09) \cdot 10^{19}$ eV.

times observed in the individual stations. If more than three stations are included, more complex models of the wavefront such as a sphere can be fitted.

The signal measured in a single station represents a sample of the particle density at a certain distance r to the shower axis. To obtain a continuous particle distribution, the signals of the triggered stations are fitted to a model of a lateral distribution function (LDF). A commonly used LDF is based on the Nishimura-Kamata-Greisen function [66],

$$f_{NKG}(r) \propto \left(\frac{r}{r_M}\right)^{s-2}\left(1+\frac{r}{r_M}\right)^{s-4.5}, \tag{3.17}$$

with the Molière radius r_M and the shower age s which can be parameterized as a function of depth X as:

$$s(X) = \frac{3X}{X+X_{max}}. \tag{3.18}$$

The evaluation of the fitted LDF at an optimum distance gives an estimate of the cosmic rays energy. This optimum distance varies mainly with the energy range and spacing of the experiment. It is chosen such that the fluctuations from shower to shower and the statistical fluctuations from particle counting are minimized.

In Fig. 3.5, a measurement of the lateral shower profile of a single air shower with the surface detector array of the Pierre Auger Observatory and the corresponding fit of the LDF are presented . Here the primary energy is estimated at an optimum distance of 1000 m.

The measurement of the lateral shower profile resembles a single snapshot of the shower and provides little information of the shower development. In particular, ground arrays usually give no direct access to the position of the shower maximum, a strong limitation for composition studies. Composition information is commonly extracted from the longitudinal profile.

3.2.2 Longitudinal Shower Profile

Secondary charged shower particles excite nitrogen molecules along their path in the atmosphere. While deexciting, the nitrogen molecules emit photons isotropically into several spectral bands in the UV regime between 300 nm and 420 nm. The number of emitted photons per energy deposit in the atmosphere is given by the 'fluorescence yield'. It depends on the atmospheric conditions and amounts to about 4 photons per charged particle per meter at ground level pressure [56].
With imaging telescopes, the emitted fluorescence light can be tracked at distances up to several 10 km from the shower axis. The imaging optics project the light track from the atmosphere onto a segmented camera. The amount of fluorescence light emitted at a certain depth X is proportional to the number of charged particles present in the shower, essentially the number of electrons $N_e(X)$ (cf. Sec. 3.1). Thus, the observed light track provides a direct image of the shower development in the telescope's field of view.
From the timing and the pointing of the camera pixels, the geometry of the air shower can be reconstructed. With known shower geometry and fluorescence yield and under consideration of the frequency dependent absorption of the fluorescence photons on their way to the telescope, the amount of fluorescence light is converted into the energy deposit in the atmosphere. The energy deposit dE/dX can be described by the Gaisser-Hillas function [67, 68] as a function of the slant depth X as

$$f_{GH}(X) = \frac{dE}{dX}(X_{max}) \left(\frac{X - X_0}{X_{max} - X_0}\right)^{\frac{x_{max}-X_0}{\lambda}} e^{\frac{x_{max}-X}{\lambda}}, \tag{3.19}$$

with the depth of the first interaction X_0 and absorption length λ. Such a calorimetric measurement of the longitudinal profile is presented in Fig. 3.6. A fit of the Gaisser-Hillas function determines the position of the shower maximum X_{max}. The total deposited energy is obtained by integrating over the whole shower development,

$$E_{cal} = \int f_{GH}(X)\, dX. \tag{3.20}$$

A small fraction of the shower particles does not contribute to the fluorescence emission. Those are mainly neutrinos, neutral hadrons and penetrating muons. This 'invisible' energy can be determined by simulations and is typically in the order of 10 % for UHECR showers. After correction for the invisible energy, E_{cal} yields the energy of the primary cosmic ray.
Beside the generation of fluorescence light, charged shower particles can directly emit photons due to the Cherenkov effect. The Cherenkov light can as well be exploited for the detection of cosmic rays (refer to [69] for a review of Cherenkov cosmic ray

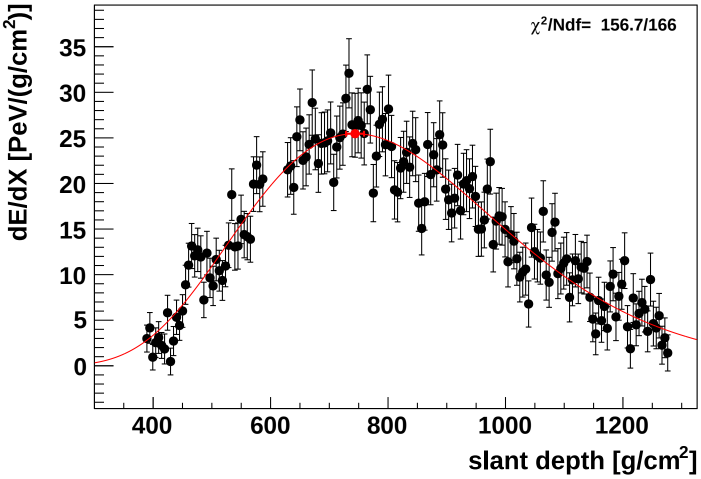

Figure 3.6: Longitudinal profile of an air shower observed with the fluorescence telescopes of the Pierre-Auger Observatory. The energy deposit in the atmosphere is shown as a function of the traversed slant depth. The red line represents the fit of the Gaisser-Hillas function (see. Eq. 3.19). The red dot marks the reconstructed position of the shower maximum $X_{max} = 744 \pm 15\,\mathrm{g/cm}^2$. The corresponding measurement of the same event with the surface detector is presented in Fig. 3.5.

detection) but is inapplicable for the UHECR regime as it is strongly beamed along the shower axis and thus can only be detected close to the shower core. Nevertheless, depending on the geometry of the shower, Cherenkov light can contribute a strong background component for fluorescence detection. Fluorescence measurements need to be corrected for a Cherenkov fraction to be determined from the shower geometry on an event-by-event basis.

The dominating uncertainties of fluorescence detection arise from changing or imprecisely known atmospheric conditions. The fluorescence yield as well as the attenuation of photons in air depend on atmospheric properties. The fluorescence yield is measured in dedicated experiments [70]. Atmospheric conditions are usually monitored by multiple instruments employed along with the telescopes.

Fluorescence measurements are only possible in cloudless and moonless nights. This reduces the duty cycle to about 10 % [56]. Despite this restriction, fluorescence detection is presently the favored technique to measure the energy and composition of UHECRs.

4. Radio Emission from Air Showers

Within an air shower, several processes take place which yield an emission of radio signals. It was first proposed by Jelly [71] back in 1958 to exploit the radio emission for the detection of cosmic rays. In 1962, Askar'yan [72] formulated a first theory of radio emission from air showers. These investigations initiated intensive research in the field of radio emission in the 1960s and 70s on both theoretical and experimental side. Despite the important results achieved in these pioneering years, the interest in radio detection ceased due to technical problems and the success of alternative techniques.

Recently, radio detection of cosmic rays has become a vivid field of research again. Several experiments have been set up to study the radio emission in detail and to examine the feasibility of radio detection for large scale cosmic ray experiments. These strongly benefit from improved electronics and computational resources compared to the 'early days'. Likewise, progress on the theoretical side has been made due to advanced emission theories and the inclusion of computer simulations.

We begin this chapter with a summary of theoretical emission processes followed by the implications for the polarization of the radio signal. The implementation of the emission theories within computer simulations and their results are discussed accordingly. We conclude with recent experimental results.

4.1 Emission Processes

For the radio emission from EAS a multitude of theories have been formulated. Within these theories the radio emission can essentially be attributed to one of the following causes:

- Differences in the nature of interaction of electrons, positrons and photons with the atmosphere. These differences cause a negative charge excess within the air shower which causes the emission of coherent radio-frequency radiation.

- The interaction of charged shower particles with the magnetic field of the earth. Charged particles are deflected and accelerated by the geomagnetic field. Consequences are a charge separation which creates an electric dipole field and yields a transverse current within the shower. The time-variation of the dipole field and the transverse current throughout the shower development are sources of radio emission.

- The interaction of charged shower particles with the electric field of the atmosphere. The static geoelectric field yields radiation mechanism similar to those caused by the geomagnetic field.

In this section we focus on 'classical' descriptions of radio emission mechanisms which allow for an intuitive understanding of fundamental properties of the radio signals from air showers derived from the above physical processes. Modern theories of radio emission are strongly associated with computer simulations and incorporate the classical mechanisms embedded in a complex mathematical formalism. They are discussed in Ch. 4.3.

Furthermore we focus on radio emission in the MHz range, that is at frequencies of the order 1 MHz – 100 MHz. It should be stated that the emission mechanisms discussed below may also yield a radio emission at higher frequencies up to the GHz range as discussed in [73]. Furthermore, at GHz frequencies additional processes such as molecular Bremsstrahlung [74] may lead to radio emission. Nevertheless, we restrict the discussion to MHz radio emission which is relevant for this thesis.

4.1.1 Charge Excess Radio Emission

Within his theory of charge excess radio emission [72], Askar'yan proposed that radio signals from air showers originate from a superposition of Cherenkov radiation of shower particles. Charged shower particles emit Cherenkov radiation as they move faster than the speed of light in air. As positive and negative charges emit radiation of opposite phase, the individual contributions cancel out if the number of negative particles equals the number of positive ones. Thus, a charge excess within the air shower becomes a necessary condition for a non-vanishing total Cherenkov emission.

Askar'yan proposed that a negative charge excess would arise from the annihilation of shower positrons with electrons from air molecules. It was shown later by detailed calculations and Monte Carlo simulations that positron annihilation only accounts for about 10% of the total charge excess (see [65] and references therein). The dominating contributions are due to Compton recoil electrons and knock-on electrons which gain relativistic speed and propagate along with the air shower. Allan calculated that the number of shower particles N_{CE} composing the charge excess can amount up to 20% of the total particle content [75] at the shower maximum.
The charge excess results in a non-canceling Cherenkov radiation which constitutes the total radio signal. The total radiated power is proportional to the number of radiating particles N_{CE} if they are considered to emit independently, i.e. incoherent. However, in case of radio waves when the wavelength is large compared to the distance between individual radiating particles, the emission becomes coherent. The maximum distance between radiating particles is identified with the longitudinal thickness of the shower disk of a few meters. For coherent emission, the total radiated power scales with N_{CE}^2, leading to an important amplification with respect to an incoherent process. Coherence of the radio emission is mostly stressed as requirement to achieve measurable radio pulses, independent of the actual emission

mechanism.
As a consequence of coherence, a frequency spectrum of the radio signal in favor of the lower frequencies is created. An upper limit to the spectrum is imposed by the loss of coherence at high frequencies.
Assuming that the number of charge excess particles N_{CE} is proportional to the total number of shower particles N and considering a linear scaling of the particle number N with the cosmic ray's energy E_0 (cf. Eq. 3.2), for the total radiated power P holds

$$E_0 \propto \sqrt{P}, \tag{4.1}$$

in case of coherent emission. The radio signal amplitude $A \propto \sqrt{P}$ is thus predicted to scale linearly with the cosmic rays energy.

Askar'yans classical theory draws an intuitive picture of fundamental characteristics of the radio emission such as coherence effects and the scaling with the cosmic rays energy. However, in contrast to Askar'yan, some recent models of radio emission (see Ch. 4.3) do not explicitly attribute the radio emission evolving from a charge excess to classical Cherenkov radiation. In these models, the radio emission is generated by the time-variation of the net charge excess in the shower front itself. This leads to a charge excess radio emission even if the index of refraction is $n = 1$.

4.1.2 Geomagnetic Radio Emission

Askar'yan already pointed out that a charge separation due to the geomagnetic field could also lead to coherent radio emission [72]. Kahn and Lerche [76] demonstrated later that this process could be dominating in a frequency range from 30 MHz to 300 MHz. Since then, several emission mechanisms based on a geomagnetic origin have been formulated.
The basic idea of geomagnetic emission is that charged shower particles (charge q) are deflected by the Lorentz force

$$\vec{F_L} = q\,(\vec{v} \times \vec{B}) \tag{4.2}$$

in the earth's magnetic field $\vec{B}$ from their direction of propagation $\vec{v}$ in the atmosphere. Positively and negatively charged particles are deflected in opposite directions which leads to a transverse charge separation. Consequently the shower emerges a transverse electric dipole moment. Since the transverse dipole is being sustained by repeated charge separation, there is also a continuous flow of transverse current throughout the lifetime of the shower. The transverse current emits dipole radiation which is strongly beamed along the shower axis due to the relativistic velocity of the dipole.
As in the case of the charge excess emission, the emission becomes coherent when the longitudinal extend of the shower front is smaller than the emitted wavelength.

An alternative approach for the geomagnetic emission is followed by Gorham and Falke [77] and Falke and Huege [78] respectively. Within their theory of 'Geosynchrotron' emission, the radio signal directly evolves from synchrotron radiation of the charged shower particles. In particular, the semi-analytical approach developed in [78] is based on the synchrotron emission of electron-positron pairs gyrating in the earth's magnetic field. The treatment of electron-positron pairs instead of single particles incorporates the pair production processes within an air shower (cf. Ch. 2) and provides an important simplification for model calculations. By applying realistic shower geometries, the total radio pulse is calculated as a superposition of synchrotron radiation from the single electron-positron pairs. An integration over the lateral and longitudinal structure of the air shower yields coherence of the radio signal. For coherent emission the radiated power scales quadratically with the number of radiating shower particles as discussed in case of the charge excess emission. Thus, for geomagnetic emission, also a linear scaling of the radio signal amplitude with the cosmic rays energy is expected.

The geosynchrotron approach allows quantitative predictions of properties of the radio signal which can be a accessed by measurements. For instance the frequency spectrum of the radio pulse is directly limited by the thickness of the shower disk. Furthermore, the lateral dependence of the emission can be understood within this model, as it is governed by the intrinsic beaming cone of the synchrotron radiation and its superposition over the whole shower development.

To what extend the geosynchrotron and the geomagnetic emission processes discussed above are separate and independent of each other is not fully resolved yet. Some authors state that they might well be alternative descriptions of equivalent physical scenarios eg. in [65, 78, 79]. In the following, if we speak of 'geomagnetic emission', we refer to the emission mechanisms described in this section as a whole.

4.1.3 Geoelectric Emission

Under normal conditions, the Earth exhibits a vertical electrostatic field with an electrostatic field gradient of ≈ 100 V/m at the surface with decreasing strength towards increasing altitude. Weather conditions can significantly influence the electric field within the atmosphere. During thunderstorms the electric field gradient can locally reach strengths of up to 200 kV/m [80].

The electrostatic field component perpendicular to the trajectory of an air shower causes a deflection and thus a separation of charged air shower particles, as discussed by Charman in 1967 [81]. Analog to the case of geomagnetic emission, an electric dipole and a transverse current evolve within the air shower, causing the radio emission. Charman calculated that under normal conditions the separation due to electric fields and the resulting radio emission is negligible compared to the geomagnetic emission. However, a strong amplification of the geoelectric emission is expected for extreme electric field gradients as present in the proximity of thunderstorms.

By incorporating recent computer simulations, Buitink et. al. [80] have revisited the topic of geoelectric radio emission. They conclude that, for normal weather conditions, atmospheric electric fields are too small to significantly influence the radio emission from air showers. For air showers that pass through thunderstorms, both the strength and the polarization of the radio signal can be altered strongly. Radio signals measured in the proximity of thunderstorms should thus be analyzed separately from those recorded under normal conditions. To allow for such a separation, a weather monitoring along with the radio detector is recommended.

4.2 Polarization of Radio Emission

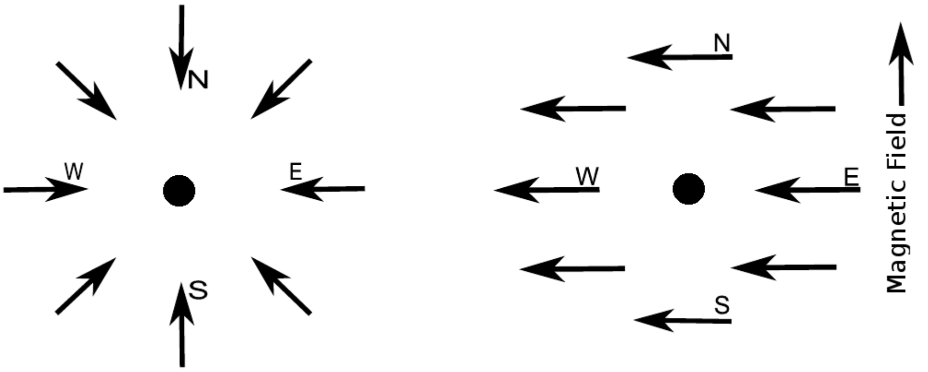

Figure 4.1: Alignment of the electric field vector as a function of the observer position for charge excess emission (left) and geomagnetic emission (right). The displayed situation corresponds to a vertical air shower and a horizontal geomagnetic field in case of the geomagnetic emission. The black dot marks the shower core. Adapted from [79].

Both, the negative charge excess and the geomagnetic emission generate linear polarized radio signals, that is the direction of the electric field vector is constant throughout the duration of the radio pulse. However, regarding the position of the observer, both mechanisms yield different polarization signatures.

In the case of the negative charge excess emission, the electric field is radially polarized towards the shower axis [65], as illustrated in Fig. 4.1, left. The polarization measured at ground level thus depends on the position of the observer relative to the shower axis.

In case of geomagnetic emission, the electric field vector $\vec{E}$ is aligned in the direction of the Lorentz force [75], (cf. Eq. 4.2) as

$$\vec{E} \propto \vec{n} \times \vec{B}, \tag{4.3}$$

where we identify $\vec{n}$ with the direction of the shower axis. The polarization is thus independent of the position of the observer. The situation for a vertical air shower and a geomagnetic field aligned in north-south direction is depicted in Fig. 4.1, right. Eq. 11.6 implies that the direction of the emitted electric field varies with the direction of the shower axis, that is the incoming direction of the air shower. Furthermore, the strength of the emission scales with the angle α between the shower axis and the geomagnetic field,

$$|\vec{E}| \propto |\vec{n} \times \vec{B}| = |\vec{n}||\vec{B}| \cdot \sin(\alpha). \tag{4.4}$$

The electric field vectors for various incoming directions as computed with Eq. 11.6 are visualized in Fig. 4.2. The geomagnetic radio emission is thus maximized for incoming directions perpendicular to the direction of the magnetic field and vanishes

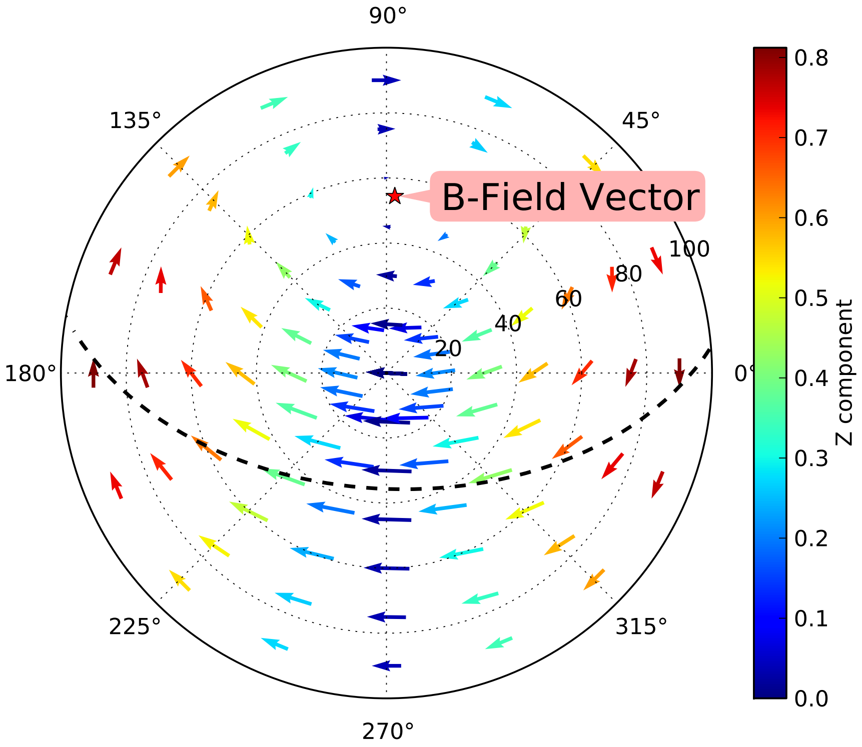

Figure 4.2: Polarization due to geomagnetic radio emission for various incoming directions of the air shower in a polar skyplot. Zenith direction is in the center, north at the top and east to the right. Each vector gives the direction of the horizontal component of the electric field. The vertical component is color coded. The length of the vectors scales with the emission strength. The dashed line indicates the directions of maximal geomagnetic emission. The geomagnetic field points almost to the north with a zenith angle of 58°, corresponding to the magnetic field at the site of the Pierre Auger Observatory in Argentina.

if the showers propagates parallel to the magnetic field vector.

For an air shower that radiates from both, geomagnetic and charge excess emission, the electric fields from the individual contributions will interfere at a given observer position. For linearly polarized contributions with an equal time structure, the superposition will also be polarized linearly [82]. The orientation of the total electric field is then given by the sum of the electric fields of the individual contributions. It depends on the position of the observer and the relative strength of the individual contributions. The polarization of the radio signal is thus sensitive to the mechanisms of emission and their relative weight.

4.3 Simulation of Radio Emission

Recent models of radio emission incorporate multiple of the emission mechanisms discussed above to predict the total radio emission. As these models are usually developed in close conjunction with associated computer simulations, they are also referred to as simulations of radio emission. They can be grouped in macroscopic and microscopic approaches.

The macroscopic approaches MGMR [83] and EVA [84] derive the radio signal from macroscopic quantities such as currents within the shower. In particular, MGMR and EVA calculate the radio emission based on the time variation of a net charge, a dipole moment and a transverse current (cf. Ch. 4.1). The underlying particle distributions are either parameterized (MGMR) or taken from individual CORSIKA showers (EVA).

Microscopic approaches follow individual particles of the air shower and calculate their radio emission from electrodynamics. The emission is directly governed by the distribution and motion of the shower particles. No direct assumptions to the actual emission mechanism are made. Such a microscopic approach is followed by REAS3 [85], CoREAS [86], SELFAS3 [87] and ZHAireS [88]. CoREAS and ZHAireS are full Monte Carlo simulations, that is, the calculation of the radio emission is directly integrated within a simulation of the air shower such as CORSIKA or AIRES (cf. Ch. 3.1.3) respectively. REAS3 and SELFAS3 apply histogrammed CORSIKA showers to describe the particle distribution within the shower.
The underlying electrodynamics are applied in a specific formalism within microscopic approaches. An example of such a methodology is the 'endpoint formalism' [89] which is incorporated in REAS3 and CoREAS. The motion of air shower particles is described by a series of discrete acceleration events or 'endpoints', with each endpoint being a source of emission. Under certain boundary conditions, the 'classical' radiation processes such as synchrotron radiation and Cherenkov radiation follow from the 'endpoint' emission. Due to its discreteness the formalism is well suited for direct numerical implementation in simulation codes.

Despite the fundamentally different approaches, recent simulations have converged in the last years and deliver consistent results. A comparison of the radio pulse as predicted by REAS3 and MGMR simulations is depicted in Fig. 4.3. Both simulations predict bipolar pulses with similar shapes. With increasing distance of the observer to the shower axis, the pulse amplitudes decrease and the shape becomes flatter. The pulse amplitudes of both simulations are in fair agreement especially towards larger lateral distances.

The frequency spectra obtained from REAS3 and MGMR simulations are presented in Fig. 4.4. Generally the spectral field strength decreases with increasing frequency. This effect can be attributed to the loss of coherence towards higher frequencies as discussed in Sec. 4.1. For observers close to the shower core, the spectrum extends to several 100 MHz. With increasing lateral distance, the high-frequency cutoff moves towards lower frequencies and the spectrum becomes dominated by low frequencies.

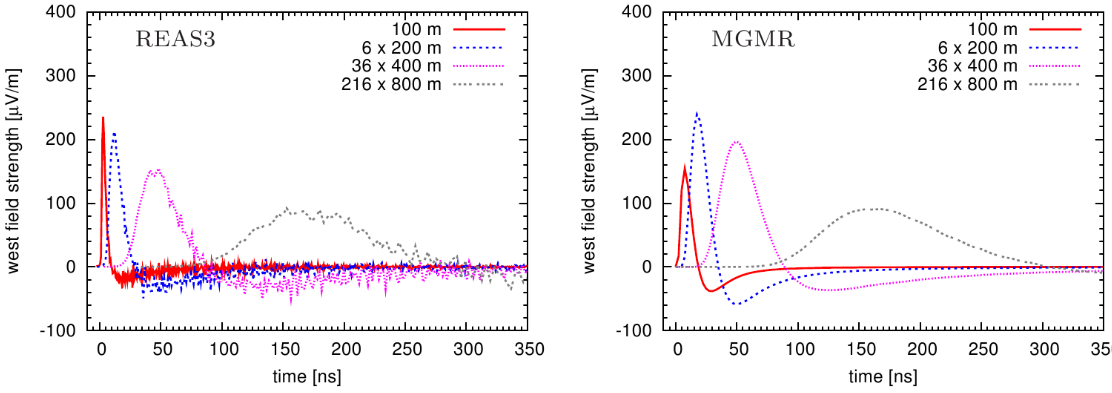

Figure 4.3: Radio pules simulated with the REAS3 (left) and the MGMR (right) for observers at different lateral distances to the shower core. The curves for distances larger than 100 m are scaled with the scaling factor denoted in the legend. Simulated is the west polarization component of a vertical air shower with a primary energy of 10^{17} eV. From [90].

An important observable for radio detectors is the lateral distribution of the radio signal amplitude. In analogy to the lateral distribution of particles within an air shower (cf. Ch. 3.2.1), it is called LDF (Lateral Distribution Function). Simulations of LDFs for different primaries and primary energies are summarized in Fig. 4.5. To compare the LDFs of showers with different energies, the field strengths are normalized with the energy deposited in the atmosphere by the electromagnetic cascade of the shower. An approximately exponential falloff of the signal amplitude with

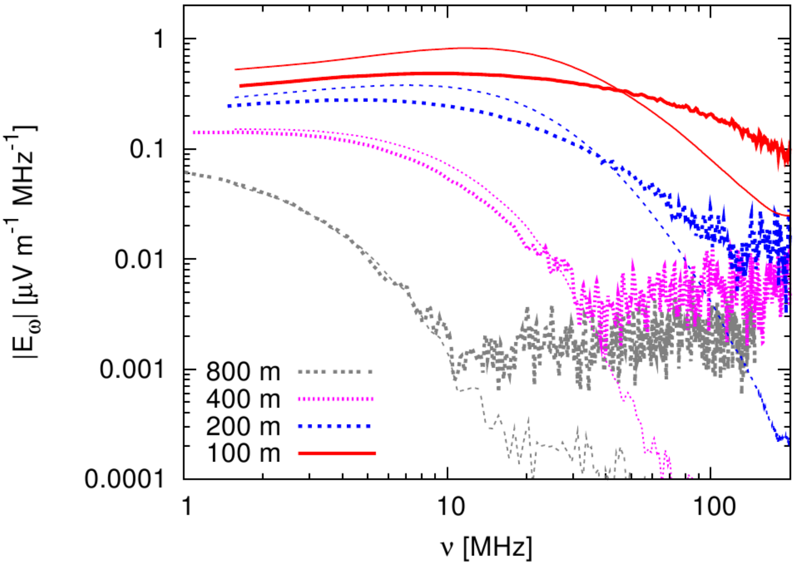

Figure 4.4: Frequency spectra of radio pules simulated with the REAS3 (thick lines) and the MGMR (thin lines) for observers at different lateral distances to the shower core. Simulated his the total spectral field strength for a vertical air shower with a primary energy of 10^{17} eV. From [90].

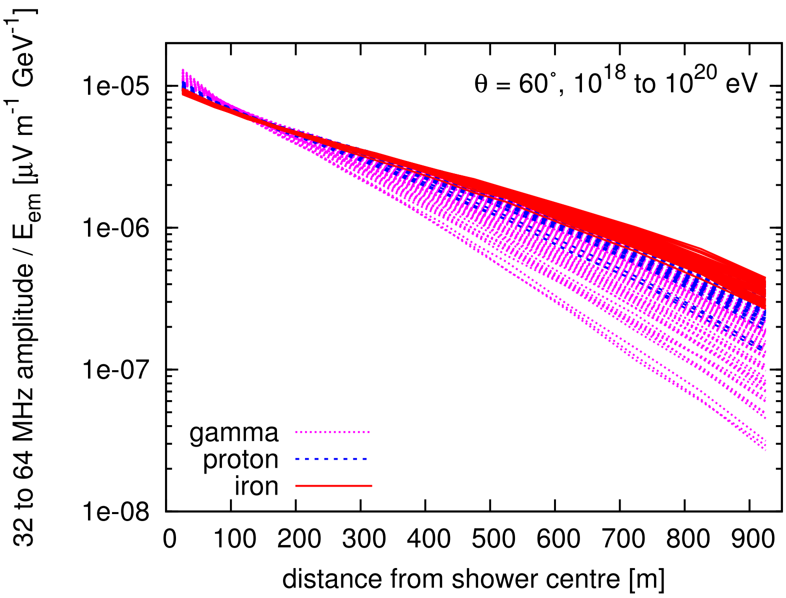

Figure 4.5: Lateral distribution of the 32 – 64 MHz filtered radio signal amplitude normalized with the energy deposited in the atmosphere by the electromagnetic cascade of the air shower. Shown are 180 air showers of different primaries in an energy range from 10^{18} to 10^{20} eV, simulated with REAS. From [91].

increasing distance is observed for all simulated showers. However, the slope of the LDF changes with energy and mass of the primary particle. This can be understood as the distance of the shower maximum to the ground varies with energy and mass of the cosmic ray (cf. Ch. 3). The collimated radio emission is distributed over a larger area on ground for showers that have their maximum higher in the atmosphere than for those with the maximum close to the ground. Consequently, the LDF becomes flatter. The slope of the LDF is thus sensitive to the depth of the shower maximum and therewith to the mass of the cosmic ray.

On closer inspection the normalized LDFs intersect in a narrow region at about 150 m lateral distance. The position of this well defined interception region does not depend on the energy of the air shower. Furthermore, shower to shower fluctuations are minimal in this region and the signal strength is independent of the primary mass. The signal strength measured at the lateral distance of the interception region, relatively close to the shower core, is thus expected to serve as a suitable energy estimator. On the other hand, an increased sensitivity to the primary mass is expected for measurements at large distances to the shower core.

The current microscopic models discussed above as well as the macroscopic approach EVA comprise a realistic treatment of the refractive index of the earth's atmosphere. The refractive index is about $n \approx 1.0003$ at sea level and decreases with increasing altitude towards $n = 1$. A consequence of the refractive index $n > 1$ is that radiation emitted at different times and points within the shower development can reach an observer at the same time for suitable geometries. In these cases the radio pulses are compressed in time which can lead to an extension of the frequency spectrum

up to GHz frequencies [73].
Furthermore simulations suggest that the interplay of different emission mechanisms together with the realistic refractive index can cause an amplification or attenuation of the total radio amplitude at certain observer distances mostly very close to the shower core [84, 88]. This could lead to significant derivations from an exponential lateral falloff of the signal amplitude close to the shower core.

4.4 Measurements of Radio Emission

The radio emission from air showers can be detected with ground-based arrays of radio antennas. The radio emission forms an electromagnetic pulse front that propagates along with the particle shower front of the air shower. When it reaches ground level, the pulse front creates a footprint around the shower core, similar to the footprint of the shower particles. Antennas placed in the vicinity of the shower core will detect short pulses in the radio frequency regime with electrical field strengths per unit bandwidth up to several $\mu\mathrm{Vm}^{-1}\mathrm{MHz}^{-1}$.

The first measurements of radio emission associated with cosmic ray induced air showers date back to the mid 1960s. Jelly and co-workers [92] used an array of 72 radio antennas to firstly detect radio pulses in coincidence with Geiger-Müller counters.
Allan et al. [75] performed systematic studies of radio emission recorded in coincidence with particle detectors at the Haverah Park cosmic ray air-shower experiment. He investigated the dependence of the radio signal on the shower geometry and the primary energy. He summarized his findings with a parameterization of the electric field amplitude ε_ν obtained from measurements at different frequencies as

$$\varepsilon_\nu = 20 \left(\frac{E_p}{10^{17} eV} \right) \cdot sin\,\alpha \cdot cos\,\theta \cdot exp \left(-\frac{R}{R_0(\nu,\theta)} \right), \qquad [\mu V m^{-1} MHz^{-1}]. \quad (4.5)$$

Here, ε_ν is the electric field strength at the center frequency ν of the used receiver divided by its bandwidth. The normalization by the bandwidth results in a quantity that is comparable also between measurement setups operating at different frequencies and different bandwidths. The parameterization incorporates the cosmic rays energy E_p, the angle α between the shower axis and the geomagnetic field vector, the zenith angle θ of the air shower and the distance R of the antenna to the shower axis.
Allan stated that his formula is valid for zenith angles smaller than 35° and lateral distances up to 300 m. In this region he observed a linear scaling of the signal amplitude with the cosmic ray's energy E_p. For the scaling factor (here 20) he found values ranging from 1.6 to 25 in different experiments. This rather large uncertainty can mainly be attributed to poor calibration of the receiving systems [65].
The $sin\,\alpha$ term in Eq. 4.5 is motivated by the scaling of the signal amplitude with

the angle between the shower axis and the geomagnetic field characteristic for geomagnetic emission mechanisms (cf. Eq. 4.4).
The factor $cos\,\theta$ is introduced to account for a reduction of the radio signal towards larger zenith angles due to an increasing distance between the shower maximum and the observer.
The observed lateral falloff of the signal amplitude is modeled with an exponential, where the scale parameter R_0 describes the lateral slope. Allan found values between $R_0 = 100$ m and $R_0 = 140$ m depending on the receiver frequency and zenith angle of the shower.
The characteristics of the radio signal found by Allan are mostly in agreement with recent experimental data. An exception is the $cos\,\theta$ term introduced by Allan which has not been explicitly reproduced in recent experiments. Some modern experiments and major results are briefly discussed in the following.

With the availability of digital electronics and computing resources, the radio detection of cosmic rays experienced a revival in the last decade. An overview of several recent MHz radio detectors can be found e.g. in [93].
For the radio detection at MHz frequencies, the digital radio arrays LOPES [94] and CODALEMA [95] have been key experiments. LOPES (LOFAR Prototype Station), located within the KASCADE cosmic ray detector at KIT in Germany, was originally planned to develop hardware for the LOFAR [96] (Low Frequency Array) telescope. It uses an array of 30 dipole antennas in the frequency range from 40 MHz to 80 MHz, externally triggered by KASCADE. LOPES has stopped data taking in 2013 after almost 10 years of operation.
CODALEMA (Cosmic ray Detection Array with Logarithmic ElectroMagnetic Antennas), embedded in the Nancay Radio Observatory in France operates 24 dipole antennas in coincidence with an array of scintillators and has recently been extended by 34 additional antenna stations. The antennas cover a relatively broad frequency range from 0.1 MHz to 230 MHz.
The experience gained from these experiments has been merged into the design of the next generation digital radio array AERA. The setup of the AERA detector and results based on AERA data will be discussed in detail later in this thesis.

LOPES and CODALEMA proved that radio detection of cosmic rays in the MHz regime is feasible and substantially contributed to the understanding of the radio emission. Both experiments identify the geomagnetic emission as the dominating source of radio emission from cosmic ray induced air showers [94, 97, 95].
The geomagnetic signature is intuitively represented in the distribution of arrival directions of cosmic ray events. The sky map presented in Fig. 4.6 (left) contains the arrival directions of 2030 air showers as detected with CODALEMA. A strong asymmetry with an excess of detected events to the north is observed. This excess points towards arrival directions perpendicular to the magnetic field at the site of the experiment. For these directions, the geomagnetic radio emission is maximized (cf. Eqs. 4.4 and 4.5), yielding a more efficient detection of the corresponding events. An equivalent anisotropy is observed at AERA (see Fig. 4.6 (right)) with an excess

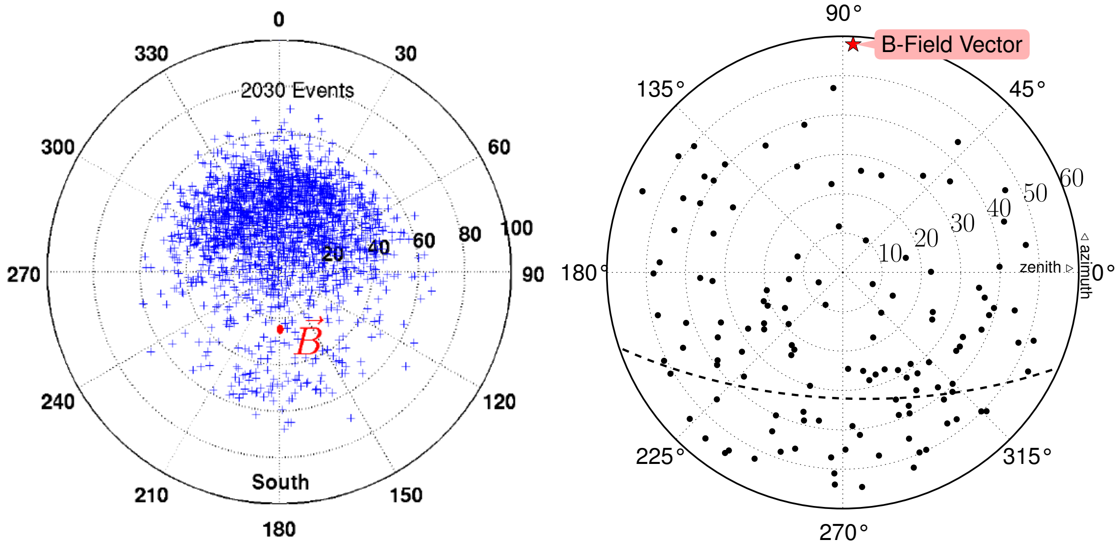

Figure 4.6: Arrival directions of 2030 radio events from air showers as observed by CODALEMA (left) in a polar sky view [98]. On the right a corresponding skyplot of 129 AERA cosmic ray events confirmed by coincidences with particle detectors of the Pierre Auger Observatory is shown. In case of AERA, only events which have triggered at least three radio detector stations and have zenith angels smaller than 55° are shown. The red dot (left) or red star (right), respectively, indicates the direction of the local geomagnetic field. The dashed line in the right plot indicates directions perpendicular to the earth's magnetic field.

to the south as the earth's magnetic field points approximately to the north at the AERA site.

Having identified the predominant role of geomagnetic emission, presently, experiments aim to determine second order contributions to the radio signal. Indications for a contribution in agreement with the emission due to a negative charge excess have recently been reported by CODALEMA [100].
Polarization studies of AERA data [99] reveal a radial polarization component of the radio signals as characteristic for charge excess emission. For a set of AERA cosmic ray events the relative strength a (referred to as charge excess fraction) of the radial polarization component with respect to the geomagnetic component has been measured (see Fig. 4.7). Although a large spread of a from event to event was observed, a significant deviation from zero with an average charge excess fraction of 14 ± 2 % was found.

The lateral distribution (LDF) of the radio signal amplitude can be measured if an air shower is detected in multiple stations at different distances to the shower axis. Systematic studies of the LDF have been performed with LOPES [101]. Typical LDFs as depicted in Fig. 4.8 feature an exponential signal falloff as already reported by Allan (cf. Eq. 4.5). For the shown LDF, the fit of an exponential results in a

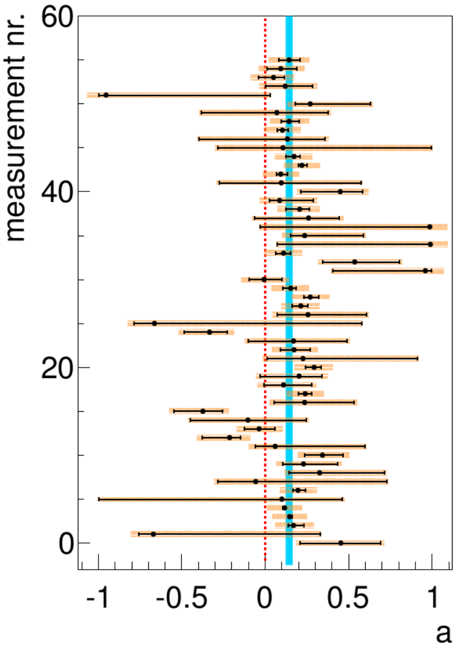

Figure 4.7: Distribution of the most probable values of the charge excess fraction a for a set of AERA cosmic ray events. The solid blue line indicates the confidence belt of 68% around the observed mean value of $a = (14 \pm 2)$ %. The error bars denote the 68% uncertainty of the most probable value. From [99].

slope parameter of $R_0 = 107$ m. On averaging over all considered LOPES events, an average slope parameter of $R_0 = 157 \pm 54$ m is obtained. Alternatively, power laws have been tested to parameterize the LDF but were found to fit the data worse.

Supporting the LOPES results, the CODALEMA collaboration as well measures an exponential falloff of the radio signal e.g. in Ref. [102].

The LOFAR detector with its extremely dense antenna array is well suited for high-resolution measurements of the radio LDF. An example LDF as measured with LOFAR is depicted in Fig. 4.9. About 95 % of all measured LOFAR events feature an LDF similar to the given example, with a flattening below 100 – 150 m distance to the shower core [103]. Although the results have to be treated with caution as no calibration of the signal amplitude has been performed yet, the flattening of the LDF might be interpreted as a consequence of the refractive index effects suggested by recent simulations (cf. Sec. 4.3). However, outside the flattening region all LOFAR events show the common steep exponential falloff.

Currently, findings obtained from the LDF studies at LOFAR have been applied to AERA data [104]. The LDF of AERA events has been parameterized by a two dimensional function with four free parameters which is composed of two gaussian distributions [105]. A good agreement between data and parameterization was found for the selected events. However, at this point the relatively low statistics and the low number of signal stations compared to LOFAR do not allow for more precise conclusions.

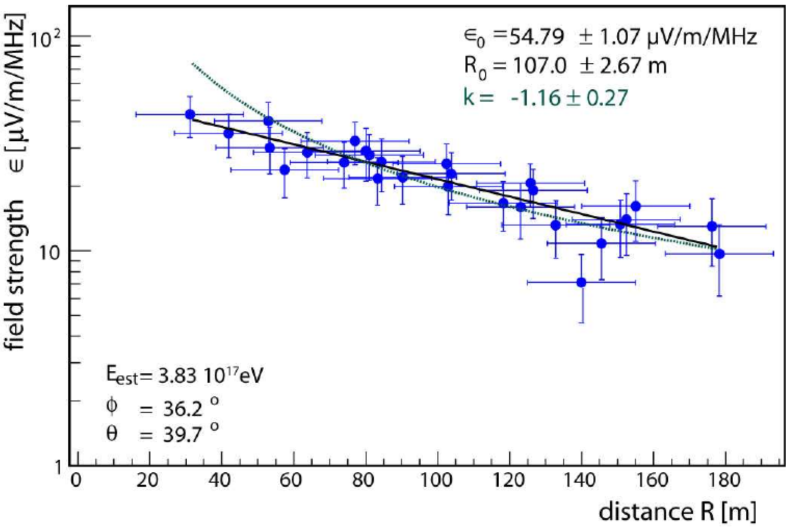

Figure 4.8: Lateral distribution (LDF) of the radio signal amplitude measured at multiple distances from the shower core with LOPES. The results of a 2 parameter exponential fit (black line) are given in the legend. A fitted power law is indicated as dashed line. Taken from [101].

The radio detectors discussed above strongly benefit from combined measurements with associated particle detectors. For instance, an energy estimator obtained from the radio measurement can be calibrated with the energy of the primary cosmic ray reconstructed from the particle detectors.

Such an energy calibration as performed by LOPES is depicted in Fig. 4.10. In this case the radio energy estimator, named $\varepsilon_{50m,\vec{P_{ew}}}$ is defined as the signal strength, corrected for the geomagnetic dependence [1], at an optimum distance [2] to the shower axis. The signal amplitude at this optimum distance is extrapolated from an exponential fit to the measured LDF. The optimum distance is chosen such that the RMS-spread around the subsequent linear energy calibration (Fig. 4.10) is minimized. For the shown calibration, an optimum distance of ≈ 50 m was found.

Finally the energy calibration is performed by fitting a linear function reading $E = p0 \cdot \varepsilon_{50m,\vec{P_{ew}}}$. The data is compatible with a linear correlation between the radio energy estimator and the cosmic rays energy. Interpreting the RMS-spread around the linear calibration as calibration accuracy, a relative energy resolution of 26 % is achieved.

In similar analysis of LOPES data [106] and CODALEMA data [102], a power law $E \propto \varepsilon^{\gamma}_{Radio}$ is adjusted to the data instead of the linear function. A power law index close to one is found in both cases. In summary, the experimental data indicates a linear scaling of the radio signal amplitude with the cosmic ray's energy as predicted

---

[1] In this case the radio amplitude is normalized by the east-west component of the $\vec{n} \times \vec{B}$ vector (cf. Eq.4.4).

[2] In the previous section we have shown based on simulations that such an optimum distance exists, and that the radio amplitude obtained at this distance is well suitable as an energy estimator.

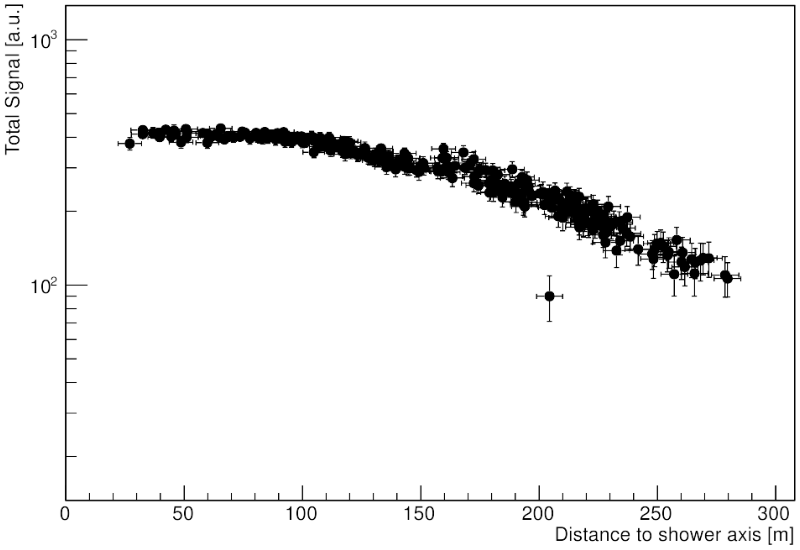

Figure 4.9: Radio LDF as measured with LOFAR. The signal amplitude is given in arbitrary units as the amplitude calibration, necessary for the reconstruction of the electric field, has not been performed yet. From [103].

by the theories discussed above.

Besides the observation of the energy and arrival directions, the measurement of the chemical composition of the primary is a major goal of cosmic rays experiments. Particularly, as the conventional method for composition measurements, the fluorescence technique, suffers from low duty cycles, alternative techniques are demanded. Simulations already suggest that radio detection is sensitive to the mass of the cosmic ray as discussed in the previous section. Recently, first experimental evidence that the depth of the shower maximum X_{max} can be reconstructed from radio measurements has been reported by the LOPES collaboration in [108, 109]. The slope of the radio LDF as X_{max} estimator has been correlated with the associated measurement of the KASCADE detectors. An X_{max} resolution of 90 g/cm^2 of the radio measurement was achieved with this method.
The question whether the accuracy of X_{max} measurements with the radio detection technique can be improved and compete with recent techniques is currently addressed by the next generation radio detector AERA.

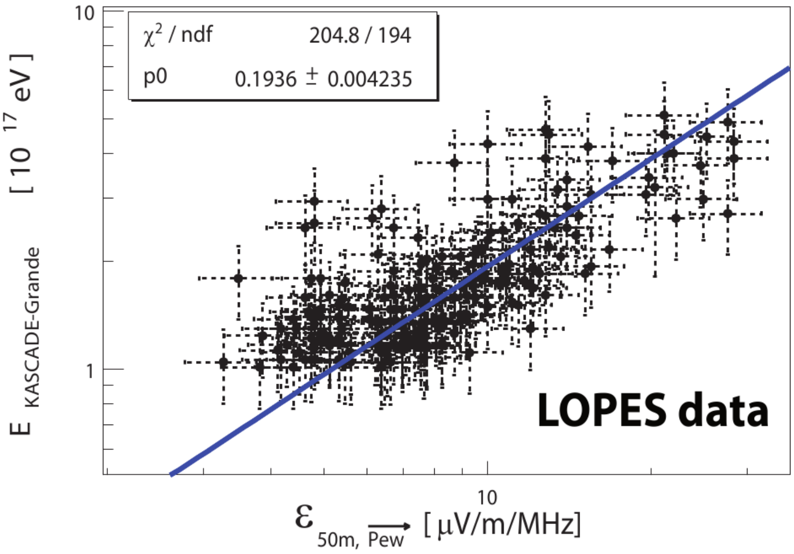

Figure 4.10: Linear correlation of the cosmic rays energy as reconstructed by the KASCADE particle detectors with the LOPES radio energy estimator $\varepsilon_{50m,\vec{P_{ew}}}$ (See text for details). Taken from [107].

5. The Pierre Auger Observatory

The Pierre Auger Observatory [110, 111, 112] is currently the largest experiment for the observation of cosmic rays. It is located in the southern hemisphere near the town Malargüe in the province of Mendoza, Argentina. The remote location provides an essentially flat area of thousands of square kilometers at an altitude of 1400 m above sea level and a low amount of light pollution, both excellent conditions for the two detection techniques applied at the observatory.
As a hybrid detector, the observatory combines a ground array of particle detectors with the fluorescence technique to detect cosmic rays indirectly by measuring their induced air showers. The layout of the observatory is depicted in Fig. 5.1. The surface detector consists of 1660 water Cherenkov detectors spread over an area of $\approx$ 3000 km^2. It is overlooked by 24 fluorescence telescopes located at four different sites at the border of the surface detector. The Cherenkov detectors sample the lateral density of secondary particles at ground level while the fluorescence telescopes provide a direct image of the longitudinal shower development in the atmosphere.
The hybrid approach allows to combine the advantages of both detection techniques. The surface detector with its near 100 % duty cycle and excellent angular resolution allows to measure the arrival directions of cosmic rays with high statistics. On the other hand, the fluorescence telescopes provide an absolute energy measurement and a direct access to the depth of the shower maximum and therewith to the composition estimation but are restricted to a relatively low duty cycle. An inter-calibration of both detectors, using so called hybrid events which are registered in both detectors simultaneously, enables energy measurements with the surface detector independently of Monte Carlo simulations. Furthermore the angular reconstruction accuracy of the fluorescence detectors is improved for hybrid events.

Besides the 'baseline' detectors introduced above, several enhancements have been installed at the POA. Their aims are to lower the energy threshold of the observatory and to incorporate new detection techniques such as specialized muon detectors or the radio detection technique. These extensions will be discussed after a detailed description of the baseline detectors.

From the start of data taking in January 2004 until December 2012, just with the baseline detectors alone, a total of more than 90000 high quality cosmic ray events with energies in excess of 3×10^{18} eV have been recorded [55]. This unprecedented statistics provide the basis for a number of breakthroughs in the field of cosmic ray research. Several results by the Pierre Auger Collaboration, such as the energy

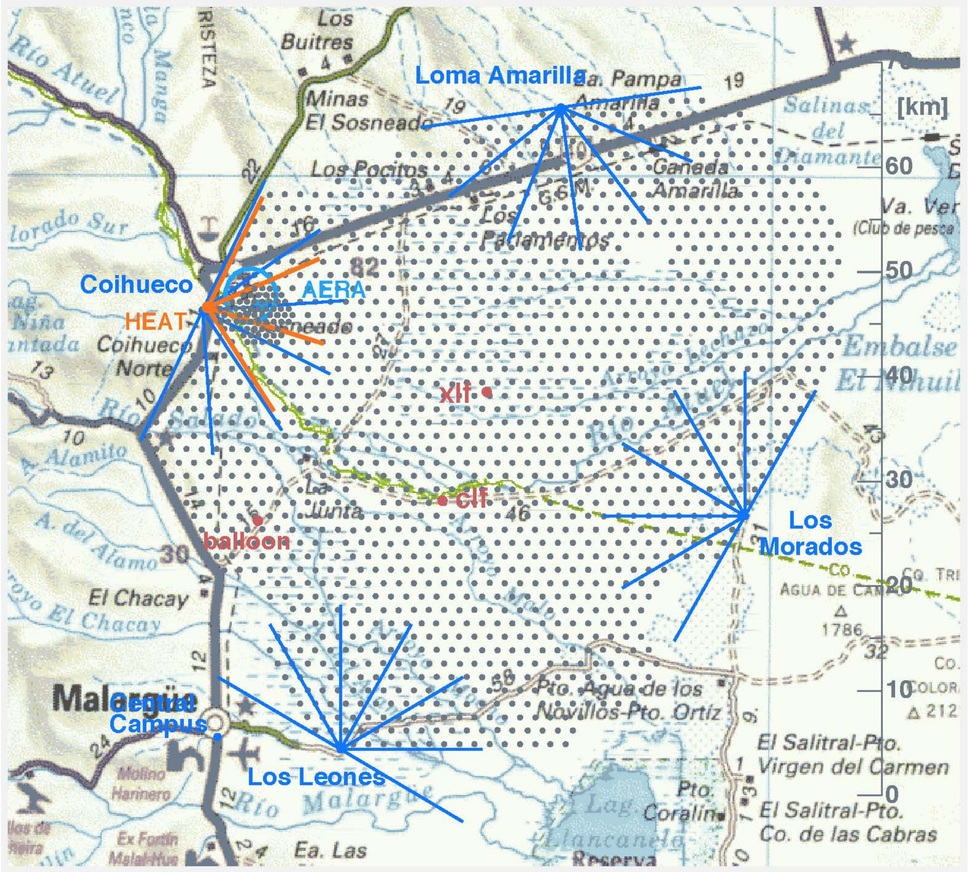

Figure 5.1: Layout of the Pierre Auger Observatory situated close to the town Malargüe, Argentina. Each dot marks the position of a water Cherenkov station composing the surface detector. The fluorescence telescopes at the periphery of the surface detector are indicated by their viewing angles as blue lines. The detector covers an area of ≈ 50 x 70 km^2.

spectrum and composition measurements at the highest energies as well as anisotropy studies have already been presented in Ch. 2. For further recent results based on Auger data refer e.g. to the 'Highlights of the Pierre Auger observatory' in [55].

5.1 The Surface Detector

The surface detector (SD) [111] of the POA is composed of 1660 water Cherenkov detectors arranged in a regular hexagonal grid of 1.5 km spacing. A picture and a sketch of an SD station is displayed in Fig. 5.2.

The detectors are made from a polyethylene cylinder of 3.6 m diameter containing a sealed liner with a reflective inner surface. The liner is filled with 12000 liters of ultra-pure water. Secondary charged shower particles produce Cherenkov light as they traverse the water volume. Energetic photons convert into $e^+ e^-$-pairs which likewise emit Cherenkov light. The Cherenkov light is reflected by the liner and collected by three nine-inch diameter photomultiplier tubes looking downwards into the water.

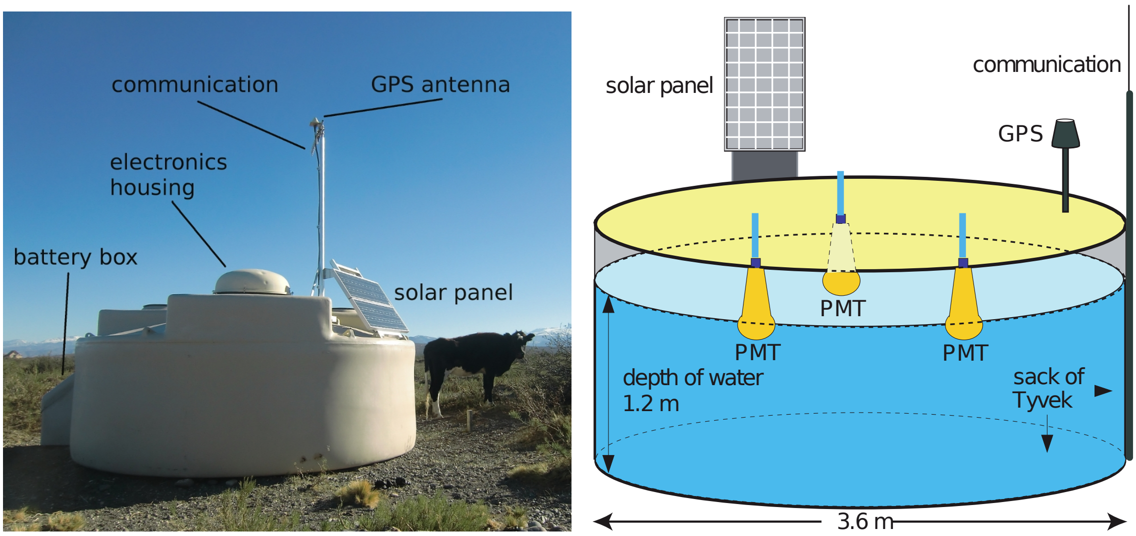

Figure 5.2: Picture of a surface detector station of the Pierre Auger Observatory (left) and schematic view of the station showing the major components (right) [57].

The stations operate fully autonomously, powered by a solar panel on top of the detectors. The photovoltaic system generates in average 10 W to feed the PMT high voltage supplies, the station electronics, the GPS system and the wireless transceiver. The station electronics are weather protected by a dome on top of the station. A battery mounted in a separate box serves as a buffer to ensure a stable power supply during nights and periods with faint solar radiation.
The stations are designed to withstand the environmental conditions throughout a lifetime of $\approx$ 20 years. Temperatures from -15 to 50 ° C as well as strong winds, UV radiation and the wildlife in the Argentinean Pampas (cf. Fig.5.2) were considered for the choice of materials and the design of the stations. As a result of the robust design, in average 98 % of the deployed stations are operational [55].

The timing as well as the amplitude of the individual PMT signals are calibrated individually for each station. The timing is measured by the GPS receivers in combination with a clock in the station electronics. For a precise timing, the exact knowledge of the detector position is crucial. In addition to the GPS measurement of the station itself, various GPS surveys of the surface detector array have been performed. The calibrated detector stations are able to measure the event time of an air shower with a precision of 14 ns [110].
The amplitude calibration of the PMTs is achieved by measuring the background noise created by single muons [113]. These originate from air showers with low energies and induce in average equal signals at a rate of about 2.5 kHz in all detector stations. The gain of the individual PMTs is then adjusted accordingly. Consequently the signal amplitude at the SD stations is measured in units of vertical equivalent muons (VEM).

The PMT signals are digitized by 10 bit flash analog-to-digital converters at 40 MHz sampling rate, yielding recorded traces with 25 ns time binning. The digitized signals are processed by a custom made electronics board on which various trigger decisions are implemented.

The triggering of the surface detector stations [114] is organized in three hierarchic levels (T1,T2,T3). The T1 trigger either requires a signal above a threshold of 1.75 VEM in all three PMTs of a station or a signal level in at least two PMTs above 0.2 VEM for the duration of at least 325 ns (time-over-threshold trigger, ToT). While the first condition corresponds to muons with a rather large but short signal, the latter applies to the electromagnetic component which typically produces numerous weak signals.

The T2 trigger is fulfilled if the T1 was either a time-over-threshold trigger or the coincident signal exceeds 3.2 VEM. The T2 trigger is implemented to reduce the local station trigger rate to 20 Hz, necessary to sent the data to the central data acquisition (CDAS) via a bandwidth limited wireless link.

The T3 trigger is formed by the CDAS located in the campus building of the observatory in the town of Malargüe. If the timestamps of at least three neighboring stations are coincident within an adequate time window, a T3 trigger is set and the CDAS requests the FADC traces from the local stations. Finally, some consistency checks [114] are applied, considering the spatial distribution of the triggered detectors and verifying that the timing is consistent with a planar shower front.

The trigger efficiency of the SD obtained from simulations of proton and iron primaries is depicted in Fig. 5.3 as a function of the cosmic ray's energy. The efficiency steeply increases for energies above $10^{17.5}$ eV and reaches full efficiency for energies above $10^{18.5}$ eV [114].

Cosmic ray events triggered as T3 are reconstructed with the Auger software framework Offline [117]. The 'standard reconstruction' in Offline applies to showers with zenith angles up to 60°. For the reconstruction of very inclined showers ($\theta > 60°$), which are not discussed here, refer to [57].

The Offline reconstruction uses the methods briefly discussed in Sec. 3.2 to obtain the properties of the primary cosmic ray. The shower axis is reconstructed by fitting a plane wave front to the signal times of the triggered SD stations. For higher station multiplicities a spherical wave is fitted as the model of the shower front. The angular resolution varies with the zenith angle and the multiplicity of the SD stations as visible in Fig. 5.4. For the worst case, a vertical shower that triggers only three stations, a resolution of 2.2° is achieved. With increasing multiplicity, the accuracy rapidly improves, being better than 1° for six or more stations over the whole zenith angle range. A multiplicity of 6 stations corresponds to vertical air showers with 10^{19} eV primary energy [116].

The energy of the primary particle is reconstructed by evaluating the LDF of the signals. An example of a LDF measured by the Auger surface detector is depicted

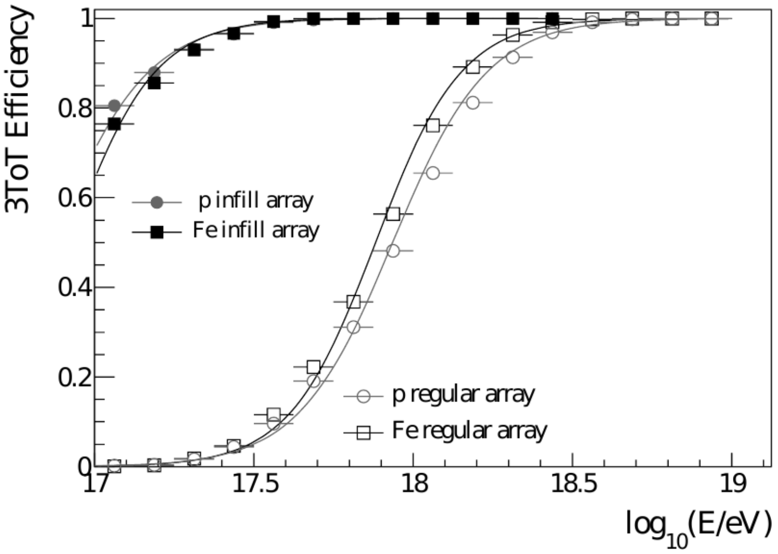

Figure 5.3: Trigger efficiency for the detection of air showers in at least three neighboring stations (3ToT) of the surface detector, obtained from simulations of proton and iron primaries for zenith angles up to 55°. Additionally the efficiency of the Auger infill array (cf. Sec. 5.3), a low-energy extension of the regular Auger surface detector with a detector spacing of 750 m is displayed. From [115].

in Fig. 3.5. The signal strength $S(r)$ measured in the SD stations at a distance r to the shower core is fitted to a model of the LDF reading

$$S(r) = S_{1000} \cdot f_{NKG}(r), \tag{5.1}$$

where $f_{NKG}(r)$ is based on the Nishimura-Kamata-Greisen function (see Eq. 3.17). The normalization is given by the parameter S_{1000}, the estimated signal strength at a distance of 1000 m from the shower core. At a distance of 1000 m the model uncertainties to the precise shape of the LDF are minimal for a detector with 1.5 km spacing [118].

The energy estimator S_{38} is obtained after correcting S_{1000} for the zenith dependency of the signal as

$$S_{38} = \frac{S_{1000}}{CIC(\theta)}, \tag{5.2}$$

with $CIC(\theta) = 1 + ax + bx^2$ with $x = cos^2\theta - cos^2 38°$. The term $CIC(\theta)$ takes into account that the value of S_{1000} for a given energy decreases with the zenith angle due to the attenuation of shower particles and geometric effects. The zenith dependency is extracted from the data under the assumption of a isotropic flux of primary cosmic rays, using the so called 'constant intensity cut' (CIC) method [119]. The measured zenith dependency is then parameterized as the $CIC(\theta)$ term with $a = (0.87 \pm 0.04)$ and $b = (-1.49 \pm 0.20)$. The energy estimator S_{38} can be understood as the signal S_{1000}, the shower would have produced if it had arrived at a zenith angle of 38°.

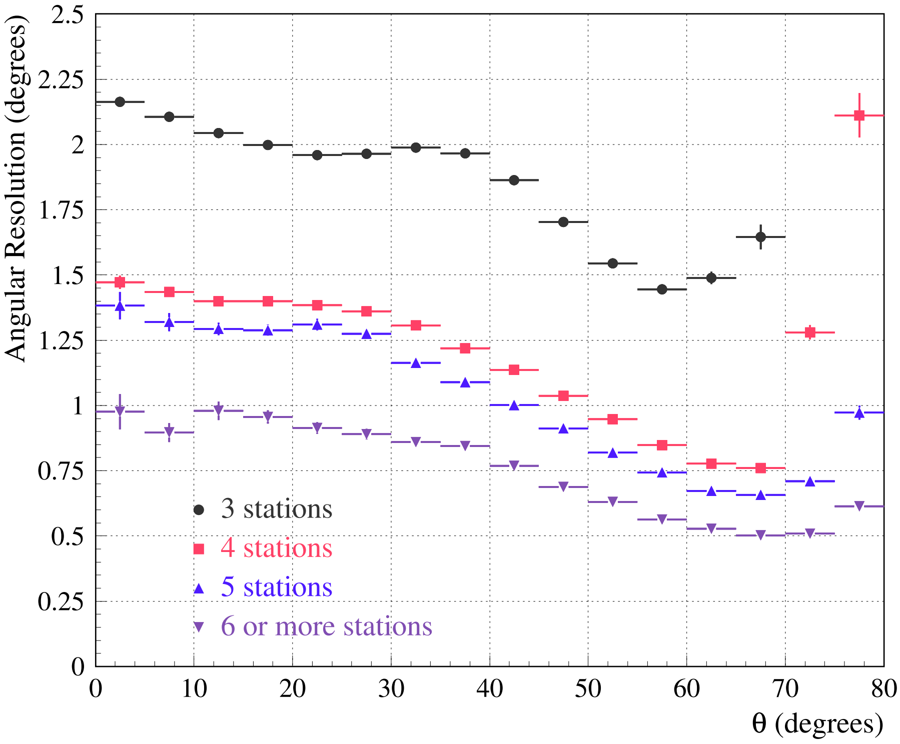

Figure 5.4: Angular resolution of the Auger surface detector as a function of the zenith angle and the station multiplicity [116].

Finally, S_{38} is calibrated with the energy measurement of the fluorescence detector using hybrid events. The relation between S_{38} and the energy E_{FD} measured by FD is well described by a power law reading

$$E_{FD} = A \cdot S_{38}^{B}. \tag{5.3}$$

The fit of the calibration function shown in Fig. 5.5 yields $A = (1.68 \pm 0.05) \times 10^{17}$ eV and $B = 1.035 \pm 0.009$. The resulting relative energy resolution σ_E/E_{SD} of the SD is denoted in the table below for different energy ranges.

Energy Range [EeV]	Energy Resolution σ_E/E_{SD} [%]
3–6	15.8 ± 0.9
6–10	13.0 ± 1.0
>10	12.0 ± 1.0

The systematic uncertainty of the SD energy measurement is given by the systematic uncertainty of the absolute energy scale of the FD of 14 % [120] (cf. next section).

5.2 The Fluorescence Detector

The fluorescence detector (FD) [112] operates at four different elevated sites, named Coihueco, Loma Amarilla, Los Leones and Los Morados, at the periphery of the surface detector. At each site 6 independent telescopes are arranged within a climate-controlled building, together forming one 'eye' of the FD. Each telescope has a field

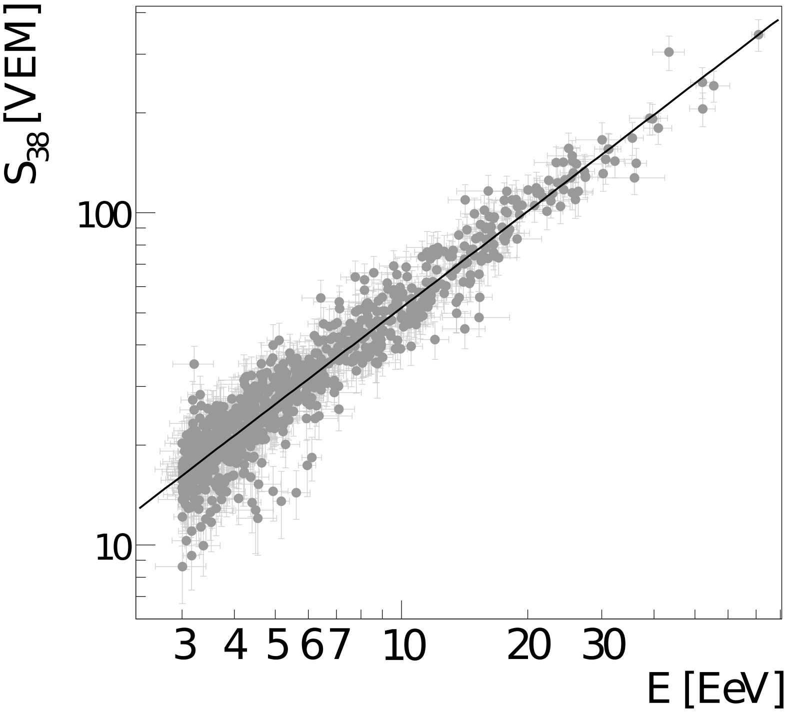

Figure 5.5: Correlation between the energy estimator S_{38} of the surface detector with the energy E measured by the fluorescence detector for 839 selected hybrid events [119]. The absolute energy calibration of the surface detector is obtained by the fit of a power law denoted as the black line.

of view of 30° in azimuth and 30° in elevation, yielding a 180° azimuthal coverage for the complete eye (cf. Fig. 5.1).

The telescopes are designed as a modified Schmidt camera as visible in Fig. 5.6. The fluorescence light emitted by the air shower passes a UV-filter window which transmits almost the complete nitrogen fluorescence spectrum and rejects visible light to reduce the background. The filtered UV-light passes a circular aperture of 2.2 m diameter and is reflected by a 13 m^2 spherical mirror into a segmented camera located on the focal surface of the telescope. A corrector ring covering the outer 25 cm of the aperture radius partially corrects spherical aberration and eliminates coma aberration of the spherical mirror. The corrected optics concentrate 90 % of the light from a distant point source anywhere within the field of view of the telescope into a circle smaller than 15 mm in diameter on the focal surface, corresponding to an angular spread of 0.5°. In comparison, a single pixel of the segmented camera of FD has a field of view of 1.5°.

The camera consists of 440 pixels, each pixel realized as a hexagonal photomultiplier tube (PMT) with a light collector. The light collectors compensate insensitive surfaces between neighboring PMTs on the focal surface and therewith increase the light collection efficiency to 94 % compared to 70 % without light collectors.

The PMT traces are digitized at 10 MHz with 12 bit analog-to-digital converters embedded in the front-end electronics of the telescope. The triggering of the digitized signals is realized by two hardware triggers within the front-end electronics and

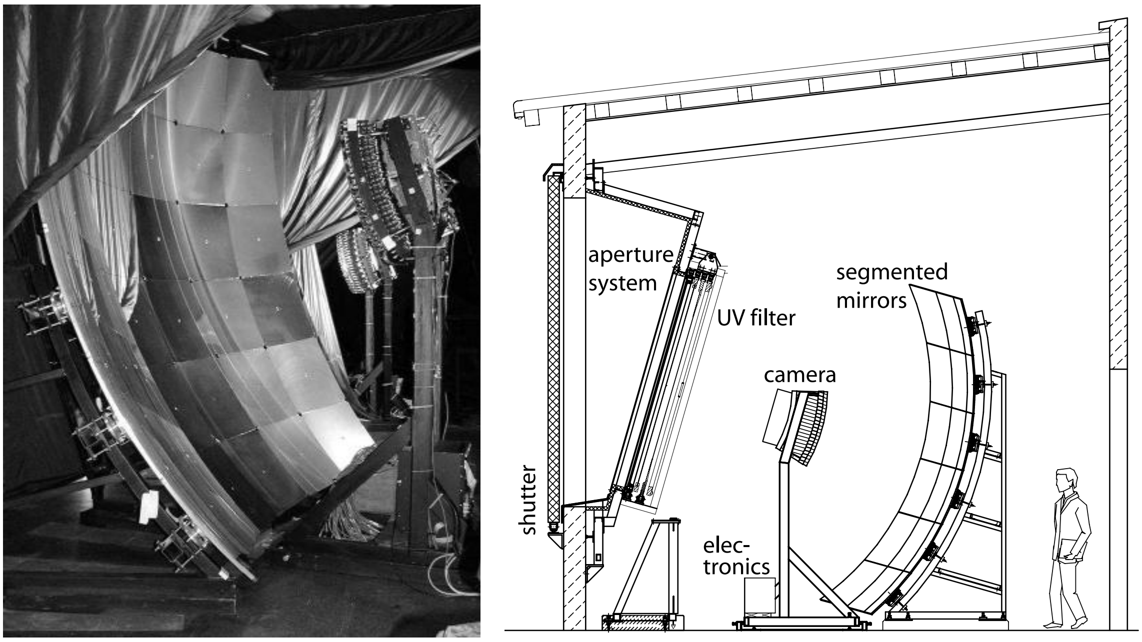

Figure 5.6: Photograph of an Auger SD telescope showing the mirror and the camera (left) and schematic view (right) [112], highlighting the major components.

a subsequent software trigger. The first level trigger (FLT) compares the voltage of a single PMT to a dynamic threshold. The threshold of each PMT is individually adjusted to maintain a constant pixel trigger rate of 100 Hz. This allows to compensate for varying background light conditions.
The second level trigger (SLT) searches for spatial coincidences of at least five time-coincident FLTs. That is, an algorithm checks if neighboring triggered pixels form a straight track within the camera which is characteristic for an air shower.
The software trigger (TLT) finally rejects lightning events that trigger large parts of the camera (hundreds of pixels) based on the multiplicity of time-coincident FLT. Furthermore, randomly triggered pixels that lie far off the light track caused by an air shower are rejected.

A typical light track of an air shower as seen by the cameras of two adjoining fluorescence telescopes of the FD eye Los Leones is shown in Fig. 5.7. The light track in the cameras determines the shower detector plane, that is the plane containing the shower axis and the telescope. The timing information of the triggered pixels together with their pointing fixes the alignment of the shower axis within the shower detector plane and the distance of the shower axis to the telescope.
The reconstruction of the shower geometry from the light track shown in Fig. 5.7 is visualized with the event display depicted in Fig. 5.8. The shown event is a stereo hybrid event, that is an event simultaneously observed in two eyes of the FD (stereo) and additionally in the SD (hybrid). The accuracy of the geometrical reconstruction of the FD can be strongly improved if the information of a second FD eye is included. Further improvement is achieved by fixing the shower axis on the ground with the

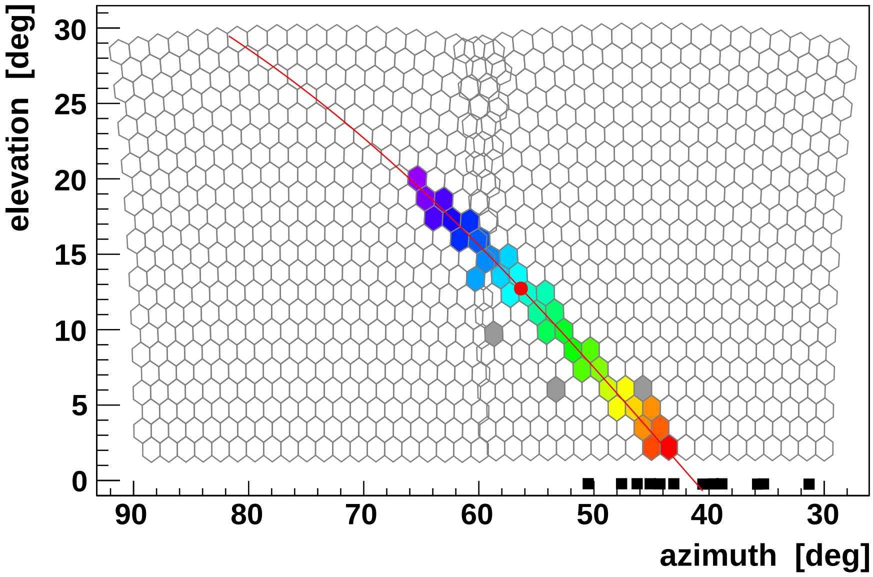

Figure 5.7: Light track of an air shower hybrid event propagating through two adjacent telescopes of the Auger fluorescence eye Los Leones. The color of the triggered camera pixels indicate the timing of the signal from early (blue) to late (red). The full red line represents the fitted shower detector plane. Gray pixels have a signal within the time of the trigger but were marked by the reconstruction algorithm as too far either in distance from the shower detector plane or in time. The black squares at the bottom mark coincident surface detector stations. The red dot indicates the position of the shower maximum. A top view with the geometrical reconstruction of the same event is displayed in Fig. 5.8.

timing and position of the SD station with the highest signal of an associated SD event. To access information also from SD stations which do not contribute in a triggered SD event (this requires at least 3 neighboring stations, cf. 5.1), a hybrid trigger (T3) is created for each FD event with TLT. The hybrid trigger estimates the impact time of the shower front on the ground from the FD reconstruction and sends an external trigger to the SD array, reading out single SD stations at the predicted impact time. For these hybrid events, the resolution of the arrival direction is better than 0.6° [112].

With known shower geometry, energy and mass of the cosmic ray are reconstructed as described in Sec. 3.2.2. The energy measurement with the Auger FD has a statistical uncertainty below 10 % [112]. Systematic uncertainties [120] are due to the uncertainty of the fluorescence yield of 4 % which has been measured by the dedicated AIRFLY experiment [121]. Further contributions are due to the reconstruction procedure, the calibration of the telescopes (refer to [112] for details of the calibration procedures), the correction for invisible energy and atmospheric effects. All uncertainties sum up to a total systematic uncertainty on the FD energy scale of 14 %. The depth of the shower maximum X_{max} can be reconstructed if it lies

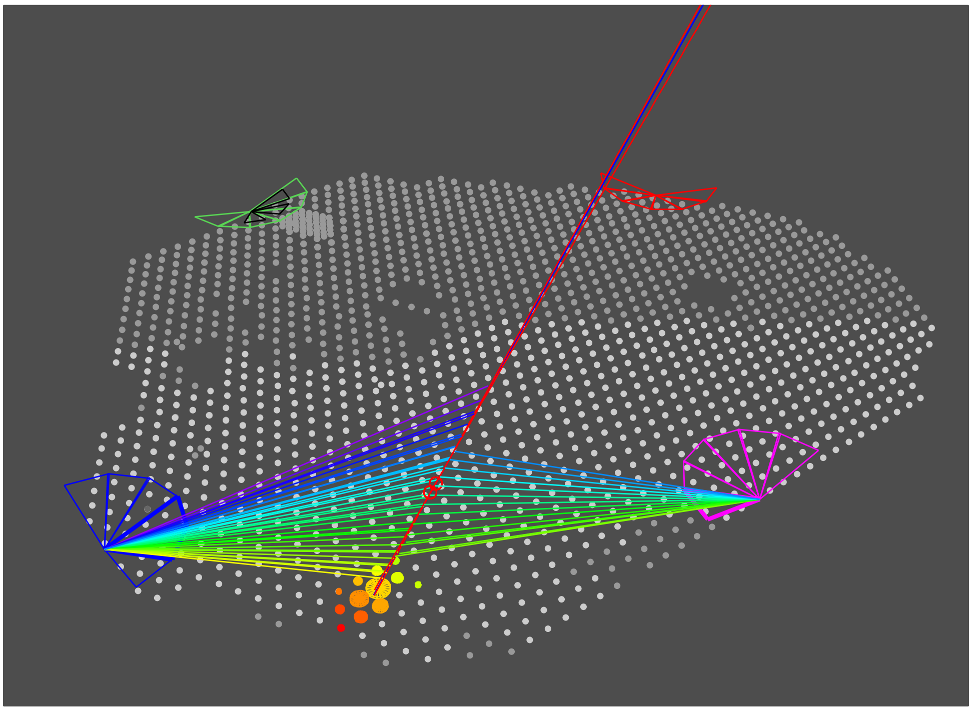

Figure 5.8: Stereo hybrid event detected with the two FD eyes Los Leones (lower left) and Los Morados (lower right) and additionally with 12 stations of the SD. The colored rays indicate the pointing and timing (from early (blue) to late (red)) of the triggered camera pixels. The shower axis as reconstructed by the individual measurements from the two FD eyes (red) and the surface detector (blue) are marked. The triggered SD stations are marked with circles scaled with the measured signal strength and color coded according to their timing. The shower maximum reconstructed by both eyes is marked with the red circles. For the shown event, the longitudinal profile of the air shower measured by Los Leones and the lateral profile observed with the SD are depicted in Fig. 3.6 and Fig. 3.5 respectively.

within the field of view of the FD. For those events an average precision of 20 g/m^2 is achieved [122].
The Auger FD operates in nights with less than 60 % moon fraction corresponding to 16 days per month with, in average, 10 hours of data taking. For higher moon fractions, the background light from the moon disturbs an efficient detection of air showers. Including restrictions due to cloud coverage of the sky the total duty cycle of the Auger FD is 13 % [119].

5.3 Extensions

The Pierre Auger Observatory is designed to detect cosmic ray's from about 10^{18} eV up to the highest energies with high precision. However, for the discrimination between astrophysical models, in particular the cosmic ray composition in the energy region between 10^{17} eV and 10^{19} eV is interesting as in this region the transition from galactic to extragalactic cosmic ray sources is expected (cf. Ch. 2).

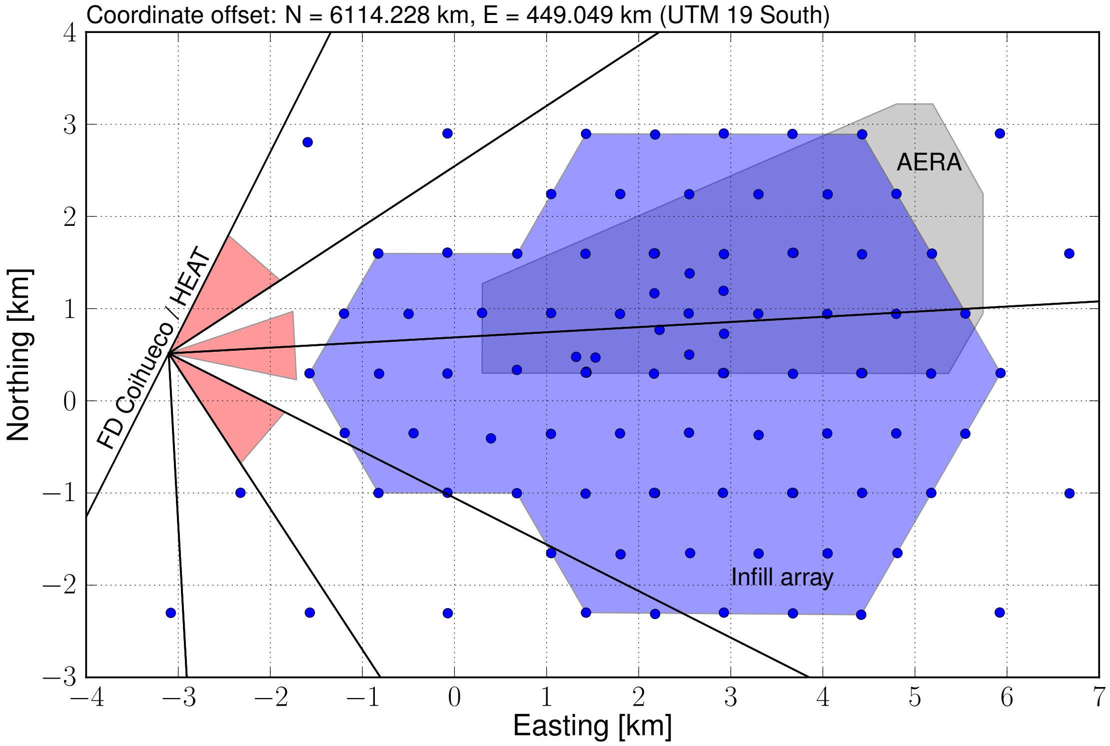

Figure 5.9: Layout of the low-energy enhancements HEAT and AMIGA of the Pierre Auger Observatory. Each blue dot marks the position of a surface detector station. The SD stations of the Infill array are highlighted with the blue shaded patch. The solid lines indicate the field of view of the six telescopes of the FD eye Coiheuco. The field of view of the tree HEAT telescopes in maintenance position is marked with the red shaded triangles. The gray patch indicates the footprint of AERA (see Ch. 6).

To extend the energy range of the Pierre Auger Observatory down to $\approx\ 10^{17}$ eV, enhancements of both baseline detectors have been installed. The low energy enhancement of the surface detector, AMIGA and its counterpart for the fluorescence telescopes, HEAT are co-located at the FD site Coihueco to keep the successful concept of hybrid detection. The layout of the low energy enhancements is depicted in Fig. 5.9.

Amiga (Auger Muons and Infill for the Ground Array) [123] is a combination of regular SD stations deployed in a denser grid of 750 m (Infill) with an associated set of muon detectors. The Infill array [115] consists of 71 regular surface detector stations covering a hexagonal area with an extension towards Coihueco of nearly 30 km^2. The halved spacing with respect to the regular array lowers the energy threshold by approximately one order of magnitude. Full trigger efficiency is reached for energies above $10^{17.5}$ eV as visible in Fig. 5.3.
An engineering array composed of seven muon detectors is currently being deployed within the Infill array. The muon detectors are scintillators with an active area of 30 m^2, buried 2.3 m deep in the ground. The soil absorbs the electromagnetic

component of the shower but is penetrated by the muons, allowing for a separate measurement of muons with the scintillators. The separate measurement of electromagnetic and muonic component can be exploited to study the cosmic ray composition with ground arrays as performed by KASCADE [24].

HEAT (High Elevation Auger Telescopes) [124] comprises three standard Auger fluorescence telescopes tilted upwards by 30°. This is realized by mounting the telescopes on a tiltable platform which can alternate between a measurement position (tilted upwards by 30°) and a maintenance position. The maintenance position allows easy access to the HEAT telescopes for maintenance and a cross calibration with the baseline telescopes of Coihueco.
The shifted field of view enables the detection of nearby low energetic showers. As the amount of emitted fluorescence light decreases with decreasing shower energy, low energetic showers can only be detected close to the telescopes. In addition, the shower maximum of these showers lies higher in the atmosphere and thus often above the field of view of the standard FD telescopes,
The HEAT telescopes are aligned towards AMIGA, which is located in an optimum distance to guarantee a maximal overlap between the two detectors for an effective hybrid detection. The combination of both low energy enhancements enables hybrid measurements at energies as low as 10^{17} eV.

The Pierre Auger Observatory with its well calibrated baseline detectors and low energy enhancements provides a perfect environment to explore the prospects of alternative detection techniques to cosmic rays. Several R&D projects are dedicated to the radio detection of cosmic rays, both at MHz and GHz frequencies.
The research for radio detection in the GHz regime has been triggered recently by laboratory experiments by Gorham et al. [74], suggesting that GHz emission due to molecular Bremsstrahlung from air showers could be exploited for the detection of cosmic rays. An overview of GHz activities at the observatory and recent results can be found in [125].
Two complementary techniques to GHz emission are being pursued at the Pierre Auger Observatory. EASIER (Extensive Air Shower Identification with Electron Radiometer) utilizes the infrastructure, that is the power supply and DAQ system, of the SD stations. A sub-array of 61 SD stations is equipped with C-band (3.4 GHz – 4.2 GHz) antennas oriented towards the zenith. The readout is triggered by the SD stations. EASIER, for the first time, detected an UHECR air shower by GHz emission.
AMBER (Air-shower Microwave Bremsstrahlung Experimental Radiometer) and MIDAS (MIcrowave Detection of Air Showers) are imaging telescopes realized as a reflector dish with a segmented receiver of GHz antennas. AMBER is mounted at the FD site Coihueco, overlooking the Infill array. The receivers are sensitive to both, the C-band and the Ku-band (10.95 GHz – 14.5 GHz). The trigger is provided by the SD. MIDAS follows the same antenna concept but aims for a self-triggered detection of air showers. The viability of GHz detection, presently remaining an open question, will be addressed by the activities at the Auger Observatory in the

near future.

MHz detection of cosmic rays at the Pierre Auger Observatory is performed with the next generation digital radio array AERA, which is the subject of the next chapter.

6. The Auger Engineering Radio Array

The Auger Engineering Radio Array (AERA) is presently the largest radio detector for the observation of cosmic rays. Motivated by the success of the digital radio arrays LOPES and CODALEMA, AERA represents the next step towards establishing the radio detection technique for large scale cosmic ray experiments at the highest energies. In particular, AERA aims at the following science goals:

- Calibration of the radio emission from air showers by hybrid [1] and super-hybrid measurements. This includes a detailed understanding of underlying dominant and sub-dominant emission mechanisms and quantifying their contribution to the total radio signal.
- Exploring the feasibility of radio detection for future large-scale cosmic-ray experiments. AERA will evaluate the quality of the angular, energy and primary mass measurements of a stand-alone radio detector and whether radio detection can compete with the precision of established detection techniques. Furthermore, the operation in coincidence with the existing Auger detectors will allow to assess the benefit of radio measurements as an ingredient of future multi-hybrid detectors.
- Composition measurements in the transition region of galactic to extragalactic cosmic rays. With its sensitivity to the longitudinal shower development, radio detection promises high-duty cycle composition measurements. The energy range of AERA fits the region between about 10^{17} eV and 10^{19} eV where the transition from galactic to extragalactic sources is expected.

The layout of AERA and the design of the used hardware evolved from several small prototype setups which have been installed at the Pierre Auger Observatory. These setups worked as a test-bench to compare hardware components such as different antenna types and electronics and to adapt to the environmental demands at the site of the experiment. The setups were located at two different sites, at the Balloon Launching Station (BLS) in the western part of the SD array (see Fig. 5.1) and close

---

[1] in this context hybrid measurement refers to cosmic ray induced air showers detected with AERA and simultaneously with one (hybrid) or multiple (super-hybrid) different detectors of the PAO.

to the Central Laser Facility (CLF).
The setup at the BLS initially consisted of three antenna stations arranged in a triangle of 100 m base length, installed in 2006. The antennas were read out by a central DAQ located in the BLS via coaxial cables. The trigger for the readout was provided by a scintillator. As antennas, Logarithmic Periodic Dipole Antennas (LPDAs) as well as dipole antennas from LOPES were used. The first radio signal in coincidence with the Auger surface detector was observed with this setup [126]. Several hundred coincident radio events were detected until 2008.
In 2008 the setup was modified and given the name MAXIMA (Multi Antenna eXperiment In Malargüe Argentina) [127]. The three previous stations were replaced by four fully autonomous stations featuring digital signal processing electronics with the capability to self-trigger on the received radio pulses, a solar power supply and a wireless communication system. The transition from a wired setup to autonomous stations provided the basis for a scalable radio detector. Furthermore, a prototype version of the LPDA, currently used at AERA has been extensively tested. MAXIMA stopped data taking in 2011.
The setup at the CLF, named RAuger, was deployed in 2006 in parallel to the BLS setup. Three autonomous stations, forming a 140 m triangle around a SD station, were equipped with CODALEMA dipole antennas. In a later upgrade the antennas were replaced with bowtie, also called butterfly antennas. RAuger firstly detected a confirmed cosmic ray air shower with a self-triggered radio detector and obtained important information about the general behavior of self-triggered radio detectors. RAuger terminated operation in 2010. An overview of RAuger and a summary of results is given in [128].

6.1 Deployment and Layout

The deployment of AERA started in April 2010 at a location in the western part of the SD array close to the FD eye Coihueco. The site was chosen to achieve a maximum overlap between AERA and the low-energy enhancements of the baseline detectors, AMIGA and HEAT, as visible in Fig. 5.9.
The deployment of AERA was organized in three subsequent phases. The first phase comprises a dense core of 24 radio detector stations, arranged as depicted in Fig. 6.1 in a triangular grid with a spacing of 150 m. Three of the 24 phase 1 stations form a 'triple station', being separated by only 30 m. The triple station allows to investigate fluctuations of the radio signal on small scales. Commissioning of phase 1 was finished in September 2010. Since then, 21 stations are taking data while three of the stations were initially used to test different hardware components during operation, but were not involved in the regular data taking.
With phase 2, AERA was expanded with 100 additional stations in 2013. The stations are grouped in two sub-arrays with different spacings. The dense core of phase 1 is surrounded by stations with a mutual distance of 250 m, enclosed by a sparse array of 375 m spacing. The detector stations of phase 1 and phase 2 cover an area of approximately 6 km^2. The graded spacing of the radio stations yields an efficient detection over a broad energy range from roughly 10^{17} eV to 10^{19} eV.

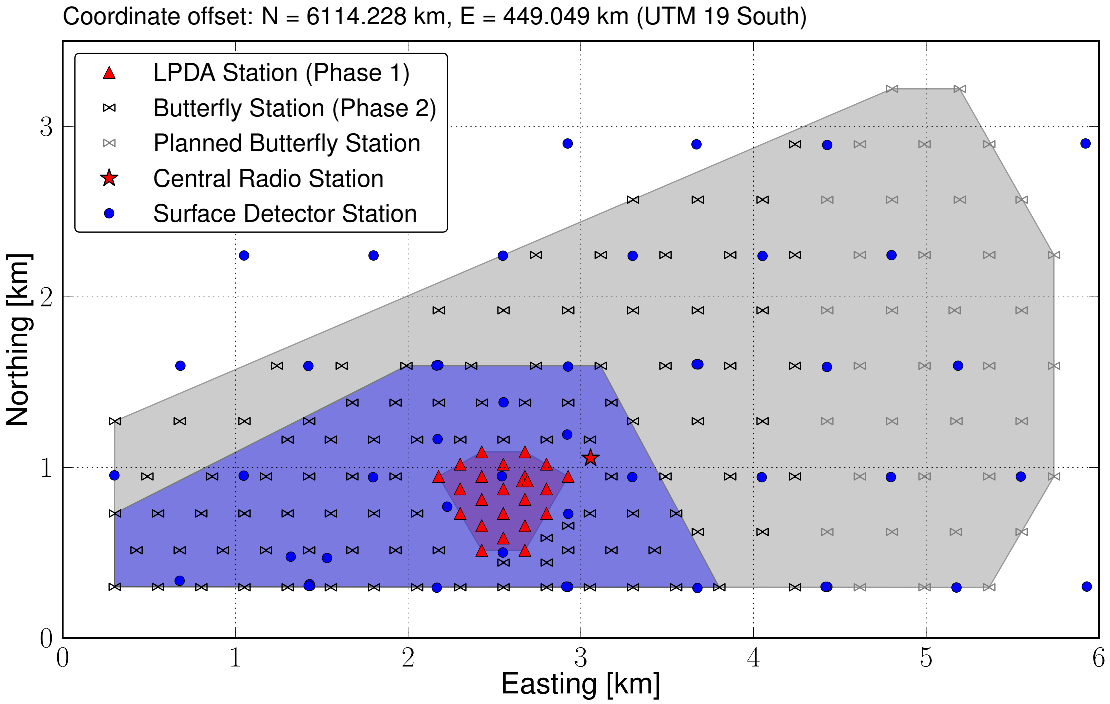

Figure 6.1: Layout of the Auger Engineering Radio Array. The position of the radio detector stations according to the different deployment phases of AERA, as well as the SD tanks are marked as denoted in the legend. The shaded patches highlight the graded spacing between the radio stations.

The phase 2 stations use an advanced hardware design evolving from the experience with the operation of phase 1. Besides improved station electronics, a different antenna type has been introduced in phase 2. While the phase 1 stations are equipped with logarithmic-periodic dipole antennas, a 'Butterfly' antenna is used for phase 2. The radio detector stations are compared in detail in the next section.
A third phase with 36 additional detector stations is planned. These will extend the sparse array of 375 m spacing towards the east, yielding a footprint of more than 10 km^2 for the complete array.

Along with the deployment of the phase 1 RDS, an infrastructure had to be created at the remote site of AERA. Dirt roads were constructed to provide access with vehicles to the RDSs for installation and maintenance. A Central Radio Station (CRS) was set up at the border of the phase 1 array (see Fig. 6.1), serving as a base for the deployment and as a shelter for the central DAQ of AERA.
The CRS (Fig. 6.2) is a 40 feet shipping container equipped with a workshop and several cabinets for the storage of tools and spare parts. A separate compartment holds the computers and electronic devices of the central DAQ of AERA. A 'reference antenna' was placed next to the CRS which can be read out from inside the container to e.g. continuously monitor the radio background at the site.
The power for the electric components inside the container is delivered by a photovoltaic system. Almost 40 m^2 of solar panels have been mounted to continuously

Figure 6.2: The Central Radio Station (CRS) of AERA. The left picture was taken during the installation of the solar panels which provide an autonomous power supply for the DAQ and electronics inside the sea-container. On the right photograph, the CRS in its present state is shown. The two masts and a cable spanned above the container compose a lightning protection for the CRS. The wireless communication antennas to the radio stations mounted at the left mast and a reference antenna in the background are visible.

supply 480 W at 12 V. Periods of low solar irradiation are buffered by batteries inside the container.

The RDSs of phase 1 were initially connected with an high-speed optical network [129] to the DAQ placed in the CRS. For this purpose, several kilometers of optical fibers had to be deployed in the ground. The optical network in principle allows to constantly stream the full amount of data recorded at the RDSs to the DAQ due to its high bandwidth. However, for an array consisting of hundreds of RDS employed at large mutual distances, an optical network is not feasible anymore due to its high costs. Hence, a wireless network was developed and tested in parallel to the operation of the phase 1 array.
With the deployment of phase 2, all RDSs communicate with the wireless network, including the phase 1 stations which have been updated with the wireless communication hardware. The limited bandwidth of the wireless communication in comparison to the optical connection is compensated by a preselection of data at the local RDS level.

6.2 Radio Detector Stations

The main components of the RDSs are the radio antennas, an analog signal processing chain, the digital electronics, the wireless communication system, a GPS reciever and the photovoltaic power supply system. Both, the phase 1 and phase 2 RDSs feature these components with some modifications in detail. The phase 2 stations are basically optimized towards a more compact design compared to the phase 1 stations which yields a cost reduction and an easier and faster deployment

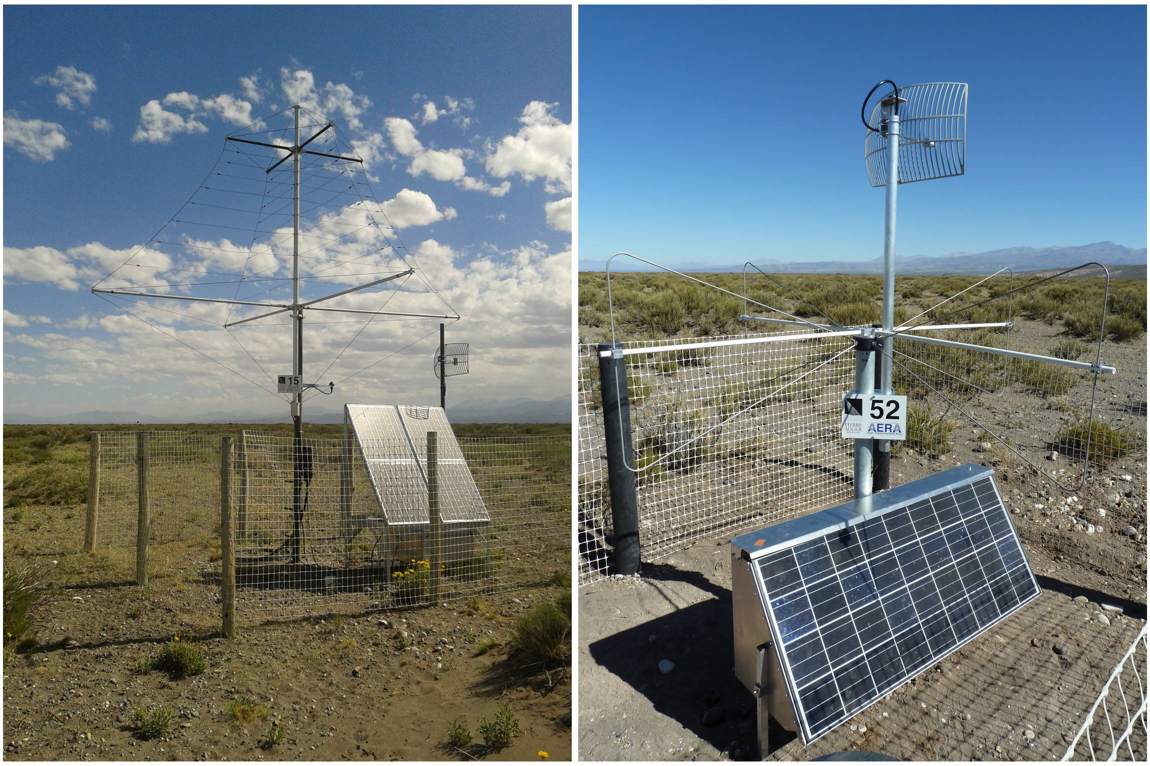

Figure 6.3: Photograph of phase 1 (left) and phase 2 (right) radio detector stations of AERA.

of the stations. A photograph of both versions of the RDSs is presented in Fig. 6.3.

While the phase 1 stations are equipped with logarithmic periodic dipole antennas, the phase 2 stations use a 'Butterfly' antenna as sensor to the radio emission of air showers. Both antenna types provide two independent channels, being sensitive to the north-south or east-west component of the impinging electric field respectively. The antennas are aligned to the magnetic north which deviates about 3° from the geographic north direction at the AERA site. To allow high precision measurements of the electric field polarization, the antennas are aligned with an accuracy better than 1°. The alignment procedure is documented in [130].
Furthermore, the antennas incorporate a low noise amplifier for a first amplification of the voltage received at the antenna terminals. The antennas are mounted on a steel pole embedded in concrete. Both antennas are described in detail in Ch. 8.

The pre-amplified antenna signals are further amplified by a filter-amplifier which also applies an analog band-pass filter from 30 MHz to 80 MHz. Accordingly, the analog signals enter the main electronics board of the station referred to as 'digitizer'. Besides the signal digitization by flash analog-to-digital converters, the digitizer boards provide a ring buffer memory for storage of the signal traces, a Field Programmable Gate Array (FPGA) where real-time trigger algorithms are implemented, slow-control and monitoring features and an interface to the wireless

communication system.
In order to test different technical solutions towards an optimization of the radio technique for future large scale observatories, two different custom-made digitizer boards are used. According to the institutes responsible for the development of the digitizers, they are referred to as Nikhef/RU and KIT/BUW digitizers respectively. Although the digitizers use a different hardware architecture, their key specifications are similar. The Nikhef/RU digitizers sample the analog traces with a dynamic range of 14 bits at 200 MHz while the KIT/BUW digitizers employ 12 bit analog-to-digital converters at 180 MHz. In total, 40 phase 2 stations, located to the east of the dense core are equipped with the Nikhef/RU digitizers. The other stations, including these of the dense core, use the KIT/BUW digitizers.

The processed signals are transferred to a central DAQ via a 5 GHz wireless system [131]. While the DAQ for the RDSs with KIT/BUW digitizers is located at the building of the FD eye Coiheuco, the RDSs with Nikhef/RU digitizers communicate to a separate DAQ housed in the CRS. The DAQ has been split up into two separate locations to first test the performance of the wireless communication system with an intermediate number of subscribers. It is planned to merge both DAQs in the near future.
The communication system is designed to support high data rates up to 10 Mbytes/s of at least 150 subscribers. To communicate over large distances up to 10 km between the RDSs and Coiheuco, the stations are equipped with directional dish antennas mounted on a pole close to the radio antennas (see Fig. 6.3).

The timing of the measured radio pulses is obtained from a GPS receiver mounted at each RDS with an accuracy of ≈ 10 ns. The timing accuracy can be improved by a 'beacon' reference transmitter [132] located at Coiheuco. By an analysis of the phases of the beacon signal observed in the RDSs, a timing resolution of 1 ns should be achievable.

The RDSs are powered by an autonomous photovoltaic system [133] consisting of solar panels, a charge controller and buffer batteries. In case of the phase 1 stations, the photovoltaic system is designed to constantly deliver 20 W at 12 V. As the power consumption of the phase 2 stations could be reduced significantly in comparison to the phase 1 stations, smaller solar panels and buffer batteries are used here.

All station electronics are sheltered in an electronics box placed in the shadow of the solar panels. Besides protection from weather influences, the electronics box shields possible noise generated by the station electronics. At prototype setups at the BLS it was observed that the station electronics itself can cause disturbing signals in the highly sensitive radio antennas if not properly shielded.
While the electronics box is directly attached to the antenna pole in case of the phase 2 stations, it is mounted in a separate frame anchored to the ground for the phase 1 stations.

The complete stations are surrounded by a fence to protect them from animals omnipresent in the Argentinean Pampas. Only non-conducting materials are used for the fence as any conducting material would influence the characteristics of the radio antennas.

6.3 Radio Background at AERA and Self-Triggering

All AERA stations are capable of self-triggering on radio pulses emitted by air showers. The challenge of self-triggering is to discriminate pulses originating from air showers from those generated by man-made noise sources. Although the remote site of AERA is relatively radio-quiet compared to urban environments such as at LOPES, several man-made sources of noise in the radio frequency domain are present. To characterize relevant noise sources, surveys using different techniques have been carried out at the AERA site [134, 135].

The nature of different noise contributions is revealed by a dynamic spectrum recorded over several days at AERA which is presented in Fig. 6.4. The spectrum was recorded with a spectrum analyzer connected to the reference antenna close to the CRS. Several continuous narrow-band transmitters can be observed as horizontal lines, mostly at frequencies below 30 MHz and above 100 MHz, corresponding to the short-wave-band and FM-band of radio broadcasting. The frequency band of AERA from 30 MHz to 80 MHz was explicitly chosen to exclude these transmitters. However, a strong transmitter at 67 MHz remains within the AERA band. Furthermore the continuous signals of the reference beacon are visible around 72 MHz.

Mainly between about 30 MHz and 40 MHz non-continuous signals occur only at certain times of the day. These 'noisy periods' indicate an increased emission of transient noise pulses which constitute a fundamentally different type of radio noise. In a directional analysis of AERA data it was found that the majority of transient noise pulses originates from several 'hot spots' located at horizontal directions in the proximity of AERA [136]. A correlation of these hot spots with the location of potential artificial noise sources such as transformer stations and power lines was observed.

Within AERA, various strategies have been developed to suppress both, continuous and transient noise for an efficient self-triggering. Continuous transmitters in the short-wave and FM-bands are suppressed by subsequent band-pass filter stages with a pass band from 30 MHz to 80 MHz. The LNAs within the antennas incorporate the first analog filter stage, followed by the analog filter of the filter amplifier. After the digitization of the analog signals, a fast fourier transform is performed by the FPGA of the digitizer and an additional digital band pass filter is applied in the frequency domain.

Continuous transmitters which remain within the AERA band (e.g. the beacon reference signals and the 67 MHz transmitter) are removed by several adjustable digital notch filters in the frequency domain. Filtering of these continuous signals reduces the noise level of the signal traces and thus allows to set lower thresholds for the successive self trigger. It should be noted that the notch filters are only applied for

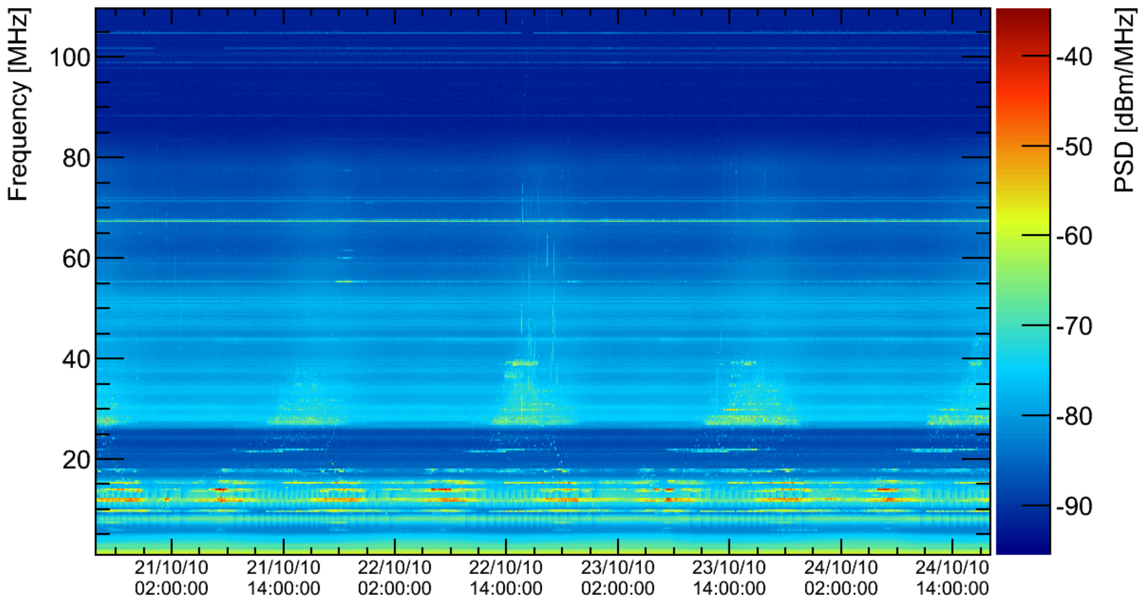

Figure 6.4: Dynamic Spectrum recorded over several days at the AERA site. The power spectral density as measured with a spectrum analyzer connected to an AERA phase 1 LPDA antenna is shown as a function of the local time.

triggering. In case of a positive trigger, the unfiltered traces are recorded.

Self-triggering is performed in the time domain after an inverse fourier transform is applied to the filtered traces. The trigger logic [137] employs multiple voltage thresholds which can be dynamically adapted to the present noise situation. A combination of these thresholds allows to set trigger conditions which are sensitive to the shape of radio pulses as expected from air showers. The majority of transient noise pulses is rejected due to their pulse shape. However, some noise pulses are very similar to these expected from air showers and pass the trigger.
Noise pulses often occur with a certain periodicity, e.g. with a frequency of 100 Hz, matching twice the frequency of the power grid in Argentina. These events are vetoed directly at the station level by an algorithm which dynamically adjusts to the phase drift of these periodic pulses [138].
The trigger conditions described above are applied to each of the two channels, corresponding to a single polarization direction, individually. The final trigger decision on station level then requires either a pulse in a single polarization direction or an 'and' condition of both channels. In both cases, 2048 samples of both channels, containing the triggered pulses, are stored in the digitizer memory and a trigger time stamp is sent to the central DAQ.

At the DAQ, an event trigger is formed considering the time stamps and positions of multiple triggered stations. An algorithm searches for patterns which are compatible with an planar shower front moving with the speed of light. In case of a positive event trigger, the stored signal traces are requested from the participating stations

and written on hard disk.
To reduce the amount of recorded data and further increase the purity, a fast directional reconstruction of triggered events can be performed by the DAQ. This fast reconstruction requires only the trigger time stamps of the stations. Events correlating with directions of known artificial hot spots can then be rejected.

Despite the advanced self-trigger strategies, a 100 % efficiency and purity of cosmic ray data has not been achieved yet. The purity of self-triggered events can be substantially improved by an offline selection taking into account various properties of the measured radio emission such as the polarization of the signals [139]. However, to clearly identify self-triggered radio events as being caused by air showers, yet the information from the SD or the FD has to be considered. In this thesis only radio data that was recorded in coincidence with the SD is used.

6.4 External and Particle Triggering

As an alternative to self-trigger on the radio emission, the AERA stations equipped with the KIT/BUW digitizers can be triggered externally by the SD and the FD. The AERA DAQ requests the trigger information of the SD stations and fluorescence telescopes which is collected at CDAS, the central DAQ of the observatory (see Ch. 5). As this request takes a few seconds, the waveform data recorded at the RDS has to be stored in the meantime. For this purpose, the KIT/BUW digitizers are equipped with a ring buffer memory which is able to store the full waveform data for up to 7.2 s. The event data can then be extracted backdated to the time of the external trigger.
To improve the efficiency of triggering by the SD for the lowest energies, the energy threshold of the infill array is locally lowered by six additional water Cherenkov tanks co-located with the dense core of AERA. This configuration is visible in Fig. 5.9 and Fig. 6.1 and is referred to as AERALET [140].

A further method of triggering is provided by particle detectors as an integral part of the RDSs. The 40 stations using the Nikhef/RU digitizers are equipped with small scintillators which register the secondary particles of the air shower. The scintillator signals are continuously sampled by the digitizer and trigger the readout of radio waveform data if they exceed a certain threshold.

6.5 Calibration and Monitoring

To perform calibrated measurements of the electric field emitted by air showers, the impact of readout electronics and especially of the radio antennas has to be unfolded from the recorded signals. The calibration of the radio antennas as a major scope of this thesis is discussed later.
The components of the analog electronics, that is the low noise amplifier, coaxial cables and the filter amplifier introduce a frequency dependent gain and furthermore frequency dependent group delays which cause a dispersion of the recorded

broad-band signals. Their characteristics can be fully described by their scattering parameters (S-Parameters). The scattering parameters of each individual analog component have been measured in a laboratory and are considered in the radio reconstruction.
Furthermore the response of the individual analog-to-digital converters used in the digitizers are a priori not identical. Hence, a calibration of each digitizer channel in a laboratory has been carried out [141].

For the analysis of radio air shower data, an exact knowledge of the environmental conditions and the detector status is essential. The radio emission from air showers can be significantly altered by atmospheric electric fields, e.g. during thunderstorms (see Ch. 4.1.3). Hence, the atmospheric electric field and several weather related quantities are constantly monitored by a weather station mounted at the CRS [142]. Air shower data recorded during exceptional weather conditions can thus be excluded from the analysis.
The functionality and status of the individual RDSs is surveyed permanently. Besides information on trigger rates and communication status, temperatures and voltages of the electronics are measured by internal sensors and sent to the DAQ.

6.6 Prospects

The physics goals of AERA as discussed at the beginning of this chapter have partly been fulfilled already with the first phase of AERA. Hundreds of self-triggered cosmic ray radio events recorded in coincidence with the surface detector demonstrate that self-triggering on the radio emission is feasible to detect cosmic rays.
With AERA, for the first time, air showers have been observed with three different detector techniques simultaneously. Several of these 'superhybrid' events were recorded and allow to study multiple aspects of air showers.
Analysis of first AERA data support the findings of previous experiments regarding the radio emission mechanisms and moreover allow to quantify their contributions to the total radio emission (cf. Ch. 4.4).

A measurement of the cosmic ray energy based on AERA data will be presented later in this thesis. Composition studies using AERA data are ongoing [143].

The instrumented area of AERA has increased by about a factor of 15 with the deployment of phase 2 and will further grow to ≈ 10 km^2 with phase 3. An estimate of the number of expected cosmic ray events for the fully equipped detector is given in Fig. 6.5. The energy dependent effective area of AERA has been simulated based on parameterizations of the radio signal obtained from extrapolations of LOPES and CODALEMA data as well as air shower simulations [144]. The number of events is then calculated by multiplying the effective area with the cosmic ray spectrum as measured by Auger.
The estimates predict several thousand cosmic ray events per year between 10^{17} eV

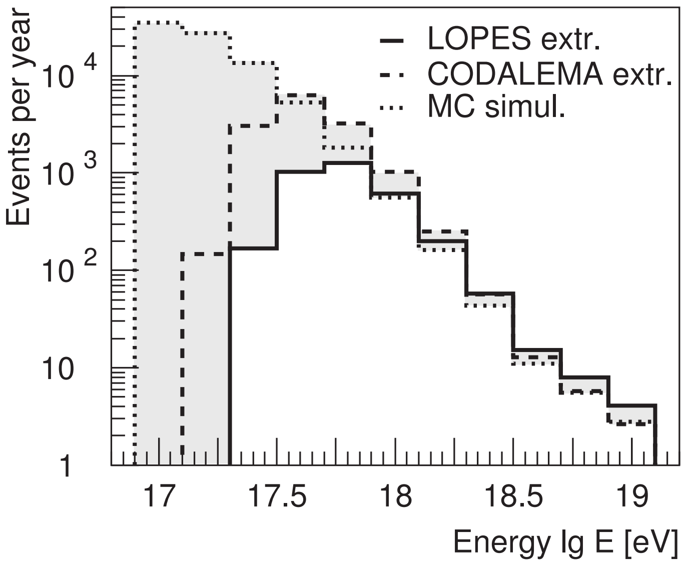

Figure 6.5: Expected number of cosmic ray events with zenith angles smaller than 60° per year for the fully deployed AERA detector. From [144].

and 10^{19} eV. The lower energy threshold of AERA varies slightly with the used extrapolation of the radio signal. However, AERA will deliver an unrivaled statistics of high-quality radio cosmic ray measurements in the next years.

7. Antenna Theory

In this chapter we discuss theoretical antenna properties to provide a basis for a characterization and calibration of radio antennas for the detection of cosmic rays. By means of the commonly used scalar power quantities, concepts such as radiation patterns and antenna efficiencies are introduced. Accordingly, we focus on the vector effective length which is suitable to fully describe the antenna response with a single vectorial quantity and which is used for the reconstruction of the electric field emitted by air showers. A last section is dedicated to the simulation of the antenna response with antenna simulation software.

7.1 Directivity, Effective Area and Gain

An antenna is a linear reciprocal device which converts electric power into electromagnetic waves and vice versa. Due to its reciprocity, antenna properties obtained in a transmitting situation also apply if the antenna is used as a receiver [145]. When deriving antenna properties, it is valid and often advantageous to switch perspectives.

The space around an antenna can be classified into a near field and far field region. The near-field directly surrounds the antenna structure and ends at a certain radial

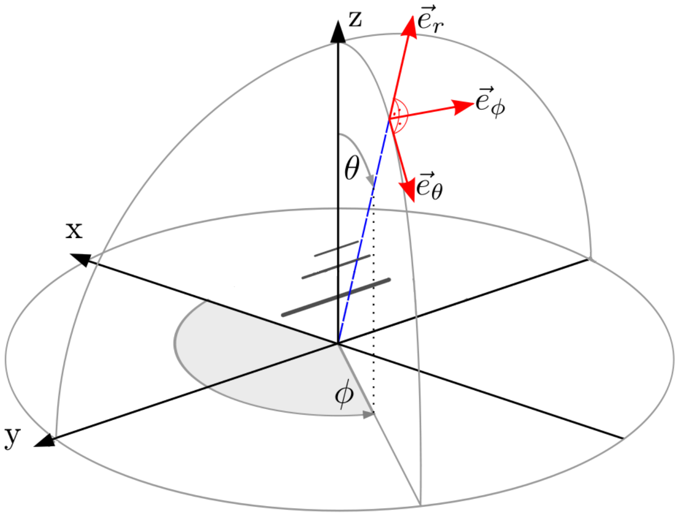

Figure 7.1: Spherical coordinate system used to describe antenna radiation properties. An exemplary antenna is displayed in the center of the coordinate system.

distance R around the antenna where it connects to the far-field region. In contrast to the near field, the angular field distribution of the radiation is essentially independent of the distance to the antenna in the far field region [145]. The field components are transverse and the radiation can be treated as a spherical wave. Definitions of the distance R where the far field begins will be discussed in a later chapter. The radiation properties of antennas discussed in the following always relate to the far-field region.

The radiation properties of antennas are commonly characterized by the power based quantities directivity and gain. According to the standard definitions given in [145], the directivity of an antenna is 'the ratio of the radiation intensity in a given direction from the antenna to the radiation intensity averaged over all directions'. The radiation intensity U in a given direction is defined as the power radiated from an antenna per unit solid angle. The unit of radiation intensity is watts per steradian $[U] = \mathrm{W/sr}$. The average radiation intensity U_0 is equal to the total power radiated by the antenna P_{rad} divided by the complete solid angle of 4π. In equation form we obtain

$$D(\theta, \phi, \omega) = \frac{U(\theta, \phi, \omega)}{U_0} = \frac{4\pi U(\theta, \phi, \omega)}{P_{rad}} \tag{7.1}$$

with the angular frequency $\omega = 2\pi f$. In other words, the directivity of a nonisotropic source equals the radiation intensity in a given direction normalized by the radiation intensity radiated by an isotropic source.
In the above definition we already included the dependencies on the spatial angles if the antenna is considered in a spherical coordinate system with the antenna in the center as depicted in Fig 7.1. In this case the electric field of the impinging plane wave can be split in the two orthogonal polarizations along the unit vectors $\vec{e_\theta}$ and $\vec{e_\phi}$ of the spherical coordinate system,

$$\vec{E} = E_\theta \vec{e_\theta} + E_\phi \vec{e_\phi}. \tag{7.2}$$

The radial component $\vec{e_r}$ vanishes for an antenna in the center of the coordinate system.

The power density of an electromagnetic wave is described by the Poynting vector. For a uniform plane wave with a certain polarization $k = (\theta, \phi)$ the time averaged power density can be expressed by the peak values[1] of the electric field only as

$$S_k = \frac{|E_k|^2}{2Z_0}, \tag{7.3}$$

with the vacuum impedance $Z_0 = \mu_0 c \approx 120\pi\Omega$ which holds in good approximation also for free space media as air.

---

[1] we will use always peak values in the following. Another common convention is to use effective values which relate to the peak values as $E_{eff} = E/\sqrt{2}$.

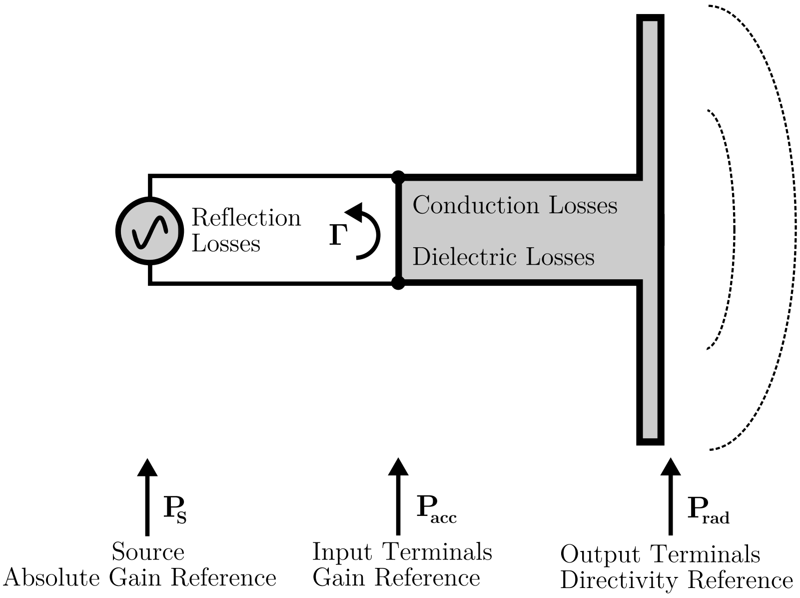

Figure 7.2: Antenna losses and their position with respect to the antenna structure (gray shaded area). Structural losses occur within the antenna structure whereas reflection losses evolve at the input terminals. The reference powers for directivity, gain and absolute gain are denoted at the corresponding terminals.

A receiving antenna captures a certain amount of power from an incoming plane wave with power density S_k. The power delivered to the readout terminals $P_{L,k}$ of the antenna can be accessed with the maximum effective area $A_{em,k}$ (also called maximum effective aperture) for an impinging plane wave with polarization k,

$$P_{L,k} = A_{em,k} S_k. \tag{7.4}$$

The maximum effective area relates to the directivity of the antenna [146] by

$$A_{em,k} = \frac{\lambda^2}{4\pi} D_k. \tag{7.5}$$

We wrote the directivity D_k with $k = \theta, \phi$ for a single polarization component in the above equation which is called partial directivity. The partial directivities sum up to the total directivity as defined in Eq. 7.1,

$$D = D_{tot} = D_\theta + D_\phi. \tag{7.6}$$

The maximum effective area is only achieved if no losses are associated with the antenna. Losses always occur in reality, both within the antenna structure and due to the connection to a readout system.

In Fig. 7.2 the possible antenna losses are visualized with respect to a transmitting antenna structure. Structural losses are composed of conduction losses due to a ohmic resistance of the antenna material and dielectric losses which occur for instance in insulators within the antenna structure. The power that is radiated by an antenna P_{rad} is reduced by the structural losses with respect to the power P_{acc} that is accepted at the antenna input terminals. In terms of power transfer, these losses can be accounted for by the dimensionless radiation efficiency ϵ,

$$P_{rad} = \epsilon P_{acc} \tag{7.7}$$

If we insert the above equation in the definition of the directivity (Eq. 7.1), we obtain the definition of the gain of an antenna

$$G(\theta, \phi, \omega) = \epsilon D(\theta, \phi, \omega) = \frac{4\pi U(\theta, \phi, \omega)}{P_{acc}}. \tag{7.8}$$

As well as the directivity, the gain of an antenna describes the spatial distribution of the radiation but takes into account the losses that occur within the antenna structure. Hence, the gain refers to the power that is accepted by the antenna and not to the power that is radiated. The gain is commonly expressed in a decibel scale wich relates to the above definition as

$$G_{dBi} = 10\, log_{10}(G), \tag{7.9}$$

where usually an i is added to the unit dB to indicate that the reference is an isotropic source.

As an illustrative example, Fig. 7.3 shows a simulation of the three dimensional distribution of the gain of an half-wave dipole which is referred to as gain pattern or gain sphere. Analog to the directivity, the total gain can be split into the partial gains G_θ and G_ϕ for the two orthogonal polarization components of the electric field

$$G = G_{tot} = G_\theta + G_\phi. \tag{7.10}$$

In terms of a receiving antenna, the middle gain pattern of Fig. 7.3 then indicates the response of the dipole to plane waves polarized in $\vec{e_\phi}$-direction while the right pattern refers to waves of $\vec{e_\theta}$-polarization. Both sum up to the total gain shown in the left pattern. For a plane wave impinging from a horizontal direction, $\vec{e_\phi}$ is aligned horizontally and $\vec{e_\theta}$ points vertically (cf. Fig. 7.1). This is why the partial gains G_ϕ and G_θ are also referred to as horizontal gain and vertical gain respectively.

Every antenna has a characteristic intrinsic impedance Z_A which depends on multiple factors mainly related to its geometrical structure and which is generally frequency dependent. It manifests at the input terminals of the antenna as ratio of complex voltage to complex current. If an antenna is connected to a source with intrinsic impedance Z_S (cf. Fig. 7.2), not all the power P_S delivered by the source will be accepted at the input terminals but will partly be reflected if the impedances Z_A and Z_S are not equal. This is called impedance mismatch. The fraction of power P_{ref} that is reflected at the input terminals can be expressed with the squared voltage reflection coefficient [146],

$$\frac{P_{ref}}{P_S} = |\Gamma|^2, \quad \Gamma = \frac{Z_A - Z_S}{Z_A + Z_S}. \tag{7.11}$$

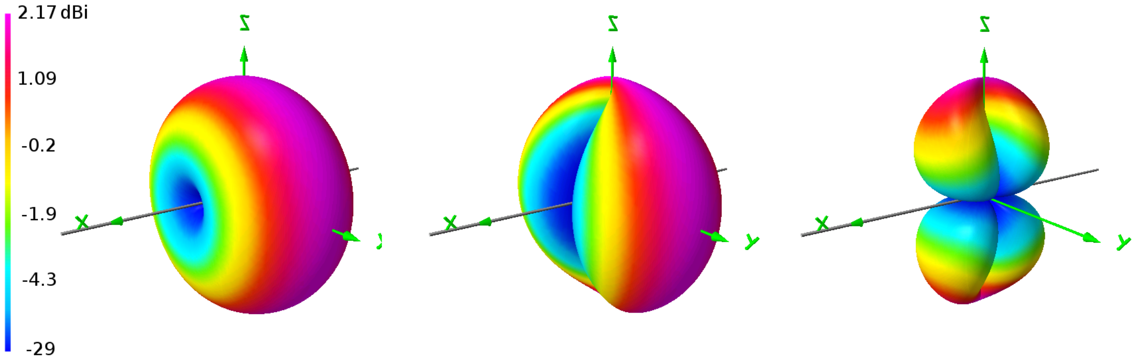

Figure 7.3: Simulation of the gain of an half wave dipole. The gain for a specific direction is depicted as the distance to the center of the coordinate system and additionally color coded. The middle and right patterns indicate the partial gains G_ϕ and G_θ respectively which add up to the total gain G_{tot} shown on the left.

The power transfer from the source to the antenna terminals can then be considered by the dimensionless reflection or mismatch efficiency ϵ_r as

$$P_{acc} = \epsilon_r P_S = (1 - |\Gamma|^2) P_S. \tag{7.12}$$

We can include the mismatch effects in the definition of the gain and define the absolute gain as

$$G_{abs}(\theta, \phi, \omega) = \frac{4\pi U(\theta, \phi, \omega)}{P_S} = (1 - |\Gamma|^2) G = \epsilon_r \epsilon D. \tag{7.13}$$

Looking at Fig. 7.2 we find that the absolute gain refers to the power that is delivered by a source.
Furthermore, the above equation implies that the quantities directivity as well as gain and absolute gain all describe the same spatial distribution of radiation. That is the shape of the spatial patterns as for instance visualized in Fig. 7.3 is the same, only the scale of the pattern varies with the considered antenna losses.

7.2 The Vector Effective Length

In the previous section we have discussed antenna properties based on scalar power quantities. We will now focus on an antenna description by complex voltages as the response to an incident electric field vector which is obtained by the vector effective length. The vector effective length (VEL) allows to treat polarization effects as well as dispersion effects within the antenna structure with a single quantity.
The vector effective length $\vec{H}$ relates the complex voltage V developed at the readout terminals of an antenna to the impinging electric vector for a given incoming direction. In the frequency domain this can be conveniently written as

$$V(\theta, \phi, \omega) = \vec{H}(\theta, \phi, \omega) \cdot \vec{E}(\theta, \phi, \omega) \tag{7.14}$$

It should be noted that the VEL can alternatively be evaluated in the time domain. In this case it maps the instantaneous electric field $\vec{E}(t)$ to the instantaneous response voltage $V(t)$. The equivalence of time and frequency domains is given through a Fourier transform [147].
Analog to the previous discussion we can divide the electric field into the orthogonal components and accordingly the vector effective length

$$\vec{H} = \vec{e_\theta} H_\theta + \vec{e_\phi} H_\phi. \tag{7.15}$$

The antenna response is then the superposition of the two response voltages due to the two components of the vector effective length

$$V = V_\theta + V_\phi = H_\theta E_\theta + H_\phi E_\phi. \tag{7.16}$$

The response voltages and electric fields are generally complex quantities which are commonly expressed in the phase vector (phasor) notation and so is the vector effective length

$$\vec{H} = \vec{e_\theta} H_\theta + \vec{e_\phi} H_\phi = \vec{e_\theta} |H_\theta| e^{i\varphi_{H_\theta}} + \vec{e_\phi} |H_\phi| e^{i\varphi_{H_\phi}}, \tag{7.17}$$

with the magnitude $|H_k|$ and phase φ_{H_k} of the phasor for the respective components.

The magnitudes $|H_k|$ are closely related to the partial gains G_k which will be demonstrated in a later section. Together, the magnitudes $|H_\theta|$ and $|H_\phi|$ form a vector in the spherical coordinate system. For a set of incoming directions we obtain a vector field as depicted in Fig. 7.4 at a single frequency. The direction of the vectors indicate the antenna polarization. The antenna polarization commonly is defined as the polarization of the plane wave emitted by a transmitting antenna in a given direction [145]. By reciprocity, a plane wave incident upon a receiving antenna will yield the maximum response voltage if the polarization of the wave matches the antenna polarization. The polarization dependency of the antenna response is expressed by the vector product in the definition of the VEL according to Eq. 7.14.
Looking at Fig. 7.4 we find that the antenna polarization of the simulated logarithmic periodic dipole antenna is given by the projection of the dipole axis towards the unit sphere. For certain incoming directions, e.g. waves impinging along the x-axis, the vector effective length vanishes. This is intuitive as the electric field of the incoming plane wave can not have a component along an antenna dipole and thus can not induce a current along the dipole. This is referred to as polarization mismatch.
The VEL thus includes polarization mismatch effects in contrast to the scalar quantities directivity and gain. The definition of directivity and gain assumes that the polarization of the impinging plane wave is always matched to the antenna polarization.

The phase of the vector effective length enables the treatment of dispersion effects which occur within an antenna structure. Impinging plane waves will be subjected to

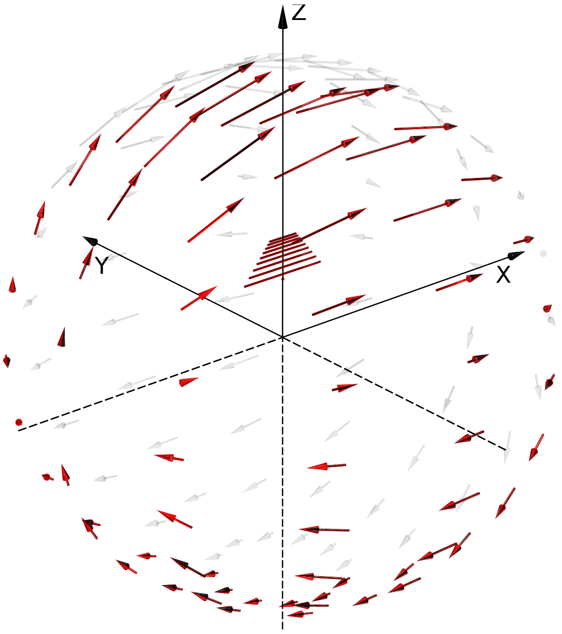

Figure 7.4: Three dimensional pattern of the vector effective length simulated for a logarithmic periodic dipole antenna. From [148].

a delay within the antenna structure depending on the frequency of the wave which is referred to as group delay. A broad band signal which is composed of multiple frequencies will then superimpose at the readout terminals depending on the delay of its spectral components and manifest as the complex voltage V. Consequently, in the time domain, a broad band signal will suffer a dispersion which is fully described by the frequency dependent phase of the vector effective length. The VEL is thus suitable to describe the response of the antenna structure to an arbitrary waveform.

In [148] the VEL of several radio antennas used at the AERA experiment was explicitly evaluated in the time domain to calculate the voltage traces obtained at the antenna terminals due to an impinging broad band pulse and therewith to determine dispersion effects. In this thesis we will describe the dispersion effects with the group delay of the antenna for mono-frequent incoming signals. The group delay is directly related to the phase φ_{H_k} of the VEL. For a single component of the VEL we write the group delay as

$$\tau_k(\theta, \phi, \omega) = -\frac{d}{d\omega} arg(H_k(\theta, \phi, \omega)) = -\frac{d\varphi_{H_k}}{d\omega} \tag{7.18}$$

Analog to the phase of the VEL, the group delay also depends on the incoming direction of the signal and is represented by a pattern of group delay in three dimensions.

We can conclude that the VEL fully describes the antenna response in terms of the voltage obtained at the readout terminals. In the following we investigate the impact of a readout system connected to the antenna terminals.

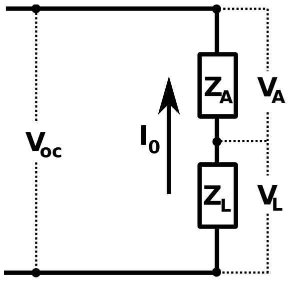

Figure 7.5: The Thevenin antenna equivalent circuit of a receiving antenna (impedance Z_A) connected to a readout system with intrinsic impedance Z_L.

7.3 The Realized Vector Effective Length

In a real measurement setup, the response voltage of the antenna is read out over a load impedance Z_L connected in series with the antenna terminals with impedance Z_A. The load impedance may be the impedance of a connected transmission line, an amplifier or, in case of a transmitting antenna, the intrinsic impedance of the source. In Fig. 7.5 the Thevenin equivalent circuit of the measurement setup is depicted. From the circuit quantities we obtain for the voltages in the loop

$$V_{oc} = V_A + V_L, \tag{7.19}$$

with the open circuit voltages V_{oc} at the antenna terminals and the voltages V_A and V_L developed over the antenna and load impedance respectively. For the current within the circuit holds

$$I_0 = \frac{V_{oc}}{Z_A + Z_L}. \tag{7.20}$$

Thus we can express the voltage measured over the load impedance as

$$V_L = \frac{Z_L}{Z_L + Z_A} V_{oc} =: \rho V_{oc}. \tag{7.21}$$

where we define the transfer function ρ. In the previous section the VEL was defined with respect to the complex voltage developed at the antenna terminals which corresponds to V_{oc} of the equivalent circuit. With the above equation we can now relate the VEL to the voltage obtained at the load. By including the transfer function we define the realized vector effective length H_r as

$$V_L = \rho \vec{H} \cdot \vec{E} = \vec{H}_r \cdot \vec{E}. \tag{7.22}$$

We can thus describe the impact of an arbitrary complex readout impedance through the realized vector effective length.

For later use we write the active power delivered to the load in terms of peak values

$$P_L = \frac{1}{2} Re(I_0 V_L^*) = \frac{1}{2} |I_0|^2 Re(Z_L^*) = \frac{1}{2} \frac{|V_{oc}|^2}{|Z_A + Z_L|^2} Re(Z_L^*), \tag{7.23}$$

where the star denotes the complex conjugate of the previously defined quantities. Maximum power transfer is reached for conjugate matching [146], that is the load impedance equals the complex conjugate of the antenna impedance, $Z_A = Z_L^*$. In case of conjugate matching, Eq. 7.23 simplifies to

$$P_L = \frac{1}{8}\frac{|V_{oc}|^2}{Re(Z_A)} \tag{7.24}$$

7.4 Amplification in Active Antennas

Besides passive antennas where the readout impedance is a constant pure resistive load of commonly $Z_L = 50\Omega$, we will examine active antennas. In this case, the antenna terminals will be directly connected to an amplifier with a frequency dependent complex input impedance. Below we derive a transfer function which can be included in the realized VEL and includes the mismatch effects between antenna and amplifier and furthermore the amplification.

Amplifiers are commonly treated as active linear two-port networks. In high-frequency electrical engineering, these networks can conveniently be described by scattering parameters (S-parameters) [149]. S-parameters can be measured with a vector network analyzer with respect to a nominal source impedance which has to be specified together with the measured S-parameters. In our case the nominal source impedance is 50 Ω which is most common.
A two-port network is fully described by the four S-parameters S11, S21, S12 and S22.

The S21 parameter relates the amplified complex voltage V_a at the output of the amplifier to the voltage delivered by the source V_S

$$S21 = \frac{V_a}{V_S}, \tag{7.25}$$

and thus indicates the amplification of an amplifier.
The S11 parameter is the ratio of the complex reflected voltage V_{ref} at the input of the amplifier to the voltage delivered by the source. In terms of circuit quantities it can be written as

$$S11 = \frac{V_{ref}}{V_S} = \frac{Z_L - Z_S}{Z_L + Z_S} \tag{7.26}$$

with Z_L, the input impedance of the amplifier. S11 corresponds to the previously discussed voltage reflection coefficient Γ (cf. Eq. 7.11).
The voltage developed over input impedance Z_L of the amplifier is the superposition of the voltage delivered by the source and the reflected voltage at the input

$$V_L = V_S + V_{ref} = V_S(1 + S11) = V_S(1 + \Gamma_L). \tag{7.27}$$

The ratio of the amplified voltage at the output of the amplifier to the input voltage is then given by

$$\frac{V_a}{V_L} = \frac{V_a}{V_S(1+S11)} = \frac{S21}{1+S11} \tag{7.28}$$

In Eq. 7.22 the realized VEL was defined with respect to the voltage delivered to an arbitrary load. For the active antenna this load becomes the input impedance of the amplifier. Solving the above equation for V_a and inserting the definition of the realized VEL yields

$$V_a = \frac{S21}{1+S11}\vec{H}_r\,\vec{E} = \frac{S21}{1+S11}\,\frac{Z_L}{Z_L+Z_A}\vec{H}\,\vec{E} =: \vec{H}_a\,\vec{E}. \tag{7.29}$$

Above we have defined the amplified vector effective length $\vec{H}_a$ which maps the incoming electric field to the amplified voltage delivered into a nominal 50 Ω system by an active antenna.

7.5 Vector Effective Length and Gain

We can access the power $P_{L,k}$ delivered to the readout impedance of a receiving antenna by the maximum effective area according to Eq. 7.4, where we insert the relation to the directivity given by Eq. 7.5 and the power density of the incoming wave with polarization $k = (\theta, \phi)$ from Eq. 7.3. Together we obtain

$$P_{L,k} = \frac{\lambda^2 |E_k|^2}{(8\pi Z_0)} D_k. \tag{7.30}$$

As the directivity does not include any losses within the antenna structure (radiation efficiency is unity) or mismatch losses (reflection efficiency is unity), Eq. 7.30 applies only for lossless antennas and conjugate matching to the load. In case of conjugate matching we can relate the power delivered to the load to the open circuit voltage using Eq. 7.24. Plugging this relation into Eq. 7.30 and rearranging yields

$$\frac{|V_{oc,k}|^2}{|E_k|^2} = \frac{\lambda^2 Re(Z_A)}{\pi Z_0} D_k = |H_k|^2, \tag{7.31}$$

and we recall the left ratio in the above equation as the definition of the VEL. Hence, we have derived the relation between partial directivity and VEL.

If the radiation efficiency is included in the VEL, which is the case when we access the VEL through measurements or simulations, we can write Eq. 7.31 in terms of the partial antenna gain G_k as

$$|H_k|^2 = \frac{\lambda^2 Re(Z_A)}{\pi Z_0}\epsilon D_k = \frac{\lambda^2 Re(Z_A)}{\pi Z_0} G_k. \tag{7.32}$$

7.6 Reconstruction of the Electric Field

When analyzing the radio emission from cosmic ray induced air showers, the quantity of choice is the vectorial electric field $\vec{E}(t)$ rather than the voltage traces $V(t)$ recorded by the radio antennas. The electric field is in principle independent of the used detector[2] and thus allows to compare results from different setups.
Recent radio detectors measure the radio emission with at least two independent antennas at one observer position which are usually aligned perpendicular to each other, commonly with one antenna aligned in north-south direction while the other points east-west. Although such setups measure only the projection of the three-dimensional electric field to the horizontal plane, they allow for a reconstruction of the tree-dimensional electric field if the incoming direction of the signal is known.

Such a reconstruction of the electric field from dual-polarized measurements is implemented within Radio Offline [150], the radio extension of the software framework Offline of the Pierre Auger Observatory. The reconstruction unfolds the antenna characteristics by evaluating the VEL in the frequency domain for a certain incoming direction. This requires a preceding conversion of the measured voltage traces into the frequency domain by a Fourier transform. Furthermore, the antenna pattern which is simulated on a certain grid has to be interpolated to the excact incoming direction. The interpolation method is described in detail in [151].
The two recorded voltages $V_1(\omega)$ and $V_2(\omega)$ are the response to the same electric field $\vec{E}$ given by the two VELs $\vec{H}_1$ and $\vec{H}_2$ of the two antennas

$$\begin{aligned} V_1(\omega) &= \vec{H}_1(\theta,\phi,\omega)\,\vec{E}(\omega) \\ &= H_{1,\theta}(\theta,\phi,\omega)\,E_\theta(\omega) + H_{1,\phi}(\theta,\phi,\omega)\,E_\phi(\omega) \qquad (7.33) \\ V_2(\omega) &= \vec{H}_2(\theta,\phi,\omega)\,\vec{E}(\omega) \\ &= H_{2,\theta}(\theta,\phi,\omega)\,E_\theta(\omega) + H_{2,\phi}(\theta,\phi,\omega)\,E_\phi(\omega). \qquad (7.34) \end{aligned}$$

This system of equations can be solved for the components of the electric field E_k for a certain incoming direction $k = (\theta, \phi)$. The incoming direction can be obtained from the signal timing in multiple radio stations or by external detectors. For the electric field components follows

$$E_\theta(\omega) = \frac{V_1(\omega)H_{2,\phi}(\omega) - V_2(\omega)H_{1,\phi}(\omega)}{H_{1,\theta}(\omega)H_{2,\phi}(\omega) - H_{1,\phi}(\omega)H_{2,\theta}(\omega)} \qquad (7.35)$$

$$E_\phi(\omega) = \frac{V_2(\omega)H_{1,\phi}(\omega) - V_1(\omega)H_{2,\phi}(\omega)H_{2,\theta}(\omega)}{H_{1,\phi}(\omega)H_{2,\phi}(\omega) - H_{1,\phi}(\omega)H_{2,\theta}(\omega)} \qquad (7.36)$$

---

[2] Exceptions are a bias due to the geometrical location of the experiment and its observation bandwidth.

Finally the electric field components E_θ and E_ϕ can be transferred back into the time-domain and transformed into a cartesian coordinate system by taking into account that the field components are transverse to the incoming direction of the signal.

7.7 Antenna Simulations

Analytic calculations, especially of the radiation properties of antennas, are only feasible for relatively simple antenna structures. For complex geometrical structures, the far field radiation evolves from an interplay of structure elements and furthermore depends on an interaction with the environment such as the ground below the antenna. These effects can be modeled to a large extend by numerical antenna simulations which provide an important tool for the design and evaluation of antennas.

7.7.1 Antenna Simulations with NEC2

An advanced and widely used software for antenna simulations is the Numerical Electromagnetics Code (NEC) [152]. In this thesis we use the version NEC2++ [153] which is available through the Linux Debian package management system as an open source code under the GNU Public License (GPL). NEC2++ is a rewrite in C++ of the original Fortran NEC2 code. Furthermore we use the graphical interface 4Nec2 [154] available for NEC2.

We briefly summarize the functionality of NEC based on the detailed description given in [152]. NEC uses an electric field integral equation to model the response of antenna structures which is especially suitable for thin-wire structures. Surfaces can be approximated with grids of thin wires. The electric field integral equation [155] can be written in a compact way as

$$\vec{E}(\vec{r}) = -\frac{i}{4\pi\epsilon_0\omega}\int_V \vec{J}(\vec{r'})\,\vec{G}(\vec{r},\vec{r'})dV' \tag{7.37}$$

with the dyadic Green's functions $\vec{G}$. The electric field $\vec{E}(\vec{r})$ at a given observer position $\vec{r}$ follows from the current density $\vec{J}(\vec{r'})$ at position $\vec{r'}$.
The integral equation is solved numerically by the so called method of moments [156]. Therefore a wire is divided into a certain amount of straight segments. The current distribution on each segment is approximated with a superposition of three terms, a constant, a sine, and a cosine. The amplitudes of the three terms are related such that their superposition satisfies physical conditions of the currents at the segment ends.
The response of the complete structure is finally computed as a superposition of the electric fields obtained from the solution of the integral equation for each individual segment with the approximated current distribution. The response is always computed at a single frequency.

Prior to the simulation of the response of an antenna, its geometrical structure has to be modeled and an excitation of the structure has to be specified by an input file. The geometrical structure is composed of thin wires which are defined by their two end points, their radii, their conductivity and the number of segments into which each wire is divided. A guideline for the segmentation is that the length of the segments should be smaller than $\lambda/10$ for the simulated frequency to obtain a sufficiently precise approximation of the currents [152].
The excitation of the structure can be realized as a complex voltage or current source placed on a certain segment within the structure. Alternatively, the structure can be excited with an impinging plane wave specified by its incoming direction and polarization.

On demand NEC stores several quantities in an output file after processing the simulation. In case of an excitation with a voltage or current source NEC2 delivers the near field and the radiated far-field as well as the impedances of the segments. For a plane wave excitation NEC2 provides the currents and the impedances of the segments.

7.7.2 Ground Effects

A significant influence on the radiation characteristics of antennas is introduced by the ground underneath an antenna. Plane waves reflected at the ground plane interfere with the wave directly impinging in the antenna. The reflected wave is phase-delayed with respect to the direct signal and thus alters the total received signal depending on the incoming direction of the wave, its frequency and the height of the antenna above the ground plane. Consequently, the directivity or gain pattern of the antenna is deformed due to the presence of a ground plane. This can cause so-called side lobes in the antenna pattern which we will discuss later in the scope of antenna calibration measurements.

The reflection of a plane wave on a uniform planar interface can be described by the Fresnel equations. For the component of the impinging wave parallel to the ground E_ϕ the reflected wave $E_{R,\phi}$ is calculated in NEC2 as

$$\vec{E}_{R,\phi} = R_\phi \vec{E}_\phi, \qquad with \qquad R_\phi = \frac{Z_R cos(\theta) - \sqrt{1 - Z_R^2 sin^2(\theta)}}{Z_R cos(\theta) + \sqrt{1 - Z_R^2 sin^2(\theta)}}, \tag{7.38}$$

where Z_R describes the properties of the ground by its relative permittivity ϵ_r and conductivity σ,

$$Z_R = (\epsilon_r - i\frac{\sigma}{\epsilon_0 \omega})^{-1/2}. \tag{7.39}$$

In Fig. 7.6, the reflection coefficient R_ϕ is plotted as a function of the ground parameters ϵ_r and σ. Within 4NEC2 a set of typical ground scenarios is predefined which is indicated in the figure. The reflection can change by several 10% throughout the range of different ground scenarios.
However, a reasonable choice for the ground conditions at AERA can be found in the

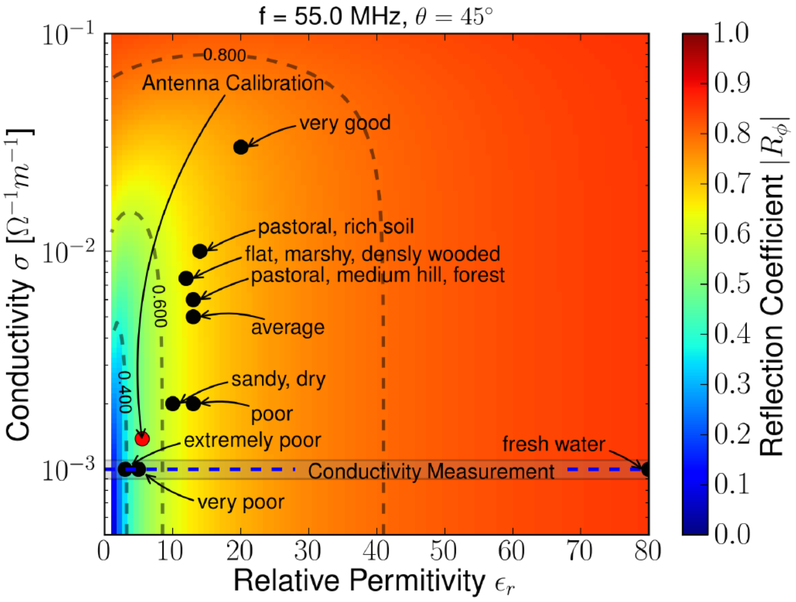

Figure 7.6: The reflection coefficient R_ϕ for horizontally polarized plane waves as a function of the ground parameters ϵ_r and σ. Typical ground scenarios as provided by the 4NEC2 antenna simulation program are indicated as well as the result of a conductivity measurement at the AERA site. From [159].

lower left region of Fig. 7.6, corresponding to the extremely dry and sandy ground at AERA. Soil measurements performed at the AERA site indicate a relatively low conductivity of $\sigma = (1 \pm 0.1) \cdot 10^{-3}$ $[\Omega^{-1}m^{-1}]$ [157]. We chose for antenna simulations associated with the AERA site values of $\sigma = (1.38) \cdot 10^{-3}$ $[\Omega^{-1}m^{-1}]$ and $\epsilon_r = 5.5$. These values have been used for previous simulations of the SBS antenna [148]. The chosen value for the conductivity is close to the measurement. The selected value for ϵ_r is motivated by typical ground scenarios with low conductivities [158].

Besides the incorporation of ground effects with the Fresnel equations, NEC2 provides a more advanced method which additionally considers a modification of the current distributions in the antenna structure due to near field interactions with a ground plane. This method, called Sommerfeld/Norten ground is especially recommended for structures placed relatively close to lossy grounds planes and is more accurate than the Fresnel method in this case [152]. For our simulations we use the Sommerfeld/Norten ground option.

7.7.3 Accessing the Vector Effective Length through NEC2 Simulations

Due to the reciprocity, the VEL can be accessed from NEC2 either by a simulation of a transmitting or a receiving antenna. In the former case we place a current source at the segment which corresponds to the input terminals of the antenna.

In antenna theory [146], the electric field $\vec{E}(R)$ radiated by a transmitting antenna with current I_0^T in its terminals is given at a distance R from the antenna as

$$\vec{E}(R) = -\frac{i\,Z_0}{2\,\lambda\,R}\,I_0^T\,\vec{H}\,e^{\frac{-i\omega R}{c}}, \tag{7.40}$$

where $\vec{H}$ denotes the VEL of the transmitting antenna and λ the wavelength of the emitted plane wave. For a given electric field we can solve the above equation to obtain the VEL

$$\vec{H} = \frac{i\,2\,\lambda\,R}{Z_0\,I_0^T}\,\vec{E}(R)\,e^{\frac{i\omega R}{c}}. \tag{7.41}$$

The radiated far-field $\vec{E}_{nec}$ given by a NEC2 simulation is always normalized to a unit distance of $R = 1$ m [152]

$$\vec{E}(R) = \frac{\vec{E}_{nec}}{R}\,e^{-\frac{i\omega R}{c}}. \tag{7.42}$$

When inserting the above equation in Eq. 7.41, the distance cancels out and we obtain the VEL as calculated from the electric field given by the simulation

$$\vec{H} = \frac{i\,2\,\lambda}{Z_0\,I_0^T}\,\vec{E}_{nec}. \tag{7.43}$$

Mismatch effects and amplification in case of an active antenna are not considered in the simulation. These effects can be included later, analog to the discussion in Sec. 7.3 and Sec. 7.4, and we obtain the amplified vector effective length $\vec{H}_a$ from a NEC2 simulation as

$$\vec{H}_a = \frac{S21}{1+S11}\,\frac{Z_L}{Z_L+Z_A}\,\vec{H} = \frac{S21}{1+S11}\,\frac{Z_L}{Z_L+Z_A}\,\frac{i\,2\,\lambda}{Z_0\,I_0^T}\,\vec{E}_{nec}. \tag{7.44}$$

The impedance Z_A of the antenna input terminals corresponds to the impedance of the segment where the current source is placed in the simulation. Z_L denotes the input impedance of the amplifier. The amplified vector effective length can then directly be compared to measurements which include mismatch and amplification.

Alternatively, the antenna structure can be excited with a linear polarized plane wave as a receiving antenna. For each incoming direction of the wave, the voltage at the antenna terminals can be computed as the product of the current and impedance of the corresponding segment delivered by NEC2. With the voltage and the initial electric field of the plane wave, the VEL can finally be obtained using Eq. 7.14.

We have verified in simulations that both methods yield equivalent results. However, as NEC2 only allows to define one plane wave with a specific incoming direction in a simulation, multiple simulations have to be performed when a three-dimensional gain pattern is desired. Thus, for technical reasons, we chose the former method.

8. Antennas for the Detection of Air Showers at AERA

The basis for the conception of radio antennas for the detection of cosmic ray air showers are various demands given by the characteristics of the radio emission and by the site of the experiment. As a consequence of these demands we will discuss in detail the design and performance aspects of the two different types of radio antennas which are currently used at AERA, the 'Small Black Spider Antenna' and the 'Butterfly' antenna. With respect to the Butterfly antenna we present an improved mechanical design optimized for the environmental conditions at AERA which was developed within the scope of this thesis.
The directional properties of both antennas will be discussed in a later chapter in conjunction with the calibration of the radio stations.

8.1 Demands on Radio Antennas for the Detection Of Air Showers

The frequency spectrum of radio emission has a broad range from several MHz to above 100 MHz as discussed in Ch. 4 (cf. Fig. 4.4). To access as much information as possible from the radio signal, a wide band reception is thus preferred.
However, the usable frequency range is limited in a measurement setup due to various noise sources. In the operational bandwidth of the receiving system, the received noise has to be sufficiently low to identify the cosmic ray radio pulse superimposed with the noise background. In other words, the signal to noise ratio of the measured radio pulse has to be sufficiently high.

The contribution of man-made noise to the received noise background can be suppressed to a large extend by an appropriate choice of the operational bandwidth. At AERA, an operational bandwidth ranging from 30 MHz to 80 MHz is used which is essentially free from signals due to radio broadcasting. Consequently, the antenna should be sensitive over this large frequency range and preferably suppress frequencies beyond. The suppression of the few continuous noise sources which remain within the AERA frequency range was discussed in Ch. 6.3 as well as the suppression of transient man-made noise.

However, what remains within the AERA bandwidth and yields an inevitable noise floor are radio emissions from natural noise sources such as the galactic radio back-

ground and the sun, and furthermore, the noise generated by the receiving system itself.
The total noise power P_S delivered to the readout terminals of a receiving system can be expressed with the system noise temperature T_S and directly depends on the bandwidth of the receiving system Δf [146]

$$P_S = k_B \, T_S \, \Delta f, \tag{8.1}$$

with the Boltzmann constant k_B. The bandwidth should not be reduced for our application to maintain the full spectral information. Thus, a preferably low system noise temperature is desired [1]. The system noise temperature is a complex quantity which combines the above mentioned contributions to the received noise floor. As the noise due to natural sources is irreducible, the reduction of the noise generated by the receiving system itself is of vital importance. Contributions to the latter are thermal noise in the antenna structure, transmission lines and noise generated in electronic components e.g. of the antenna amplifiers. They can be reduced by preferably short transmission lines and the application of low noise amplifiers.

Radio pulses should preferably be detectable from air showers with any arrival directions. The antenna should thus exhibit a uniform directivity towards the upper hemisphere which maintains stable over the whole frequency range of AERA. On the other hand, most of the man made noise impinges from directions close to the horizon. Hence it is favorable to suppress signals from this directions directly with the antenna characteristics.

The weather conditions at the Argentinean Pampa alternate from hot dry summers to cold snowy winters. An antenna has to cope with temperatures from -20 to 50° C, it has to be water and frost proof and resistant against UV-radiation. Strong winds with squalls up to 150 km/h occur frequently at the AERA site located close to the Andes. The antenna exposed on a pole in the flat environment has to withstand the permanent oscillations induced by the wind. These oscillations can be reduced by a preferably small wind load and a low mass of the antenna structure. The antenna must survive these conditions without any damage for years as expenses for maintenance are extensive in this environment.

Particularly with regard to future large scale radio detectors the production costs of of the antenna play an important role.

Among a large diversity of antenna types, only few exist which combine all of the mentioned properties. In the scope of the predecessor experiments of AERA, various suitable antenna types have been tested. Finally a dedicated comparison of antenna types explicitly designed for the detection of air showers [148] has led to the choice of the two currently used antennas types which are described in the following.

---

[1] Contrary to most of the recent radio detectors, early experiments such as described in [75] mainly used relatively small bandwidths to reduce the noise floor.

Figure 8.1: Photograph of the Small Black Spider LPDA installed at AERA.

8.2 Small Black Spider LPDA

The 'Small Black Spider' antenna used for phase 1 of AERA utilizes the principle of a Logarithmic Periodic Dipole Antenna (LPDA). LPDAs essentially combine dipoles of different resonance frequencies to achieve a broad band sensitivity. LPDAs have firstly been adapted to the needs of radio detection for the LOPES experiment [160]. The LOPES type LPDA has been successfully used to detect air showers at the predecessor setup of AERA at the balloon launching station [126], however, it turned out that the antenna dipoles made from aluminum rods brake due to the permanent oscillations induced by the strong winds at the site. This issue was solved with the 'Black Spider' LPDA [161] which used wires as dipoles and performed well over several years of operation at MAXIMA.
Finally the current design of the Small Black Spider LPDA was developed at the RWTH-Aachen University [162] and represents an optimization of the Black Spider antenna towards a more compact design and with respect to the production in large quantities. A photograph of the Small Black Spider installed at AERA is shown in Fig. 8.1.

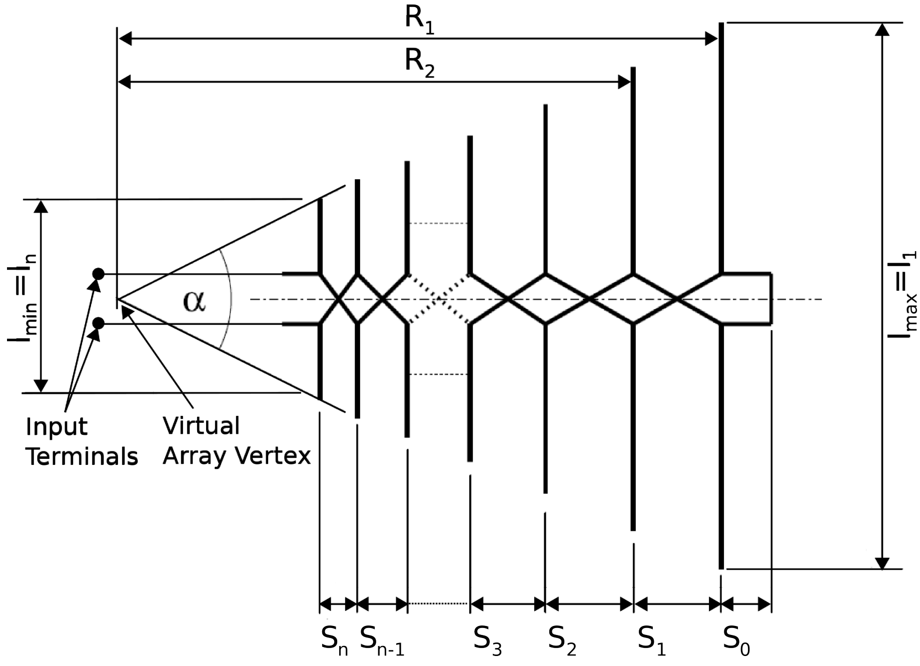

Figure 8.2: Principle construction of an LPDA. Adapted from [163]).

8.2.1 The Principle of a Logarithmic Periodic Dipole Antenna

In Fig. 8.2 the construction of an LPDA consisting of n $\lambda/2$-dipoles is illustrated. The dipoles are connected to a central waveguide in an alternating way which is visualized in the sketch by the crossed connections. The input terminals of the antenna, also called footpoint, are located at the upper end of the waveguide close to the shortest dipole. The lower end of the waveguide is short-circuited at a certain distance S_0 from the longest dipole.

The power of an incoming monochromatic wave with wavelength λ will be primarily absorbed by the dipole with length $l_i \approx \lambda/2$. If we assume an incoming broad band radio pulse e.g. from an EAS, every dipole will feed the waveguide with a different wavelength λ_i. The signals from the single dipoles should interfere preferably constructively at the footpoint to gain a maximum total amplitude. This is realized by a constant ratio of the wavelengths to the distances R_i from the corresponding dipole to a virtual array vertex

$$\frac{\lambda_i}{R_i} = const. \qquad\qquad i = 1...n. \tag{8.2}$$

This condition is fulfilled by constant ratios of sequenced distances and wavelengths

$$\frac{\lambda_i}{R_i} = \frac{\lambda_{i-1}}{R_{i-1}} \qquad\qquad \Rightarrow \frac{R_i}{R_{i-1}} = \frac{\lambda_i}{\lambda_{i-1}} =: \tau. \tag{8.3}$$

The design parameter τ sets the ratio of the lengths of sequenced dipoles if we assume $\lambda_i \propto l_i$. We can calculate the dipole lengths l_i and the distances R_i successive from the resulting geometric series

$$l_i = l_1 \tau^{i-1}, \qquad R_i = R_1 \tau^{i-1}, \qquad i = 1...n, \tag{8.4}$$

whereas l_1 and R_1 are the initial values. These equations imply that the antenna structure becomes periodic in the logarithm of both the dipole length and the distances from the virtual footpoint. With given distances R_i the spacing S_i between the dipoles follows:

$$S_i = R_i - R_{i+1} = R_i(1-\tau). \tag{8.5}$$

The ratio of the spacings to their corresponding dipole lengths is also constant

$$\frac{S_i}{\lambda_i} \approx \frac{S_i}{2l_i} = const. =: \sigma. \tag{8.6}$$

It defines the second design parameter σ which indicates the relative spacing between the dipoles. The parameter σ relates to τ and the opening angle α of the structure

$$\sigma = \frac{1-\tau}{4} cot\left(\frac{\alpha}{2}\right). \tag{8.7}$$

With the two design parameters σ and τ and the choice of the operational frequency range, the complete antenna design is described. The operational frequency range from f_{min} to f_{max} can be estimated by the length of the longest and shortest dipole

$$l_{max} \approx \frac{\lambda_{max}}{2} \qquad \Rightarrow \qquad f_{min} \approx \frac{c}{2l_{max}}, \tag{8.8}$$

$$l_{min} \approx \frac{\lambda_{min}}{3} \qquad \Rightarrow \qquad f_{max} \approx \frac{c}{3l_{min}}. \tag{8.9}$$

Note that the upper frequency limit deviates from the assumption of a half-wave resonance of the corresponding dipole as the complex interplay with the waveguide is empirically taken into account by the formula. A detailed investigation of these effects for the Small Black Spider LPDA can be found in [162]. Nevertheless, the above formulae only give a rough estimate, the actually achieved bandwidth is usually somewhat larger [146].

The design parameter τ affects the number of dipoles between l_{min} and l_{max}. More dipoles in this range will cause a more constant sensitivity as the resonances of sequenced dipoles will overlap to a larger extend. Assuming a constant relative spacing σ the antenna height will increase with a increasing value of τ. The height can be reduced by choosing a smaller value of σ. From Eq. 8.7 we can conclude that a smaller σ results in a wider opening angle α. The opening angle directly affects the directivity of the antenna, the wider the opening angle, the lower the directivity.

8.2.2 Electrical Layout

The design parameters of the Small Black Spider (SBS) were optimized with respect to the demands of radio detection at AERA by means of the LPDA design program

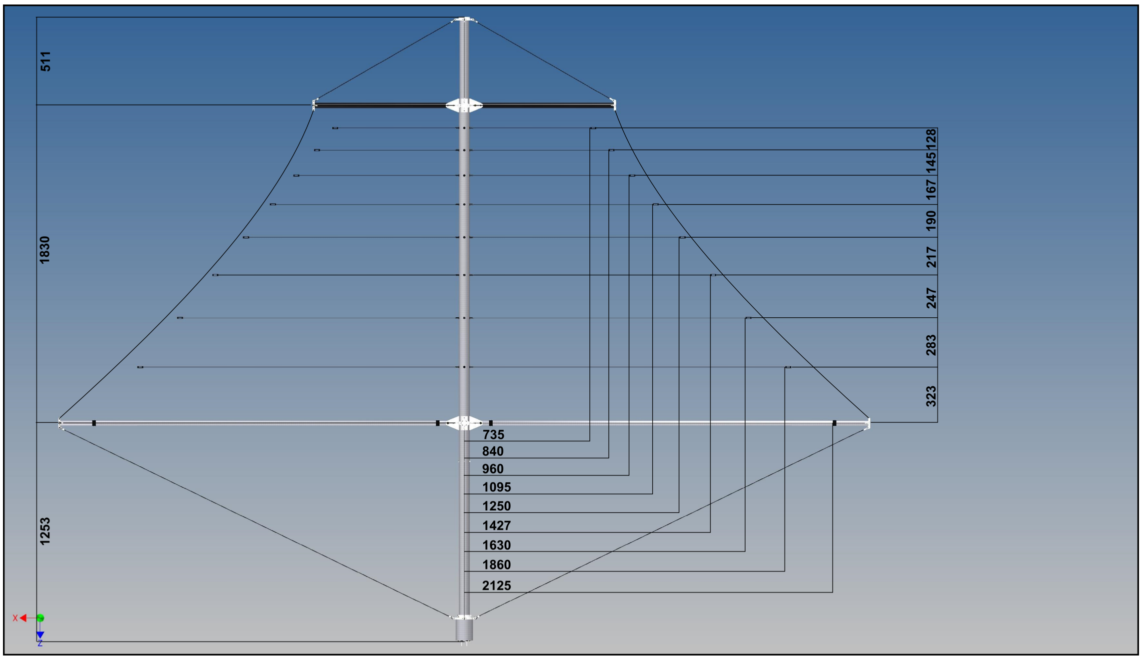

Figure 8.3: Engineering drawing of the Small Black Spider LPDA. Dimensions are given in mm.

LPCAD [164]. LPCAD estimates the antenna gain and computes the structural dimensions for a set of specifications such as the desired bandwidth and the design parameters τ and σ.
The bandwidth was chosen according to the radio quiet frequency range from 30 MHz to 80 MHz at the AERA site. The design parameters τ and σ were chosen to achieve a compromise between a preferably constant sensitivity over the entire bandwidth, a reasonable number of dipoles, a relatively low gain to cover a broad area of the sky and reasonably small overall dimensions.
The design process lead to the following design parameters

$$\begin{aligned} \tau &= 0.875, & \sigma &= 0.038, \\ l_{max} &= 4250\text{ mm}, & l_{min} &= 1470\text{ mm}. \end{aligned}$$

The remaining dipole lengths and their spacings can be calculated with Eq. 8.4 and Eq. 8.5 and are given in Fig. 8.3. From Eq. 8.7 an opening angle of 78 ° is obtained.

The, in total, 9 dipoles feed the received signals into a central waveguide consisting of two parallel wires, referred to as Lecher line. The cross connection of the dipoles to the Lecher line (cf. Fig 8.2) is realized by Printed Circuit Boards (PCB) attached to the waveguide. The uppermost PCB, located closely to the shortest dipoles (see Fig. 8.7 c)) constitutes the footpoint of the antenna. Note that the position of the footpoint is slightly shifted downwards with respect to the virtual array index due to practical reasons. It has been found in previous studies that the deviation from the virtual array index does not yield any performance losses in case of the SBS.

The footpoint of the antenna is usually the optimal place for a low noise amplifier, following the rule that weak signals should be amplified as soon as possible in order to minimize additional noise from transmission lines. However, in case of the SBS installed at AERA, the footpoint is located about 5 m above ground and is thus not accessible for maintenance. Hence, the LNA has been moved to the bottom of the antenna. The footpoint is connected through a transmission line transformer to a low loss coaxial cable which runs downwards to the LNA. The transmission line transformer, also called balun (balanced - unbalanced), is mounted on the uppermost PCB and serves two purposes. Firstly it transforms the balanced signal[2] from the Lecher line to the unbalanced coaxial cable whose outer shielding is grounded through the radio detector station. Secondly it provides a 4:1 impedance transformation from the Lecher line with an intrinsic impedance of about 200 Ω to the 50 Ω coaxial cable. It thus minimizes reflections due to an impedance mismatch between Lecher line and coaxial cable.

The antenna impedance of the SBS can be accessed through reflection measurements with a Vector Network Analyzer (VNA). The VNA feeds the antenna at its input terminals, which is in case of the SBS the 50 Ω coaxial connector at the bottom of the antenna, with a defined voltage amplitude V_S and measures the magnitude and phase of the reflected voltage V_{ref}. The VNA thus delivers the complex S-parameter S11 as a function of the frequency. We rewrite the definition of S11 given in Eq. 7.26 in terms of the antenna impedance Z_A

$$S11 = \frac{V_{ref}}{V_S} = \frac{Z_A - Z_S}{Z_A + Z_S}, \tag{8.10}$$

where Z_S is the source impedance of the VNA of 50 Ω. Solving the above equation for the antenna impedance yields

$$Z_A = Z_S \frac{1 + S11}{1 - S11}. \tag{8.11}$$

The real and imaginary part of the antenna impedance obtained by a reflection measurement is shown in Fig. 8.4. Additionally, the antenna impedance is displayed in a Smith Chart, commonly used in electrical engineering to visualize impedances, in appendix A.1.

We find that the real part (resistance) of the antenna impedance oscillates around a value of about 50 Ω within the AERA bandwidth. By taking into account only the frequency bins from 30 MHz to 80 MHz we obtain a mean value of $Re(Z_A) = 48.8 \pm 18.2\ \Omega$. The imaginary part (reactance) shows a similar oscillation with a mean of $Im(Z_A) = -0.3 \pm 18.1\ \Omega$ within the AERA band.

The oscillations of the antenna impedance are due to the resonances of the single dipoles. An antenna is referred to as resonant when the input impedance becomes purely resistive, that is its reactance vanishes. The input impedance of a single dipole is a function of its length l with respect to the impinging wavelength. For

---

[2] Balanced or symmetric signals denote inversely phased voltages working against the same electrical potential whereas unbalanced signals denote a single voltage working against ground.

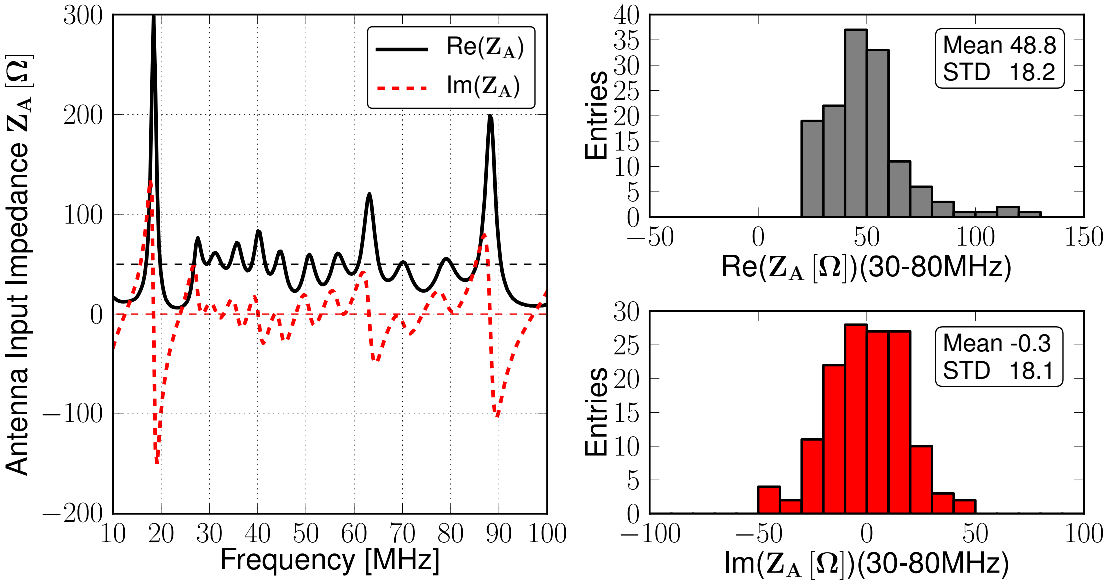

Figure 8.4: Input impedance of the SBS as obtained from the reflection measurement depicted in Fig. 8.5. The histograms on the right contain the frequency bins within the AERA bandwidth from 30 MHz to 80 MHz.

$l = \lambda/2$ it equals $Z_A = 73 + i42.5\ \Omega$ in case of a dipole of infinitesimal thickness in free space [146]. The non-vanishing reactance implies losses in terms of a signal transfer to a pure resistive readout load and is commonly reduced to zero by slightly reducing the dipole length until the dipole becomes resonant. Consequently the resonance frequency deviates in practice slightly from the the one implied by $l = \lambda/2$. In case of the SBS the interplay of the dipole impedances together with the intrinsic impedance of the Lecher line and the impedance transformation of the balun enables a broad band matching to a readout impedance of 50 Ω as observed in Fig. 8.4.

Having investigated the impedance behavior of the SBS we can understand the behavior of the reflected power which evolves as a consequence of the former.
In Fig.8.5 the ratio of reflected to input power $|S11|^2 = |\Gamma|^2$ (cf. Eq. 7.11 and Eq. 8.10) of the same reflection measurement that delivered the previously discussed antenna impedance is given as function of the frequency. The measurement indicates that the power reflection within the AERA bandwidth is always smaller than 20%, typically only a few percent of the input power. Furthermore we observe similar oscillations as in case of the antenna impedance. The minima of reflection correspond to the resonances of the dipoles of the SBS. As discussed before they indicate an optimal impedance matching from the source throughout the LPDA structure to the dipole and thus minimal reflections.
The measured resonance frequencies significantly deviate from those given by the condition of $l = \lambda/2$. Assuming the latter we obtain for the shortest dipole of the SBS $f_{max} = 102.0$ MHz and for the longest dipole $f_{min} = 35.3$ MHz. Furthermore it might be somewhat surprising that we only observe eight resonances in the reflec-

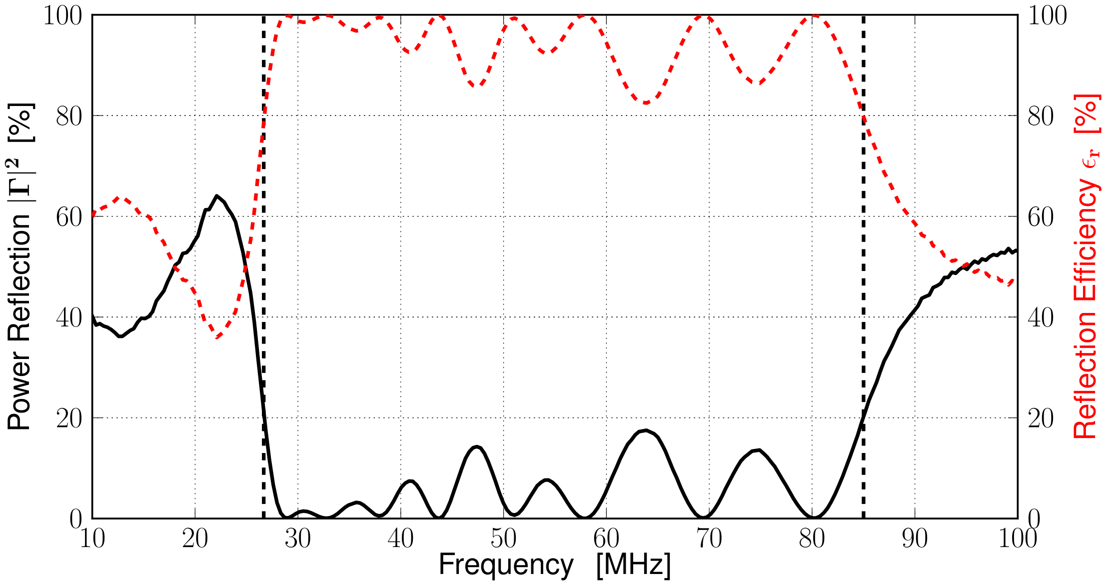

Figure 8.5: Power reflection (full curve) and reflection efficiency (dashed curve) measured at the input of a SBS antenna installed at the AERA site. The dashed vertical lines denote the bandwidth of the SBS from 26.7 MHz to 85.0 MHz.

tion measurement although the SBS has nine dipoles. Both can be explained by the complex interplay of impedances within the antenna structure and the associated shift of resonance frequencies.

Beyond the resonances of the dipoles the reflection steeply increases. Comparing with the impedance behavior we find that this is due to the mismatch caused by large absolute values of both the resistance and reactance of the antenna impedance.

The fraction of power that is not reflected at the antenna terminals is accepted by the antenna structure. Without any structural losses within the antenna, that is the radiation efficiency ϵ equals unity (cf. Eq. 7.7), all of the accepted power will be radiated by the antenna structure. Simulations of the SBS with Nec2 yield a radiation efficiency close to 99% throughout the AERA bandwidth [162]. The assumption of $\epsilon = 1$ is thus fulfilled in good approximation.

From the reflection measurement we can then compute the frequency dependent fraction of radiated power by (cf. Eq. 7.7 and Eq. 7.12)

$$P_{rad} = \epsilon\, P_{acc} = \epsilon\, \epsilon_r\, P_S = \epsilon\,(1-|\Gamma|^2)\, P_S \qquad \Rightarrow \qquad \frac{P_{rad}}{P_S} = \epsilon_r = (1-|\Gamma|^2), \qquad \epsilon = 1. \tag{8.12}$$

The quantity $(1 - |\Gamma|^2)$ was previously defined as the reflection efficiency ϵ_r and is depicted in Fig. 8.5.

The reflection efficiency provides a convenient way to give a proper definition of the bandwidth of the SBS. According to the standards in [145], the bandwidth denotes 'the range of frequencies within which the performance of the antenna, with respect to some characteristic, conforms to a specified standard'. We here characterize the

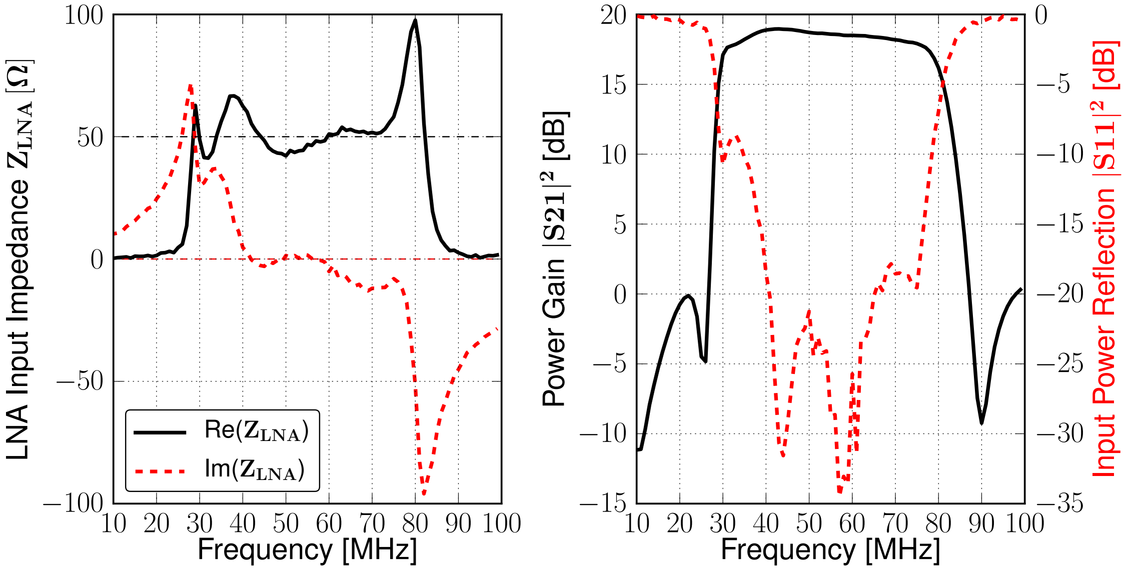

Figure 8.6: Input impedance (left) and power gain and input power reflection (right) of the LNA of the SBS.

performance by demanding that the reflection efficiency is always larger than 80% within the bandwidth. For the SBS this yields a bandwidth from 26.7 MHz to 85.0 MHz which is depicted in Fig. 8.5.
Within this bandwidth we find an average reflection efficiency of 94.0%. Thus for $\epsilon = 1$, 94% of the input power is radiated by the antenna. Due to the reciprocity, this performance characteristics are likewise valid for reception. With the steep decline of sensitivity beyond the bandwidth, the SBS thus explicitly introduces a bandpass filter to attenuate man-made noise sources.

For the SBS a dedicated LNA has been developed which is described in detail in [165, 166]. It is attached at the bottom of the SBS (see Fig. 8.7 b)) to the coaxial cable which runs upwards to the antenna footpoint.
Amplifiers are commonly characterized by their power gain $|S21|^2$ and input power reflection $|S11|^2$ rather than discussing the full set of complex S-parameters (cf. Ch. 7.4). It is convenient to express these power ratios in a decibel (dB) scale which relates to a linear scale as

$$X_{dB} = 10\,log_{10}(X_{lin}), \tag{8.13}$$

where X denotes a arbitrary ratio of physical quantities.

A measurement of the power gain and the input power reflection is depicted in Fig. 8.6 together with the input impedance calculated from S11 with Eq. 7.12. The LNA input impedance with a resistance mostly close to 50 Ω and a relatively small reactance within the AERA bandwidth is designed to match the antenna impedance of the SBS. This results in a low input power reflection, typically lower than -10 dB within the AERA band which corresponds to 10% reflected power.

The power gain which denotes the amplification of the LNA is about 18 dB within the AERA band. Beyond, the gain steeply decreases due to a bandpass filter integrated at the LNA input for the purpose of noise supression.

8.2.3 Mechanical Layout

The mechanical design of the SBS was developed by means of a Computer-Aided Design (CAD) program according to the parameters specified by the electrical design. The three dimensional CAD model of the SBS is presented in Fig. 8.7.
The SBS unites two self-contained LPDA antennas in a single mechanical structure. The two antenna planes are aligned perpendicular and intersect at the central aluminum pole which carries the entire antenna structure. Two crosses of rigid tubes span an outer frame out of Dyneema ropes on which the dipoles are fixed. This frame yields overall dimensions of the SBS of about 4.5 x 4.5 x 3.5 m^3. The overall weight of the SBS amounts to about 18 kg.
Eight of the nine SBS dipoles are made from coated copper wires which reduces their wind load and mass and prevents them from breaking due to oscillations induced by the wind. They are spanned and aligned horizontally by coil springs attached to the outer frame. The springs as a whole introduce sufficient tension in the outer frame to keep a rigid structure and compensate for a potential distension due to aging of the ropes. The inner end of the dipole wires is guided by silicone plugs through bores in the central pole where they are soldered to the PCBs of the waveguide (see Fig. 8.7 c)). For the longest dipoles, the lower cross which spans the structure is utilized. It is made of aluminum tubing connected by a short flexible wire to the waveguide inside the central pole. The dipole tubes are insulated from the central pole and the outer wiring by short inserts of plastic. The upper cross does not have any electrical function and is made from tubes of non conducting fiberglass compound.
Both, the upper and lower cross are attached to the central pole by pivot joints (cf. Fig. 8.7 c)) which allow to fold the tubes against the pole once the lower ropes of the frame are released. Due to this folding mechanism, the size of the antenna can be reduced to only 0.2 x 0.2 x 3.5 m^3. It can thus be assembled in a lab, easily and cost efficiently shipped, and finally, unfolded in a few minutes for installation at the AERA site.

The Lecher lines are made of 0.5 mm wires fixed at a distance of 12 mm by the PCBs. The coaxial cables attached at the uppermost PCB are guided through two plastic tubes, which serve as a stabilization for the waveguide at the same time, to the bottom of the antenna. They end in a coaxial connector where the LNAs, placed in a separate housing for each antenna plane (see Fig. 8.7 b)), are directly connected. The LNAs are additionally sheltered by an aluminum cylinder.
The close positioning of the two Lecher lines within the waveguide may suggest an electrical crosstalk between the two antenna planes. In measurements it was verified that the crosstalk is actually less than 0.06% of the received signal power within the bandwidth [167].

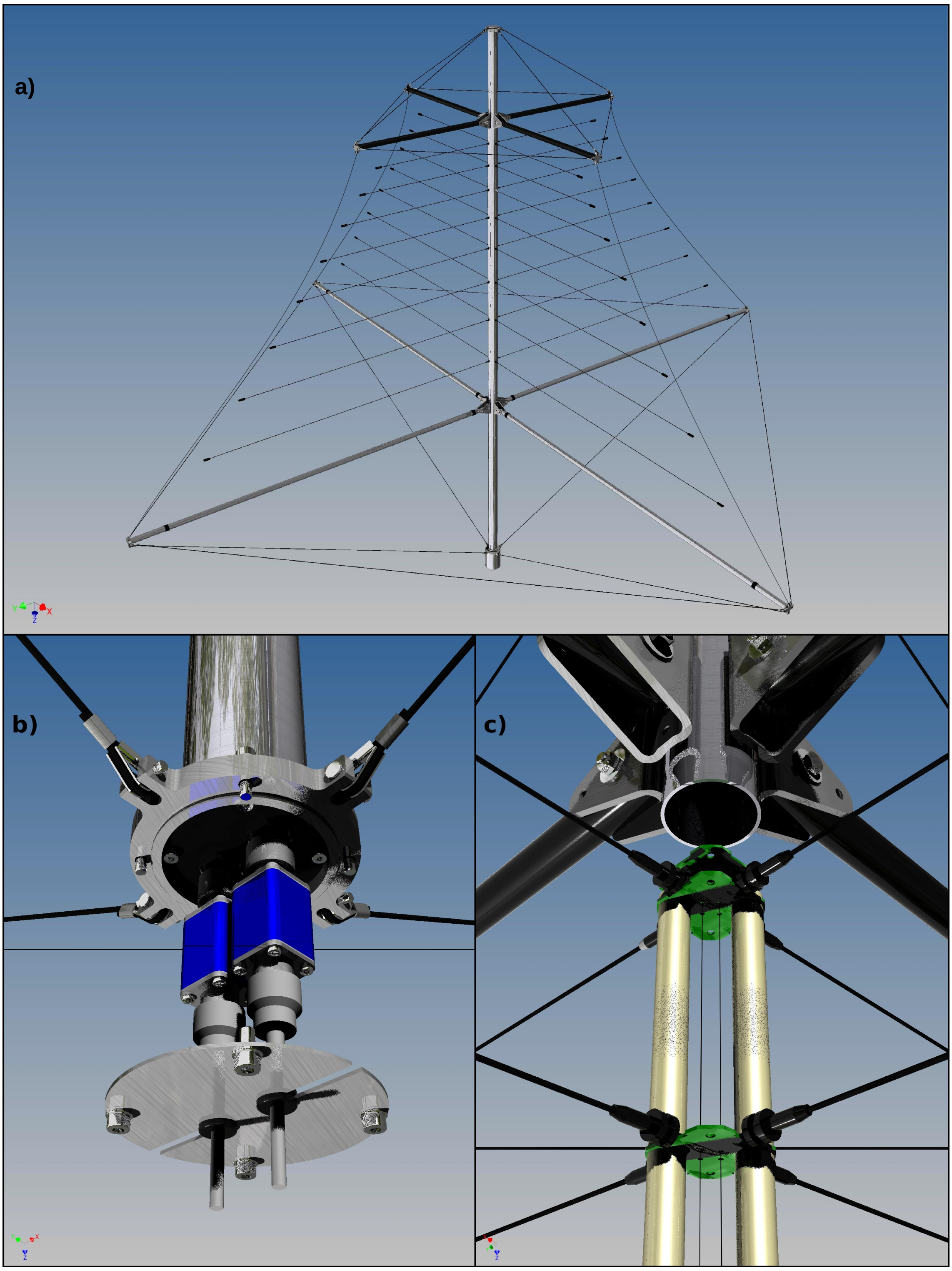

Figure 8.7: Engineering drawings based on the three dimensional CAD model of the SBS antenna. Fig. a) shows the complete antenna, Fig. b) the bottom of the antenna with the two attached LNAs in their blue housing (the aluminum cylinder was removed for demonstration). In Fig. c) the upper central region is shown with the central pole removed to allow a view on the internal waveguide.

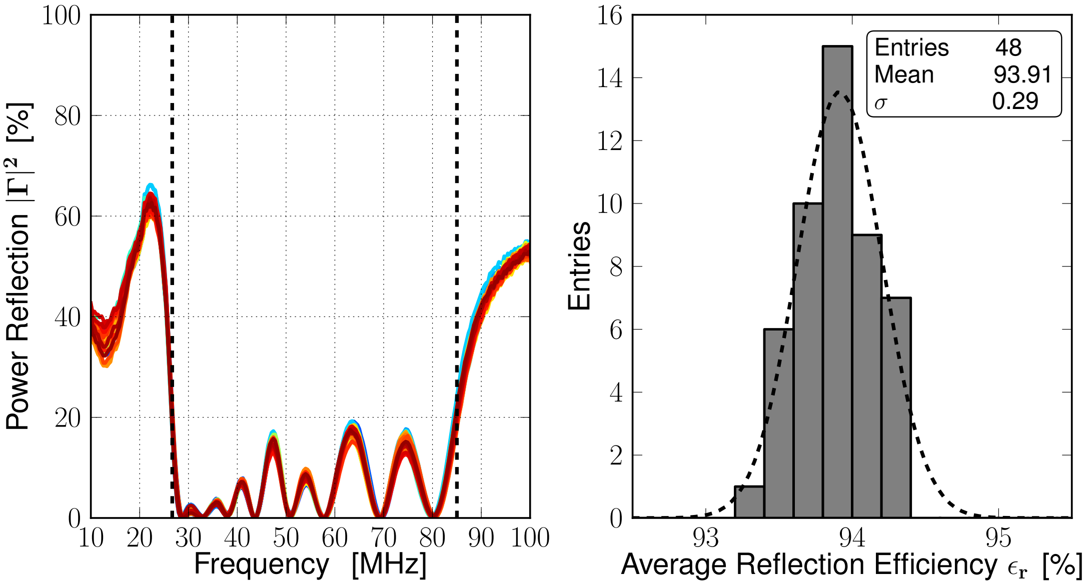

Figure 8.8: Reflection measurements of both channels of the 24 SBS antennas installed at AERA. The bandwidth (cf. Sec. 8.2.2) is indicated by the dashed vertical lines. The reflection efficiency within the bandwidth is histogrammed on the right. A gaussian fit to the data is shown.

Stress tests have been performed on subcomponents of the antenna prior to the installation at AERA. In temperature tests of the waveguide it was verified that the thermal expansions are within the elastic limits of the used materials and the Lecher lines keep their parallel alignment during the expected temperature drifts. Furthermore, the oscillation of the dipoles stimulated by wind has been simulated over a period of one year in a dedicated test bench. Except a few dipoles which got detached from the outer frame during a storm in 2012, no damages to the SBS have been observed over almost 4 years of operation at AERA.

Most of the mechanical parts of the SBS are manufactured by CNC (Computer Numeric Control) machines to ensure a high precision and reproducibility during series production. As a benchmark of the reproducibility of the electrical properties, reflection measurements of both channels of the 24 SBS antennas installed at AERA have been performed and are summarized in Fig. 8.8. Very little deviations between different antennas are visible, indicating an excellent production quality. The reflection efficiency within the bandwidth of the SBS amounts 93.9% with a spread of only 0.3%.

8.3 Butterfly Antenna

The 100 radio detector stations of phase 2 of AERA are equipped with a Butterfly antenna as a sensor to the radio emission. The predecessor version of this antenna [168] has been developed in the scope of the CODALEMA experiment. Three

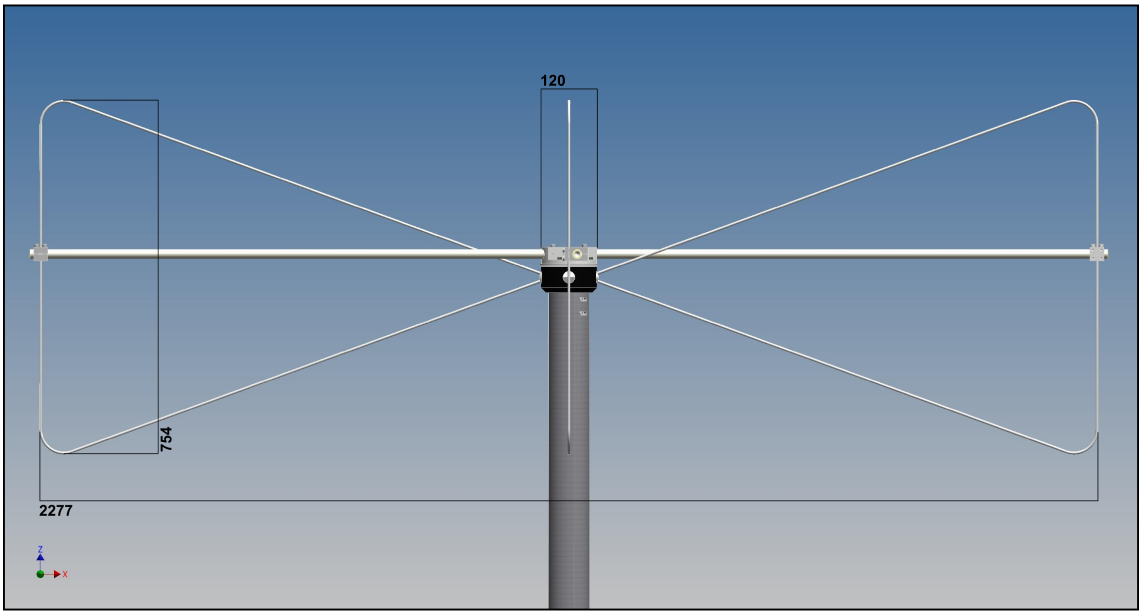

Figure 8.9: Side face of the Butterfly antenna used for phase 2 of AERA. Dimensions are given in mm.

Butterfly antennas were successfully used at the Auger Observatory in an upgrade of RAuger [128] to detect cosmic rays. The current version of the Butterfly antenna was developed within the scope of this thesis as an optimization towards the application on large scales at AERA. It maintains to a large extend the electrical layout of the predecessor version.

8.3.1 Electrical Layout

The Butterfly antenna belongs to the family of broad band dipoles, more specific, it is an approximation of a so called bow-tie antenna. Its active elements, in the following referred to as radiator, are two triangular arms arranged as depicted in the side face of Fig. 8.9. In case of a classical bow-tie antenna the areas enclosed by the triangles are filled by a plane conducting patch. The Butterfly antenna approximates the patch by a wire to minimize the wind load and weight of the radiator while the electric properties of the classical bow-tie antenna are maintained to a large extend [146].

The Butterfly antenna is explicitly designed as an active antenna, meaning that the antenna characteristics arise from an interplay of the antenna radiator together with a dedicated LNA. The terminals of the radiator are the inner tips of the triangles. They are directly connected to the input terminals of the LNA placed inside the central nut (the black cylinder in Fig. 8.9).
To access the input impedance of the antenna radiator only, a reflection measurement was performed at the input terminals of the radiator analog to the measurement discussed Sec. 8.2.2. To transform the unbalanced signal of the network analyzer to a balanced signal at the input terminals of the radiator elements, a balun was

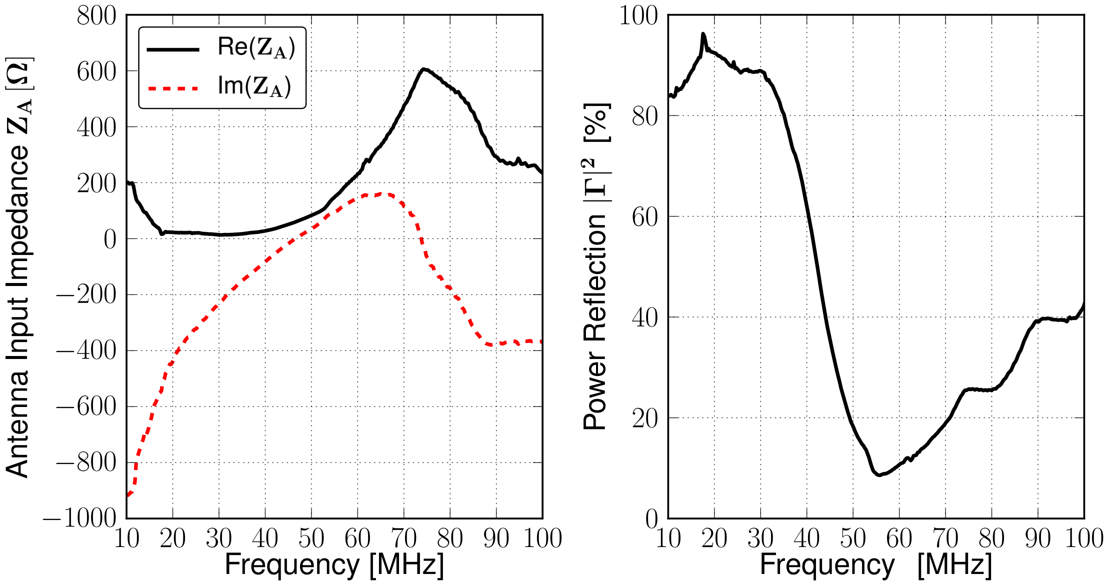

Figure 8.10: Input impedance (left) and power reflection of the Butterfly radiator (right) measured with a Vector Network Analyzer at 50 Ω.

used. Its influence has been removed from the result depicted in Fig. 8.10 by a null calibration of the setup. A Smith chart of the reflection measurement is attached in appendix A.2.

The impedance of the Butterfly radiator shows a strong variation with the frequency, typical for dipole like antennas. A matching to the 50 Ω system of the VNA is only achieved around 50 MHz contrary to the broad band matching of the SBS.

Consequently the power reflection becomes minimal around 50 MHz. A relatively broad resonance compared to a simple dipole of infinitesimal thickness is indicated by the power reflection.

However, the Butterfly radiator is not designed for an operation in a 50 Ω system as during the reflection measurement, but for a coupling to the input impedance of the Butterfly LNA.

The conception and design of the Butterfly LNA is described in detail in [168]. Its electrical characteristics obtained from measurements with a VNA are depicted in Fig. 8.11.

The LNA input impedance is designed to achieve conjugate matching with the impedance of the Butterfly radiator. The LNA input resistance increases with the frequency, reaches a maximum around 70 MHz and then decreases again to about 200 Ω at 100 MHz, following the behavior of the radiator resistance.

The positive input reactance of the LNA at lower frequencies partly compensates the negative reactance of the radiator for frequencies lower than about 50 MHz. Thus, with the frequency dependent tuning of the LNA input impedance, a broad band matching to the Butterfly radiator is achieved despite its strong impedance variation. The broad band performance of the Butterfly antenna including its LNA

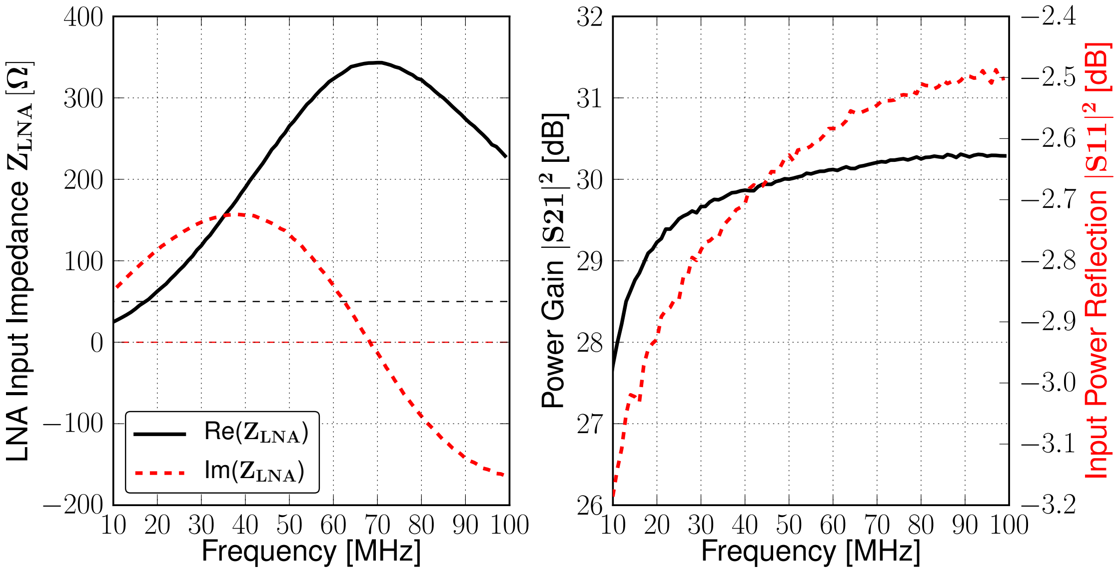

Figure 8.11: Input impedance (left), power gain and input power reflection of the Butterfly LNA (right) measured with a Vector Network Analyzer at 50 Ω.

will be discussed further in the scope of the calibration of the radio detector stations.

The Butterfly LNA provides a high power gain of about 30 dB (corresponding to an amplification factor of 1000), almost constant over the AERA bandwidth as depicted in Fig. 8.11 (right). The input reflection is relatively high as the input impedance is not matched to the 50 Ω system of the VNA.

8.3.2 Mechanical Layout

To enable dual polarized measurements of the radio emission, the Butterfly antenna unites two perpendicular aligned antennas in a single structure (see Fig. 8.13). The radiators are bent out of 6 mm aluminum rods. Their endings fit into an aluminum plug (see Fig. 8.13 b)) which is plugged into the central nut. On their inner side, the plugs provide screw threads (see Fig. 8.13 c)) where the input terminals of the LNA are connected through short wires.
The central nut is CNC machined from a special UV resistant non-conducting plastic to electrically insulate the radiators from each other. Each plug is fixed by a headless screw in the nut to ensure a vertical alignment of the radiator triangles. The nut is made watertight by rubber seals at the radiator plugs and by a silicone seal (white ring in Fig. 8.13 c)) on the top of the nut. The two LNAs for the two channels of the antenna are realized on a single PCB placed in the interior of the nut. Its output signals are guided by coaxial connectors through the bottom of the nut and then further through the antenna pole to the station electronics.

The flexible radiator rods tend to oscillate or even permanently bent due to the strong winds at the AERA site and furthermore sag due to their self-weight. To

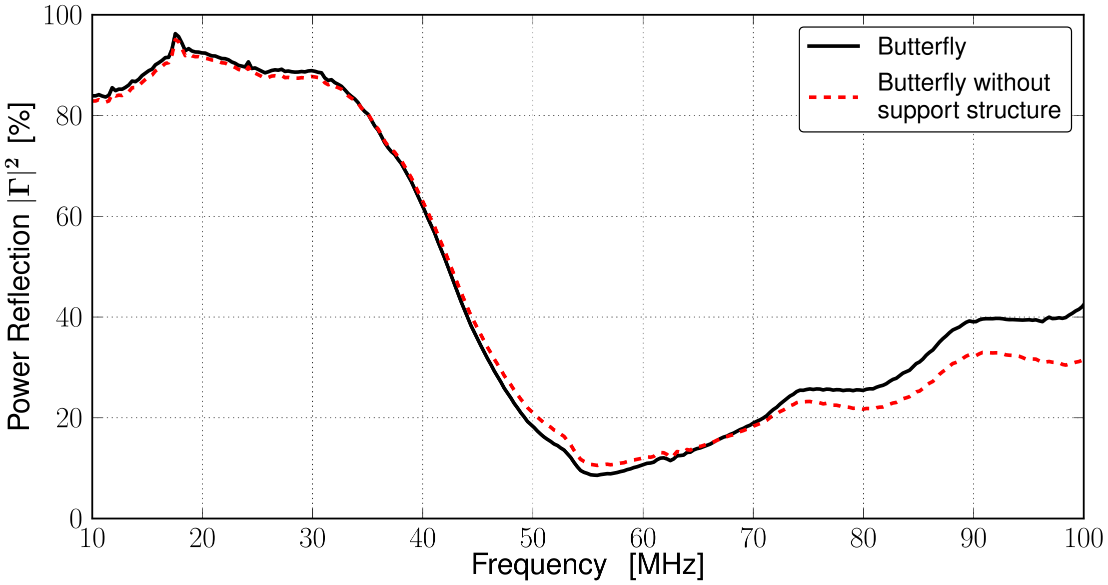

Figure 8.12: Comparison of the power reflections of the Butterfly radiator with and without attached support structure.

solve these issues a support structure was developed for the Butterfly antenna. A machined aluminum cap (see Fig. 8.13 b)) is screwed on top of central nut and holds four rigid tubes of non-conducting fiberglass compound. The fiberglass tubes are connected to the dipole ends by aluminum clamps as visible in Fig. 8.13 d). Thereby forces acting on the radiator are absorbed by the support structure and the radiators are fixed in their design position.

A potential influence of the support structure on the electrical characteristics of the Butterfly antenna is studied by an additional reflection measurement of the radiator performed with the support structure detached from the antenna. A comparison to the reflection measurement shown in Fig. 8.10 is presented in Fig. 8.12. The measurements indicate no significant influence of the support structure on the power reflection within the AERA bandwidth. The mean deviation of the two measurements between 30 MHz to 80 MHz is 1.5% in reflected power only.

In conclusion it can be stated that the Butterfly antenna features a very compact, cost effective and relatively simple electrical and mechanical design compared to complex antennas such as the SBS. These are mayor arguments why the Butterfly antenna was chosen for phase 2 of AERA.

8.3.3 Stress Testing in a Wind Tunnel

To estimate the degree of deflection of the Butterfly radiator, a stress test in the wind tunnel of the Institut für Stahl und Leichtmetallbau at the RWTH Aachen University was performed. The wind tunnel provides a platform on which the Butterfly antenna, equipped with a single radiator, was mounted perpendicular to the

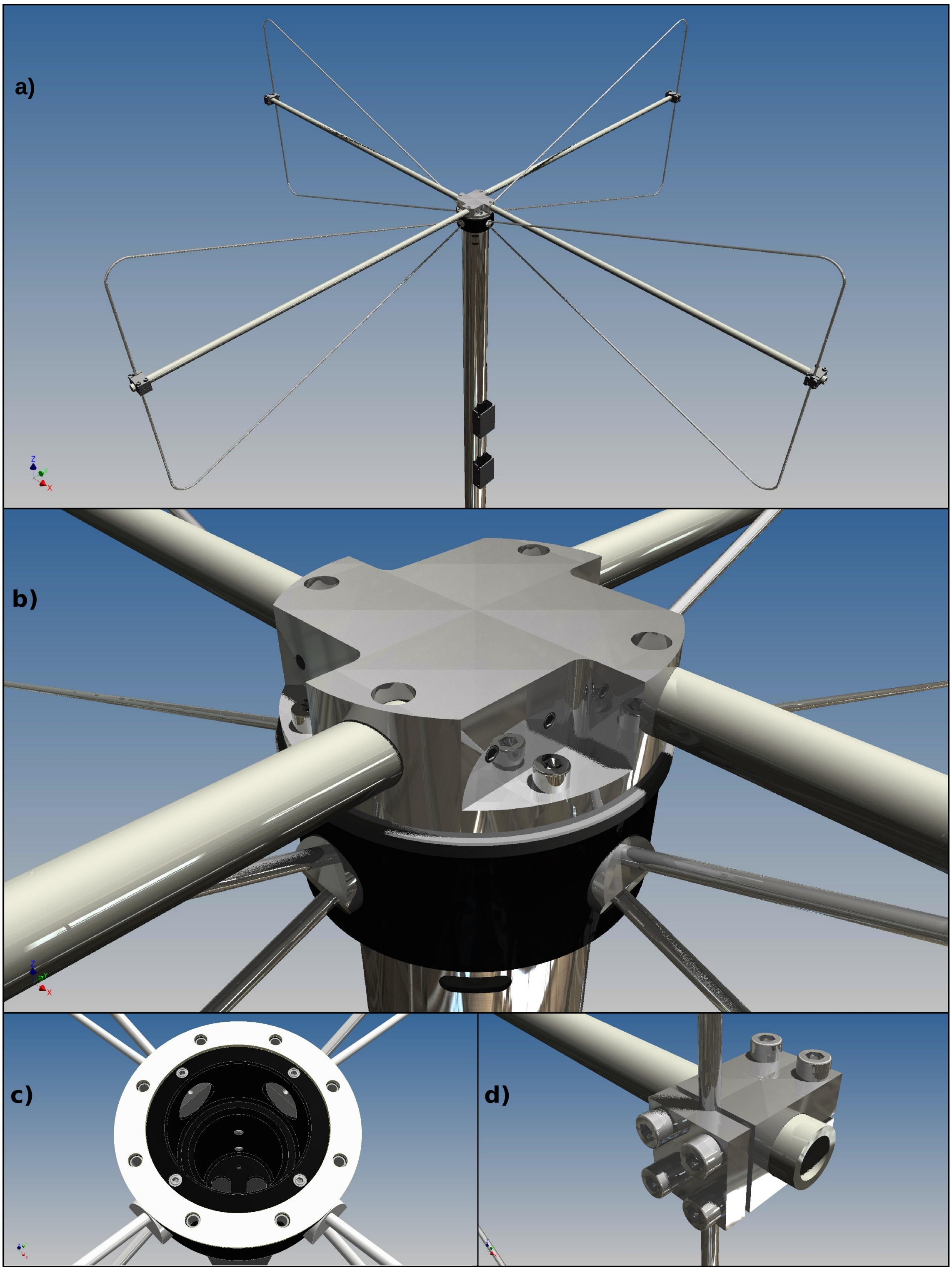

Figure 8.13: Engineering drawings based on the three dimensional CAD model of the Butterfly antenna. Fig. a) shows the complete antenna, Fig. b) the central nut (black cylinder) with the support structure on top. In Fig. c) the interior of the central nut and in Fig. d) the clamp fixing the radiator to the support structure is depicted.

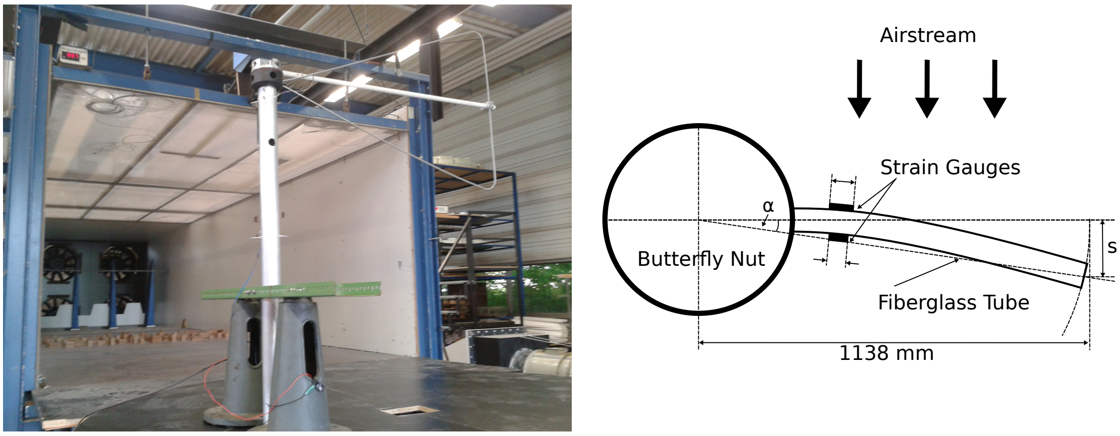

Figure 8.14: Measurement setup for the stress testing of the Butterfly antenna in a wind tunnel (left) and schematic top view of the Butterfly antenna with attached strain gauges for the monitoring of the deflection of the Butterfly radiator (right).

airstream as visible in Fig. 8.14 (left).

To dynamically monitor the deflection of the butterfly radiator, the fiberglass tube of the support structure was assembled with strain gauges. Strain gauges are used in engineering to measure very small deformations of solid objects. They consist of a metallic foil pattern embedded in a thin plastic layer which is applied to the object under test by special adhesives. As the object is deformed, the strain gauge is deformed, causing its electrical resistance to change.

In case of the measurement setup for the Butterfly antenna two strain gauges have been glued on opposite sides to the vertical faces of the fiberglass tube in a distance of about 10 cm from the nut as illustrated in Fig. 8.14 (right). When the fiberglass tube is bent in the horizontal plane, one of the strain gauges is stretched while the other is compressed. The small changes in resistance are converted by a Wheatstone bridge to a measurable voltage signal. The two strain gauges are connected within the Wheatstone bridge such that a simultaneous stretching due to thermal expansion of the fiberglass tube is compensated. The voltage delivered by the Wheastone bridge thus only depends on the horizontal deflection of the fiberglass tube.

The voltage delivered by the Wheatstone bridge was recorded with a data logger at a sampling rate of 500 Hz. Wind speeds between 0 m/s and 20 m/s in steps of 2.5 m/s were set. The wind tunnel monitors the present wind speed with a sensor placed at the exhaust port at about 1 m distance from the Butterfly radiator and adjusts the power of the fans until the set value is reached. For each adjusted wind speed, voltage traces of 32 s were recorded.

An exemplary voltage trace recorded at a wind speed of 10 m/s is shown in Fig. 8.15. A driven oscillation with a varying amplitude is observed. On closer inspection we find a constant frequency of about 5 Hz. The voltage traces recorded at different wind speeds yield essentially the same frequency of oscillation and thus indicate the resonance frequency of the Butterfly radiator together with the support structure.

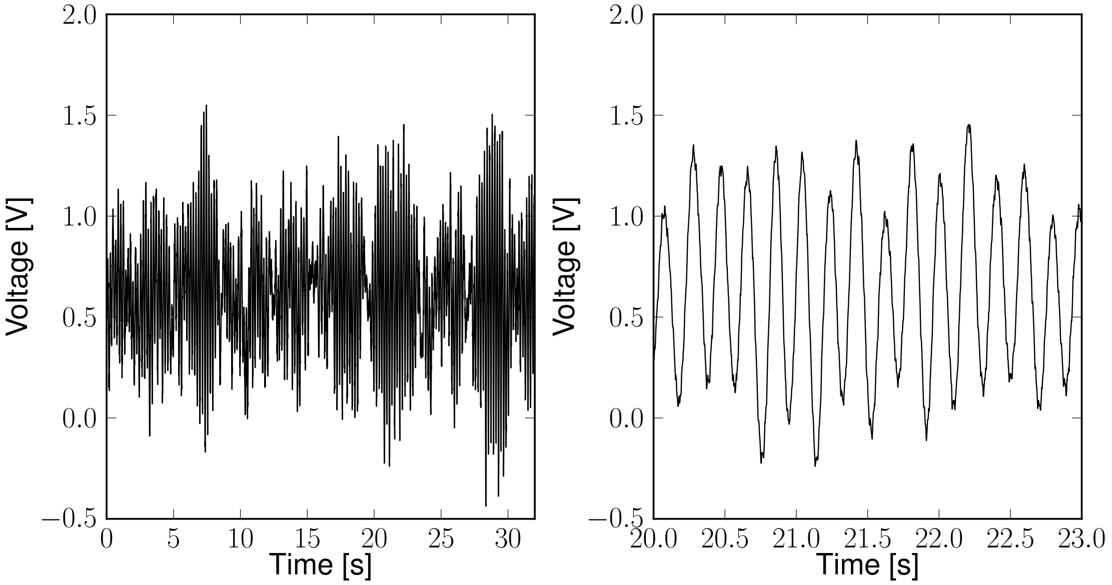

Figure 8.15: Voltage trace indicating the oscillation of the Butterfly radiator induced by an airstream with a speed of 10 m/s. On the right, a zoom of the left trace is depicted.

To translate the measured voltage to the deflection of the radiator, a calibration was performed. A scale has been mounted in front of the outer ending of the fiberglass tube. The tube was deflected from $s = -5$ cm to $s = 5$ cm from its rest position in steps of 5 mm. For each deflection the voltage delivered by the Wheatstone bridge was recorded. A linear correlation between adjusted deflection s and measured voltage V was observed. A linear regression yields

$$s[cm] = V[V] \cdot 2.575 \pm 0.052[cm/V]. \tag{8.14}$$

Looking at Fig. 8.14 (right) we can compute the deflection α in degrees as

$$\alpha = arctan\left(\frac{s[cm]}{113.8cm}\right). \tag{8.15}$$

The deflections measured at two specific windspeeds are shown in the histograms of Fig. 8.16. We observe a normal distribution of the data samples. The mean of the distribution shifts towards higher deflections with increasing windspeed indicating that the center of oscillation deviates from the rest position. Furthermore, the amplitudes of the oscillation become larger with increasing windspeed which manifests in the increasing width of the distribution. We thus characterize the deflection with the mean and the standard deviation observed at a specific windspeed.

These values are plotted in Fig. 8.17 as a function of the accessed windspeeds. The mean deflection is below 1° for wind speeds smaller than 10 m/s. Even at maximum accessed wind speed of 20 m/s the mean deflection stays below 2°.

If it is demanded that the deflection of the radiator is always below a certain maximum value, e.g. for precision polarization measurements of the radio emission,

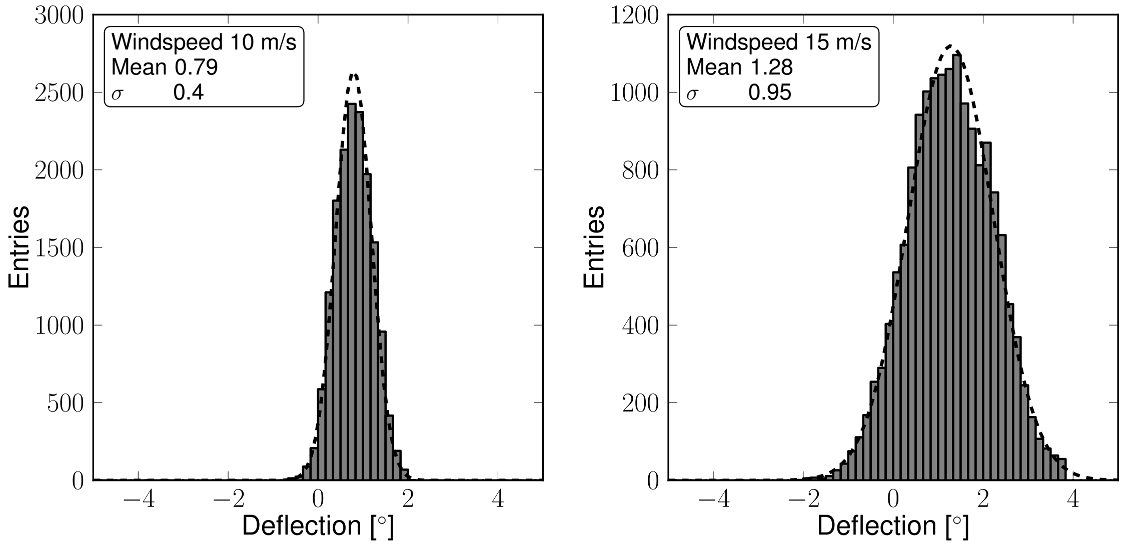

Figure 8.16: Deflection of the Butterfly radiator for windspeeds of 10 m/s and 15 m/s. The Histograms contain 16,000 entries computed from the voltage samples of a 32 s trace. Fitted normal distributions are shown as the dashed lines.

criteria could be formulated based on the maximum amplitudes which are additionally denoted in Fig. 8.17.

The wind speed at the AERA site recorded over a period of almost nine months is depicted in Fig. 8.18. In 93.3% of the total observation time, the wind speed at the AERA site is below 10 m/s, corresponding to a mean deflection of the Butterfly radiator below 1°. Respectively, in 99.96% of the time, wind speeds are below 20 m/s according to a mean deflection below 2°.

To continuously monitor the alignment of the Butterfly antenna at AERA, a monitoring system based on the discussed setup is in preparation [169]. The monitoring data could then be included as an uncertainty on the antenna alignment in data analysis.

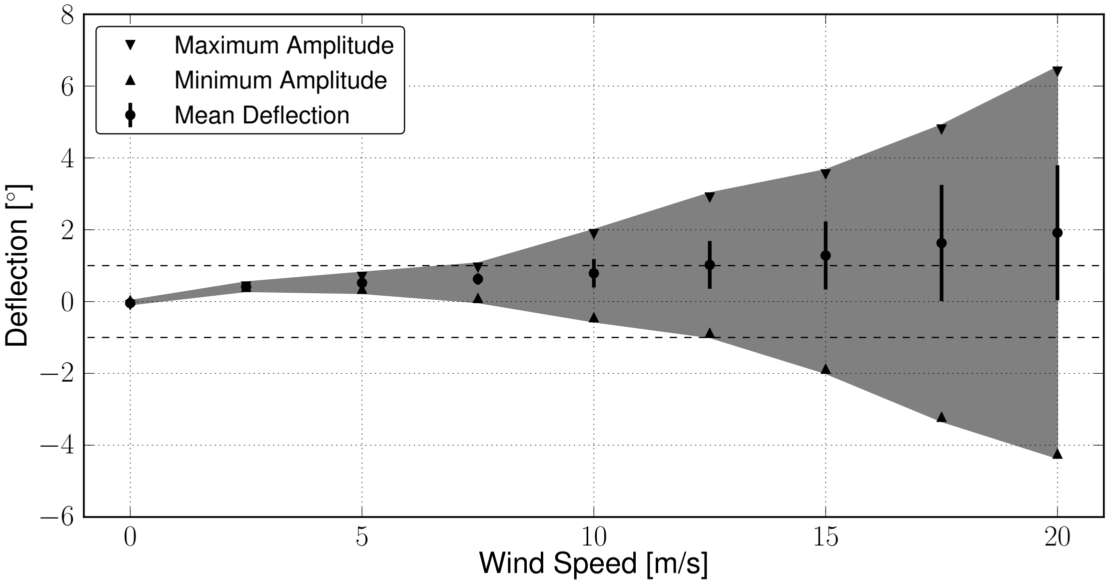

Figure 8.17: Mean deflection of the Butterfly radiator from its rest position measured at various wind speeds. The errorbars indicate the standard deviation of the samples corresponding to the histograms of Fig. 8.16. Additionally the maximum and minimum amplitudes are denoted. A linear interpolation of these amplitudes is given by the gray band.

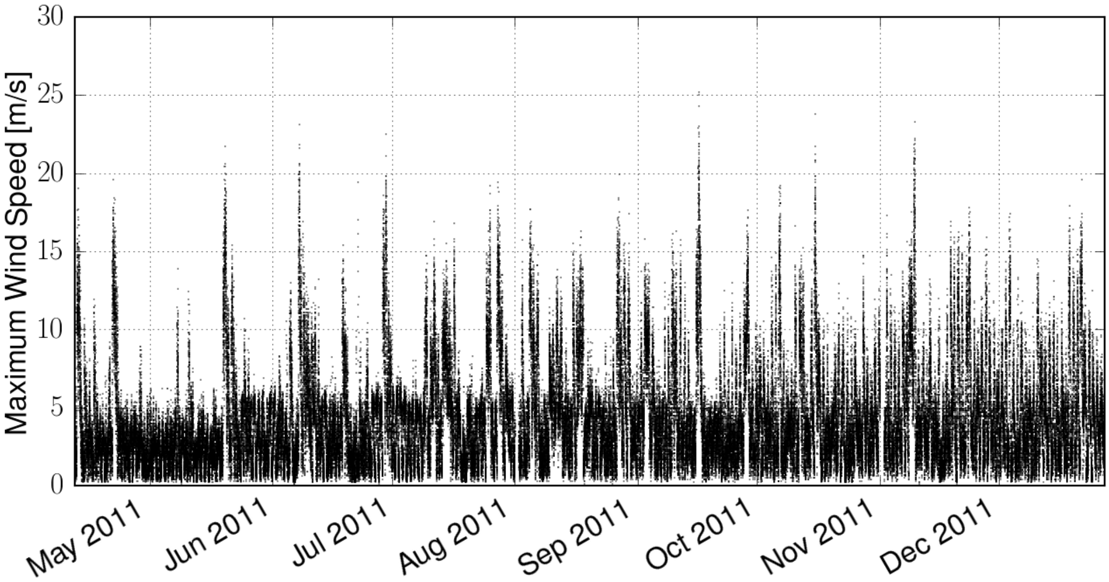

Figure 8.18: Wind Speed as measured with a weather station [142] installed at AERA. The weather station samples the wind speed each second. Each dot indicates the maximum value of the wind speed observed in an interval of 2 minutes.

9. Setups for in situ Calibration of Radio Antennas

For the reconstruction of the electric field emitted by cosmic ray air showers a precise knowledge of the antenna response is essential. The antenna response does not only depend on the frequency and incoming direction of the signal but also on the environment in which the antenna is operated. A calibration of the antenna response directly at the site of the experiment which incorporates realistic ground effects and potential influences of the radio detector station is thus preferred.

Major challenges of such calibration measurements in the MHz regime are to realize far field conditions and to minimize the influence of the measurement setup itself. In the following we introduce two alternative measurement setups which allow to determine the directional properties of MHz antennas in the far field region at the site of the experiment. Both setups are based on a calibrated signal source that is placed in the sky by either a helium balloon or a GPS-controlled drone, the octocopter. The setups enable a three dimensional measurement of the antenna radiation pattern including the vectorial phase information. That is, the complex vector effective length which gives a complete description of the antenna response is obtained.

It should be stated that so far, the directional properties of antennas for the detection of cosmic rays have been measured with down-scaled versions of the antenna under test [170] or were constrained to a measurement of the scalar power transfer without the vectorial phase information [171].

9.1 Baloon Setup

The principle of the measurement setup is to measure the signal transfer between a calibrated transmitting antenna and the Antenna Under Test (AUT) for various directions. The transmitting antenna is carried by a helium balloon and hold in position by a system of ropes according to Fig.9.1. Two ropes are arranged analog to a swing such that the movement of the transmitting antenna is restricted to a circular path lying in the YZ-plane with a radius of 30 m. A third rope is used to set the zenith angle by moving its anchorage point over the ground along the Y-axis. To account for irregularities in the planarity of the ground, a reference Y-axis was realized in the setup by spanning a horizontal rope.

When a vertical force induced by the balloon acts upon the system of ropes, the transmitting antenna is automatically aligned parallel to the AUT.

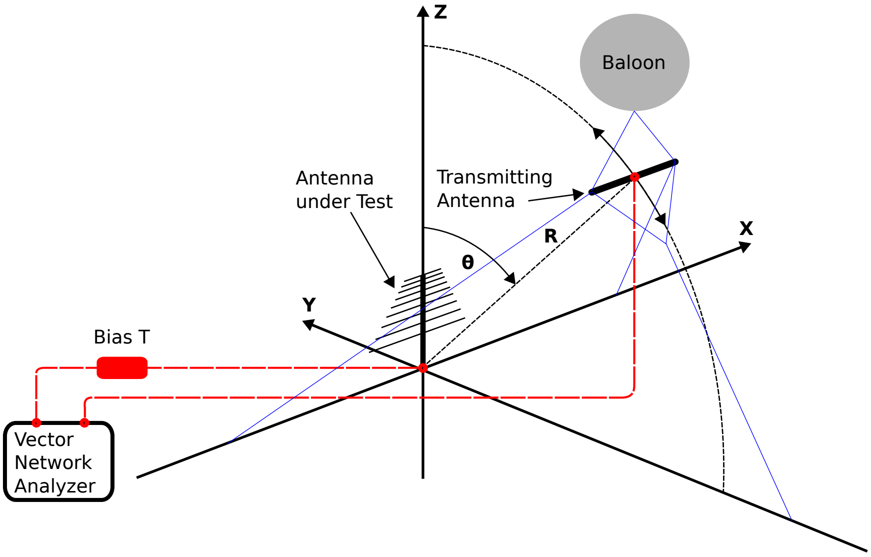

Figure 9.1: Schematic of the balloon calibration setup. Transmission lines are shown in red, the rope system to align the transmitting antenna in blue. An SBS antenna is depicted as AUT.

The used balloon, a conventional weather balloon filled with 5 m^2 of helium is shown in Fig. 9.2. Following the principle of Archimedes the static buoyancy of the helium balloon is given by the weight of the displaced air volume reduced by the weight of the balloon and the payload

$$F = g(m_{Air} - m_{Bal}) = g(\rho_{Air} V_{Bal} - \rho_{He} V_{Bal} - m_{Payload}) \tag{9.1}$$

The ratio of densities of helium and air is $\rho_{He}/\rho_{Air} = 0.138$, given that both gases are maintained at the same pressure and temperature [172, 173]. Thus we can write

$$F = g\rho_{Air} V_{Bal}(1 - 0.138) - g\, m_{Payload}. \tag{9.2}$$

According to the barometric formula [174], the air density at AERA at 1400 m above sea level is about $\rho_{Air}(1400\, m) \approx 1.05$ kg/m^3 (1.24 kg/m^3 at sea level). The buoyancy of the used 5 m^2 helium balloon itself is then $F \approx 44.3$ N. The balloon is thus able to lift about 4.5 kg.
The payload consisting of the transmitting antenna ($\approx$ 2.5 kg), a wooden rod used to attach the antenna to the ropes, the balloon hull and the signal cable has a total weight of about 3.2 kg. Hence, a vertical force of about 13 N lifts the transmitting antenna, sufficient to tension the system of ropes and to align the antenna stable.

The electrical measurement setup is as follows. A calibrated sinusoidal signal is generated by a Rhode&Schwarz FSH4 type [175] vector network analyzer and runs through a RG58 [176] type coaxial cable up to the transmitting antenna. The latter is a biconical antenna [177] by the manufacturer Schwarzbeck, especially designed for reference measurements. The antenna has a dipole like radiation pattern (cf. Fig. 7.3) with a constant gain in the main beam direction which is the plane perpendicular to

Figure 9.2: Photograph of the balloon calibration setup at the AERA site. The left photograph was taken during a calibration measurement of the SBS antenna with the balloon hoovering almost in the zenith of the detector station in the foreground. On the right a zoom to the balloon with the transmitting antenna is depicted.

the antenna axis. Its free space gain is calibrated including the reflection efficiency within a 50 Ω system, thus G^T_{abs} is given as a function of the frequency. The calibration data of the antenna is attached in appendix A.3.
The radiated signal is received by the AUT and runs through a readout coaxial cable towards the input of the VNA. As the antennas discussed in this thesis operate together with a dedicated LNA we include the LNA in the antenna calibration. A DC voltage to supply the LNA is coupled into the readout coaxial cable by a so called bias tee.
The influences of the cables and the bias tee (red components in Fig. 9.1) are removed prior to the measurement by a null calibration of the VNA. Thus the signal transmission measured in terms of the S21 parameter by the VNA only includes the characteristics of both antennas and the signal propagation in air.
The VNA allows to access the entire AERA frequency range in a single measurement by performing a predefined frequency sweep. Thereby, the time synchronization of output and input signal is done automatically.

For radio waves the helium balloon acts in good approximation as a free space media. Furthermore no conducting structures are introduced in the near field of the transmitting antenna. We can thus assume that the balloon setup has no influence on the calibrated characteristic of the transmitting antenna.

Due to the horizontal alignment of the transmitting antenna the emitted field is horizontally polarized, that is in e_ϕ direction. The setup depicted in Fig. 9.1 thus allows to measure the frequency and zenith dependency of $H_{a,\phi}$ of the AUT. The azimuth dependency can in principle be accessed by turning the AUT. However, for antenna structures which are contained in a single vertical plane as the case for the antennas discussed in this thesis, the azimuth dependency is given by the polarization mismatch (cf. Ch. 7.2) and follows a simple sinusodial pattern. This has already been confirmed in measurements for the SBS [162, 167].

9.2 Octocopter Setup

The octocopter setup was developed as an optimization of the balloon setup towards better practicability and to achieve a higher data output with lower measurement efforts. Although the balloon setup proved to be very successful (see next chapter) it suffered from its high sensitivity to wind. Due to the large wind load of the balloon, measurements can only be performed when it is completely windless which is rarely the case at AERA (cf. Fig. 8.18). Furthermore, for each desired measurement direction the balloon setup has to be adjusted. With the octocopter setup it is possible to access the entire zenith range in a single flight of about ten minutes. Thereby, the GPS-controlled positioning system of the octocopter allows to compensate even for intermediate wind speeds.

The principle of the octocopter measurement depicted in Fig. 9.3 is essentially the same as for the balloon setup. Instead of the balloon the transmitting antenna is lifted by the octocopter and aligned by its position control system instead of the system of ropes. The flight path of the octocopter is not necessarily circular as the distance to the AUT can be obtained from GPS position and elevation measurements of the octocopter at any time.

The transmission measurement between the transmitting antenna and the AUT is likewise performed with the FSH4 VNA. The output signal is fed through a lightweight LMR-100 type coaxial cable [178] into the transmitting antenna. To further reduce the payload of the octocopter, a weight optimized biconical transmitting antenna [179] has been custom made by the manufacturer Schwarzbeck. It is attached to the octocopter by a special support structure as depicted in Fig. 9.5.
As a consequence of the small size of the transmitting antenna, the absolute gain within the accessed frequency range is significantly lower than in case of the antenna used for the balloon setup (cf. appendix A.3). To achieve sufficient signal strengths at the AUT the signal from the VNA is amplified by a Minicircuits (Type ZFL-1000H+) amplifier [180]. The amplifier is directly attached to the octocopter to prevent high signal levels on the long coaxial cable running towards the ground.

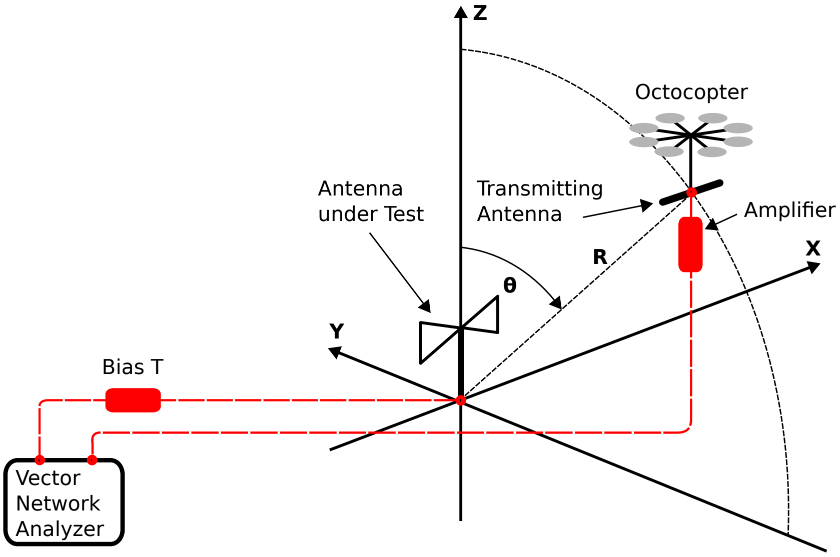

Figure 9.3: Schematic of the octocopter calibration setup. The cabled signal chain is shown in red. A Butterfly antenna is depicted as AUT.

The inevitable attenuation occuring along the cable and potential radiative losses (see next chapter) are reduced to a minimum by this configuration. The amplifier is powered by a custom voltage divider with a stabilized DC voltage from the octocopter battery.
As in case of the balloon setup, the influences of the cables, bias tee and the amplifier are removed from the transmission measurement by a null calibration of the VNA.

The octocopter was assembled from a construction kit developed by the German company HiSystems GmbH [181]. A photograph of the octocopter prepared for its most common application, the aerial photography, is shown in Fig. 9.4. It is propelled by eight electric motors mounted on aluminum beams. The beams are assembled with center plates from fiber composite composing a rigid frame.
The center plates hold the battery beneath, and on top, three modular electronics boards (see Fig.9.4 (right)). The power board features eight individual controllers for the three-phase brushless motors. The 'flight control' board holds various sensors, in particular 3 gyroscopes (one for each rotation axis) a three-axis acceleration sensor and a barometric altimeter. The data of all sensors is processed by the flight control to compute control commands for the eight motor controllers, based on the desired flight attitude. The latter is either a stable flight attitude, maintaining the optocopter in a hoovering position or a pilots command given by a radio control.
The 'navi control' board enhances the octocoper electronics with navigation capabilities by adding an electronic compass and an interface to a GPS module. The octocopter can thus determine its GPS position and alignment with respect to the earth's magnetic field at any time during the flight.
The navi control communicates via a separate wireless link to a computer on the ground. The pilot can predefine a flight path by setting GPS way points with a

Figure 9.4: Photograph of the 'Mikrocopter Okto XL' prepared for aerial photography. On the right picture the center with the electronics boards is shown. Photographs from [181].

special software. For each way point, the alignment of the octocopter, a standby time where the octocopter holds its position as well as a constant climb or sink rate can be set. The flight path can then be sent to the navi control board and activated by a command of the pilot. The octocopter will then autonomously perform the flight according to the flight plan.

Furthermore, the data sent by the navi control provides an important tool for the pilot to monitor certain flight parameters in real-time. Particularly important is to supervise position, alignment, altitude and remaining battery capacity to ensure a save and successful 'mission'.

All information gathered by the octocopter electronics during the flight is recorded on an micro SD card hold by the navi control board. The position data is then merged offline (see next section) with the transmission measurements obtained from the VNA to process the measured antenna characteristics.

The transmitting antenna is mounted on a rigid support structure of lightweight fiberglass compound tubing about 80 cm below the center plate (cf. Fig. 9.5). The installation at this distance from any conducting structures, in particular the aluminium beams of the frame, minimizes the influence on the gain of the transmitting antenna (see Sec. 9.4). To allow for a safe take-off and landing with attached transmitting antenna, the landing gear was replaced by a custom version from fiberglass tubing.

An important parameter for the development of the octocopter setup was the maximum payload of the octocopter. In test measurements a maximum payload of about 2 kg was determined to allow a save performance of calibration flights. All components attached to the octocopter were chosen to fulfill this criterion.

Figure 9.5: Photograph of the octocopter calibration setup at the AERA site with the octocopter hoovering in about 30 m height above an AERA phase 2 station equipped with a Butterfly antenna (left). On the right the octocopter with attached transmitting antenna and prepared with an additional differential GPS for test measurements at the LOFAR radio detector in the Netherlands is shown.

9.3 Data Processing

9.3.1 Measurement Equation

With the schematic of the measurement setup and recalling the antenna theory of Ch. 7 we can now derive the equation for the measurement of the VEL of the AUT. We first derive the relation of the VEL of the transmitting antenna to its realized gain.

The active power delivered by the VNA to the coaxial cable during the transmission measurement is

$$P_S = \frac{|V_S|^2}{2Z_{TL}}. \tag{9.3}$$

Only a fraction of P_S is available for the transmitter due to the impedance mismatch between the cable and the transmitter antenna. The available power P_T for the transmitter can be expressed with the voltage reflection coefficient Γ_T between the cable and the transmitter with

$$P_T = P_S(1 - |\Gamma_T|^2), \quad \Gamma_T = \frac{Z_{TL} - Z_A^T}{Z_{TL} + Z_A^T} \tag{9.4}$$

The active power consumed by the transmitting antenna in terms of the current developed in the antenna terminals is given by

$$P_T = \frac{|I_0^T|^2 Re(Z_A^T)}{2}. \tag{9.5}$$

Combining the above equations yields

$$|I_0^T|^2 Re(Z_A^T) = \frac{|V_S|^2}{Z_{TL}}(1 - |\Gamma_T|^2). \tag{9.6}$$

After multiplying with the squared VEL of the transmitter we obtain

$$\frac{|I_0^T|^2}{|V_S|^2}|H_k^T|^2 = \frac{(1 - |\Gamma_T|^2)}{Re(Z_A^T)Z_{TL}}|H_k^T|^2. \tag{9.7}$$

We write the relation between VEL and partial gain (Eq. 7.32) in terms of the transmitting antenna and insert in the above equation,

$$\frac{|I_0^T|^2}{|V_S|^2}|H_k^T|^2 = \frac{\lambda^2}{\pi Z_0 Z_{TL}}(1 - |\Gamma_T|^2)G^T = \frac{\lambda^2}{\pi Z_0 Z_{TL}}G_{abs}^T. \tag{9.8}$$

We can thus express the VEL of the transmitting antenna by its absolute gain. This step is necessary as only the gain is given by the manufacturer of the transmitting antennas. Note that in contrast to the VEL the gain does not include information on the phase shifting within the transmitting antenna. Such simplification is acceptable as the transmitting antennas are explicitly designed to introduce only minor distortions to the phasing due to an almost constant group delay. This has been verified in preceding test measurements of the transmitting antennas and will be demonstrated by simulations in a later section.

We now go back to the voltage based calculations to infer the characteristics of the AUT. The electric field E_k^T radiated by the transmitter antenna with current I_0^T in its terminals is given at a distance R from the antenna as [146]

$$E_k^T = \frac{-iZ_0}{2\lambda R} I_0^T H_k^T e^{\frac{-i\omega R}{c}}, \tag{9.9}$$

where H_k^T denotes the VEL of the transmitting antenna and λ the wavelength of the emitted plane wave. The radiated electric field induces a response voltage V_A in the receiving AUT which is obtained through the VEL of the receiving antenna $H_{a,k}$,

$$V_A = H_{a,k}E_k^T. \tag{9.10}$$

The VEL $H_{a,k}$ includes the antenna efficiency, all possible mismatch effects and the amplification of the antenna under test. We measure the response voltage in terms of the S21 parameter in relation to the voltage V_S delivered by the VNA,

$$S21 = \frac{V_A}{V_S} \tag{9.11}$$

Plugging Eq. 9.10 and Eq. 9.11 into Eq. 9.9 and rearranging yields

$$S21 = \frac{-iZ_0}{2\lambda R}\frac{I_0^T}{V_S}H_k^T H_{a,k} e^{\frac{-i\omega R}{c}}. \tag{9.12}$$

The above equation represents a voltage based form of the Friis Transmission Equation. In its most common form, as for instance given in [146], it relates the scalar power delivered to a receiver load to the input power of the transmitting antenna via the power gains of the antennas. The above equation gives the signal transfer in terms of the complex VEL and also includes the phase information.
After introducing Eq. 9.8 on the right hand side of the above equation, we obtain the measurement equation for our setup

$$H_{a,k} = iRS21\sqrt{\frac{4\pi Z_{TL}}{Z_0 G_{abs}^T}}e^{\frac{i\omega R}{c}}, \tag{9.13}$$

where we measure magnitude $|S21|$ and phase φ_{S21} of the S-parameter $S21$ and the distance R between the antennas for a certain direction of the transmitting antenna with respect to the AUT.
We can write the above equation separately for the magnitude and phase of the VEL

$$\begin{aligned} |H_{a,k}| &= R|S21|\sqrt{\frac{4\pi Z_{TL}}{Z_0 G_{abs}^T}}, \\ \varphi_{H_{a,k}} &= arg(H_{a,k}) = \varphi_{S21} + \frac{\omega R}{c} + \frac{\pi}{2}. \end{aligned} \tag{9.14}$$

We will express the phasing of the VEL by the group delay

$$\tau = -\frac{d\,\varphi_{H_{a,k}}}{d\,\omega} = -\frac{d\,\varphi_{S21}}{d\,\omega} - \frac{R}{c} \tag{9.15}$$

9.3.2 Data Merging

In case of the balloon setup, a certain zenith angle is accessed by setting the anchorage point of the third rope on the y-axis (cf. 9.1) to a corresponding distance from the AUT. This distance is measured with a laser rangefinder commonly used in construction industries with a precision of a few mm. The lengths of the remaining ropes as well as the distance of their anchorage points on the x-axis are measured likewise. From these information, the zenith angle of the transmitting antenna with respect to the AUT can be computed. For each adjusted zenith angle θ, a measurement of S21 is performed and $H_{a,\phi}(\theta)$ is computed from Eq. 9.13 with R=30 m.

In case of the octocopter setup, the zenith angle and distance to the AUT are obtained from the GPS position X_{OCT} and elevation above ground h measured by the octocopter. This information is written on the internal micro SD card each second together with a GPS time stamp. The GPS position of the AUT, X_{AUT} is measured by placing the octocopter at the position of the AUT for about 20 minutes and averaging the measured GPS coordinates. The distance R and zenith angle θ of the transmitting antenna to the AUT are then computed by

$$R = \sqrt{(X_{AUT} - X_{OCT})^2 + h^2}, \qquad \theta = 90° - arcsin(\frac{h}{R}). \tag{9.16}$$

In the above equation the height h is corrected for the difference between the reference point of the position measurement and the position of the transmitting antenna underneath the octocopter. Uncertainties of the position measurement are discussed in the next chapter.

The VNA is steered by a laptop computer during the octocopter measurement. For this purpose a software library enabling a remote control of the VNA has been developed which is documented in detail in [182]. Basically, a script running on the laptop starts a transmission measurement of the VNA each second and reads out the data to store it on hard disk together with a time stamp from the computer clock. The computer clock is synchronized with an internet clock prior to the measurement. By a comparison of the timestamps, the single transmission measurements can be assigned to the corresponding GPS position and therewith to a distance and zenith angle.

9.4 Measurement Uncertainties

9.4.1 Uncertainty of the Transmission Measurement

For both measurement setups, the dominating systematic uncertainties on the measurement of the VEL are given by the uncertainty of the transmitted signal. These are due to the calibration of the transmitting antenna and the measurement uncertainty of the VNA.

The absolute gain G^T_{abs} of the biconical antenna used for the balloon setup is given by the manufacturer with a 2σ uncertainty of 0.7 dB [177]. In case of the small biconical antenna used for the octocopter setup, the 2σ calibration uncertainty is 1.0 dB [179]. As these uncertainties are normally distributed [183] we assume 1σ uncertainties of 0.35 dB and 0.5 dB respectively. Both uncertainties are given independent of the frequency.

The systematic uncertainty of the VNA for the measured magnitude of the transmission $|S21|$ increases with decreasing signal level [175]. For the signal levels realized in our measurement setups the uncertainty is smaller than 0.6 dB.

The phase of S21 is measured with a systematic uncertainty smaller than 3° [175] within the accessed frequency range. As we evaluate the phasing of the signals in terms of the group delay (cf. eq. 9.15), a systematic phase offset is not relevant. We will determine the uncertainty on the group delay by its variation observed in multiple measurements.

9.4.2 Uncertainty on Position Measurements

A position uncertainty of the transmitting antenna introduces an uncertainty on the measured magnitude and phase of the VEL through the distance R between transmitter and AUT (see Eq. 9.13).

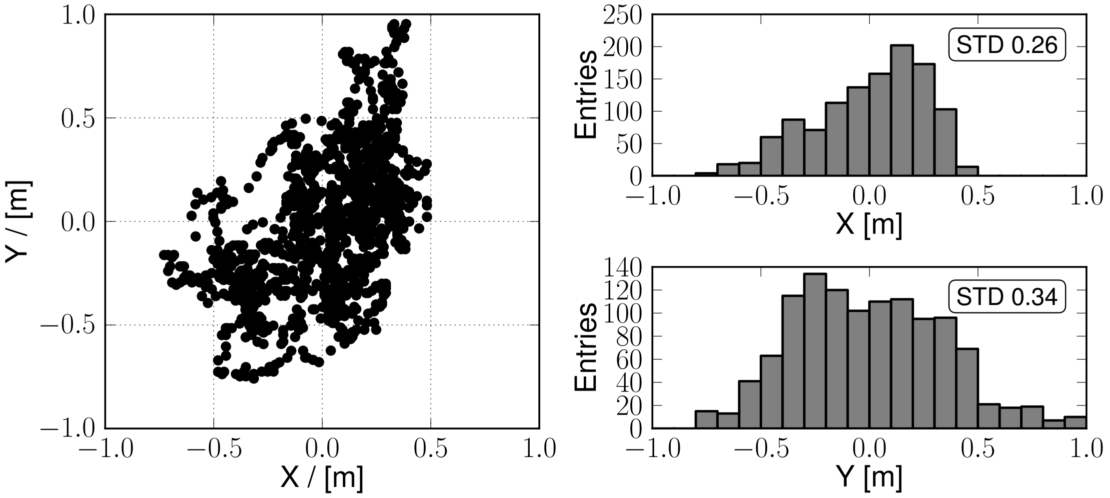

Figure 9.6: Uncertainty of the octocopter GPS position measurement. The left figure shows the distribution of the GPS positions measured every second over about 20 minutes with the octocopter maintained at the same position on the ground. On the right, histograms of the x and y coordinates are plotted.

For the balloon setup, the position of the transmitting antenna is determined by the lengths of the ropes fixing the antenna which are measured with a precision of a few mm. A potential elastic elongation of the ropes due to the acting forces was determined to be less than 10 cm in preceding measurements. We can thus conservatively assume an uncertainty of $\Delta R = 10$ cm on the distance between the transmitter and the AUT. Looking at the measurement equation (Eq. 9.14), a variation of $\Delta R = 10$ cm would cause a variation of the magnitude of the VEL of about 0.3 % for $R = 30$ m which is negligible compared to the variation caused by the uncertainty of the transmitted signal. From Eq. 9.15 we conclude that an uncertainty on the group delay smaller than 0.4 ns is introduced for $R = 30$ m and $\Delta R = 10$ cm.

In case of the octocopter setup we can estimate the position uncertainty by a continuous measurement with the octocopter maintained at the same position. Such a measurement performed over 20 minutes at AERA is depicted in Fig. 9.6.
The maximum deviation of a single measured GPS position from its mean value is smaller than 1 m. The standard deviation of the distribution is 0.26 m in x-direction and 0.34 m in y-direction.
Besides the GPS position, the octocopter measures its elevation above ground and its three dimensional alignment with internal sensors. These information, as likewise recorded during the 20 minutes measurement on the ground, are summarized in Fig. 9.7.
The elevation which is initially set to zero, mostly maintains this value throughout the measurement. Besides, a relatively broad distribution extending up to 1.5 m is observed which can be attributed to a change of the air pressure during the measurement. During multiple measurements deviations up to 2 m have been observed

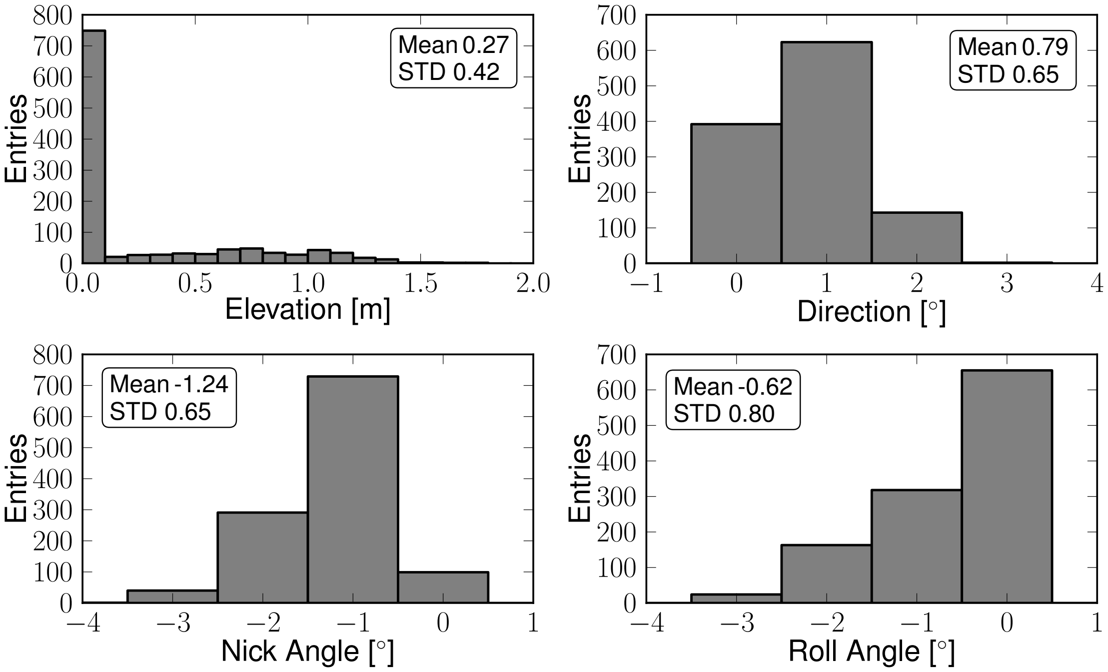

Figure 9.7: Uncertainty of the octocopter elevation and alignment measurement. During the continuous measurement over 20 minutes the octocopter is maintained at the same position on the ground. See text for details.

which we take as the uncertainty on the elevation.
These uncertainties on the position and the elevation are propagated to the VEL for each accessed position of the octocopter individually.

Although the octocopter is symmetric with respect to the vertical axis it has a dedicated front direction which is indicated by the red aluminum beam visible in Fig. 9.4. With respect to the front direction, the roll angle denotes the rotation around the longitudinal axis while the nick angle defines the rotation around the lateral axis. Together with the compass direction giving the rotation around the vertical axis, the alignment of the octocopter is completely determined.
With the start of the measurement all angles are calibrated to zero. Throughout the measurement the angles deviate less than 2° - 3° as visible in Fig. 9.7. The octocopter maintains its alignment during the flight based on the measurement of these angles. Thus, comparable small deviations of the alignment of the transmitting antenna with respect to the AUT occur during the calibration measurement. The impact of a misaligned transmitting antenna on the calibration measurement is discussed in a following section.

9.4.3 Influence of the Octocopter on the Transmitter Gain

Any conducting structure in the proximity of an antenna influences its characteristics. To estimate the influence of the octocopter, in particular its aluminum frame,

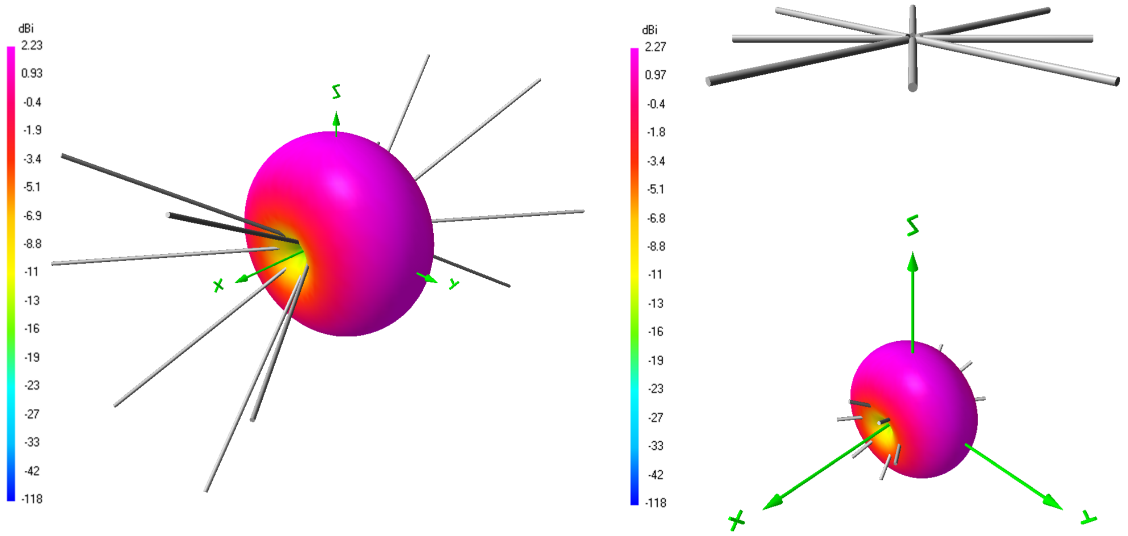

Figure 9.8: Simulation model of the small biconical antenna (left) and the antenna together with the frame of the octocopter (right). The simulated gain pattern is shown centered around the antenna.

on the small biconical transmitting antenna, the setup was modeled in NEC2.
The simulation model of the biconical antenna is depicted in Fig. 9.8 (left) together with the gain delivered by NEC2 at a frequency of 55 MHz. In comparison to the simulation of a simple half-wave dipole (cf. Fig. 7.3) we observe a very similar symmetric gain pattern. The maximum gain of 2.23 dBi is very close to the gain of a lossless thin half-wave dipole of 2.15 dBi [184].
With the simulated antenna input impedance we can compute the absolute gain realized in a 50 Ω- system using Eq. 7.13. The absolute gain in the main beam direction (plane perpendicular to the antenna axis) is shown in Fig. 9.9 as a function of the frequency. The absolute gain is strongly reduced with respect to the gain due to the mismatch of the antenna impedance at the given frequencies. Furthermore we observe a remarkably good agreement with the calibration data of the manufacturer which gives confidence in the developed antenna model.

The octocopter frame is now modeled and placed below the model of the biconical antenna in a distance of 80 cm (cf. Fig. 9.8 (right)). The simulated absolute gain in the main beam direction for $\theta = 90°$ is compared in Fig. 9.10 to the absolute gain of the biconical antenna only. The curves lie almost on top of each other indicating that the influence of the octocopter for this specific direction is minimal. To allow a quantitative statement for all relevant directions and frequencies, a scan was performed covering the entire zenith range in 1° steps and the AERA frequency range in 1 MHz steps. This results in 360 x 50 simulated gain values for both simulated scenarios. The difference of the absolute gain values with and without the octocopter frame are filled into the histogram shown in Fig. 9.10 (right). The maximum deviations in gain due to the influence of the octocopter are about 0.1 dB, for most

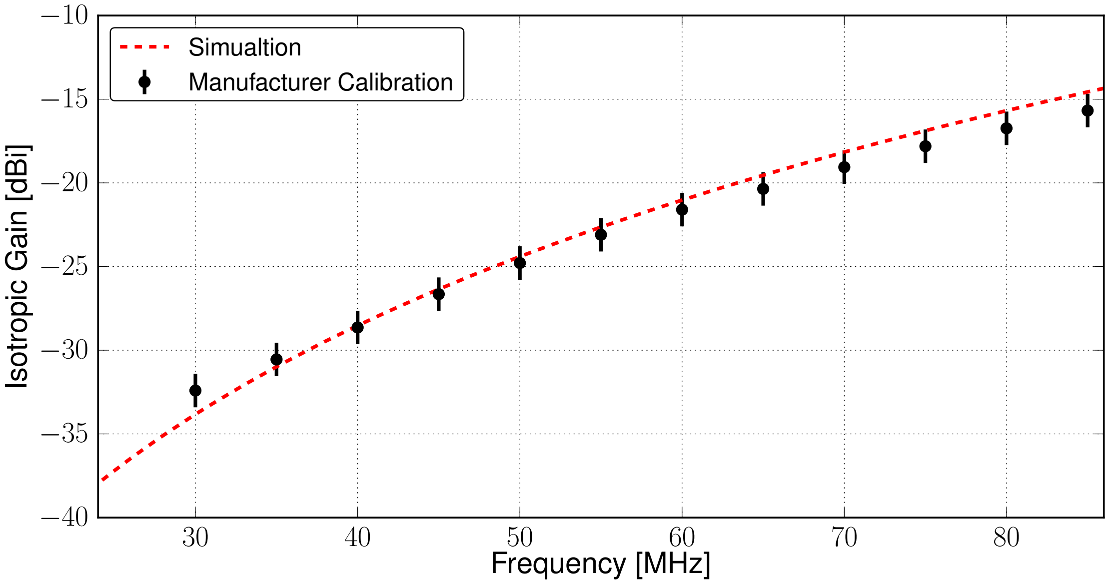

Figure 9.9: Absolute gain of the small biconical antenna simulated in the main beam direction. The manufacturer calibration data is shown for comparison.

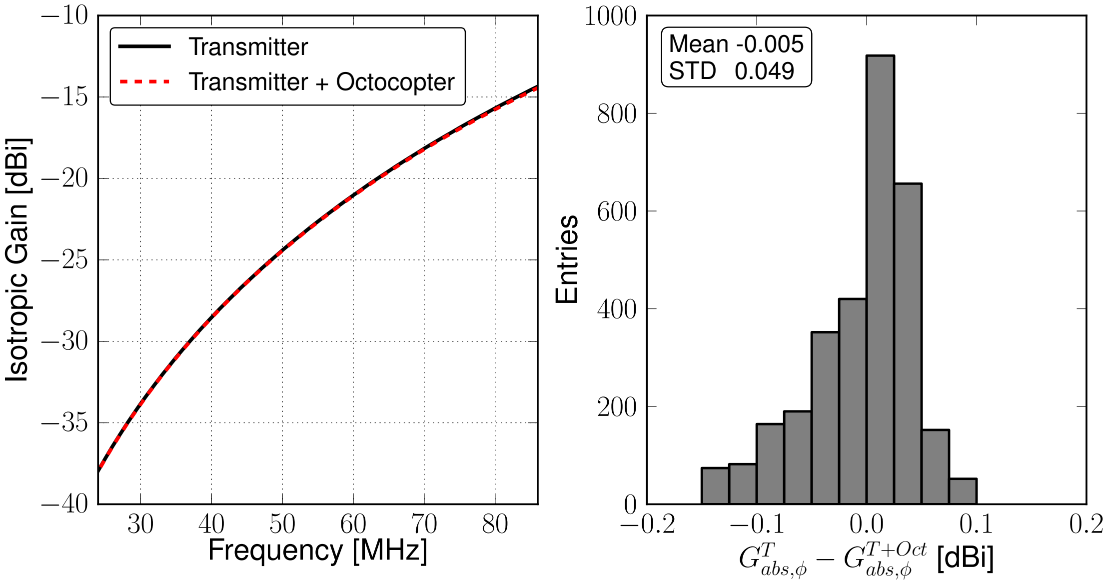

Figure 9.10: Influence of the octocopter on the absolute gain of the biconical transmitting antenna. The gains in the main beam direction for $\theta = 90°$ are compared in the left figure. On the right the gain differences over the AERA bandwidth and the full zenith range are histogrammed. See text for details.

frequencies and directions much lower. Compared to the calibration uncertainty of 1.0 dB of the biconical antenna we can thus neglect these influences.

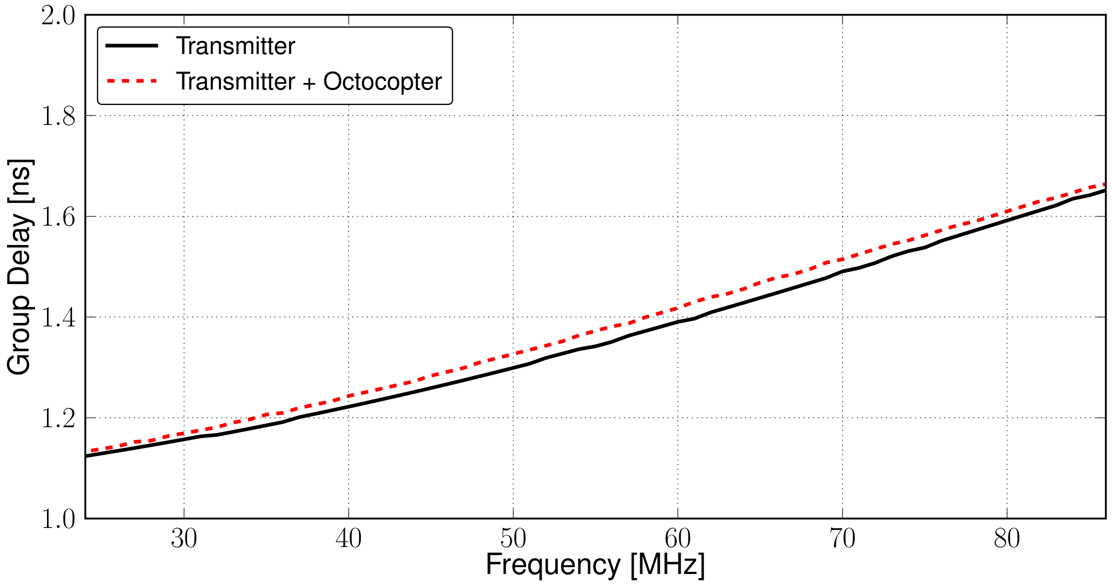

Figure 9.11: Influence of the octocopter on the group delay of the biconical transmitting antenna simulated in the main beam direction for $\theta = 90°$.

We can inspect a potential influence of the octocopter frame on the phasing of the transmitted signal by simulating the group delay for both scenarios. Fig. 9.11 indicates that the group delay introduced by the transmitting antenna is in the order of 1 ns only and almost constant over the AERA bandwidth. We will find later that for the AUT the group delay and its variation over the bandwidth is at least one order of magnitude larger. This justifies the simplification made in the measurement equation (cf. Sec. 9.3.1) where the group delay of the transmitting antenna is not considered.

Furthermore, the comparison shows that the influence of the octocopter frame on the group delay is minimal.

Besides the influence of the octocopter on the transmitter gain it is conceivable that the electronics of the octocopter or its radio control system emit transient radio signals that would disturb calibration measurements. We have performed dedicated test measurements during the operation of the octocopter by monitoring the radio noise in both the time and frequency domain. No indication of radio signals of neither transient nor of continuous nature emitted by the octocopter could be found in the relevant frequency range.

9.4.4 Influence of Octocopter Misalignment

Uncertainties of the octocopter alignment, and therewith the transmitter alignment, and uncertainties of the octocopter position can influence the transmitted signal. The effect of a misaligned octocopter to the measurement setup is illustrated in Fig. 9.12 (left) while the effect of an octocopter deviating by a distance s from its reference position is depicted in the middle figure. The consequence of both effects

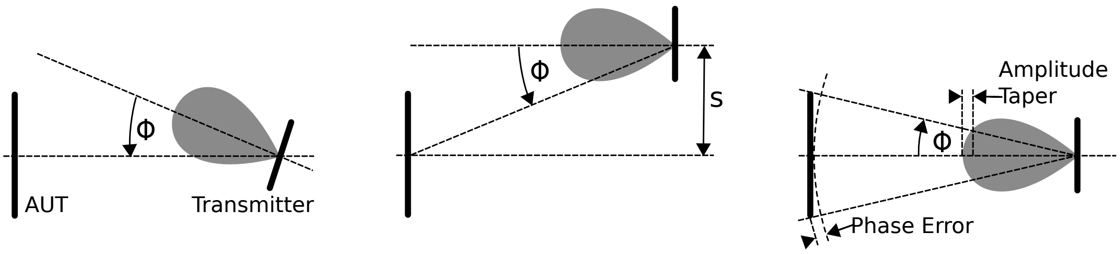

Figure 9.12: Effect of a misaligned (left) and shifted (middle) transmitting antenna on the measurement setup. On the right, measurement errors caused by a spherical wave front are illustrated.

is that the calibrated main beam of the transmitting antenna is not pointing exactly towards the AUT anymore. The transmitted signal then depends on the transmitter gain in the direction of the azimuth angle θ.

The azimuthal dependence of the absolute gain of the small biconical antenna is shown in Fig. 9.13 at 55 MHz. The shape of the pattern is essentially the same over the entire AERA bandwidth. When looking at the main beam direction around 90° we find that the gain varies less than 0.1 dB for deviations smaller than about 8° in azimuth. Keeping in mind the uncertainty of the octocopter alignment and position measurement, such deviations are very unlikely at a measurement distance of 30 m.

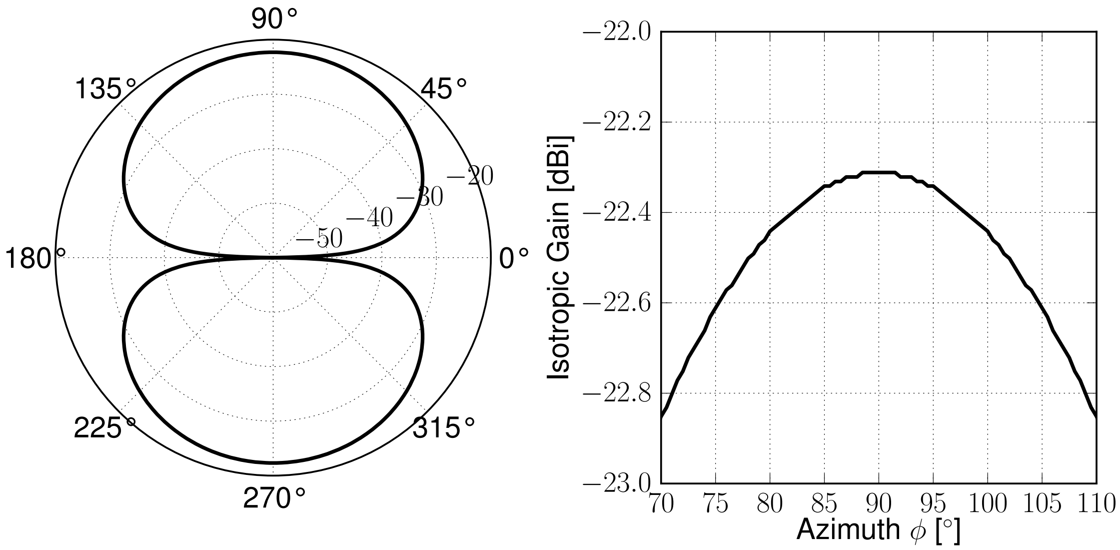

Figure 9.13: Simulated azimuthal dependence of the absolute gain of the biconical transmitter. The right figure shows a zoom in the main beam direction.

9.4.5 Far Field Approximation

Various definitions of the of the distance R from the antenna where the far field region (cf. Ch. 7) begins are discussed in literature. The most common one is that the far-field is taken to exist at distances greater than

$$R = 2\,D^2/\,\lambda, \tag{9.17}$$

with the largest dimension D of the antenna structure and λ, the emitted wavelength [145, 146]. This definition is generally only valid if D is large compared to the wavelength (D>λ), which is typically the case for instance for dish antennas. For the antennas discussed in this thesis, the wavelength is in the same order of magnitude as the antenna dimension and the condition is thus not fulfilled.
In Ref. [185] further criteria are added to the above far-field condition to extend the definition towards antennas of intermediate size such as half-wave dipoles

$$(1)\ R > 2\,D^2/\,\lambda, \qquad (2)\ R > 5\,D, \qquad (3)\ R > 1.6\,\lambda. \tag{9.18}$$

Far-field conditions can be assumed if all of the above criteria are fulfilled. For the SBS and Butterfly antenna respectively, the minimum far-field distances according to the above conditions are summarized in the table below.

Condition	SBS (D=4.25 m)	Butterfly (D=2.28 m)
$R = 2\,D^2/\,\lambda$ (80 MHz)	9.76 m	2.81 m
$R = 5\,D$	21.25 m	11.38 m
$R = 1.6\,\lambda$ (30 MHz)	15.99 m	15.99 m

Following a conservative approach we realize measurement distances between 30 m and 50 m in our calibration setup which is safely in the far-field over the entire AERA frequency range.

In the far-field region, the emitted radiation can be treated as a spherical wave. In the scope of a measurement setup the spherical wave front emitted by the transmitter causes a phase error between the center of the AUT and its edges. Based on the geometry in Fig. 9.12 (right), the phase error can be calculated as [186]

$$\Delta\phi \approx \frac{\pi\,D^2}{4\,\lambda\,R} \tag{9.19}$$

Demanding that the phase error is smaller than $\pi/8$ which corresponds to 22.5° leads to the far field condition of Eq. 9.17, also called Rayleigh distance. A phase error of 22.5° typically yields acceptable uncertainties in antenna measurements [184].
For our measurement setup with a distance of 30 m the maximum phase error at 80 MHz according to the above equation is smaller than 7.3° for the SBS and smaller than 2.1° the Butterfly antenna and thus well within the common standards.

From Fig. 9.12 (right) we identify another common source of uncertainties in antenna measurements, referred to as amplitude taper. Due to the source antenna pattern, the field amplitudes are slightly larger in the center of the AUT than at its edges. The AUT is illuminated by the transmitter by a cone of opening angle 2α with $sin(\alpha) = D/(2R)$, which gives $\alpha = 4.1°$ for the SBS and $\alpha = 2.2°$ in case of the Butterfly antenna. Looking at the gain pattern of our transmitting antenna (see Fig.9.13) we find an amplitude taper below 0.03 dB for $\alpha < 5°$. Even an amplitude taper of 0.25 dB typically causes uncertainties below 0.1 dB in the measured gain [186]. This effect is thus negligible for our setup.

10. Calibration of the Radio Detector Stations of AERA

In this chapter we present the results of the calibration measurements of the SBS antenna and the Butterfly antenna station performed at AERA. The corresponding simulation models are introduced to allow for direct comparisons with the measurements. Furthermore, we discuss calibration measurements of the Butterfly antenna performed at the RWTH-Aachen university using a modified octocopter setup.

10.1 Small Black Spider LPDA

The measurement campaign to calibrate the SBS was carried out in 2010 in the scope of the deployment of the first phase of AERA. An SBS was installed at one of the AERA triple stations (see. Fig. 6.1) with its lowest dipole having a height of 3 m above ground. At the time of the measurement no station components, except the pole and the fence, were installed yet. The measurement thus contains a realistic ground scenario but does not include a potential influence of the AERA phase 1 station components.

It should be stated that the influence of conducting station components to the antenna characteristics is expected to be very low in case of the SBS. The LPDA principle introduces a strong directivity towards the upper hemisphere and makes the antenna essentially insensitive to directions from the ground. A radiative coupling to any conducting station components below the antenna is thus suppressed.

10.1.1 Simulation Model of the Small Black Spider LPDA

The antenna model of the SBS depicted in Fig. 10.1 consists of all active elements of the SBS, the eight wire dipoles, the lower aluminum dipole and the waveguide corresponding to their exact dimensions. The waveguide is implemented as an assembly of non-radiating crossed transmission lines. In case of the real SBS, the waveguide is electrically shielded by the central tube which to a large extend corresponds to the simulated situation.

The SBS model is placed above a ground plane of infinite extension at a height corresponding to the measurement. The ground parameters are adjusted to the values discussed in Ch. 7.7.2). The structure is excited with a current source and the radiated far field is simulated over the AERA frequency range. The amplified vector effective length is processed as described in Ch. 7.7.3 based on the measured characteristics of the SBS LNA introduced in Ch. 8.2.2.

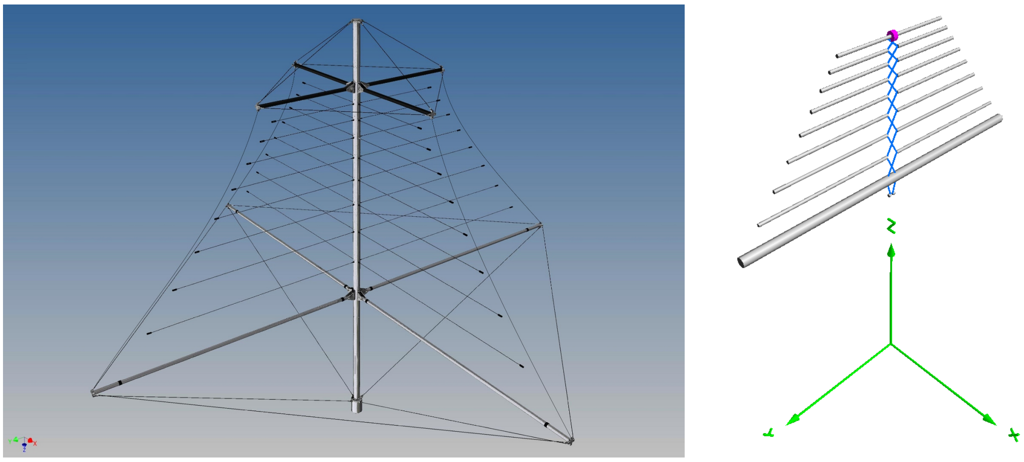

Figure 10.1: Simulation model (right) of the SBS designed following the dimensions of the corresponding CAD model (left). Transmission lines are blue and the current source is depicted as the pink dot.

10.1.2 Calibration Measurements

The calibration of the SBS was performed using the balloon setup, adjusted to access the H_ϕ- component of the VEL in the south direction of the AERA station. In the coordinate system of Fig. 9.1 this corresponds to an azimuth angle of $\phi = 270°$ with the negative x-axis pointing to the south. The antenna plane aligned in east-west direction is read out. Due to the symmetry of the SBS, the response characteristics obtained at $\phi = 270°$ are identical to those at $\phi = 90°$ and $\phi = 0°, \phi = 180°$ respectively, if the antenna plane in north-south direction is read out.
The setup was adjusted to access 31 zenith angles covering the range from 0° to 90°. For each zenith angle the transmission was measured thirty times in consecutive frequency sweeps ranging from 20 MHz to 90 MHz. Exemplary, the magnitude of the thirty transmission measurements obtained at a zenith angle of $\theta = 30.6°$ is depicted in Fig. 10.2. The variations between the different sweeps are very small indicating an excellent reproducibility. For further analysis, the mean value of the transmission in each frequency bin is used. The standard deviation in each frequency bin (see. Fig. 10.2 (right)) represents the statistical uncertainty of the transmission measurement and is below 0.05 dB over the AERA frequency range. The statistical uncertainty of the phase of the transmission is determined in an analogous manner.

The frequency dependence of the magnitude of the VEL $|H_\phi(\theta = 270°)|$ is depicted in Fig. 10.3 for two different zenith angles, $\theta = 0°$ and $\theta = 45°$. Beyond the AERA frequency range from 30 MHz to 80 MHz, the VEL steeply decreases towards zero as the reception is suppressed by both, the antenna characteristics and the filter elements of the LNA. Within the AERA band, the VEL decreases with increasing frequency. Given a gain approximately independent of the frequency which is typically the case for LPDAs towards the main beam direction [146], such a constant decrease of the VEL is expected when looking at Eq. 7.32. For $\theta = 45°$ a steeper decrease from 30 MHz to 50 MHz is observed followed by an almost constant response.

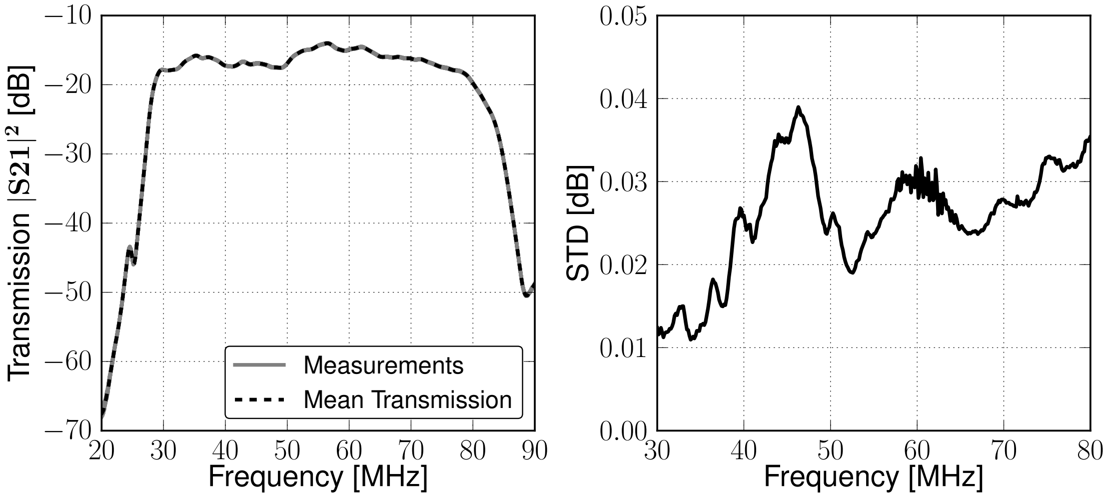

Figure 10.2: Magnitude of the transmission (left) between the transmitting antenna and the SBS as measured with the balloon setup at a zenith angle of $\theta = 30.6°$. The figure contains thirty frequency sweeps plotted on top of each other. The mean transmission is denoted as dashed curve. On the right, the standard deviation of the thirty curves in each frequency bin within the AERA band is shown.

Ripples in the frequency dependence are a consequence of the resonance behavior of the different dipoles as discussed in Ch. 8.2.2.
Both, the magnitude and the functional dependence are in fair agreement with the corresponding simulations.

The measured phasing of the VEL expressed as group delay is depicted in Fig. 10.4. The group delay and its frequency dependence is caused by the circuits of the LNA, in particular the integrated bandpass filter, and by the antenna structure itself. With increasing frequency the radio signals are mainly received by the shorter dipoles of the LPDA which are located closer to the footpoint (cf. Fig. 8.2) at the top of the antenna. This leads to a decreasing propagation time of the signals within the antenna structure and thus a decreasing group delay with increasing frequency.
While a constant group delay has no impact on the pulse shape of a broad band radio pulse, the change of the group delay over the AERA frequency range leads to a dispersion of the pulse. A variation of the group delay of about 50 ns is observed within the AERA band. The resulting dispersion is corrected for in the reconstruction of the electric field.
The simulations predict a similar magnitude and overall decrease of the group delay compared to the measurements. In detail, deviations of up to about 30% are visible in the frequency range from 30 MHz to about 50 MHz.

The zenith dependencies of the magnitude of the VEL and the group delay are depicted in Fig. 10.5 for three frequencies within the AERA band. At low frequencies a broad coverage of the sky with a maximum response at about $\theta = 45°$ is observed.

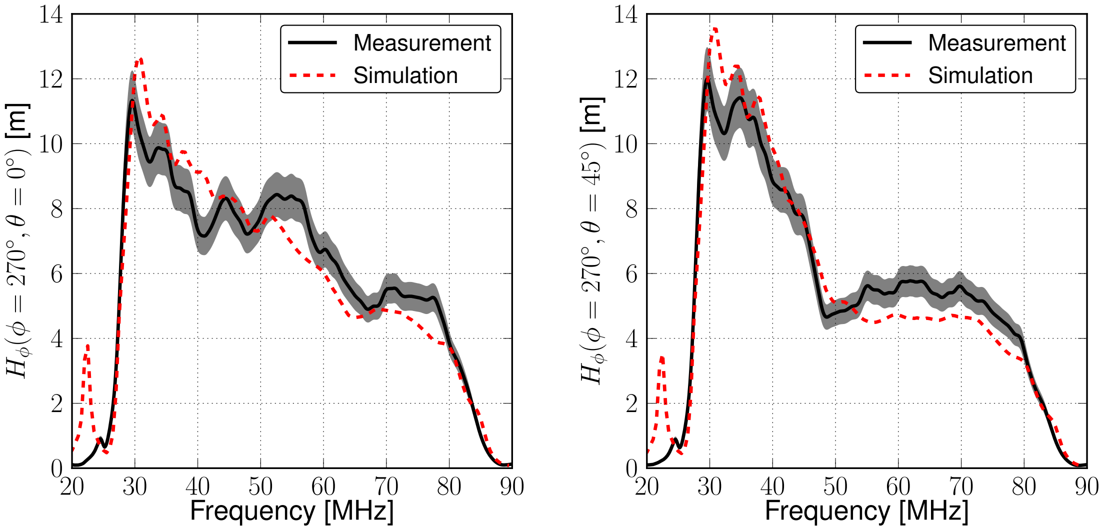

Figure 10.3: Magnitude of the VEL of the SBS for $\theta = 0°$ and $\theta = 45°$ as a function of the frequency. The gray band indicates the systematic uncertainties (see. Ch. 9.4). The statistical uncertainties obtained from multiple measurements (cf. Fig. 10.2) are smaller than the line width.

With higher frequency a side lobe pattern evolves. The position of the side lobe shifts to lower zenith angles with increasing frequencies and a second side lobe appears at the highest frequencies. The lobes are mainly caused by constructive and destructive interference of the direct impinging monochromatic wave and the wave

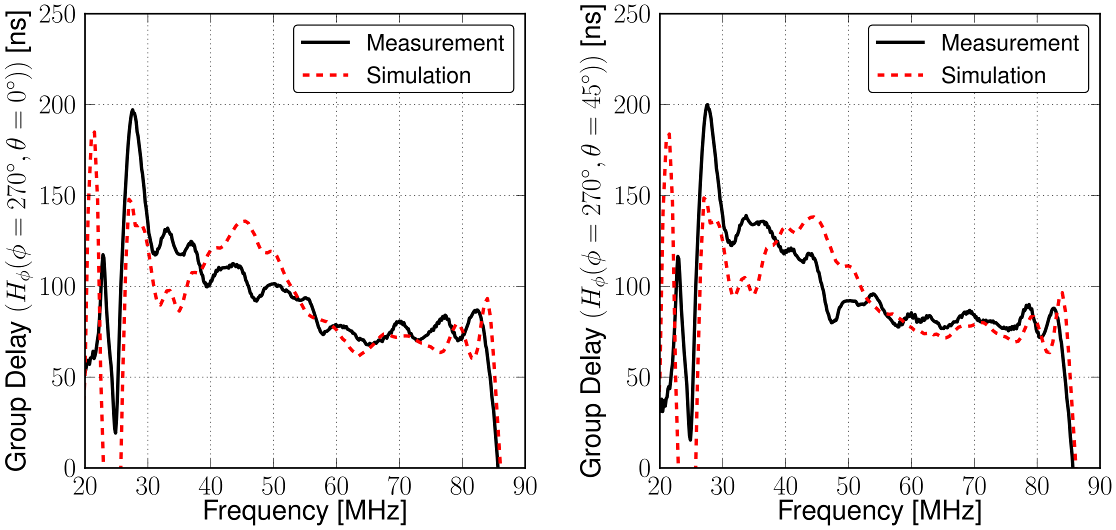

Figure 10.4: Group delay of the SBS for zenith angles of $\theta = 0°$ and $\theta = 45°$ as a function of the frequency. Systematic uncertainties are smaller than 0.4 ns (see. Ch. 9.4). Statistical uncertainties observed in multiple measurements are smaller than 1.3 ns.

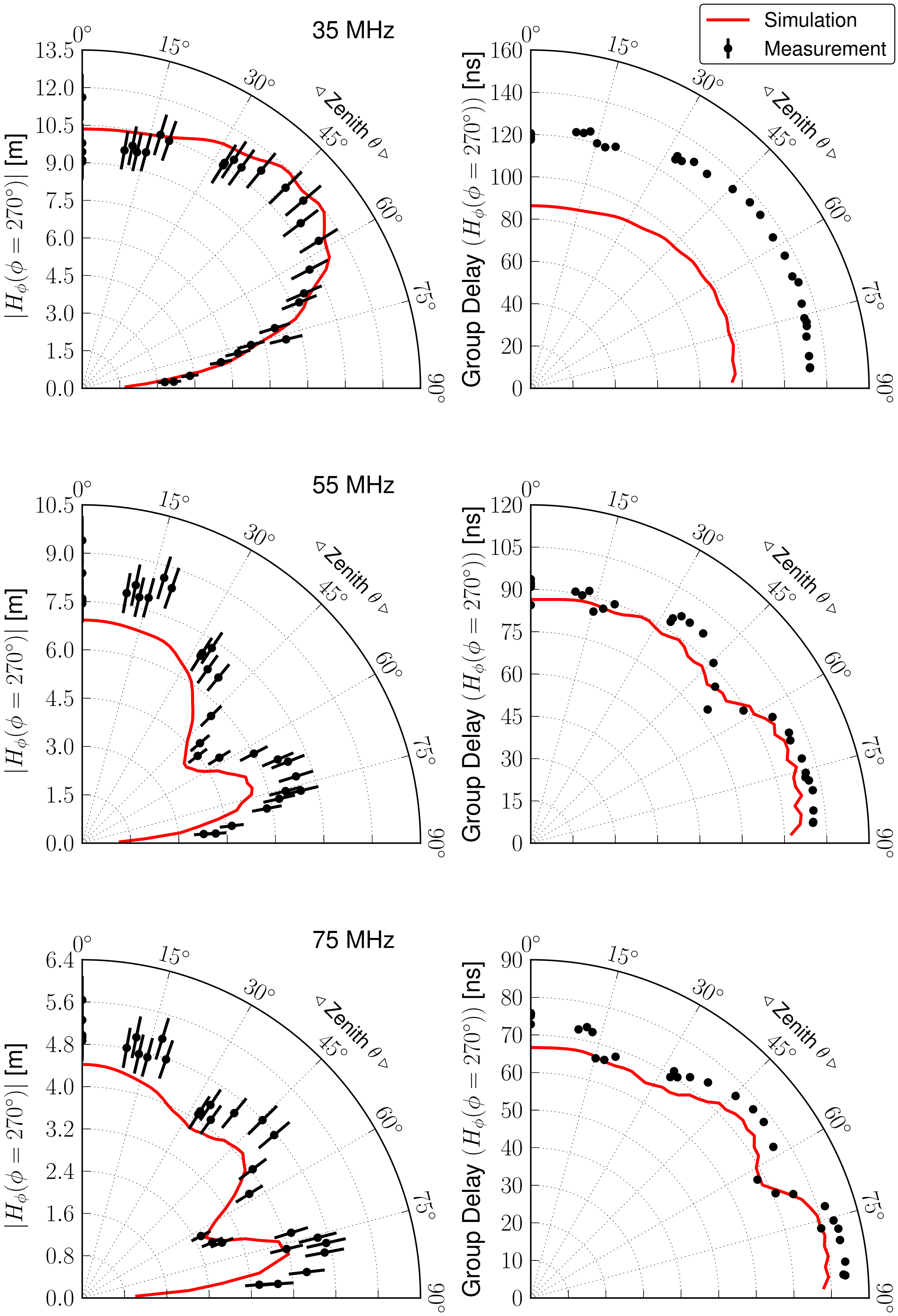

Figure 10.5: Zenith dependencies of the magnitude of the VEL (left) and the group delay (right) of the SBS for 35 MHz, 55 MHz and 75 MHz. The uncertainties correspond to those of Fig. 10.3 and Fig. 10.4.

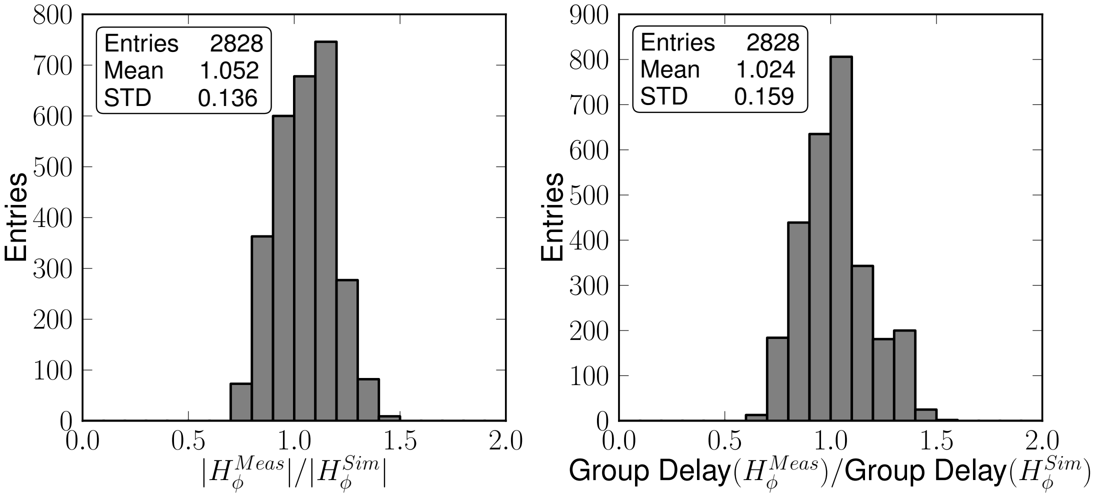

Figure 10.6: Comparison of measurement and simulation for the magnitude of the VEL (left) and the group delay (right) of the SBS. See text for details.

reflected on the ground at the position of the antenna placed in a certain height above ground (see. Ch. 7.7.2).
A remarkably good agreement of the shape of the zenith patterns is observed between measurements and simulations. When comparing the absolute scales of the patterns, offsets occur at certain frequencies, for instance at 35 MHz in the case of the group delay (cf. also Fig. 10.4).
The group delay exhibits similar but less distinct side lobe patterns as in the case of the magnitude of the VEL which is observed in both, measurements and simulations.

To further quantify the agreement between measurement and simulation, the ratio of the measured and the simulated values in a zenith range from 0° to 80° has been computed in 0.5 MHz steps from 30 MHz to 80 MHz. The resulting 2828 ratios for the magnitude of the VEL and the group delay are summarized with the histograms of Fig. 10.6. Regarding the magnitude of the VEL, the mean of the histogram indicates an overall agreement, that is in average over all frequencies and zenith angles, of about 5% between measurement and simulation. We conclude that the simulation, in average, slightly underestimates the antenna response. For certain frequencies and zenith angles, the simulations deviate up to 50% from the measurements. The standard deviation of the distribution is about 14%.
Concerning the group delay, the overall agreement between measurement and simulation amounts to about 2.5% with a standard deviation of about 16%.

10.2 Butterfly Antenna Station

In contrast to the SBS, the Butterfly antenna is a priory equally sensitive to the sky and to the ground. The directivity towards the upper hemisphere is explicitly introduced by placing the antenna in a short distance above the ground plane. A

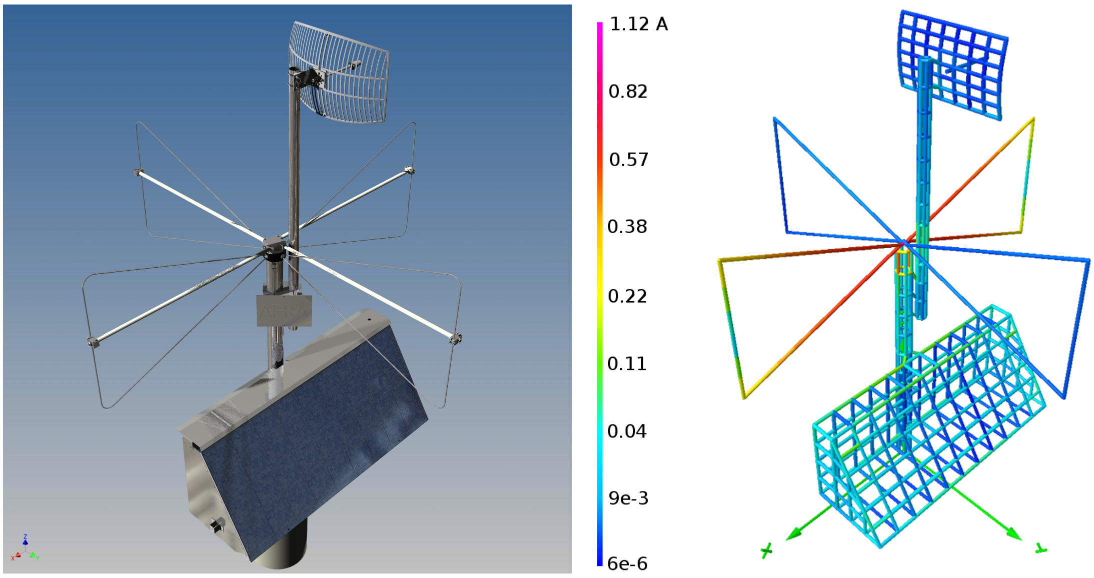

Figure 10.7: Simulation model (right) of the AERA phase 2 station in comparison the the CAD model (left). The color scale indicates the magnitude of the currents simulated at a frequency of 55 MHz.

consequence is that the Butterfly antenna is more sensitive to the ground conditions and to any conducting components placed below the antenna. It is thus necessary to treat the antenna together with the station as a whole. Consequently, the calibration measurements were performed using a 'dummy station', assembled of the relevant mechanical parts such as the electronics box and the antenna poles.

10.2.1 Simulation Model of the Butterfy Antenna Station

The corresponding simulation model (Fig. 10.7) is directly derived from the CAD model of the AERA phase 2 station. The only 'active' element is one of the two polarization planes of the butterfly radiator which is excited by a current source in the center. Any other station components are electrically isolated as in case of the real butterfly antenna station but can couple radiatively to the fields generated by the active radiator. All conducting station components are approximated by wire grids with a segmentation and mesh size following the modeling guidelines of NEC2 (cf. Ch. 7.7.1). The ground conditions for the simulation are equal to those used for the SBS simulations.

The radiative coupling of the station components to the active radiator can already be studied by looking at the simulated current distribution within the simulation model(cf. Fig. 10.7). The radiator itself shows a standing wave current distribution with a maximum in the center and knots at the dipole radiator ends. Moreover, currents are induced particularly in the antenna poles close to the radiator and the electronics box. These parasitic currents influence the radiation characteristics of the butterfly antenna depending on the frequency and incoming direction.

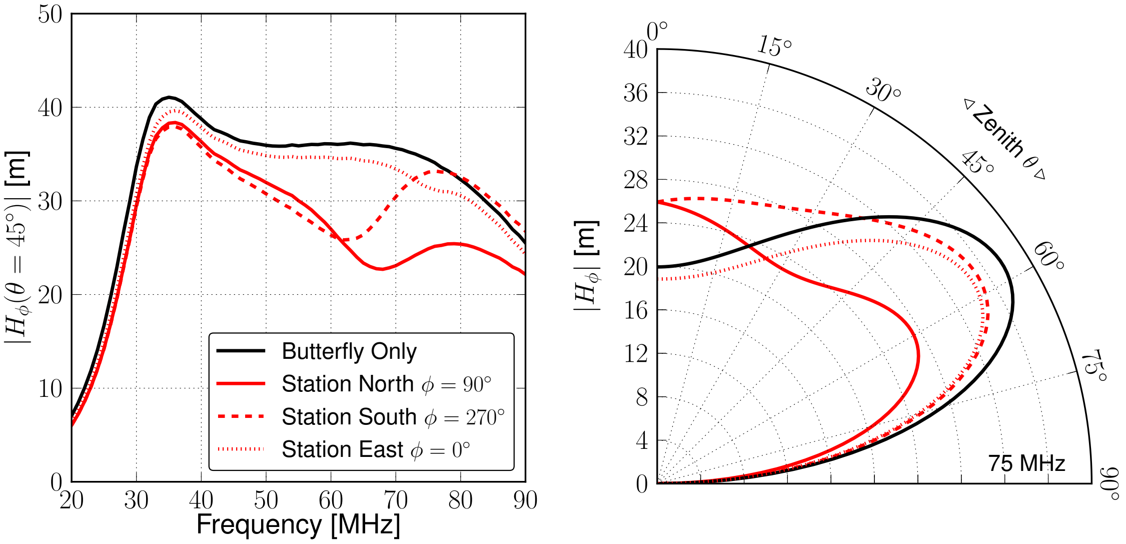

Figure 10.8: Impact of the station components to the frequency dependence (left) and the zenith pattern (right) of the butterfly antenna station. The black curve represents the simulation of the single butterfly radiator without any station components present in the simulation model. The red curves show the corresponding simulations performed with the full model of the AERA phase 2 station for three different azimuth angles. The response in west direction is almost identical to the one in east direction and is thus not plotted.

The impact of the station components becomes evident when comparing the antenna characteristics obtained from the above simulation model with those of the butterfly radiator only, without any station components. The frequency dependence of $|H_\phi|$ of the antenna station is summarized in Fig. 10.8 (left) for three different azimuth angles corresponding to the north, south and east direction in comparison to the simulation of the butterfly radiator only. The response of the latter is equal for all of the four cardinal points due to the symmetry of the butterfly antenna.

This symmetry is broken mainly due to the asymmetric placement of the electronics box with respect to the butterfly antenna. The effect is most distinct for e_ϕ-polarized waves impinging from north or south directions. Their electric field vector is aligned parallel to the electronics box allowing a maximum power transfer due to the induction of currents in the box. The electronics box consequently becomes a resonant antenna for frequencies matching approximately its length and interferes with the butterfly radiator. This causes the drop in sensitivity for the butterfly antenna around 65 MHz. For waves impinging from east or west, the resonance of the electronics box is at higher frequencies beyond the AERA band and the response of the station remains close to the one of the single butterfly radiator. The response for east and west directions is almost equal as the station is symmetric with respect to the north-south axis, except the placement of the comms-antenna pole slightly off the antenna center (cf. Fig. 10.7).

Similar considerations explain the deformation of the zenith patterns due to the inclusion of the station components depicted in Fig. 10.8 (right). Here it is observed that the response of the station is not always reduced as in the case of the previously discussed frequency dependency at a zenith angle of $\theta = 45°$. In fact, for small zenith angles the response can be enhanced due to a constructive interference of the radiation fields from the antenna and the station components. In conclusion it can be stated that the influence of the station can alter the antenna response up to about 40% for certain frequencies and incoming directions and has thus to be considered for a precise reconstruction of the electric field emitted from air showers. The presented simulation model has been implemented as the default antenna model for the reconstruction of radio data in the Auger reconstruction framework Offline.

10.2.2 Calibration Measurements

The measurements were performed using the octocopter setup as described in Ch. 9.2. The zenith and frequency dependencies of the VEL were accessed for the north and south direction of the AERA station in multiple flights. During each flight of about 5 min effective measurement time, in the order of 200 transmission measurements were performed maintaining a distance of 30 m to 50 m between the octocopter and the AUT. The data is merged and processed as described in Ch. 9.3.

Exemplary, the zenith dependency of the magnitude of the VEL obtained in 2 consecutive flights is shown in Fig. 10.9 for 35 MHz. The same smooth pattern is observed in both flights indicating that the measurement is reproducible. However, in particular for small zenith angles a relatively large spread of the data is observed. This spread is unlikely to be caused by the uncertainties of the individual data points which are due to the uncertainty of the octocopter position. Furthermore, various other sources of uncertainties have been discussed in Ch. 9.4 and were found to be negligible. We thus conclude that an additional source of uncertainties is present in the setup which has not been considered yet.

In systematic tests during the operation, components of the setup as the octocopter and the VNA could be excluded as the source of uncertainties. Finally, the signal cable running vertically from the VNA on the ground to the octocopter was revealed as the cause of the fluctuations. Despite the shielding of the used coaxial cable, it emits radiation which interferes with the signal of the calibrated transmitting antenna. Due to its random orientation and movement during the flight, this causes a spread of the data points observed in Fig. 10.9. The effect increases with decreasing zenith angle as the cable moves closer to the AUT.

To quantify the influence of the cable, the setup has been modified to perform a background measurement. The transmitting antenna was aligned vertically below the octocopter which yields a maximum polarization mismatch between the transmitting antenna and the AUT. Furthermore, if the octocopter is maintained at small zenith angles, the gain of the transmitting antenna towards the AUT is essentially zero (cf. Fig. 9.4.3) so that no signals are transmitted to the AUT. The transmitter has not been completely removed from the setup as it provides an impedance termination of the coaxial cable which influences standing waves within the cable that can be a source of radiation [184].

With the modified setup, a flight following the same procedure as for the calibration

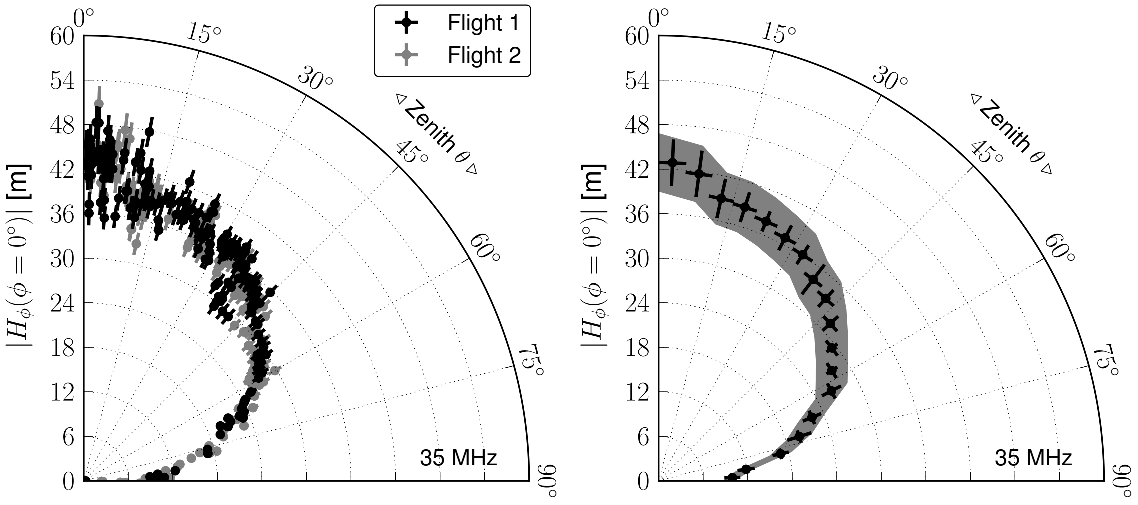

Figure 10.9: Measurement of the magnitude of the VEL of the AERA phase 2 station as a function of the zenith angle at 35 MHz. The, in total, 381 data points (left) were recorded in 2 consecutive flights in the east direction of the AERA station. The errorbars result from the uncertainty of the octocopter position (cf. Ch. 9.4.2). On the right, a profile of the combined measurement is shown. The errorbars indicate the standard deviation of the data in zenith bins of 5°. The systematic uncertainties of the transmission measurement (cf. 9.4) is indicated by the gray band.

measurements was performed. In Fig. 10.10 the transmission $|S21|^2$ of the noise measurement is compared to the transmission obtained with the regular measurement shown in Fig. 10.9. For small zenith angles, noise signals that can exceed the magnitude of the signals emitted by the transmitting antenna during a regular measurement are observed. We identify those as radiation from the cable. Further proof of this finding will be given in a later section based on a octocopter setup which completely omits the cable.

We quantify the impact of noise on the measurement by defining a signal to noise ratio (SNR) depending on the zenith angle. The transmission magnitude gives the direct power ratio $|S21|^2 = P_A/P_S$ between the received power at the antenna P_A and the power delivered by the VNA, P_S. Dividing the transmission magnitude of the regular and noise measurement thus gives the direct ratio of signal to noise power

$$SNR = \frac{|S21_{Signal}|^2}{|S21_{Noise}|^2} = \frac{P_A^{Signal}}{P_A^{Noise}}. \tag{10.1}$$

The resulting SNR is shown in Fig. 10.10 (right) in 5° zenith bins. An increase with increasing zenith angle is observed. To ensure that the influence the cable to the calibration measurement is minimal, we demand that the SNR is always larger than 20. Considering the SNR distribution of all accessed frequencies, this leads to an exclusion of events with zenith angles smaller than 40° in the further analysis.

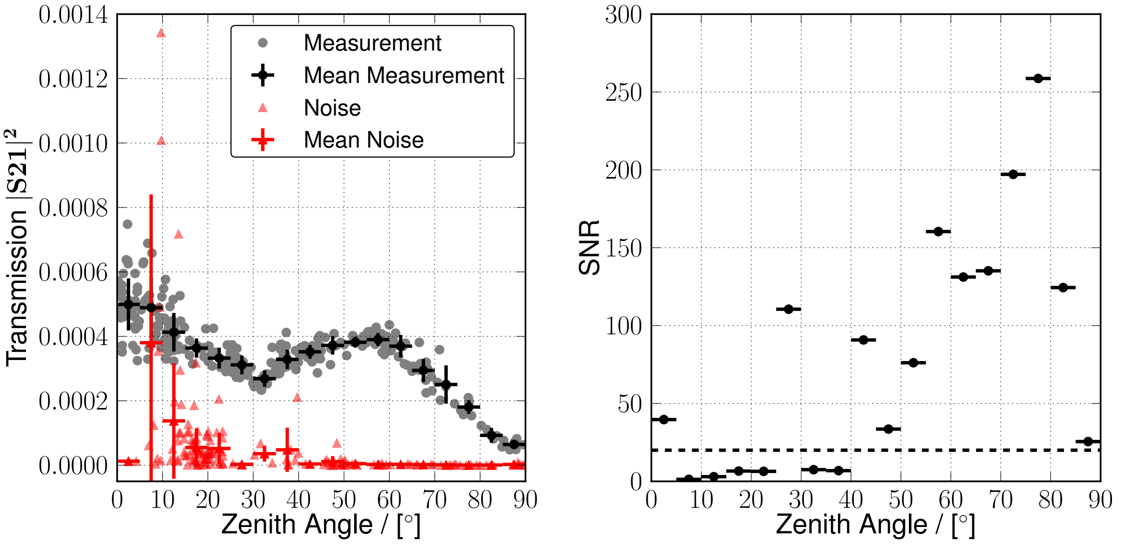

Figure 10.10: Measurement of the noise background introduced by the coaxial cable of the octocopter setup in comparison to a regular calibration measurement as a function of the zenith angle (left). The errorbars indicate the standard deviation of the data points in zenith bins of 5°. On the right the signal to noise ratio, defined as $SNR = |S21_{Signal}|^2/|S21_{Noise}|^2$ is shown.

The measured zenith patterns of the AERA phase 2 station in north and east direction are presented in Fig. 10.11 after the application of the zenith cut. Compared to the SBS, the response is relatively smooth as no side lobes are observed in the accessed zenith range. A reduction of the response in the north direction, compared to the east direction is observed which is most distinctive at 75 MHz. This behavior is predicted by the simulations and can be attributed mainly to the presence of the electronics box. Except at 35 MHz, a fair agreement between measurements and simulation is observed for the shape and the magnitude of the response.

The frequency dependence of the VEL (see. Fig. 10.12) is on a relatively constant high level compared to the SBS which is mainly due to the high gain of the integrated LNA. Beyond the AERA bandwidth the reception is suppressed due to an increasing impedance mismatch between the butterfly radiator and the LNA (cf. Ch. 8.3.1). A distinct bump is visible around 60 MHz which is not predicted by the simulation. Going to larger zenith angles (see. Fig. 10.12 (right)), a slight increase of the VEL with increasing frequency is observed over the AERA bandwidth in measurement and simulation.
For the north direction (Fig. 10.13) a similar flat response is observed with a slightly lower overall magnitude.

The group delay of the AERA phase 2 station depicted in Fig. 10.14 exhibits a characteristic bump around 30 MHz followed by a plateau towards the higher frequencies. The change in group delay over the bandwidth of about 20 ns is small compared to

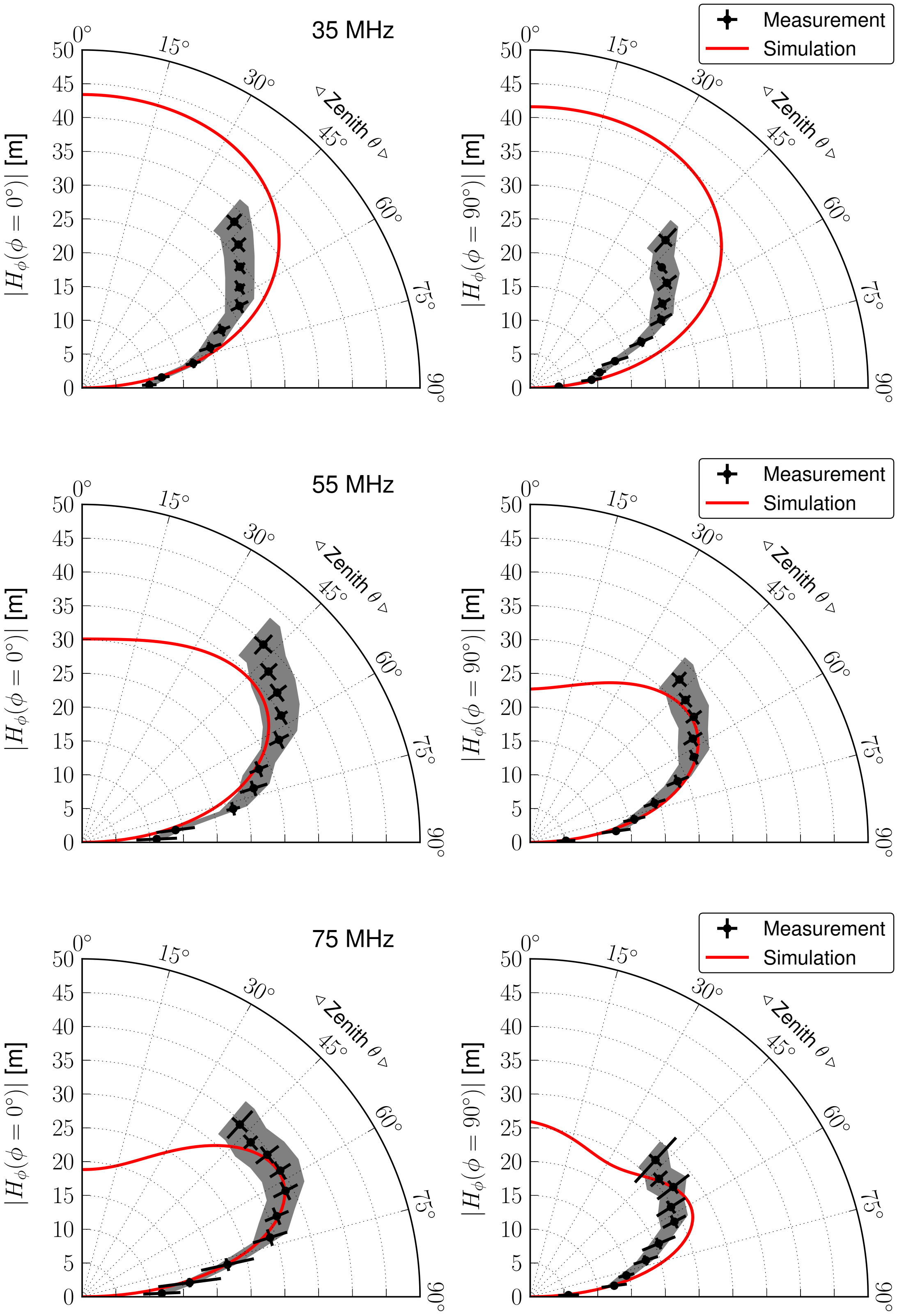

Figure 10.11: Zenith dependencies of the magnitude of the VEL for east (left) and north direction (right) of the AERA phase 2 station for various frequencies. The errorbars indicate the standard deviation of data points in 5° zenith bins. Systematic uncertainties (gray band) are due to the systematics of the transmitted signal (see Ch. 9.4).

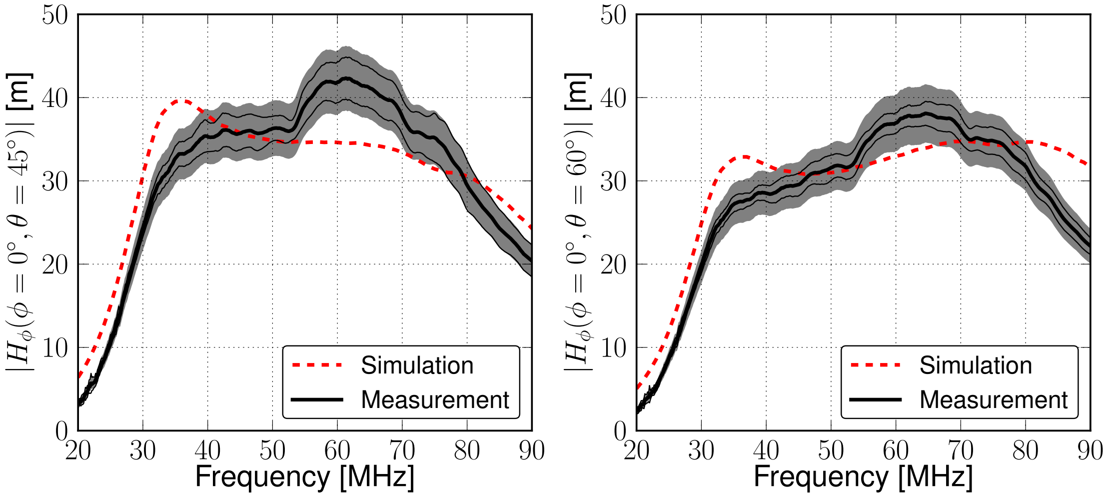

Figure 10.12: Magnitude of the VEL of the AERA phase 2 station in east direction for $\theta = 45°$ and $\theta = 60°$ as a function of the frequency. The shown curves are the average of measurements in a zenith bin of $\pm 2.5°$ around the denoted zenith angle. The thin lines indicate the standard deviation of data in this interval. The gray band indicates the systematic uncertainties (see. Ch. 9.4).

the SBS (about 50 ns) which leads to lower dispersion of the received broadband pulses from air showers. The shape of the frequency dependence is an fair agreement with the simulations. The observed offset from the simulations is of minor interest for the signal reconstruction as it only causes a constant signal delay. Comparing the group delay at different zenith angles Fig. 10.14 (right) results in only minor differences, indicating that the group delay is in first approximation independent of the zenith angle as predicted by the simulations. The group delay for the north direction is similar and depicted in appendix A.4.

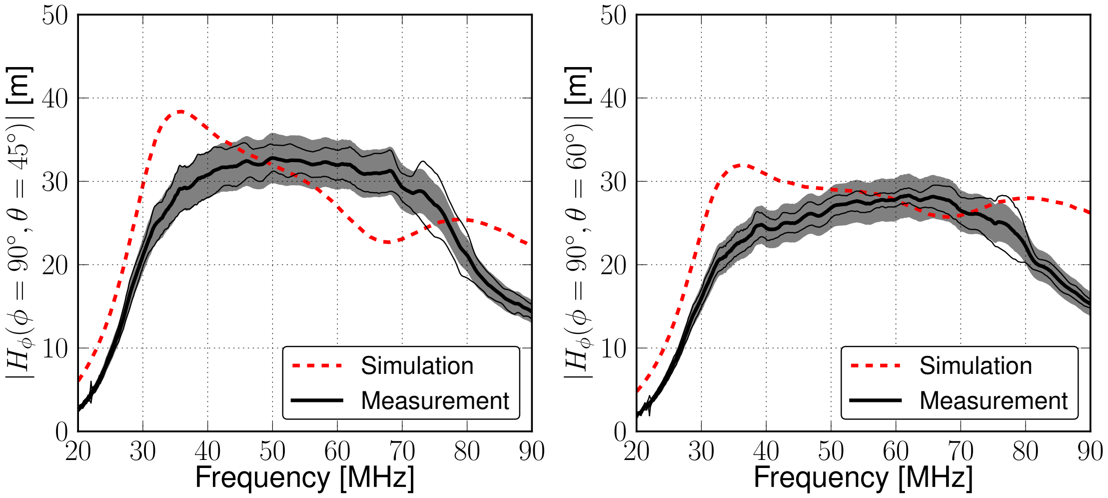

Figure 10.13: Same as Fig. 10.12 for the north direction.

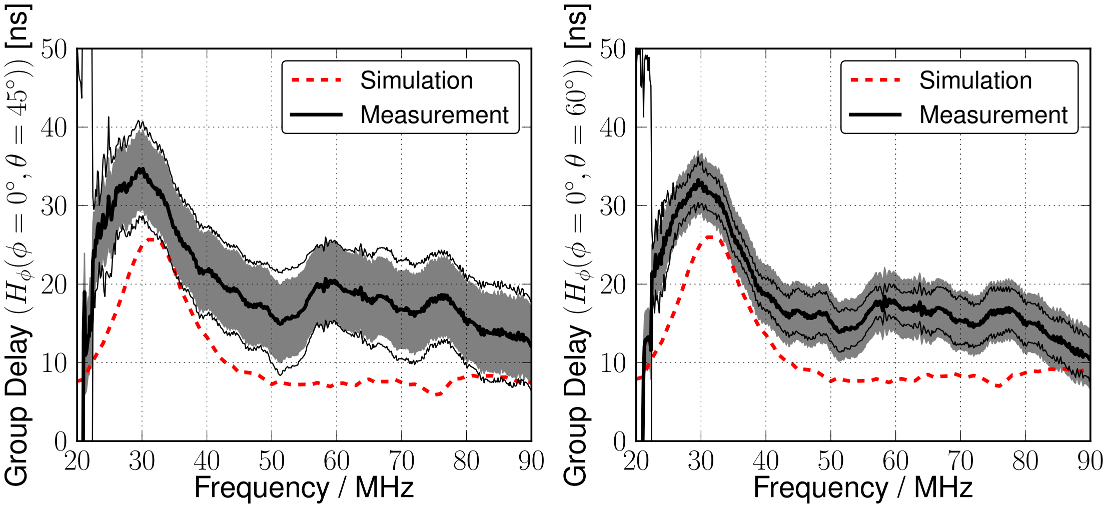

Figure 10.14: Group delay of the AERA phase 2 station measured in the east direction for $\theta = 45°$ and $\theta = 60°$ as a function of the frequency. The shown curves are the average of measurements in a zenith bin of $\pm 2.5°$ around the denoted zenith angle. The thin lines indicate the standard deviation of data in this interval. The gray band indicates the systematic uncertainties resulting from the position uncertainty of the octocopter (see. Ch. 9.4.2).

10.3 Calibration Measurements with a Modified Octocopter Setup

To omit the restrictions resulting from the influence of the signal cable used in the octocopter setup, a modified setup was developed. The signal cable was completely removed from the setup by replacing the signal generated on the ground by the VNA with a custom calibrated signal source attached to the octocopter. In consequence, an automatic synchronization between transmitted and received signal as done by the VNA during the transmission measurement is not possible anymore. The complex voltage transmission $S21$ has to be replaced by the scalar power transfer $|S21|$

$$S21 = \frac{V_A}{V_S} \qquad \rightarrow \qquad |S21| = \frac{\sqrt{P_A}}{\sqrt{P_S}}, \tag{10.2}$$

with the power received at the antenna P_A and the source power P_S which have to be determined in separate measurements. The phase information of the VEL (cf. Eq. 9.13) is thus a priori lost using this setup. It can in principle be obtained by performing measurements in the time domain at multiple frequencies. From the relative phasing of the signals at different frequencies, the group delay can be computed. However, the previously discussed measurements and simulations of the group delay indicate that the group delay exhibits only small variations with the zenith angle, in particular for the AERA phase 2 station. Extensive directional measurements of the group delay may thus not be necessary.

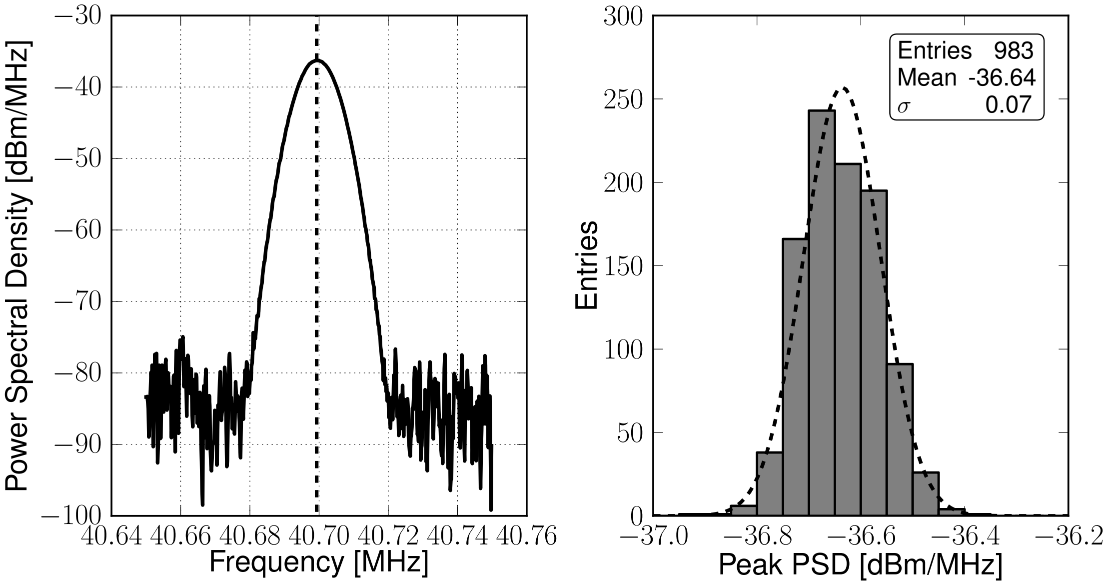

Figure 10.15: Calibration signal received by the AUT during a test setup in the lab. The peak power of the signal (vertical dashed line) as observed in 983 consecutive spectrum measurements is histogrammed on the right. A fit to a normal distribution is shown.

The used signal generator is based on a stabilized oscillator circuit generating a sinusoidal voltage with a frequency of 40.7 MHz. It has a weight of about 100 g only and is powered with the stabilized voltage divider (cf. Ch. 9.2) from the octocopter battery. The amplifier attached to the octocopter, which was used to amplify the signals coming from the VNA in case of the regular setup, can now be omitted as the signal generator provides a sufficient output level.

The signal power delivered by the generator was calibrated prior to the octocopter flights with the FSH4 spectrum analyzer directly attached to the generator output. An output power of 9.2±0.5 dBm at 40.7 MHz was found. The denoted systematic uncertainty [175] is given by the manufacturer for measurements in the spectrum mode of the FSH4 VNA and applies likewise to the measurement of the received power P_A at the AUT. Both uncertainties together with the uncertainty of the transmitter calibration are considered as the total systematic uncertainty for further analysis.

To investigate the frequency and power level stability of the calibration signal, the complete calibration setup was set up in a lab. The signal received by the AUT (Fig. 10.15) peaks at 40.698 MHz and appears about 50 dB above the noise floor. In a continuous measurement over about 20 min, 983 spectrum measurements were performed. The peak values of the calibration signal obtained from each spectrum are filled in the histogram depicted in Fig. 10.15 (right). The small variance of 0.07 dBm of the fitted normal distribution indicates that the signal is both frequency and time stable. The variations are negligible compared to further uncertainties of the setup.

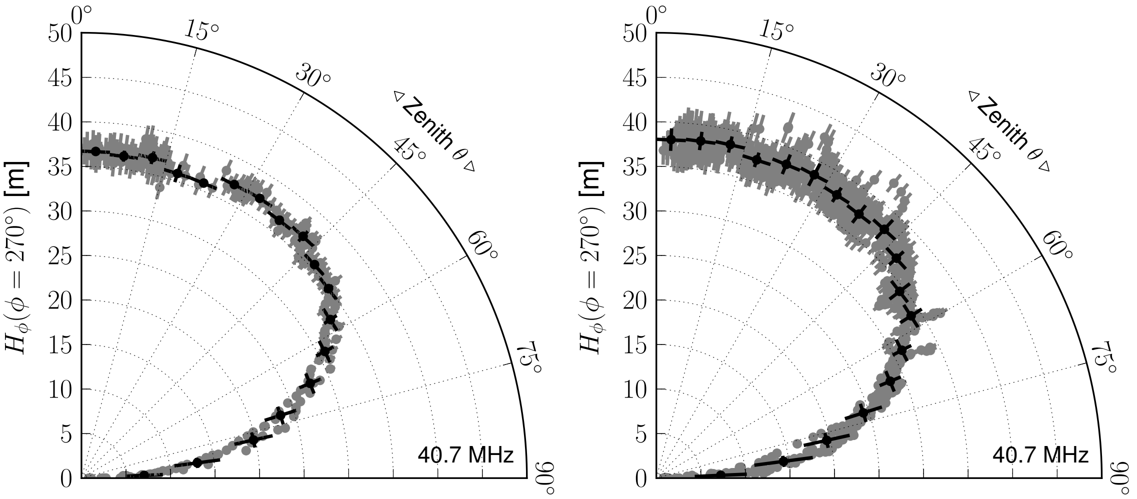

Figure 10.16: Magnitude of the VEL of the Butterfly antenna obtained from three calibration flights with the modified octocopter setup. The left plot contains 314 measurement points recorded during the first flight. The right plot shows in total 1023 measurement points combined from 2 consecutive flights performed a week later than the first flight. The errorbars of the individual measurement points are due to the uncertainty of the octocopter position. Additionally, a profile is shown with the black radial errorbars denoting the spread of data in 5° zenith bins.

First calibration measurements with the modified setup have been carried out at the RWTH-Aachen University. A single butterfly antenna has been deployed on a plane meadow and three calibration flights were performed realizing distances of 30 m to 50 m between the octocopter and the AUT.
The zenith dependencies of the VEL obtained in these measurements are summarized in Fig. 10.16. A smooth pattern is observed in all of the flights. The remarkably low spread of the data is compatible with the uncertainties of the individual data points given by the position uncertainty of the octocopter. The patterns recorded at different days (Fig. 10.16 (left) and (right)) are compatible within their uncertainties. However, they are not merged to a single pattern as they were recorded at different days and the ground condition may have changed slightly between the measurements.
Regarding the statistical uncertainties, the introduction of the modified setup leads to a significant improvement compared to the regular setup, in particular for the small zenith angles. The fact that, except the omission of the signal cable, both setups use the same hardware further supports that the signal cable was the source of uncertainties in the previous octocopter setup.

The above measurements are shown in Fig. 10.17 in comparison to the simulations and including the systematic uncertainties. The used simulation models correspond to the modified setup where no components of the AERA station were present, thus,

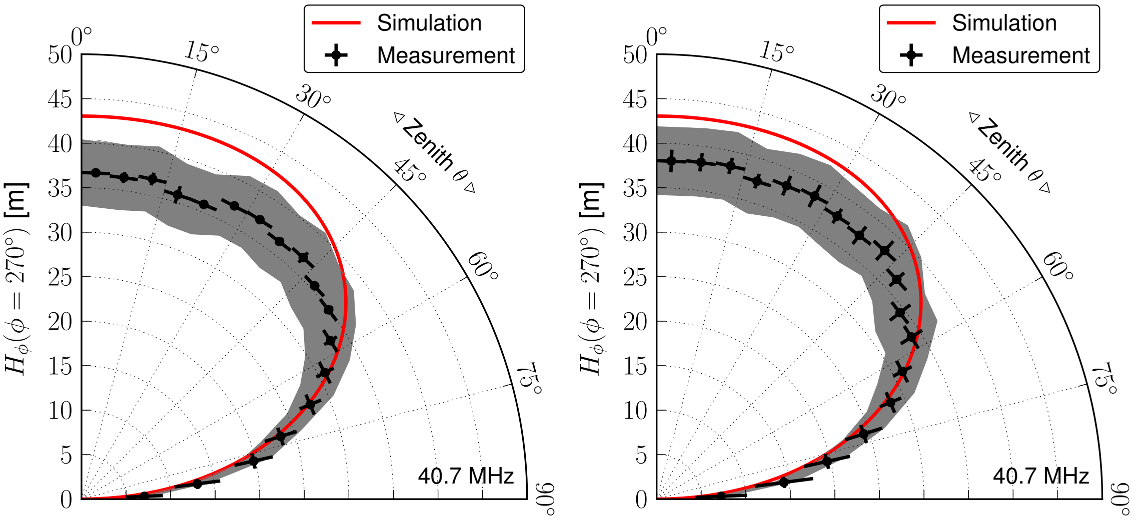

Figure 10.17: Comparison between measurement and simulation of the VEL of the butterfly antenna. Instead of the individual data points of Fig. 10.16 the profiles are shown here. The systematic uncertainties resulting from the calibration of the transmitting antenna and the power measurements of the VNA are given with the gray band.

only the butterfly antenna is simulated. The ground conditions for the simulation were adjusted to $\sigma = 5 \cdot 10^{-3}$ $[\Omega^{-1} m^{-1}]$ and $\epsilon_r = 10$ which corresponds to an average ground scenario in 4NEC2 (see Fig7.6).

The simulations overestimate the antenna response slightly for small zenith angles. The histograms shown in Fig. 10.18 indicate that the deviations between measurement and simulation are in average about 9% in the range from $\theta = 0°$ to $\theta = 80°$. The distributions show a relatively small standard deviation of about 7%.

The deviations may be caused by the choice of ground conditions for the simulations. The latter are an estimate of typical conditions for the environment where the measurements were performed but are not confirmed by dedicated measurements as in the case of the measurements performed at AERA.

10.4 Conclusions

Some conclusive remarks concerning the calibration of cosmic ray radio detectors shall be drawn at this point based on the results obtained with the developed calibration setups.

The balloon setup applied for the calibration of the SBS antenna features small statistical uncertainties for the measurement of the magnitude and phase of the VEL due to the static operation. The consequence of the latter is that the setup has to be extensively adjusted to access the angular distribution of the antenna response.

The octocopter setup allows a fast dynamic measurement of the directional antenna response and is in principle suitable to measure the three dimensional response pattern with a high angular resolution. The losses of accuracy caused by the influence

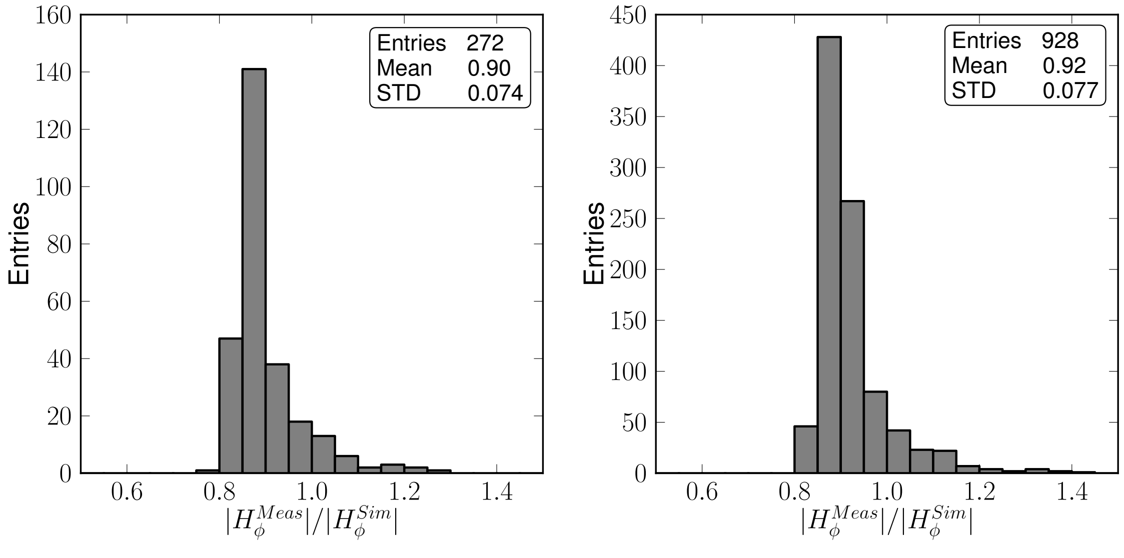

Figure 10.18: Ratio between measurement and simulation for each data point of Fig. 10.16 in a zenith range from $\theta = 0°$ to $\theta = 80°$.

of the signal cable as observed at calibration measurements of the AERA phase 2 stations have been eliminated with the modified octocopter setup. The modified setup has recently been enhanced to allow broad band measurements and is being prepared for an upcoming calibration campaign at AERA.
Systematic uncertainties are for all setups dominated by the calibration of the transmitting antenna and the precision of the signal measurement. Transmitting antennas suitable for the developed setups and providing a significantly better calibration accuracy are currently only available for narrow band applications. The accuracy of the signal measurements could be improved by high precision VNAs or spectrum analyzers respectively.

At the present state, the calibration measurements provide a benchmark for the simulations used in the radio reconstruction. The comparisons of simulations and measurements for the antenna response of the SBS discussed in this thesis indicate a mean agreement on a 5% level in average over the AERA bandwidth and the relevant zenith range. In particular when it comes to complex structures such as the AERA phase 2 stations, larger deviations from the simulations appear in detail, that is for certain frequencies or incoming directions. A future goal to increase the reconstruction accuracy of radio signals would thus be to implement measured antenna characteristics in the reconstruction or to scale the simulated characteristics based on measurements. This would require further measurements of the H_θ-component of the VEL (in this thesis the H_ϕ-component is discussed) and of the azimuthal dependencies. The presented calibration setups are suitable tools to achieve theses goals.

The antenna response is likely to be still the largest hardware-based uncertainty in radio measurements of air showers. Hence, the precision of the antenna calibration will influence the accuracy of the reconstruction of the cosmic rays parameters and will play a key role in exploring the future potential of radio detection.

11. Polarization Signature of Cosmic Ray Radio Data

The polarization of the electric field emitted by cosmic ray air showers is an indicator of the underlying radio emission mechanisms (see Ch. 4.2). We describe in the following how the polarization and the amplitude of the radio pulse are extracted from the instantaneous electric field vector measured by AERA. We will then study the polarization signature of AERA cosmic ray data and identify the dominating emission processes. Under consideration of the identified radio emission mechanisms we derive geometrical corrections for the radio signal amplitude. Based on the latter we will formulate a radio energy estimator for the energy of the primary cosmic ray in the next chapter.

11.1 Definition of the Amplitude and the Polarization of Radio Pulses

The instantaneous electric field $\vec{E}(t)$ as a basis for analysis of the radio emission has to be reconstructed from the voltage traces measured at the individual antenna stations. For this task we use the standard sequence of the Offline reconstruction framework which follows the calculus described in Ch. 7.6. This procedure incorporates the antenna response, given by the VEL obtained from the antenna simulations discussed in the previous chapter and, furthermore, requires the knowledge of the incoming direction of the radio signal. The latter can be reconstructed by fitting a model of the radio wavefront to the arrival times of the radio pulses. Alternatively, the incoming direction measured by other Auger detectors can be used for the radio reconstruction. As we will focus on radio events which are confirmed as cosmic ray events by coincidences with the Auger surface detector we apply the directional information from the SD.

An example of a time series of the reconstructed electric field vector $\vec{E}(t)$, containing a cosmic ray radio pulse is depicted in Fig. 11.1. A pulse consisting of several oscillations is observed in all three components of the electric field. Beyond the pulse, the omnipresent noise is visible.
The dispersion introduced by the varying group delay of the antenna is unfolded from the pulse in Fig. 11.1 through the reconstruction of the electric field. Looking at simulations of cosmic ray radio signals we would expect a bipolar pulse as e.g.

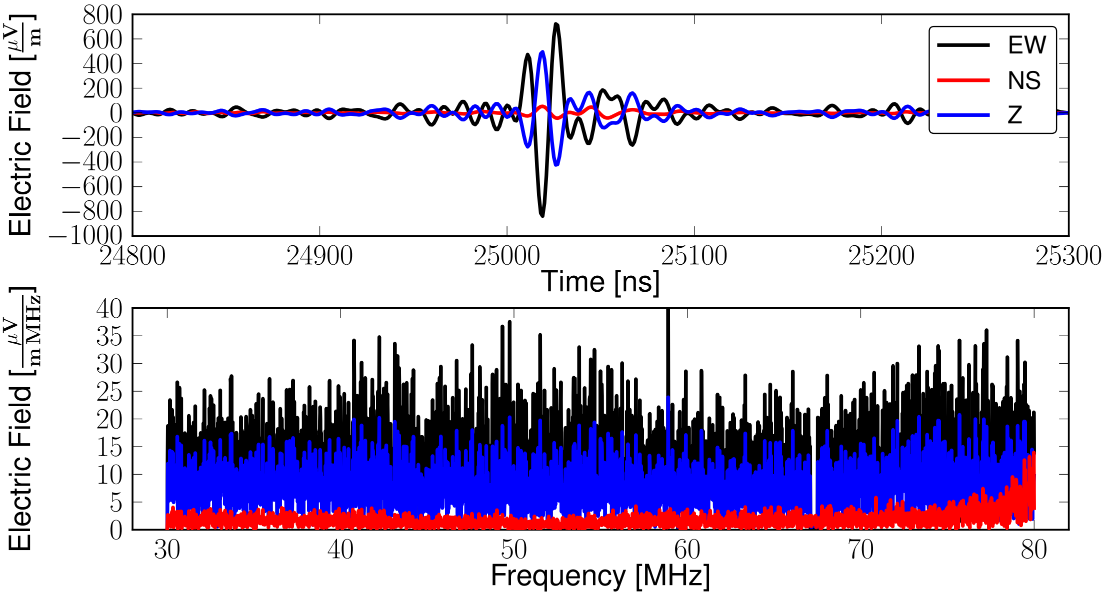

Figure 11.1: Reconstructed electric field in the cartesian coordinate system of the radio detector (NS = North-South axis, EW = East-West axis, Z = vertical axis) of a cosmic ray radio pulse recorded with AERA station 13 (Radio Event Id: 48861). An upsampling by a factor of 5 has been applied (see text). The lower plot shows the frequency spectrum. Note that the frequency spectrum of the entire trace is shown, including the noise.

shown in Fig. 4.3. The fact that the reconstructed electric field pulses still consist of several oscillations is due to the bandwidth limitation of the setup [148]. Besides the bandwidth limitation of the AERA station hardware, the signals are filtered from 30 MHz to 80 MHz during the reconstruction as visible in the frequency spectrum depicted in Fig. 11.1. Furthermore, the transmitter at 67 MHz and the AERA beacon signals (cf. Ch. 6.3) are filtered prior to the reconstruction. The 67 MHz transmitter is removed by a bandpass filter which results in a gap in the spectrum. The signals of the AERA beacon can be removed without the loss of spectral information by a sine wave suppressor [187] as they have a well defined sinusodial time structure.

Given the time series of the reconstructed electric field vector $\vec{E}(t)$, it is a priori not clear how the amplitude and the polarization of the radio pulse are defined.
To estimate the total amplitude S of a radio pulse consisting of several oscillations we use the maximum of the Hilbert envelope as depicted in Fig. 11.2. More specific, the maximum of the quadratical sum of the Hilbert envelopes of the single electric field components

$$S = max\left(\sqrt{H_{NS}^2 + H_{EW}^2 + H_Z^2}\right). \tag{11.1}$$

The definition of the polarization, that is the direction of the electric field vector $\vec{E}$, is illustrated in the middle and lower plot of Fig. 11.2. We find that in the pulse

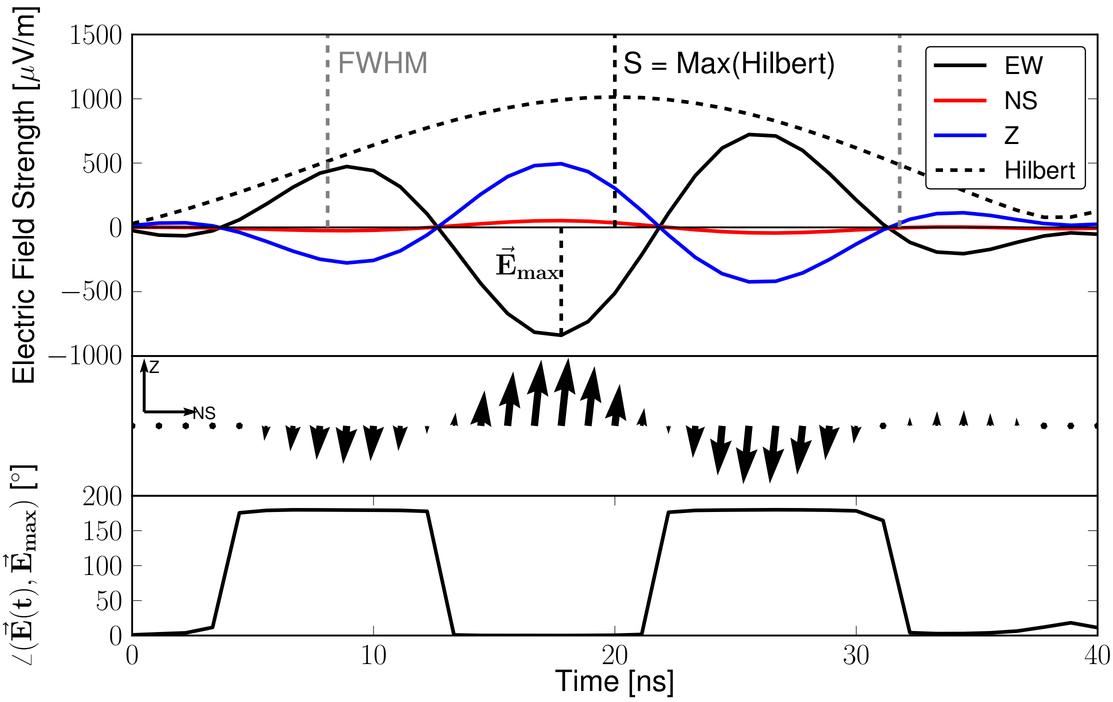

Figure 11.2: Definition of the total signal amplitude S (vertical dashed gray line) of a radio pulse as the maximum of the Hilbert envelope. The Hilbert envelope (dashed black curve) is computed from the components of the electric field according to Eq. 11.1. The shown electric field trace is a zoom into the pulse region of Fig. 11.1. The middle plot exemplarily shows the time-series of the polarization vector composed of the NS-component and the Z-component of the above electric field. The lower plot shows the angular difference between the three dimensional electric field vector $\vec{E}(t)$ and the maximum vector $\vec{E}_{max}$ (marked in the upper plot).

region, $\vec{E}(t)$ essentially points in the same direction for each time sample t, except a flip in the sign of the vector. In two dimensions this can be visualized by plotting two components of the electric field vector (for instance E_Z vs E_{NS}, see Fig. 11.2 (middle)) for each time bin. The observed time-invariant linear polarization also occurs in three dimensions. This becomes clear when computing the angular distance between $\vec{E}(t)$ and an arbitrary reference vector, for example the maximum observed electric field vector as done in Fig. 11.2 (bottom). The angular difference within the pulse region is either close to zero or close to 180° which is due to the sign flip of the electric field vector.
To demonstrate that the observed time-variant linear polarization is a feature of the radio pulse only, the above considerations can be applied to a time series within the noise region of the electric field trace (see. Fig. 11.3). A random like variation of the polarization is observed in this case.

Given the linear polarization of the radio pulse, we could, in principle, determine the polarization by evaluating any time sample within the pulse region. An exception are the zero crossings of the electric field where the polarization becomes uncertain

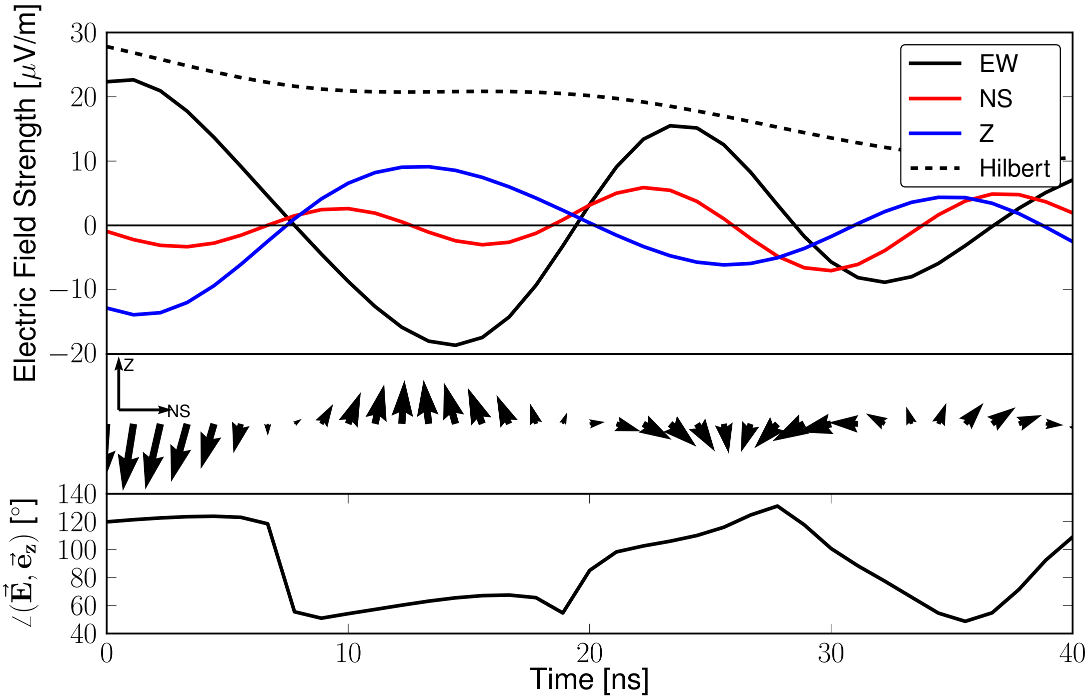

Figure 11.3: Polarization of a noise trace extracted from the electric field trace shown in Fig. 11.1. The same plots as in Fig. 11.2 are shown except that the $\vec{e}_Z$-axis is chosen as the reference vector to compute the angular distance (lower plot). Note the scale of the electric field in the upper plot, which is about a factor of 50 lower than in the pulse region.

due to the superposition of noise. To achieve an optimal precision we determine the mean electric field vector $\langle \vec{E} \rangle$ by averaging over all electric field vectors $\vec{E}(t)$ within the FWHM interval of the Hilbert envelope (see. Fig. 11.2),

$$\vec{E} = \langle \vec{E} \rangle = \sum_{t \in \text{FWHM}} \vec{E}(t). \tag{11.2}$$

The above sum implies that the vectors are averaged with a weight corresponding to their magnitude. This further increases the accuracy as vectors with low amplitudes and consequently a low signal to noise ratio have less influence.
The sign flips of the vectors are corrected prior to the averaging as follows. A start vector for the averaging process is chosen as the maximum amplitude $\vec{E}_{max}$ of the three components left of the signal amplitude S. Each vector within the FWHM that has an angular difference larger than 90° is flipped by 180°.
In the following, we will refer to the quantities defined in Eq. 11.1 and Eq. 11.2 as radio signal amplitude S and the electric field vector (or polarization vector) $\vec{E}$ respectively. The calculation of these quantities as described above has been implemented into the radio functionality of Offline.

The uncertainties on the reconstructed radio signal amplitude and the polarization vector caused by the superposition of noise have been studied in detail by simulations

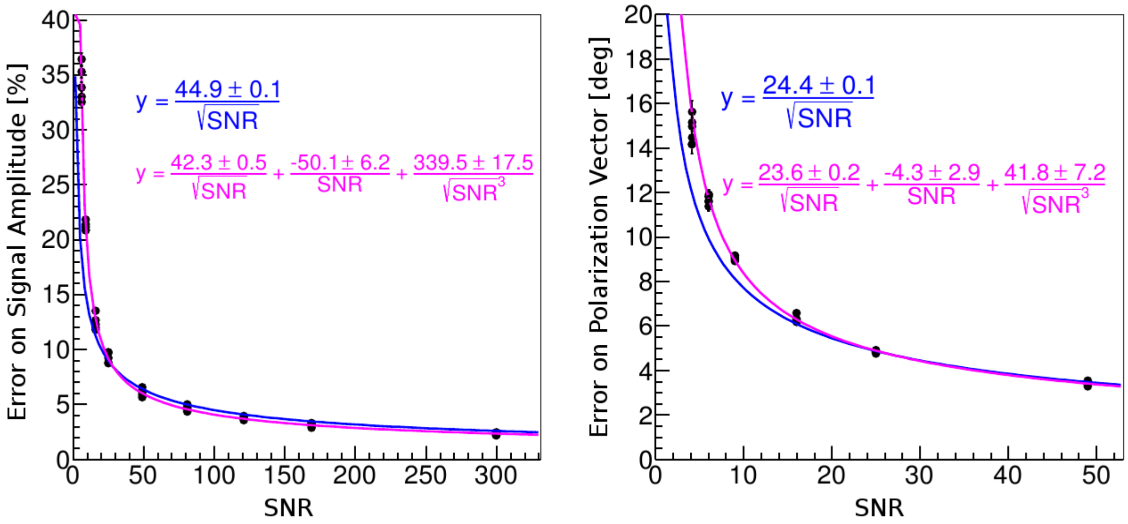

Figure 11.4: Uncertainties on the Signal amplitude S (left) and the direction of the electric field vector $\vec{E}$ (right) due to the influence of noise for different SNRs. Two parameterizations are adjusted to the simulated data and are shown in the plots with different colors. Adapted from [188].

in [188]. For this purpose, electric field traces have been generated as a superposition of a bandwidth limited delta pulse which mimics the cosmic ray pulse and a noise trace obtained from recorded AERA cosmic ray events. The relative amplitudes of the three components of the simulated cosmic ray pulse were adjusted according to the geomagnetic emission model (see. Eq. 11.6). The pulses were scaled relative to the superimposed noise traces such that multiple SNRs ranging from 6 to 300 were realized. The SNR corresponds to the definition commonly used in Offline

$$SNR = \frac{H_{max}^2}{H_{RMS}^2} = \frac{S^2}{H_{RMS}^2}, \tag{11.3}$$

with the maximum of the Hilbert envelope H_{max} and the root mean square of the Hilbert envelope H_{RMS} and the definition of the Hilbert envelope as in Eq. 11.1.
For each SNR, the signal amplitude and the polarization vector was processed for 2100 simulated electric field traces. From the deviations between the processed values and the true values (without the superimposed noise), the uncertainties on the signal amplitude and polarization were determined for each SNR.
The results are shown in Fig. 11.4. Both uncertainties decrease with increasing SNR. The uncertainty on the signal amplitude σ_S can be parameterized as

$$\frac{\sigma_S}{S} = \frac{0.423 \pm 0.005}{\sqrt{SNR}} - \frac{0.501 \pm 0.062}{SNR} + \frac{3.395 \pm 0.175}{\sqrt{SNR}^3}. \tag{11.4}$$

The uncertainty on the polarization vector σ_{Pol} can be described with the parameterization

$$\sigma_{Pol} = \frac{23.6^\circ \pm 0.2^\circ}{\sqrt{SNR}} - \frac{4.3^\circ \pm 2.9^\circ}{SNR} + \frac{41.8^\circ \pm 7.2^\circ}{\sqrt{SNR}^3}. \tag{11.5}$$

We will use the above parameterizations to describe the uncertainties on signal amplitude and polarization in the following.

11.2 Data Set and Cuts

We will investigate the polarization signature of AERA radio events that have been identified as cosmic ray air showers by coincidences with the Auger surface detector. That is, radio events which occur within a certain time window with respect to the event time stamp given by SD have been selected from the total amount of recorded radio events. Furthermore only radio events which allow a directional reconstruction were taken into account. This implies that at least three radio stations have identified a pulse and furthermore that the timing of the pulses in different stations is in agreement with a planar shower front.
The selected radio events are time-coincident with the low energy enhancement of the surface detector, the infill array (see Ch. 5.3). As we incorporate the information of the infill reconstruction (directional and energy reconstruction), we reject cosmic ray events with zenith angles larger than 55° and energies lower than $2.8 \cdot 10^{17}$ eV, following the standard quality cuts for the infill energy reconstruction [189].

The application of the above criteria yields an initial dataset of 97 cosmic ray radio events recorded in the period from 29-Apr-2011 to 18-Mar-2013. The data were taken with the phase 1 setup of AERA, that is with the 24 LPDA detector stations. 33 of these events were recorded in a self-trigger mode while for the remaining 64 events the detector was triggered externally by SD.

Cut Condition	# Events	Comment
$\theta_{SD} < 55°$	154	SD quality cut
$E_{SD} > 2.8 \cdot 10^{17}$ eV	97	SD quality cut
$\angle(n\vec{_{SD}}, n\vec{_{RD}}) < 20°$	85	Reconstruction quality cut
At least 3 stations with SNR > 10	82	Reconstruction quality cut
No Thunderstorm	77	Weather cut
No weather data	47	Weather cut -> Golden Dataset

We apply further cuts listed in the above table to ensure a reliable radio reconstruction and to exclude events which have been recorded under abnormal or undefined weather conditions. Demanding that the shower axis reconstructed by AERA agrees within 20° with the shower axis obtained by SD leads to the rejection of twelve events. In our analysis we exclude data from stations which have recorded a pulse with a SNR smaller than 10 to allow a precise reconstruction of the signal amplitude and polarization. If less than three stations have a SNR larger than 10 we reject the entire event which applies to three events.
Abnormal weather conditions such as thunderstorms can alter the atmospheric electric field and therewith the radio emission from air showers as described in Ch. 4.1.3. We identify periods of abnormal atmospheric conditions based on the electric field monitoring of the AERA weather station. If the electric field strength either exceeds 50 V/m, falls below -150 V/m or shows an RMS greater than 30 V/m the period is flagged as abnormal. A second algorithm [190] which was explicitly developed to

identify thunderstorm conditions at the LOPES radio detector is used additionally. We identify five events as thunderstorm events and reject them.

For thirty of the remaining events the AERA weather station was not operational. These events are excluded as we can not guarantee normal weather conditions.

A dataset of 47 high quality 'golden events' which we use for our analysis remains. Major physical quantities of this dataset are summarized in Fig. 11.5. A list of the events is attached in appendix A.5.

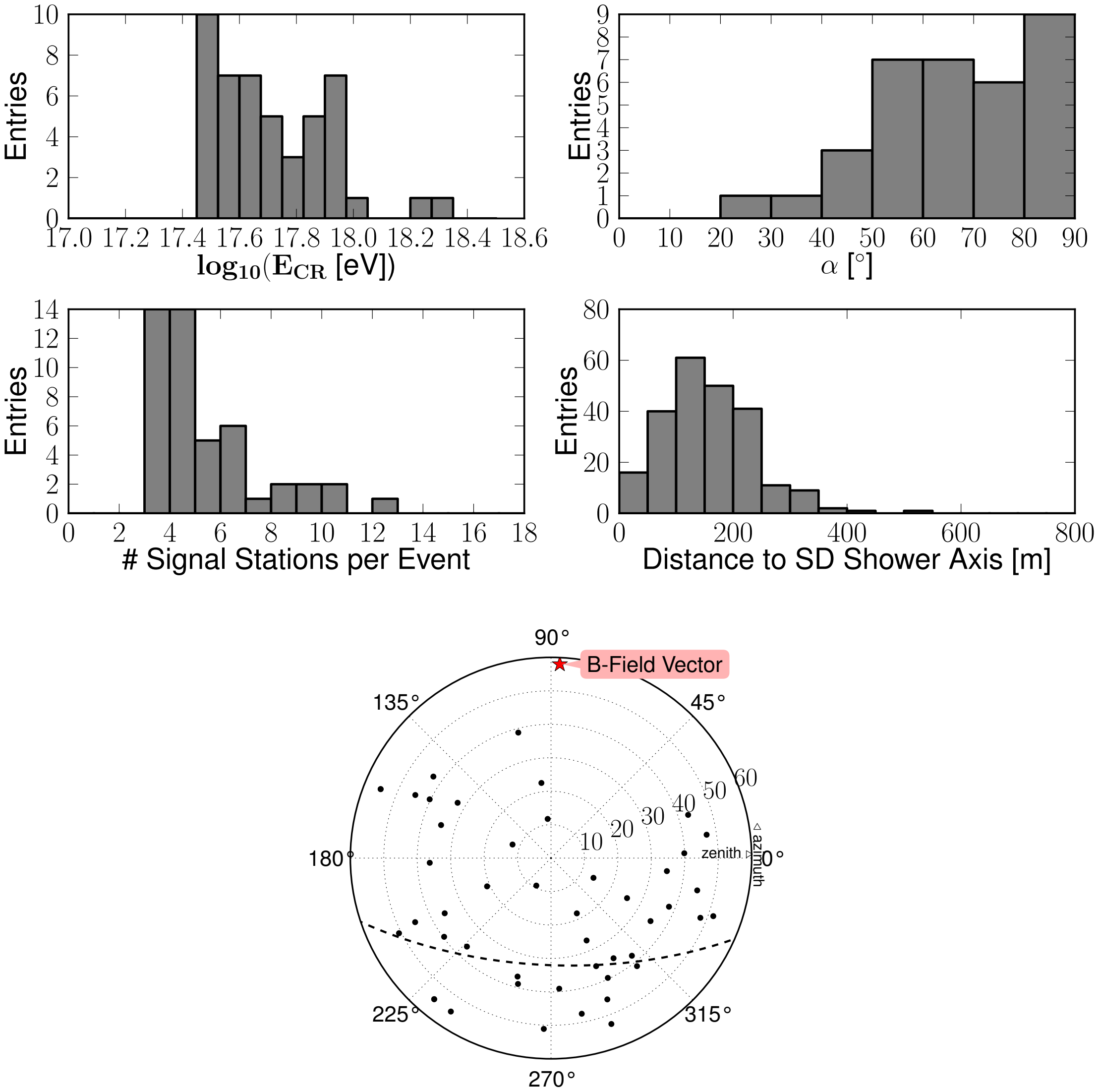

Figure 11.5: Overview of physical quantities of the golden dataset of SD coincident cosmic ray radio events recorded with AERA. The cosmic ray energy as measured by the surface detector, the angle α between SD shower axis and the geomagnetic field, the number of signal stations (stations with a SNR > 10) per event, and the distance of the signal stations to the SD shower axis are shown. The arrival directions are given with the skyplot on the bottom. The dashed curve indicates incoming directions perpendicular to the magnetic field vector (red star) at the AERA site.

11.3 Probing Radio Emission Mechanisms with the Polarization of AERA Cosmic Ray Events

For the golden dataset we can test the measured polarization vectors with regard to the two predominant radio emission mechanisms, geomagnetic and charge excess emission.

Recalling the discussion of Ch. 4 we find that the polarization of the emitted electric field is determined only by the incoming direction of the air shower $\vec{n}$ and the direction of the geomagnetic field $\vec{B}$ in the case of geomagnetic emission. The unity vector indicating the geomagnetic polarization $\vec{e}_{GM}$ points into the direction of the Lorentz force (see also Fig. 4.2),

$$\vec{e}_{GM} \propto \vec{E} \propto \vec{n} \times \vec{B}. \tag{11.6}$$

The distribution of arrival directions (see Fig. 11.5) of AERA events already reveals the characteristics of the dominating geomagnetic radio emission process. The typical asymmetry with respect to the direction of the geomagnetic field is observed. The distribution of α (Fig. 11.5) shows a clear deviation from isotropic arrival directions towards directions perpendicular to the geomagnetic field where the maximum geomagnetic radio emission is expected.

In case of charge excess emission the electric field is polarized radially towards the shower axis. The polarization vector $\vec{e}_{CE}$ points from the position of the observer perpendicular to the shower axis. The polarization thus changes with the position of the radio station relative to the shower axis. Using vector calculus $\vec{e}_{CE}$ can be obtained from the shower axis defined by the position of the SD shower core and the arrival direction and by the position of the individual radio station as shown in appendix A.6.

We consider two radio emission models, the pure geomagnetic emission

$$\vec{E}^{GM}_{Model} := \vec{e}_{GM}, \tag{11.7}$$

and the combination of geomagnetic and charge excess emission

$$\vec{E}^{GM+CE}_{Model} := \sin(\alpha)\, \vec{e}_{GM} + a\, \vec{e}_{CE}. \tag{11.8}$$

For the latter model we assume that the total electric field vector is the vectorial sum of the two linearly polarized electric field vectors from geomagnetic and charge excess emission. The scaling of the strength of the geomagnetic emission with the angle α between shower axis and geomagnetic field (cf. Eq. 4.4) is considered with the $\sin(\alpha)$ term. The relative strength of the charge excess emission (charge excess fraction) is set to the average value recently measured at AERA of $a = 14\%$ (see Ch. 4.4).

Note that, in this chapter, we are only interested in the direction of the electric field predicted by the above models. We thus might as well normalize the vector $\vec{E}^{GM+CE}_{Model}$ to unity. However, as we focus on the magnitude of the emission in the next chapter we directly define the models in the above manner.

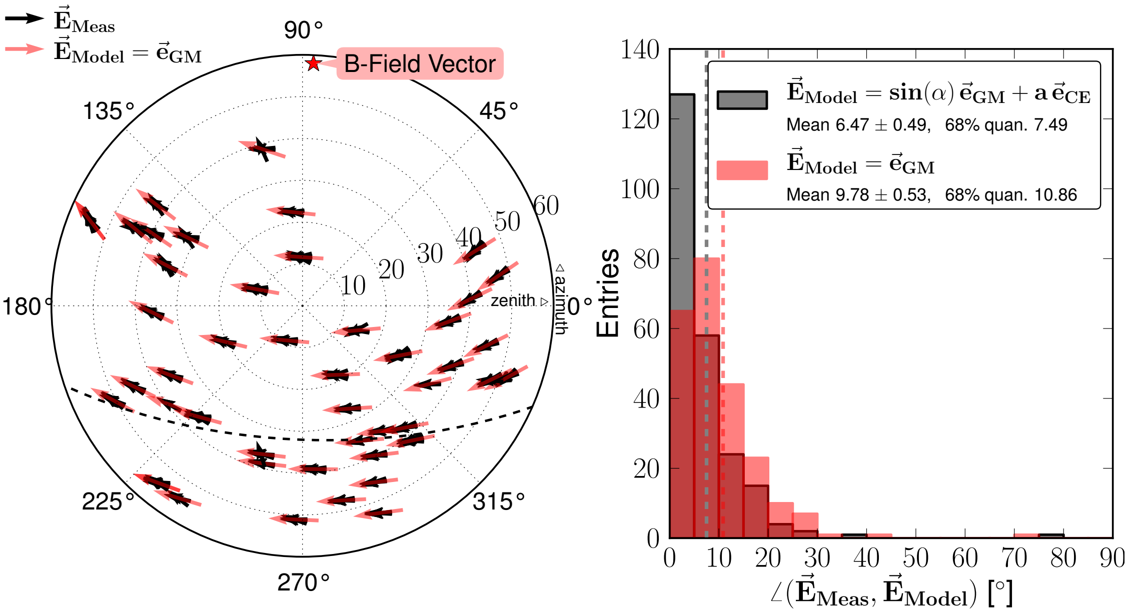

Figure 11.6: Polar skyplot of measured polarizations (horizontal components) in comparison to the expectation from the geomagnetic emission model (left). All vectors are normalized to unity. Note that at least three black vectors are plotted on top of each other for a specific incoming direction according to the multiple measurements of the electric field vector at the different radio stations triggered in the event. The dashed curve indicates incoming directions perpendicular to the magnetic field vector (red star) at the AERA site. The histograms on the right show the angular deviation between the three-dimensional measured vectors and the polarization vectors predicted by two different radio emission models - the pure geomagnetic emission (red histogram) and the combination of geomagnetic and charge excess emission (gray histogram). To quantify the deviations, the mean of the histograms and the 68% quantile (maked as vertical dashed lines) are denoted. Both histograms contain 232 entries corresponding to the total number of signal station in 47 events.

An intuitive way to visualize the polarization and its dependence on the direction is to plot the horizontal projection of the polarization vectors measured at the radio stations in a skyplot according to the incoming direction of the corresponding event as shown in Fig. 11.6. In first approximation, the same linear polarization is observed in all stations participating in a radio event. Furthermore, only small deviations from the prediction of the pure geomagnetic emission are visible in the skyplot, supporting its dominant role but also suggesting the contribution of second order effects.

We can also take the vertical component of the polarization vector into account and compute the angular difference between measured vector and geomagnetic model prediction for each station. The resulting distribution shown in Fig. 11.6 (red histogram) indicates only small deviations from the polarization of geomagnetic emission. 68% of the stations measure a deviation smaller than 10.86°.

An analog comparison for the combined model yields the distribution shown in the gray histogram of Fig. 11.6. With 68% of the stations measuring an angular de-

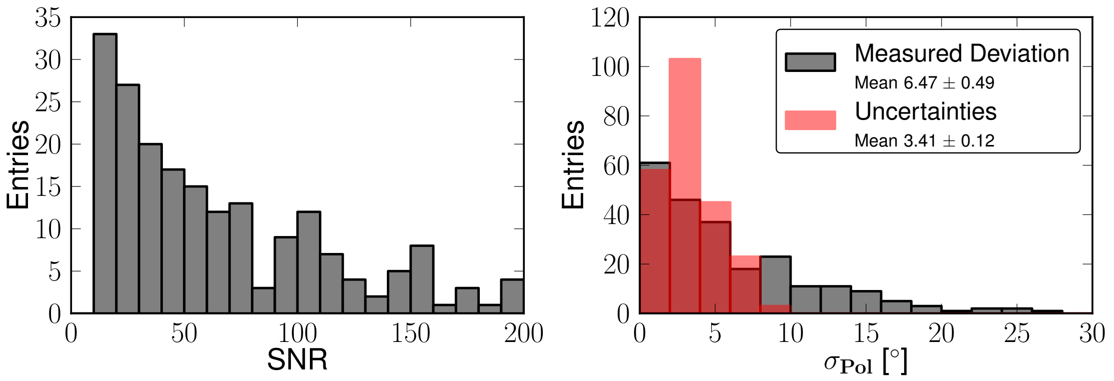

Figure 11.7: The left histogram shows the SNRs of the cosmic ray radio pulses of the golden dataset. 26 pulses have a SNR larger than 200 and are in the overflow of the histogram. On the right the uncertainty on the polarization direction σ_{Pol} (red histogram) due to the noise is depicted. For comparison the observed deviation from the model prediction (same as the gray histogram in Fig. 11.6) is shown.

viation smaller than 7.49° an even better agreement with the model prediction is observed. The mean deviation of $(6.47 \pm 0.49)^\circ$ is significantly smaller than in case of the pure geomagnetic model $((9.78 \pm 0.53)^\circ)$. The combined model thus delivers a better description of the polarization of the investigated AERA events. We conclude that a radial polarization component compatible with the charge excess emission is present in the AERA data which supports the results found in [99].

We also estimate the uncertainty of the angular measurement. In Sec. 11.1 the uncertainties on the measured polarization were parameterized as a function of the SNR. The SNRs of the cosmic ray radio pulses for our dataset are shown in Fig. 11.7. Using Eq. 11.5 the uncertainties are computed and shown in comparison to the measured distribution of Fig. 11.6. The comparison suggests that the observed deviations from the model prediction are to a large extend caused by the measurement uncertainty. Substracting these uncertainties yields

$$\sigma_{Pol} = \sqrt{6.47^{\circ\,2} - 3.4^{\circ\,2}} = 5.49^\circ. \tag{11.9}$$

Given this, we estimate that, in average, the assumed combined model describes the polarization with a precision of about 5.5°.

By varying the charge excess fraction a in the combined model we can test the agreement between measured polarization and model prediction for different relative strengths of the charge excess component. For large values of a (an example for $a = 50\%$ is shown in Fig. 11.8 (left)) the distribution of the angular deviations becomes significantly broader. We estimate the average agreement between measurement and model prediction of the entire dataset by the mean of the distribution. Performing a scan of the mean angular deviation for charge excess fractions from 0% to 50% results in the distribution depicted in Fig. 11.8. A global minimum at

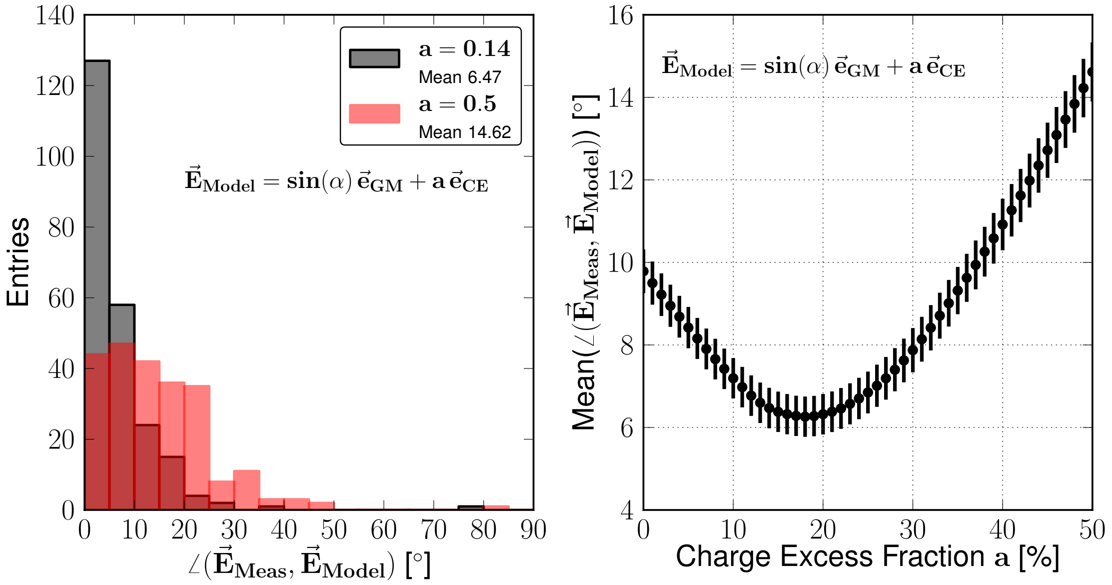

Figure 11.8: Distribution of the angular deviation of the measured polarization from the model prediction for charge excess fractions of $a = 0.14$ and $a = 0.5$. On the right a scan of the mean angular deviation for charge excess fractions from 0% to 50% is shown. The values correspond to the mean of the corresponding histograms, the errorbars are the standard error on the mean.

a charge excess fraction of $a = 18\%$ is observed. This value corresponds to the best agreement between the assumed model and the measured polarization for the considered dataset and is within 2σ in agreement with the value of $a = (14 \pm 2)$ % found in [99].
It is beyond the scope of this thesis to investigate the significance and uncertainties of the determination of the charge excess fraction with this method in detail. In this scope we understand the above considerations as a crosscheck which confirms that the introduction of the charge excess component with a suitable choice of a indeed leads to a better description of the polarization data. We maintain a charge excess fraction of 14% for the further analysis.
However, the shown approach represents an intuitive way to test models of radio emission mechanisms by a direct comparison of polarization vectors. An alternative approach was followed in the polarization analysis presented in [99], where the polarization was probed based on the Stokes parameters of the horizontal electric field.

Having demonstrated the capability of the combined model to describe the electric field polarization we will use the combined model as a basis for radio measurements of the cosmic ray energy in the next chapter.

12. Energy Measurement

In this chapter we develop a radio energy estimator to enable measurements of the cosmic ray energy based on the radio signals measured with AERA. The initial point is the reconstructed electric field which requires the calibration of the antenna response as done in this thesis.

We first discuss geometrical corrections on the signal amplitude which incorporate the emission mechanisms identified in the previous chapter. As the signal amplitude is measured at different distances from the shower axis from event to event, we need to interpolate the lateral signal distribution to define a unified estimator which is done in a second step. Finally we calibrate the radio energy estimator with the energy measurement of the Auger surface detector.

12.1 Geometrical Corrections on the Radio Signal Amplitude

The signal amplitude S of a cosmic ray pulse measured in a single antenna station was defined based on the Hilbert envelope according to Eq. 11.1. We define a corrected signal amplitude S_{Corr} by a scaling with the absolute value of the polarization vector of the combined model (cf. Eq. 11.8)

$$S_{Corr} = \frac{S}{|\vec{E}^{GM+CE}_{Model}|} = \frac{S}{|\sin(\alpha)\,\vec{e}_{GM} + a\,\vec{e}_{CE}|}. \tag{12.1}$$

By adding the unity vectors $\vec{e}_{GM}$ and $\vec{e}_{CE}$ according to the above equation we consider two geometrical effects. First, the relative strength of the two emission mechanisms which scales with the angle α between the incoming direction and the Earth's magnetic field and the charge excess fraction a. Second, the effect on the total signal amplitude due to a superposition of the geomagnetic and charge excess electric field vector. This superposition is either constructive or destructive depending on the position of the observer relative to the shower axis.

This is exemplary visualized for a single event in Fig. 12.1. Basically the electric field of the geomagnetic emission component is increased by the addition of the charge excess component for stations on the right hand side of the shower core and decreased for stations on the left.

Besides the change of the total signal amplitude, the vectorial sum of both emission components alters the direction of the total polarization vector. We notice in Fig. 12.1 that the sum of both emission vectors is in better agreement with the

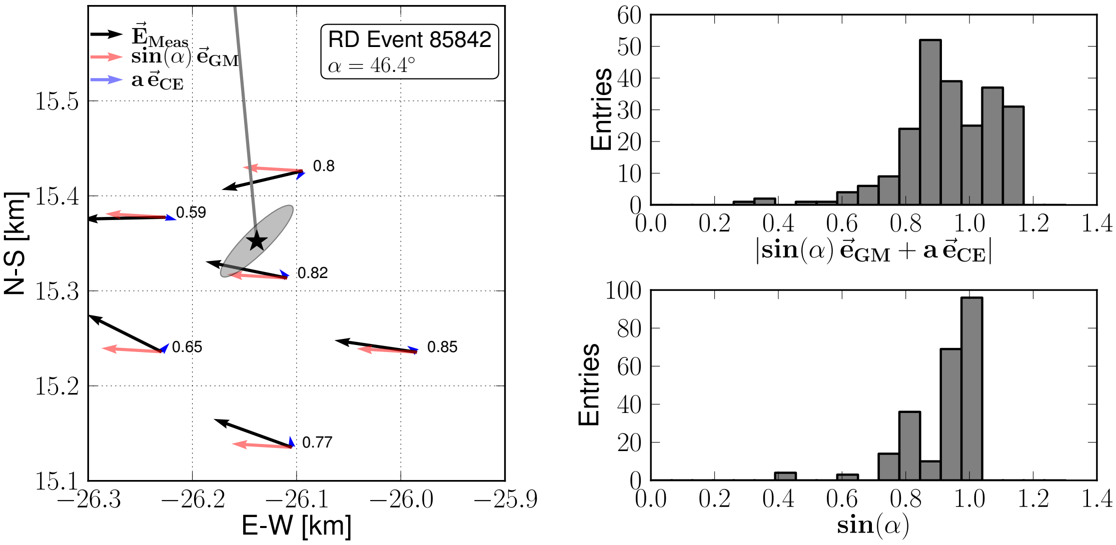

Figure 12.1: Array map of an AERA cosmic ray event (Radio Event Id: 48861) showing the horizontal components of the measured electric field vectors (normalized to unity) and the predicted vectors from geomagnetic and charge excess emission in comparison. The vectors end at the position of the corresponding AERA station. The predicted vectors are scaled corresponding to their relative strength. The star denotes the SD shower core, the ellipse its uncertainties and the gray line is the shower axis. Note that the event shown is almost vertical ($\theta_{SD} = 12°$). On the right, the geometrical corrections on the total signal amplitude for all signal stations of the golden dataset are shown for the combined emission model (top) and the pure geomagnetic model (bottom). The corresponding corrections due to the combined model are denoted in the array map on the left.

measured polarization vector than the pure geomagnetic vector. We have analyzed this behavior for the entire dataset in the previous chapter.

The amplitude corrections of the entire dataset are histogrammed in Fig. 12.1(right) for the combined and the pure geomagnetic model. In case of the latter the amplitude correction is simply given by $\sin(\alpha)$ and is consequently for most of the stations close to one as the majority of events impinges approximately perpendicular to the geomagnetic field (cf. Fig. 11.5). For the combined model the distribution becomes broader as the charge excess component modulates the total signal strength depending on the relative position of the station.

12.2 Interpolation of the Lateral Signal Distribution

The radio emission from air showers features a characteristic lateral falloff of the signal strength with increasing distance from the shower axis. In Ch. 4 we discussed that most experiments and simulations report a lateral distribution function (LDF)

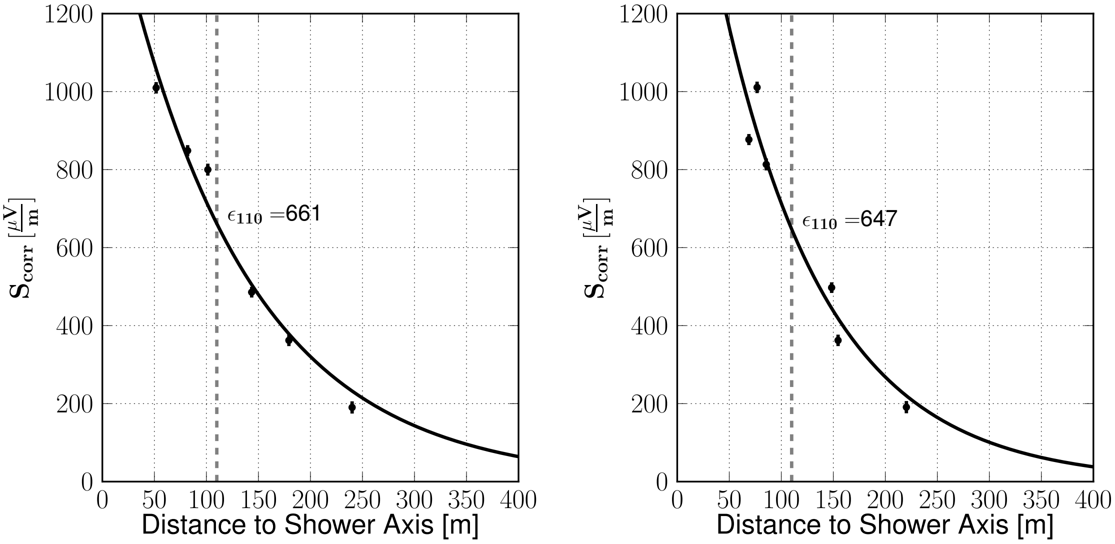

Figure 12.2: Lateral signal distribution of an AERA cosmic ray event (Radio Event Id: 4981) with an exponential fit. The errorbars indicate the signal uncertainty due to noise (cf. Eq. 11.4). On the right the LDF of the same event is shown after a variation of the shower core (see text for details). The dashed line indicates the distance D_0 where the energy estimator ϵ_{110} is evaluated.

compatible with an exponential falloff. An exception are recent results from LOFAR which suggest deviations from the exponential behavior for distances close to the shower axis.

Current LDF studies at AERA using a two dimensional LDF (cf. Ch. 4.4) are promising but require a minimum number of five signal stations to fit the LDF parameterization. Looking at Fig. 11.5 we find that we would reduce our dataset from 47 to 19 events by applying the two dimensional LDF model in our analysis. For our dataset and in the scope of an energy calibration we find that the LDF is sufficiently described with an exponential falloff.

The LDF is obtained for each cosmic ray event by plotting the corrected signal amplitudes S_{Corr} (Eq. 12.1) versus the distances of the signal stations to the shower axis. An example is presented in Fig. 12.2. The measured LDF is parameterized by adjusting an exponential function

$$S_{Corr}(R) = C\ \exp(-\frac{R}{R_0}), \tag{12.2}$$

with the two parameters C and R_0. The energy estimator ϵ_{110} is than defined as the corrected signal amplitude at a fixed distance of $D_0 = 110$ m obtained from the LDF fit. We will motivate the choice of D_0 later.

The dominating uncertainty on ϵ_{110} is caused by the uncertainty of the shower core given by SD. The error ellipse of Fig. 12.1 indicates that the uncertainty of the shower core can be in the same order as the distances between adjacent radio detector stations. A shift of the shower core not only changes the distances of the RDS

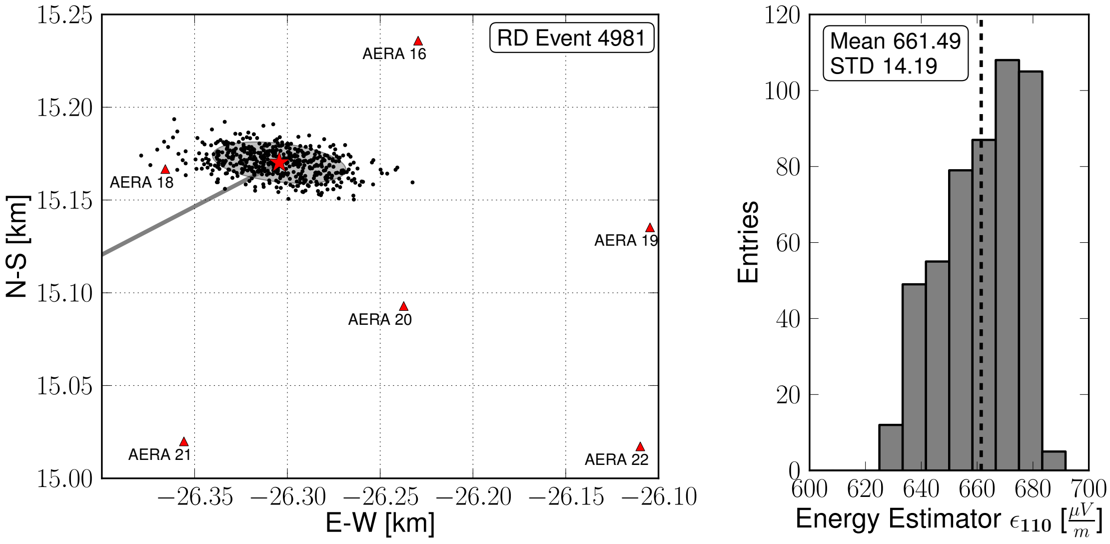

Figure 12.3: Uncertainty on the energy estimator ϵ_{110} due to the variation of the shower core. The left figure shows the positions of the 500 random generated shower cores. 68% of the generated cores lie within the error ellipse representing the shower core uncertainty of SD. On the right the distribution of the energy estimator obtained from the LDF for each core position is shown. The standard deviation of the histogram is taken as the uncertainty on ϵ_{110}. The dashed vertical line gives the energy estimator for the unvaried SD core.

to the shower axis but also the direction of the charge excess component included in the geometrical correction. Thus a complicated systematic uncertainty is introduced which can not be described by a simple uncertainty on the distance to the shower axis in the LDF fit.
We account for this uncertainty by a Monte Carlo simulation which varies the shower core (see Fig. 12.3) and repeat the LDF fit for each realization. The shower cores are generated following the two dimensional normal distribution given by the uncertainty of the SD core. For each realization, ϵ_{110} is evaluated from the LDF. The uncertainty on the energy estimator is then defined as the standard deviation of the resulting distribution of ϵ_{110} as exemplarily depicted in Fig. 12.3 (right)). This uncertainty is always larger than the uncertainty on ϵ_{110} of the LDF fit itself.

Besides the dominating uncertainty due to the variation of the shower core, further uncertainties on the signal amplitude are introduced by the uncertainty of the shower axis. A change of the latter affects the antenna response as the antenna pattern is evaluated at a different incoming direction and furthermore the distance of the stations to the shower axis. The latter effect is already considered with the Monte Carlo variation of the shower core. For the given dataset the maximal uncertainty on the SD arrival direction is about 3° and typically below 1°. For such small variations of the incoming direction, the associated change of the antenna response can be neglected compared to the error on the signal amplitude due to noise.

Also the antenna model introduces uncertainties on the signal amplitude. An estimate of the uncertainty of the antenna model can be obtained from the comparisons of the simulated response of the SBS with the corresponding measurements (cf. Ch. 10.1.2). The comparisons indicated that the SBS is described well by the simulated model with a mean agreement of the VEL in average over the AERA frequency range and the relevant zenith range of about 5%. Due to the linear scaling of the VEL with the reconstructed electric field we estimate that a systematic uncertainty on the signal amplitude equal to the one of the VEL is introduced by the antenna model.
The uncertainty of the signal amplitude causes a systematic shift of the energy estimator ϵ_{110}. We have verified that, for a broadband radio pulse, this shift is in first order independent of the arrival direction of the event and is thus equal for all observed cosmic ray events. As we calibrate the radio energy estimator with the energy of the surface detector in the following, the systematic uncertainty introduced by the antenna model is not relevant for our analysis.

Above, we have defined the energy estimator at a fixed distance of $D_0 = 110$ m. Simulations already predict that the LDF exhibits a region relatively close to the shower core where the impact of shower to shower fluctuations on the signal amplitude is minimal and the amplitude is independent of the primary mass (cf. Ch. 4.3).
We determine the optimal distance D_0 in a data driven approach. An energy cal-

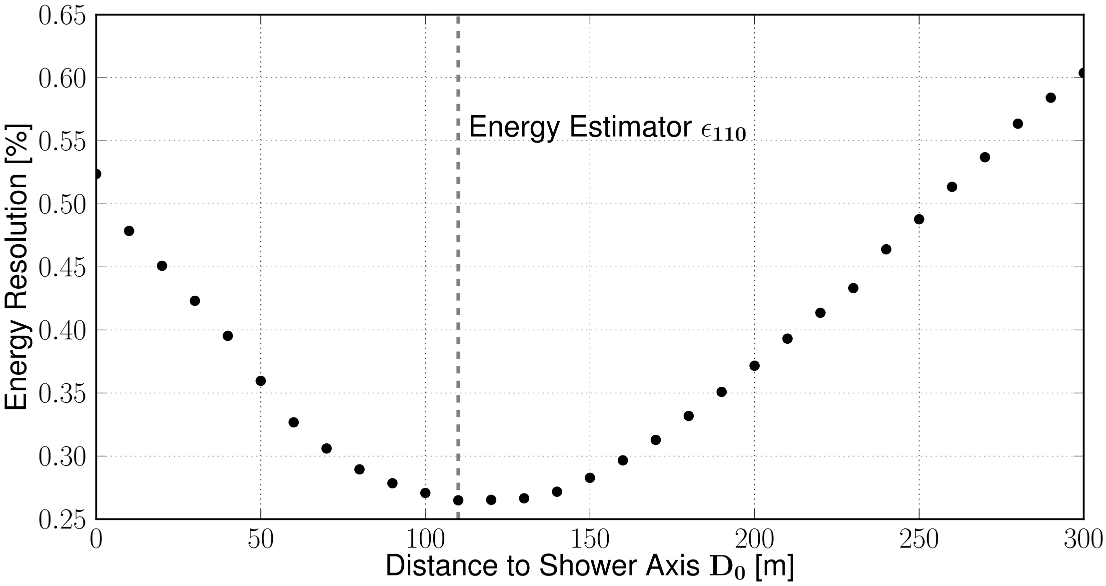

Figure 12.4: Scan for the optimum distance to the shower axis D_0 for the definition of a radio energy estimator. On the y-axis the energy resolution obtained in an energy calibration with the surface detector is plotted. See text for details.

ibration of the radio energy estimator ϵ_{D_0} with the energy measurement of SD[1] is performed for various choices of D_0. From the calibration we compute the radio energy resolution for the corresponding choice of D_0.
The results of this scan for the optimal D_0 are presented in Fig. 12.4. The best energy resolution is achieved at $D_0 = 110$ m which leads to our definition of the energy estimator ϵ_{110}.
The same result for D_0 was obtained by a previous analysis of a smaller AERA dataset [191]. Simulations and measurements at LOPES indicate similar values of D_0 [91, 192].

12.3 Calibration with the Energy Measurement of the Surface Detector

Having defined the radio energy estimator ϵ_{110} and its uncertainties we can perform a calibration with the energy measurement given by the Auger surface detector. The calibration depicted in Fig. 12.5 shows a clear correlation over about one order of magnitude in cosmic ray energy with the radio energy estimator ϵ_{110}. We parameterize the correlation by adjusting a linear function in the double-logarithmic representation

$$\log_{10}(E_{RD}[\mathrm{eV}]) = c + m\ \log_{10}(\epsilon_{110}[\mu\mathrm{V/m}]). \tag{12.3}$$

The fit yields $c = 14.96 \pm 0.08$ and $m = 1.06 \pm 0.03$ with a χ^2 per degree of freedom of 2.5. After transferring to a linear scale we obtain the calibration equation which gives the energy of the cosmic ray E_{RD} measured by the radio detector

$$E_{RD}[\mathrm{eV}] = 10^{14.96\pm0.08}\,(\epsilon_{110}[\mu\mathrm{V/m}])^{1.06\pm0.03}. \tag{12.4}$$

The power law index m is within 2σ compatible with one. As the energy estimator corresponds to the signal amplitude at a certain distance, this is equivalent to a linear scaling of the radio signal amplitude with the cosmic rays energy. This behavior is expected from theories of radio emission and was observed by other experiments as discussed in Ch. 4.

We can estimate the energy resolution of the radio energy measurement by computing the relative differences $(E_{CR} - E_{RD})/E_{CR}$ between the energy E_{RD} predicted by the calibration equation and the energy E_{CR} measured by SD. The resulting distribution is depicted in Fig. 12.5 (right). The standard deviation of the distribution indicates the energy resolution of the radio energy reconstruction of 26%. The distribution includes the energy resolution of the surface detector which is better than 17% for the Infill array in the accessed energy range [189]. Subtracting the energy resolution of the Infill array yields

$$\sigma_{E_{RD}} = \sqrt{26\%^2 - 17\%^2} = 19.7\%. \tag{12.5}$$

---

[1] The procedure of the energy calibration is described in detail in the next section.

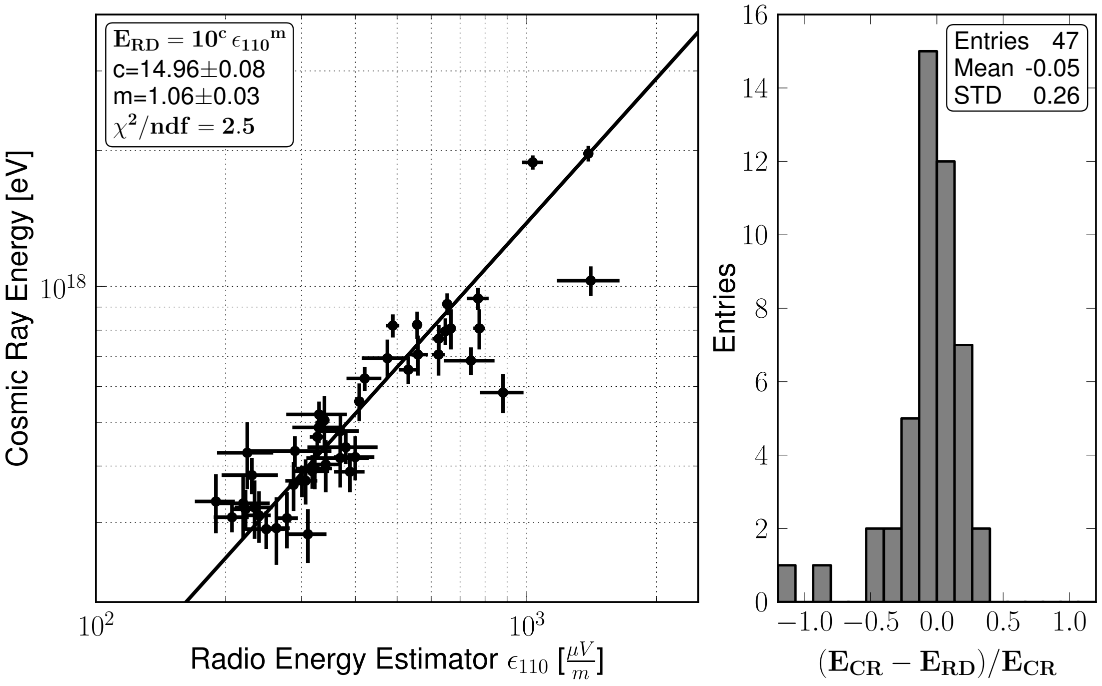

Figure 12.5: Energy calibration of the radio energy estimator ϵ_{110} with the cosmic ray energy measured by the Auger surface detector. The parameters of the fitted power law (black line) are denoted in the box. Uncertainties on the SD energy are given by the standard SD reconstruction [189]. The histogram indicates the relative energy resolution for the given calibration.

We can thus estimate that the energy resolution $\sigma_{E_{RD}}$ of the radio measurement alone is about 20%.

In conclusion it can be stated that the achieved quality of the radio energy reconstruction is about to become competitive to established detection techniques. With the commissioning of AERA phase 2, the instrumented area was recently increased by about a factor of 15. The resulting advance in statistics and energy range will certainly push the prospects of cosmic ray radio detection in the next years.

13. Summary

With the Auger Engineering Radio Array, radio technique for the detection of high-energy cosmic rays is being probed for applications in large scale future cosmic ray detectors. The success of this technique will be judged by its capabilities to measure the primary parameters of cosmic rays such as arrival direction, energy and composition. The precision of these measurements depends on the calibration of the detector response, in particular the antenna response and on the definition of suitable estimators for the cosmic ray parameters.
The work performed within this thesis includes major contributions to the R&D of MHz antennas as well as to the construction and commissioning of the first AERA setup with 24 radio stations. Furthermore, we developed and applied novel methods for the in situ calibration of MHz radio antennas of cosmic ray radio detectors. Based on calibrated measurements of the AERA radio stations we developed an estimator for the cosmic ray energy and determined the cosmic ray energy resolution with AERA.

A fundamental ingredient for the radio detection of cosmic rays are antennas which are optimized for the detection of radio emission from air showers and adapted to the environment of the experiment. AERA's sensors to the radio emission are the SBS logarithmic-periodic dipole antenna and the Butterfly bow-tie antenna. Important contributions to the development and optimization of these antennas have been delivered within the scope of this thesis. By means of antenna measurements, we evaluated the electrical properties and monitored the production quality of all antennas currently deployed at AERA. We have successfully adapted the Butterfly antenna to the harsh environmental conditions at AERA by redesigning the mechanical structure and conducting extensive testing in a wind tunnel. Both antenna types have performed flawless over years of operation at AERA.

Reconstruction of the vectorial electric field emitted by air showers requires knowledge of the directional and frequency dependent antenna response including the dispersion effects within the antenna structure and preferably the influence of the environment on the antenna characteristics.
Within this thesis we have developed novel methods to access the entity of these information by measuring the vector effective length of MHz radio antennas directly at the site of the experiment. We have presented measurement setups which are based on a calibrated signal source placed in the far field region of the antenna under test by either a balloon or a flying drone.

We have successfully applied the balloon setup to perform a calibration of the SBS antenna. The calibration represents the first directional measurement of the antenna response including signal dispersion effects for the AERA detector. In a comparison with corresponding simulations we found a remarkable agreement of the zenith sidelobe pattern of the vector effective length. The mean deviation between measurement and simulation is 5% on average over the entire frequency and zenith range.
The octocopter setup was used to conduct a measurement of the vector effective length of the Butterfly antenna station at AERA. The measurements indicated that an azimuthal asymmetry of the antenna response is introduced by the presence of the AERA station components. A corresponding simulation model of the Butterfly station which includes the influence of the station components was developed in the scope of this thesis and is currently used for the radio reconstruction at AERA.
From the experience gained with the calibration measurements at AERA, a modified octocopter setup was developed to overcome limitations in the measurement accuracy at small zenith angles. First measurements with the modified setup demonstrated superior precision. Further calibration campaigns at AERA are currently under preparation and will build on our extensive R&D of calibration techniques.

Measurements of the primary cosmic ray energies using radio detectors appear to be a challenging task as the observed total radio emission evolves from a superposition of different radio emission mechanisms which exhibit individual dependencies on the geometry of the air shower.
In a first step we have identified the dominant emission mechanisms in a set of high-quality cosmic ray induced radio events by probing the polarization of the emitted electric field. For this purpose, we exploited theories of radio emission in the form of two emission models describing the polarization of cosmic ray radio data, the pure geomagnetic model and a combined model which includes the superposition of a charge excess component.
By comparison of the measured polarization vector of the electric field and the prediction of the emission models we confirmed the dominant role of the geomagnetic emission. Moreover, we found that the combined model yields a significantly better description of the polarization in AERA cosmic ray events which confirms the existence of a sub-dominant charge excess emission component. A remarkably small mean angular deviation between the measured polarization and the prediction of the combined model of 5.5° was observed. Furthermore, we found that the charge excess component contributes with a relative strength of 18% to the total radio emission which supports previous polarization studies at AERA.

Having identified the dominant and sub-dominant emission mechanisms we were able to define a corrected radio signal amplitude which considers the interplay of both emission mechanisms at each individual radio station. We modeled the lateral distribution of the corrected signal amplitude by an exponential falloff to obtain a unified radio energy estimator at an optimal lateral distance from the shower axis. The optimal distance of 110 m was determined to yield the best energy resolution in the subsequent energy calibration.

We finally performed a calibration of our energy estimator with the corresponding energy measurement of the Auger surface detector. The obtained correlation indicates a linear dependency of the radio signal amplitude with the cosmic ray energy, which is compatible with theories of radio emission and radio energy measurements of other radio detectors. With our method, we achieved a relative energy resolution of 26% for the radio measurement of the cosmic ray energy, including the energy resolution of the surface detector. Using preliminary studies of the energy resolution of the surface detector of 17% implies that the cosmic ray energy resolution of the radio measurement alone amounts to 20%.

Further improvement can be expected by the rapidly growing statistics of cosmic ray radio data due to the recent commissioning of 100 radio stations extending the instrumented area of AERA by a factor of 15 to 6 km^2.

A. Appendix

A.1 Antenna Input Impedance of the SBS Antenna

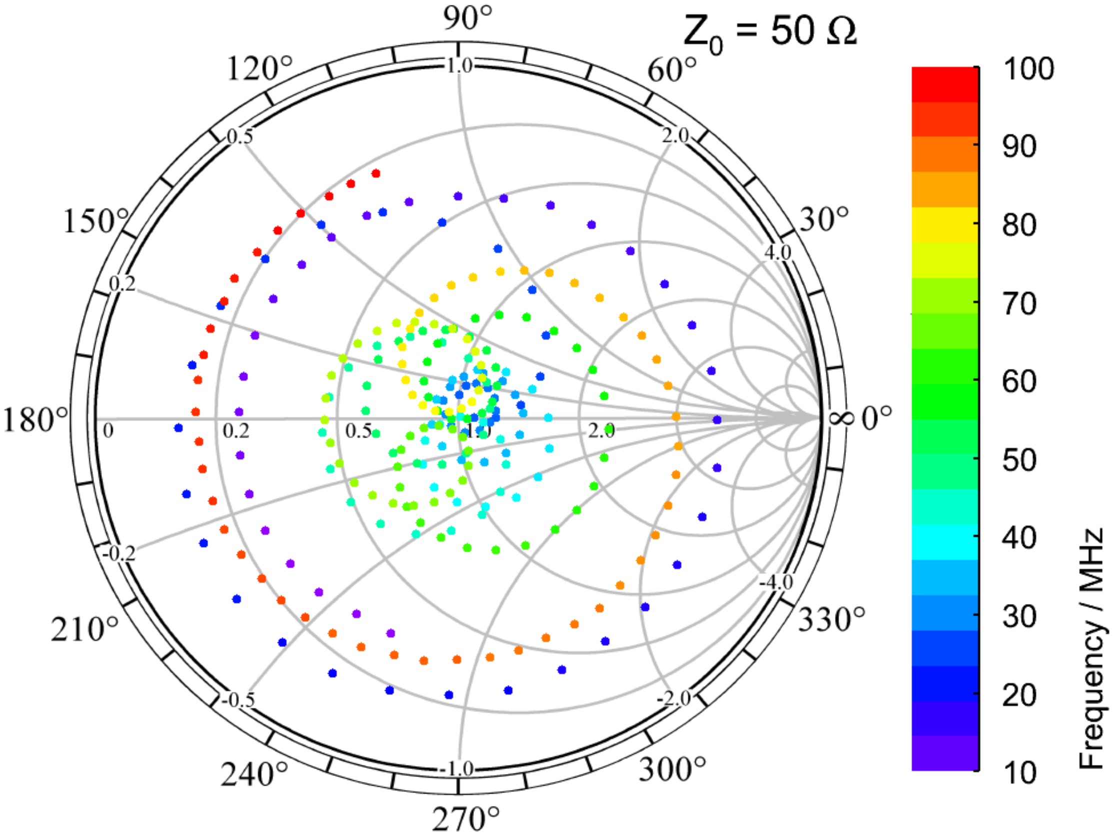

Figure A.1: Smith chart of the measured complex antenna input impedance of the SBS antenna obtained by a reflection measurement. The frequency is color coded. The center is normalized to the pure resistive source impedance of 50 Ω. For the interpretation of Smith chart diagrams refer to e.g. [193]

A.2 Antenna Input Impedance of the Butterfly Antenna

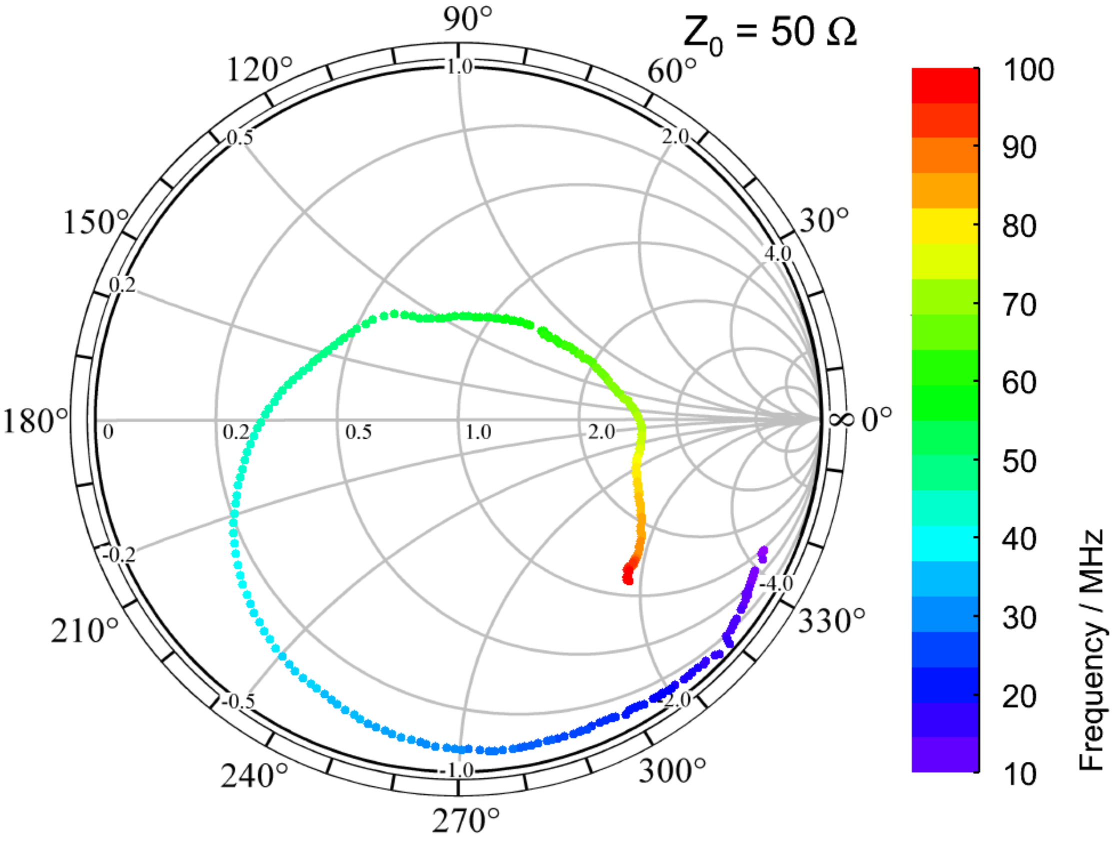

Figure A.2: Smith chart of the measured complex antenna input impedance of the Butterfly antenna obtained by a reflection measurement. The frequency is color coded. The center is normalized to the pure resistive source impedance of 50 Ω. For the interpretation of Smith chart diagrams refer to e.g. [193]

A.3 Manufacturer Calibration of the Transmitting Antennas

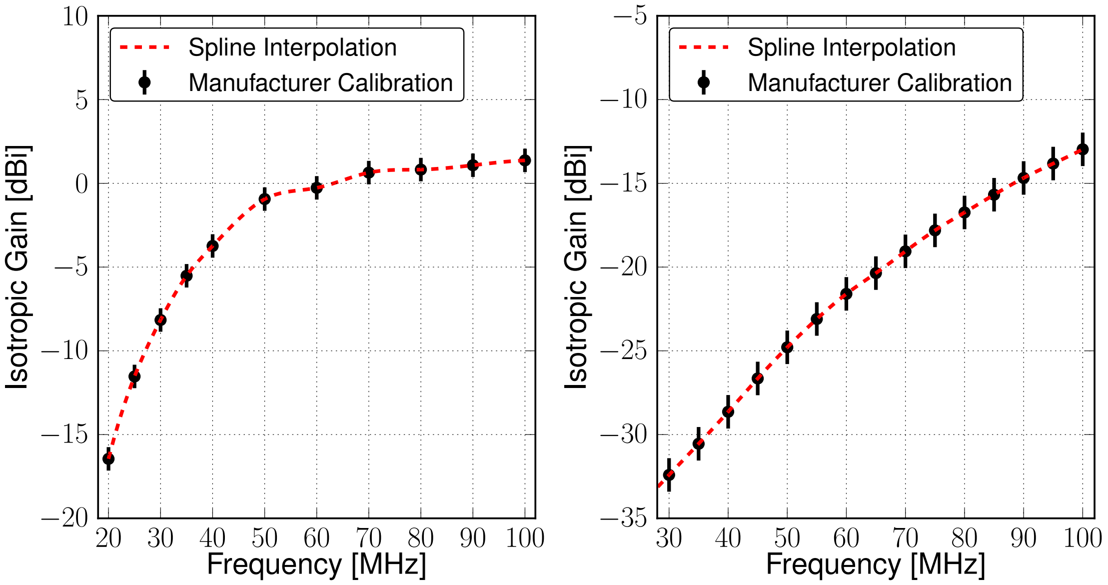

Figure A.3: Manufacturer calibration of the biconical (left) and small biconical (right) transmitting antennas used for the antenna calibration measurements. Systematic calibration uncertainties of 0.7 dB (left) and 1.0 dB (right) as given by the manufacturer are denoted as errorbars. The red dashed lines show spline interpolations.

A.4 Group Delay of the AERA phase 2 Station in North Direction

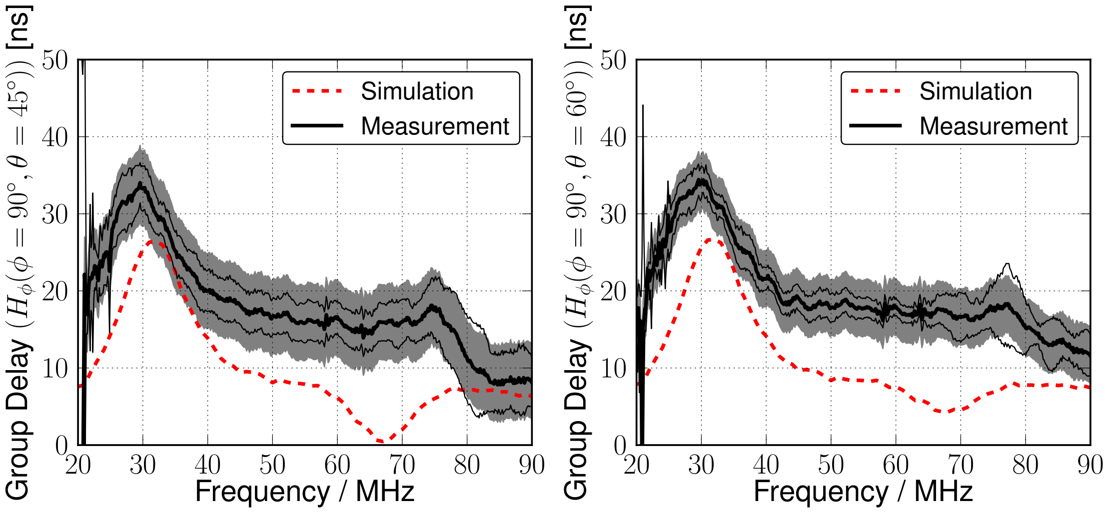

Figure A.4: Group delay of the AERA phase 2 station measured in the north direction for $\theta = 45°$ and $\theta = 60°$ as a function of the frequency. The shown curves are the average of measurements in a zenith bin of ±2.5° around the denoted zenith angle. The thin lines indicate the standard deviation of data in this interval. The gray band indicates the systematic uncertainties resulting from the position uncertainty of the octocopter (see. Ch. 9.4.2).

A.5 List of Radio Events of the Golden Dataset

Number	Radio Run Id	Radio Event Id
1	2161	1228094
2	2162	66963
3	2162	432988
4	2162	3577029
5	2169	283437
6	200200	178857
7	200207	2404336
8	200207	3001396
9	200216	210413
10	200259	78544
11	200266	1076751
12	200270	915194
13	200270	946864
14	200270	995888
15	200270	1623268
16	200277	253774

17	200277	554064
18	200279	1052125
19	200282	663394
20	200282	768615
21	200283	9466377
22	200284	3999806
23	200285	1741117
24	200285	2818596
25	100122	30272
26	100155	85842
27	100155	86566
28	100189	9559
29	100189	111914
30	100189	218106
31	100189	327770
32	100189	347978
33	100189	400454
34	100190	48861
35	100192	45932
36	100192	271987
37	100192	340134
38	100192	365777
39	100192	486607
40	100194	81019
41	100194	242772
42	100196	4981
43	100198	794948
44	100223	94080
45	100220	65340
46	100231	189815
47	100231	904692

Table A.5: AERA radio events included in the selection of the golden dataset for polarization analysis and energy calibration.

A.6 Calculation of the Charge Excess Vector

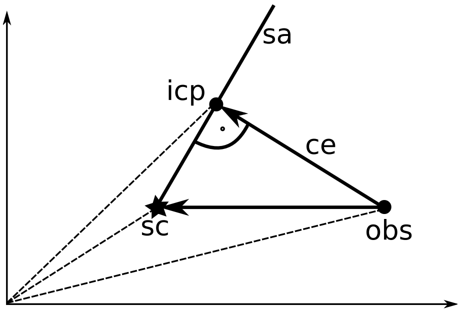

Figure A.6: Sketch illustrating the calculation of the charge excess vector.

The charge excess vector $\vec{ce}$ is the vector pointing from the position of the observer perpendicular to the shower axis (cf. Fig. A.6). It is equal to the difference of the position vector $\vec{obs}$ of the observer and the position vector of the intercept point $\vec{icp}$ on the shower axis.

$$\vec{ce} = \vec{icp} - \vec{obs} \tag{A.7}$$

The position vector of the intercept point is obtained by the projection of the difference vector of the observer $\vec{obs}$ and the shower core $\vec{sc}$ onto the shower axis $\vec{sa}$

$$\vec{icp} = \frac{((\vec{obs} - \vec{sc}) \cdot \vec{sa})}{|\vec{sa}|^2} \cdot \vec{sa} = ((\vec{obs} - \vec{sc}) \cdot \vec{e}_{sa}) \cdot \vec{e}_{sa} \tag{A.8}$$

The unity vector $\vec{e}_{sa}$ of the shower axis is given by the azimuth and zenith angle of the SD directional reconstruction after a transformation into cartesian coordinates. The unity charge excess vector as used in the radio emission models is

$$\vec{e}_{CE} = \frac{\vec{ce}}{|\vec{ce}|} \tag{A.9}$$

Bibliography

[1] J. Blumer, R. Engel, and J. R. Horandel, *Cosmic Rays from the Knee to the Highest Energies*, Prog.Part.Nucl.Phys. **63**, 293 (2009).

[2] V. F. Hess, *Über Beobachtungen der durchdringenden Strahlung bei sieben Freiballonfahrten*, Phys. Zeit. **13**, 1084 (1912).

[3] W. Kohlhörster, Phys. Zeitschrift. 26 654 (1925).

[4] E. S. Seo, J. F. Ormes, and R. E. Streitmatter, *Measurement of cosmic-ray proton and helium spectra during the 1987 solar minimum*, Astrophysical Journal **378**, 763 (1991).

[5] I. P. Ivanenko *et al.*, *Energy Spectra of Cosmic Rays above 2 TeV as Measured by the SOKOL Apparatus*, 23rd International Cosmic Ray Conference, Calgary, Canada **2**, 17 (1993).

[6] N. L. Grigorov *et al.*, *Energy Spectrum of Primary Cosmic Rays in the* 10^{11} - 10^{15} *eV Range According to the Data of Proton-4 Measurements*, International Cosmic Ray Conference **1**, 170 (1971).

[7] M. Nagano *et al.*, *Energy spectrum of primary cosmic rays above* 10^{17} *eV determined from extensive air shower experiments at Akeno*, Journal of Physics **G 18**, (1992).

[8] M. A. K. Glasmacher *et al.*, *The cosmic ray energy spectrum between* 10^{14} *and* 10^{16} *eV*, Astroparticle Physics **10**, 291 (1999).

[9] The IceCube Collaboration, R. Abbasi, et al., *All-particle cosmic ray energy spectrum measured with 26 IceTop stations*, Astroparticle Physics **44**, 40 (2013).

[10] T. Antoni *et al.*, *KASCADE measurements of energy spectra for elemental groups of cosmic rays: Results and open problems*, Astroparticle Physics **24**, 1 (2005).

[11] W. Apel *et al.*, *The spectrum of high-energy cosmic rays measured with KASCADE-Grande*, Astroparticle Physics **36**, 183 (2012).

[12] B. N. Afanasiev *et al.*, Proceedings Int. Symposium of Extremely High Energy Cosmic Rays **32**, (1996).

[13] M. Ave *et al.*, *The energy spectrum of cosmic rays above* $3{*}10^{17} eV$ *as measured with the Haverah Park array*, Astroparticle Physics **19**, 47 (2003).

[14] D. Bird, S. Corbato, H. Dai, and B. Dawson, *The cosmic ray energy spectrum observed by Fly‘s Eye*, Astrophysical Journal **424**, 491 (1994).

[15] The HiRes Collaboration, R. U. Abbasi, et al, *First Observation of the Greisen-Zatsepin-Kuzmin Suppression*, Physical Review Letters **100**, 101101 (2008).

[16] D. Ivanov, *Energy Spectrum Measured by the Telescope Array Surface Detector*, Ph.D. thesis, Rutgers, The State University of New Jersey, 2012.

[17] A. Schulz for the Pierre Auger Collaboration, *The measurement of the energy spectrum of cosmic rays above* $3 * 10^{17}$ eV *with the Pierre Auger Observatory*, 33rd International Cosmic Ray Conference, Rio de Janeiro, Brazil (2013).

[18] J. Simpson, *Elemental and Isotopic Composition of Galactic Cosmic Rays*, Annual Review of Nuclear and Particle Science **33**, 323 (1983).

[19] J. Abraham *et al.*, *Observation of the suppression of the flux of cosmic rays above* $4 \times 10^{19} eV$, Phys.Rev.Lett. **101**, 061101 (2008).

[20] D. Bird, *Detection of a Cosmic Ray with Measured Energy Well Beyond the Expected Spectral Cutoff due to Cosmic Microwave Radiation*, Astrophysical Journal **441**, 144 (1994).

[21] N. Grigorov, V. Nesterov, I. Rapoport, and I. Savenko, *Study of energy spectra of primary cosmic rays at very high energies on the Proton series of satellites*, Space Research XII, Academic Verlag, Berlin 1617 (1972).

[22] P. Abreu *et al.*, *The Pierre Auger Observatory II: Studies of Cosmic Ray Composition and Hadronic Interaction models*, arXiv:1107.4804 (2011).

[23] J. Beringer *et al.*, *Review of Particle Physics*, Phys. Rev. D **86**, 010001 (2012).

[24] D. Fuhrmann *et al.*, *KASCADE-Grande measurements of energy spectra for elemental groups of cosmic rays*, arXiv:1308.2098 (2013).

[25] T. Antoni *et al.*, *KASCADE measurements of energy spectra for elemental groups of cosmic rays: Results and open problems*, Astropart.Phys. **24**, 1 (2005).

[26] T. Abu-Zayyad *et al.*, *Evidence for Changing of Cosmic Ray Composition between* 10^{17} *and* 10^{18} eV *from Multicomponent Measurements*, Phys. Rev. Lett. **84**, 4276 (2000).

[27] Y. Tsunesada, *Highlights from Telescope Array*, arXiv:1111.2507 (2011).

[28] R. Abbasi *et al.*, *Indications of Proton-Dominated Cosmic Ray Composition above 1.6 EeV*, Phys.Rev.Lett. **104**, 161101 (2010).

[29] S. Mao *et al.*, *New Constraints on the Galactic Halo Magnetic Field using Rotation Measures of Extragalactic Sources Towards the Outer Galaxy*, Astrophys.J. **755**, 21 (2012).

[30] D. G. Yamazaki, K. Ichiki, T. Kajino, and G. J. Mathews, *New Constraints on the Primordial Magnetic Field*, Phys.Rev. **D81**, 023008 (2010).

[31] P. L. Biermann, H. Kang, J. P. Rachen, and D. Ryu, *Cosmic structure of magnetic fields*, arXiv:astro-ph/9709252 (1997).

[32] D. Ryu, H. Kang, and P. L. Biermann, *Cosmic magnetic fields in large scale filaments and sheets*, Astron.Astrophys. **335**, 19 (1998).

[33] J. R. Hoerandel, *Models of the knee in the energy spectrum of cosmic rays*, Astropart.Phys. **21**, 241 (2004).

[34] K. Greisen, *End to the cosmic-ray spectrum*, Phys. Rev. Lett. **16**, 748 (1966).

[35] F. Stecker and M. Salamon, *Photodisintegration of ultrahigh-energy cosmic rays: A New determination*, Astrophys.J. **512**, 521 (1999).

[36] G. Zatsepin and V. Kuzmin, *Upper limit of the spectrum of cosmic rays*, JETP Lett. (USSR) **4**, 78 (1966).

[37] J. Cronin, *Cosmic rays: the most energetic particles in the universe*, Rev. Mod. Phys. **71**, 2 (1999).

[38] A. M. Hillas, *The origin of ultra-high-energy cosmic rays*, Ann. Rev. Astron. Astrophys. **22**, 425 (1984).

[39] K. Kotera and A. V. Olinto, *The Astrophysics of Ultrahigh Energy Cosmic Rays*, Ann.Rev.Astron.Astrophys. **49**, 119 (2011).

[40] E. Fermi, *On the origin of the cosmic radiation*, Phys. Rev. **75**, 1169 (1949).

[41] R. Blandford and D. Eichler, *Particle acceleration at astrophysical shocks: A theory of cosmic ray origin*, Physics Reports **154**, 1 (1987).

[42] P. O. Lagage and C. J. Cesarsky, *The maximum energy of cosmic rays accelerated by supernova shocks*, Astron. Astrophys. **125**, 249 (1983).

[43] E. Berezhko, *Maximum energy of cosmic rays accelerated by supernova shocks*, Astroparticle Physics **5**, 367 (1996).

[44] A. M. Hillas, *Cosmic Rays: Recent Progress and some Current Questions*, arXiv:astro-ph/0607109 (2006).

[45] W. Baade and F. Zwicky, *Remarks on Super-Novae and Cosmic Rays*, Phys. Rev. **46**, 76 (1934).

[46] D. Caprioli, *From E. Fermi to Fermi-LAT: watching particle acceleration in supernova remnants*, arXiv:1303.2326 (2013).

[47] M. Ackermann *et al.*, *Detection of the Characteristic Pion-Decay Signature in Supernova Remnants*, Science **339**, 807 (2013).

[48] K. Dolag, D. Grasso, V. Springel, and I. Tkachev, *Constrained simulations of the magnetic field in the local universe and the propagation of ultrahigh energy cosmic rays*, Astropart. Phys. **1**, (2005).

[49] M.-P. Véron-Cetty and P. Véron, *A catalogue of quasars and active nuclei: 12th edition*, Astronomy and Astrophysics **455**, 773 (2006).

[50] The Pierre Auger Collaboration, *Correlation of the Highest-Energy Cosmic Rays with Nearby Extragalactic Objects*, Science **318**, 938 (2007).

[51] P. Abreu *et al.*, *Update on the correlation of the highest energy cosmic rays with nearby extragalactic matter*, Astropart.Phys. **34**, 314 (2010).

[52] K. H. Kampert for the Pierre Auger Collaboration, *Highlights from the Pierre Auger Observatory*, Proceedings of the 32nd International Cosmic Ray Conference, Beijing, China (2011).

[53] R. Abbasi *et al.*, *Search for Correlations between HiRes Stereo Events and Active Galactic Nuclei*, Astropart.Phys. **30**, 175 (2008).

[54] T. Abu-Zayyad *et al.*, *Search for Anisotropy of Ultra-High Energy Cosmic Rays with the Telescope Array Experiment*, Astrophys.J. **757**, 26 (2012).

[55] A. Letessier-Selvon for the Pierre Auger Collaboration, *Highlights from the Pierre Auger Observatory*, Proceedings of the 33nd International Cosmic Ray Conference, Rio de Janeiro, Brasil (2013).

[56] A. Letessier-Selvon and T. Stanev, *Ultrahigh Energy Cosmic Rays*, Rev.Mod.Phys. **83**, 907 (2011).

[57] H. Dembinski, *Measurement of the Ultra High Energy Cosmic Ray Flux from Data of very inclined showers at the Pierre Auger Observatory*, Ph.D. thesis, PHD thesis, RWTH Aachen University, Aachen, Germany, 2009.

[58] B. Keilhauer, *Investigation of Atmospheric Effects on the Development of Extensive Air Showers and their Detection with the Pierre Auger Observatory*, Ph.D. thesis, Karlsruhe University, Karlsruhe, Germany, 2003.

[59] J. Matthews, *A Heitler model of extensive air showers*, Astropart. Phys. **22**, 387 (2005).

[60] W. Heitler, *The Quantum Theory of Radiation*, 3rd ed. (Oxford University Press, Oxford, 1954).

[61] D. Heck *et al.*, CORSIKA: A Monte Carlo Code to Simulate Extensive Air Showers, Report FZKA 6019, Karlsruhe, 1998.

[62] F. Schmidt, *CORSIKA Shower Images*, http://www.ast.leeds.ac.uk/ fs/shower-images.html .

[63] S. Sciutto, *AIRES: A System for air shower simulations. User's guide and reference manual. Version 2.2.0*, arXiv:astro-ph/9911331 (1999).

[64] J. Allen *et al.*, *Air Shower Simulation and Hadronic Interactions*, EPJ Web Conf. **53**, 01007 (2013).

[65] P. Grieder, *Extensive Air Showers*, Springer Berlin Heidelberg (2010).

[66] K. Kamata and J. Nishimura, *The Lateral and the Angular Structure Functions of Electron Showers*, Progress of Theoretical Physics Supplement **6**, 93 (1958).

[67] T. Gaisser and A. Hillas, *Reliability of the method of constant intensity cuts for reconstructing the average development of vertical showers*, 15th International Cosmic Ray Conference **8**, 353 (1977).

[68] M. Unger, *Shower Profile Reconstruction from Fluorescence and Cherenkov light*, Internal note of the Pierre Auger Collaboration, GAP-2006-010 (2006).

[69] A. S. Lidvansky, *Air Cerenkov methods in cosmic rays: A Review and some history*, arXiv:astro-ph/0504269 (2005).

[70] F. Arciprete *et al.*, *AIRFLY: Measurement of the Air Fluorescence Radiation Induced by Electrons*, Nuclear Physics B Proceedings Supplements **150**, 186 (2006).

[71] J. Jelley, Nuovo Cimento **VIII, Suppl. 2**, 578 (1958).

[72] G. Askaryan, Soviet Phys. JETP Lett. (USSR) **14**, 441 (1962).

[73] J. Alvarez-Muniz *et al.*, *Coherent Radiation from Extensive Air Showers in the Ultra-High Frequency Band*, Phys.Rev. **D86**, 123007 (2012).

[74] P. W. Gorham *et al.*, *Observations of microwave continuum emission from air shower plasmas*, Phys. Rev. D **78**, 032007 (2008).

[75] H. Allan, *Radio emission from extensive air showers*, Progress in elementary particle and cosmic ray physics **X**, 171 (1971).

[76] F. D. Kahn and I. Lerche, *Radiation from cosmic ray air showers*, Proceedings of the Royal Society of London **289**, 206 (1966).

[77] H. Falcke and P. Gorham, *Detecting radio emission from cosmic ray air showers and neutrinos with a digital radio telescope*, Astropart.Phys. **19**, 477 (2003).

[78] T.Huege and H.Falcke, *Radio Emission from Cosmic Ray Air Showers: Coherent Geosynchrotron Radiation* , Astron.Astrophys. **412**, 19 (2003).

[79] T. Huege, *Theory and simulations of air shower radio emission*, ARENA 2012 workshop (Erlangen, Germany), AIP Conf. Proc. 1535 (2013).

[80] S. Buitink, T. Huege, H. Falcke, and J. Kuijpers, *Simulation of radio emission from air showers in atmospheric electric fields*, Astropart.Phys. **33**, 296 (2010).

[81] W. N. Charman, *Atmospheric Electric Field as a Possible Cause of Radio Pulses from Extensive Air Showers*, Nature **215**, 497 (1967).

[82] H. Schoorlemmer, *Tuning in on Cosmic Rays. Polarization of Radio Signals from Air Showers as a Probe of Emission Mechanisms*, Ph.D. thesis, Radboud Universiteit Nijmegen, 2012.

[83] O. Scholten, K. Werner, and F. Rusydi, *A Macroscopic Description of Coherent Geo-Magnetic Radiation from Cosmic Ray Air Showers*, Astropart.Phys. **29**, 94 (2008).

[84] K. Werner, K. D. de Vries, and O. Scholten, *A realistic treatment of geomagnetic Cherenkov radiation from cosmic ray air showers*, Astroparticle Physics **37**, 5 (2012).

[85] M. Ludwig and T. Huege, *REAS3: Monte Carlo simulations of radio emission from cosmic ray air showers using an 'end-point' formalism*, Astropart.Phys. **34**, 438 (2011).

[86] T. Huege, M. Ludwig, and C. James, *Simulating radio emission from air showers with CoREAS*, ARENA 2012 workshop (Erlangen, Germany), AIP Conf. Proc. 1535 .

[87] V. Marin and B. Revenu, *Simulation of radio emission from cosmic ray air shower with SELFAS2*, Astropart.Phys. **35**, 733 (2012).

[88] J. Alvarez-Muniz, W. R. J. Carvalho, and E. Zas, *Monte Carlo simulations of radio pulses in atmospheric showers using ZHAireS*, Astropart.Phys. **35**, 325 (2012).

[89] C. W. James, H. Falcke, T. Huege, and M. Ludwig, *General description of electromagnetic radiation processes based on instantaneous charge acceleration in 'endpoints'*, Phys.Rev.E **84**, 056602 (2011).

[90] T. Huege, M. Ludwig, O. Scholten, and K. D. de Vriew, *The convergence of EAS radio emission models and a detailed comparison of REAS3 and MGMR simulations*, Nucl.Instrum.Meth. **A662**, S179 (2012).

[91] T. Huege, R. Ulrich, and R. Engel, *Dependence of geosynchrotron radio emission on the energy and depth of maximum of cosmic ray showers*, Astroparticle Physics **30**, 96 (2008).

[92] J. V. Jelley *et al.*, *Radio Pulses from Extensive Cosmic-Ray Air Showers*, Nature **205**, 327.

[93] B. Revenu, *Overview of MHz air shower radio experiments and results*, ARENA 2012 workshop (Erlangen, Germany), AIP Conf. Proc. 1535 (2013).

[94] F. Schroder *et al.*, *Cosmic Ray Measurements with LOPES: Status and Recent Results*, ARENA 2012 workshop (Erlangen, Germany), AIP Conf. Proc. 1535 (2013).

[95] C. Riviere *et al.*, *Radio emission of extensive air shower at CODALEMA: Polarization of the radio emission among the v*B vector*, arXiv:0906.2720 (2009).

[96] A. Corstanje *et al.*, *LOFAR: Detecting Cosmic Rays with a Radio Telescope*, arXiv:1109.5805 (2011).

[97] D. Ardouin *et al.*, *Geomagnetic origin of the radio emission from cosmic ray induced air showers observed by CODALEMA*, arXiv:0901.4502 .

[98] A. Rebai, *Some recent results of the CODALEMA experiment*, arXiv:1211.3273 (2012).

[99] The Pierre Auger Collaboration, *Probing the radio emission from air showers with polarization measurements*, Physical Review D **89**, (2014).

[100] V. Marin, *Charge excess signature in the CODALEMA data. Interpretation with SELFAS2*, in Proceedings of the 32th ICRC, Beijing, China (2011).

[101] W. Apel *et al.*, *Lateral Distribution of the Radio Signal in Extensive Air Showers Measured with LOPES*, Astropart.Phys. **32**, 294 (2010).

[102] A. Rebai, P. Lautridou, A. Lecacheux, and O. Ravel, *Correlations in energy in cosmic ray air showers radio-detected by CODALEMA*, arXiv:1210.1739 (2012).

[103] A. Nelles *et al.*, *Detecting Radio Emission from Air Showers with LOFAR*, ARENA 2012 workshop (Erlangen, Germany), AIP Conf. Proc. 1535 (2013).

[104] A. Nelles, J. Schulz, and J. Horandel, *A parameterization for the radio signal measured with AERA.*, Internal note of the Pierre Auger Collaboration, GAP-note, under review (2014).

[105] C. Welling, *Investigation of the Lateral Distribution and Polarization of Radio Signals from Cosmic Ray Induced Air Showers at the Pierre Auger Observatory*, Bachelor Thesis, RWTH Aachen University (2014).

[106] A. Horneffer et al. (LOPES Collaboration), *Primary Particle Energy Calibration of the EAS Radio Pulse Height*, In Proceedings of the 30th ICRC, Merida, Mexico, volume 4, 83–86 (2007).

[107] N. Palmieri *et al.*, *Investigation on the energy and mass composition of cosmic rays using LOPES radio data*, Proceedings for International Cosmic Ray Conference (ICRC) 2013, Rio De Janeiro; paper ID 439 (2013).

[108] W. Apel *et al.*, *Experimental evidence for the sensitivity of the air-shower radio signal to the longitudinal shower development*, Phys.Rev. **D85**, 071101 (2012).

[109] W. Apel *et al.*, *Reconstructing energy and Xmax of cosmic ray air showers using the radio lateral distribution measured with LOPES*, AIP Conf. Proc. 1535, **89**, (2013).

[110] T. P. A. Collaboration, *Properties and performance of the prototype instrument for the pierre auger observatory*, Nuclear Instruments and Methods in Physics Research Section A **518**, 172 (2004).

[111] I. Allekotte *et al.*, *The Surface Detector System of the Pierre Auger Observatory*, Nucl.Instrum.Meth. **A586**, 409 (2008).

[112] J. Abraham *et al.*, *The Fluorescence Detector of the Pierre Auger Observatory*, Nucl.Instrum.Meth. **A620**, 227 (2010).

[113] X. Bertou *et al.*, *Calibration of the surface array of the Pierre Auger Observatory*, Nuclear Instruments and Methods in Physics Research Section A: Accelerators, Spectrometers, Detectors and Associated Equipment **568**, 839 (2006).

[114] J. Abraham *et al.*, *Trigger and aperture of the surface detector array of the Pierre Auger Observatory*, Nucl.Instrum.Meth. **A613**, 29 (2010).

[115] I. C. Maris for the Pierre Auger Collaboration, *The Amiga infill detector of the Pierre Auger Observtory: performance and first data*, Proceedings of the 32nd International Cosmic Ray Conference, Beijing, China (2011).

[116] C. Bonifazi, *The angular resolution of the Pierre Auger Observatory*, Nucl.Phys.Proc.Suppl. **190**, 20 (2009).

[117] S. Argiro *et al.*, *The Offline Software Framework of the Pierre Auger Observatory*, Nucl.Instrum.Meth. **A580**, 1485 (2007).

[118] D. Newton, J. Knapp, and A. A. Watson, *The Optimum Distance at which to Determine the Size of a Giant Air Shower*, Astropart.Phys. **26**, 414 (2007).

[119] R. Pesce for the Pierre Auger Collaboration, *Energy calibration of data recorded with the surface detectors of the Pierre Auger Observatory: an update*, Proceedings of the 32nd International Cosmic Ray Conference, Beijing, China (2011).

[120] V. Verzi for the Pierre Auger Collaboration, *The Energy Scale of the Pierre Auger Observatory*, Proceedings of the 33nd International Cosmic Ray Conference, Rio de Janeiro, Brasil (2013).

[121] M. Ave *et al.*, *Precise measurement of the absolute fluorescence yield of the 337 nm band in atmospheric gases*, Astropart.Phys. **42**, 90 (2013).

[122] V. Souza for the Pierre Auger Collaboration, *An update on the measurements of the depth of shower maximum made at the Pierre Auger Observatory*, Proceedings of the 33nd International Cosmic Ray Conference, Rio de Janeiro, Brasil (2013).

[123] F. Sanchez for the Pierre Auger Collaboration, *The AMIGA detector of the Pierre Auger Observatory: an overview*, Proceedings of the 32nd International Cosmic Ray Conference, Beijing, China (2011).

[124] H. J. Mathes for the Pierre Auger Collaboration, *The HEAT Telescopes of the Pierre Auger Observatory - Status and First Data*, Proceedings of the 32nd International Cosmic Ray Conference, Beijing, China (2011).

[125] R. Gaior for the Pierre Auger Collaboration, *Detection of cosmic rays using microwave radiation at the Pierre Auger Observatory*, Proceedings of the 33nd International Cosmic Ray Conference, Rio de Janeiro, Brasil (2013).

[126] A. M. van den Berg *et al.*, *First detection of radio signals from cosmic rays at the Pierre Auger Observatory*, Internal note of the Pierre Auger Collaboration, GAP-2007-065 (2007).

[127] J. Coppens *et al.*, *Observation of radio signals from air showers at the Pierre Auger Observatory*, Nuclear Instruments and Methods in Physics Research Section A **604**, 41 (2009).

[128] P. Abreu *et al.*, *Results of a self-triggered prototype system for radio-detection of extensive air showers at the Pierre Auger Observatory*, JINST **7**, P11023 (2012).

[129] A. M. van den Berg, G. Zarza, and D. M. Varnav, *Communication System for the Auger Engineering Radio Array at the Southern Auger Observatory*, Internal note of the Pierre Auger Collaboration, GAP-2011-035 (2011).

[130] K. Weidenhaupt, B. Philipps, M. Erdmann, and S. Fliescher, *Antenna Alignment for the first 24 Station of AERA*, Internal note of the Pierre Auger Collaboration, GAP-2010-083 (2010).

[131] J. L. Kelley *et al.*, *Design and Testing of a 5 GHz Commercial Wireless Network for AERA*, Internal note of the Pierre Auger Collaboration, GAP-2012-054 (2012).

[132] F. Schröder *et al.*, *New method for the time calibration of an interferometric radio antenna array*, Nuclear Instruments and Methods in Physics Research Section A: Accelerators, Spectrometers, Detectors and Associated Equipment **615**, 277 (2010).

[133] A. Hevinga *et al.*, *Photo-Voltaic System for the Auger Engineering Radio Array at the Southern Auger Observatory* , Internal note of the Pierre Auger Collaboration, GAP-2011-034 (2011).

[134] K. Weidenhaupt *et al.*, *A Survey of Narrowband and Broadband Radiofrequency Interference at AERA*, Internal note of the Pierre Auger Collaboration, GAP-2011-062 (2011).

[135] A. M. van den Berg *et al.*, *Locating transient noise sources at Radio Detection sites*, Internal note of the Pierre Auger Collaboration, GAP-2011-083 (2011).

[136] K. Weidenhaupt for the Pierre Auger Collaboration, *The Auger Engineering Radio Array*, Proc. of 14th Vulcano Workshop on Frontier Objects in Astrophysics and Particle Physics, Vulcano, Italy, (published in Acta Polytechnica, Vol. 53 (2013) Supplement) (2012).

[137] J. L. Kelley and Pierre Auger Collaboration, *Data acquisition, triggering, and filtering at the Auger Engineering Radio Array*, Nuclear Instruments and Methods in Physics Research A **725**, 133 (2013).

[138] C. Ruehle, *Advanced digital self-triggering of radio emission of cosmic rays*, Nuclear Instruments and Methods in Physics Research Section A: Accelerators, Spectrometers, Detectors and Associated Equipment **662, Supplement 1**, S146 (2012).

[139] K. Weidenhaupt, S. Fliescher, L. Mohrmann, and M. Erdmann, *A Novel Method of Selecting Cosmic Ray Candidates from Self-Triggered AERA Events*, Internal note of the Pierre Auger Collaboration, GAP-2011-108 (2011).

[140] A. M. van den Berg *et al.*, *Fiber Communication System for the 433m AERALET SD infill of the Auger Engineering Radio Array at the Pierre Auger Observatory*, Internal note of the Pierre Auger Collaboration, GAP-2012-111 (2012).

[141] C. Timmermanns and J. Kelley, *Calibration of the AERA Phase I Digitizer*, Internal note of the Pierre Auger Collaboration, GAP-2011-028 (2011).

[142] M. Melissas, T. Huege, and H. Schieler, *Weather monitoring at the central radio station*, Internal note of the Pierre Auger Collaboration, GAP-2011-066 (2011).

[143] S. Grebe, *Spectral index analysis of the data from the Auger Engineering Radio Array*, AIP Conference Proceedings **1535**, 73 (2013).

[144] The AERA Group, *Proposal for the construction of the 20 km^2 Auger Engineering Radio Array at the Southern Auger Observatory*, Internal note of the Pierre Auger Collaboration, GAP-2009-172 (2009).

[145] *IEEE Standard Definitions in Terms of Antennas*, IEEE Std 145-1993 (R2004) (2004).

[146] C. Balanis, *Antenna Theory - Analysis and Design, third edition*, Wiley-Interscience (2005).

[147] J. Reed, *Introduction to Ultra Wideband Communication Systems, an*, 1st ed. (Prentice Hall Press, Upper Saddle River, NJ, USA, 2005).

[148] P. Abreu *et al.*, *Antennas for the Detection of Radio Emission Pulses from Cosmic-Ray induced Air Showers at the Pierre Auger Observatory*, JINST **7**, P10011 (2012).

[149] H. Carlin, *The Scattering Matrix in Network Theory*, IRE Transactions on Circuit Theory **3**, 88 (1956).

[150] P. Abreu *et al.*, *Advanced functionality for radio analysis in the Offline software framework of the Pierre Auger Observatory*, Nucl.Instrum.Meth. **A635**, 92 (2011).

[151] K. Weidenhaupt, C. Glaser, and M. Erdmann, *A new Method of the Interpolation of the Antenna Response Pattern*, Internal note of the Pierre Auger Collaboration, GAP-2013-090 (2013).

[152] G. Burke and A. Poggio, *Numerical electromagnetics code (nec) method of moments, parts i, ii, iii.*, Technical report, Lawrence Livermore National Laboratory, NEC-l (1977), NEC-2 (1981), NEC-3 (1983) .

[153] NEC2++, *http://elec.otago.ac.nz/w/index.php/Necpp*, .

[154] A. Voors, *4Nec2*, http://home.ict.nl/∼arivoors/ .

[155] A. Poggio and E. Miller, *Integral Equation Solutions of Three-dimensional Scattering Problems*, MBA technical memo: MBAssociates (1970).

[156] R. Harrington, *Field Computation by Moment Methods*, IEEE/OUP Series on Electromagnetic Wave Theory (Oxford University Press, USA) (1993).

[157] A. M. van den Berg, G. Zarza, and K. Weidenhaupt, *Measurement of the Low Frequency Resistivity of Soil at the Auger Engineering Radio Array*, Internal note of the Pierre Auger Collaboration, GAP-2011-036 (2011).

[158] I. R. I.-R. P527-3 *et al.*, *Electrical Characteristics of the Surface of the Earth*, ITU-R Recommendations and Reports (1992).

[159] S. Fliescher, *Antenna Devices and Measurement of Radio Emission from Cosmic Ray induced Air Showers at the Pierre Auger Observatory*, Ph.D. thesis, RWTH Aachen University, 2011.

[160] H. Gemmeke *et al.*, *Advanced detection methods of radio signals from cosmic rays for KASCADE GRANDE and Auger*, Int.J.Mod.Phys. **A21S1**, 242 (2006).

[161] S. Fliescher, *Radio Detection and Detector Simulation for Extensive Air Showers at the Pierre Auger Observatory*, Diploma Thesis, RWTH Aachen University (2008).

[162] K. Weidenhaupt, *LPDA-Antennas for Large Scale Radio Detection of Cosmic Rays at the Pierre-Auger-Observatory*, Diploma Thesis, RWTH Aachen University (2009).

[163] K. Rothammel and A. Krischke, *Rothammels Antennenbuch*, DARC Verlag Baunatal **12**, (2001).

[164] R. Cox, *LPCAD 3.0*, http://www.wb0dgf.com/LPCAD.htm (2013).

[165] M. Stephan for the Pierre Auger Collaboration, *Antennas, Filters and Preamplifiers designed for the Radio Detection of Ultra-High-Energy Cosmic Rays.*, Proceedings of Asia-Pacific-Microwave Conference 2010, pp. 1455–1458 (2010).

[166] M. Stephan, *Design and Test of a Low Noise Amplifier for Radio Antennas Measuring Atmospheric Showers*, Internal note of the Pierre Auger Collaboration, GAP-2010-045 (2010).

[167] O. Seeger, *Logarithmic periodic dipole antennas for the Auger engineering radio array*, Nuclear Instruments and Methods in Physics Research Section A: Accelerators, Spectrometers, Detectors and Associated Equipment **662, Supplement 1**, S138 (2012), 4th International workshop on Acoustic and Radio EeV Neutrino detection Activities.

[168] D. Charrier, *Antenna development for astroparticle and radioastronomy experiments*, Nuclear Instruments and Methods in Physics Research Section A: Accelerators, Spectrometers, Detectors and Associated Equipment **662, Supplement 1**, S142 (2012), 4th International workshop on Acoustic and Radio EeV Neutrino detection Activities.

[169] D. Maschmann, *A Monitoring System for Motions of Butterfly Antennas for the Auger Engineering Radio Array*, Bachelor Thesis, RWTH Aachen University (2014).

[170] O. Krömer, *Empfangssystem zur Radioobservation hochenergetischer kosmischer Schauer und sein Verhalten bei Selbsttriggerung*, PhD thesis, University of Karlsruhe (2008).

[171] S. Nehls *et al.*, *Amplitude calibration of a digital radio antenna array for measuring cosmic ray air showers*, Nucl.Instrum.Meth. **A589**, 350 (2008).

[172] GESTIS, *GESTIS-Stoffdatenbank*, http://www.dguv.de/ifa/Gefahrstoffdatenbanken/GESTIS-Stoffdatenbank/index.jsp (2013).

[173] Air Liquide Company, *Gas Encyclopedia*, http://encyclopedia.airliquide.com/encyclopedia.asp (2013).

[174] W. Demtröder, *Experimentalphysik 1*, Springer (2008).

[175] Rhode & Schwarz, *FSH4 (ver. 24) Handheld Spectrum and Vector Network Analyzer 100kHz - 3.6 GHz*, http://www.rohde-schwarz.com.

[176] Huber+Suhner, *Type RG 58 C/U coaxial cable*, http://www.hubersuhner.com/ (2013).

[177] Schwarzbeck Mess-Elektronik, *BBAL 9136 Biconical Antenna with VHHBB 9124 Balun*, http://www.schwarzbeck.de/index.php/en/.

[178] Times Microwave Systems, *Type LMR-100 coaxial cable*, http://www.timesmicrowave.com/cms/products/cables/lmr/ (2013).

[179] Schwarzbeck Mess-Elektronik, *Customized Version of BBOC 9217 Biconical Antenna with UBAA 9114 Balun*, http://www.schwarzbeck.de/index.php/en/ (2013).

[180] Mini-Circuits, RF/IF & Microwave Components, *Type ZFL-1000H+ amplifier*, http://www.minicircuits.com/ (â).

[181] HiSystems GmbH, *Mikrokopter Okto XL*, http://www.mikrokopter.de.

[182] L. Mohrmann, *Continuous Spectrum Observation of the Aachen Radio Sky*, Bachelor Thesis, RWTH Aachen University (2009).

[183] Schwarzbeck Mess-Elektronik, *Private Communication.*

[184] J. Kraus and R. Marhefka, *Antennas for all applications*, *McGraw-Hill series in electrical engineering* (McGraw-Hill, ADDRESS, 2002).

[185] W. L. Stutzman and G. A. Thiele, *Antenna theory and design*, (John Wiley & Sons) (1998).

[186] *IEEE Standard Test Procedures for Antennas*, IEEE Std 149-1979 (R2008) (2008).

[187] S. Grebe, S. Jansen, and C. Timmermans, *Suppression of self-introduced narrowband RFI in the time domain.*, Internal note of the Pierre Auger Collaboration, GAP-2013-012 (2013).

[188] K. Weidenhaupt, C. Glaser, and M. Erdmann, *Error Estimation of Cosmic Ray Radio Signals*, Internal note of the Pierre Auger Collaboration, GAP-2013-059 (2013).

[189] A. Schulz, *Measurement of the Energy Spectrum of Cosmic Rays between 0.1 EeV and 30 Eev with the Infill Extension of the Surface Detector of the Pierre Auger Observatory*, Internal note of the Pierre Auger Collaboration, GAP-2012-136 (2012).

[190] S. Nehls, *Calibrated Measurements of the Radio Emission of Cosmic Ray Air Showers*, Ph.D. thesis, PHD thesis, Institut für Kernphysik, Universität Karlsruhe, Karlsruhe, Germany, 2008.

[191] C. Glaser, *Energy estimation for cosmic rays measured with the Auger Engineering Radio Array*, ARENA 2012 workshop (Erlangen, Germany), AIP Conf. Proc. 1535 (2013).

[192] N. Palmieri, *Reconstructing Energy and Xmax of cosmic-ray air showers using the radio lateral distribution measured with LOPES*, ARENA 2012 workshop (Erlangen, Germany), AIP Conf. Proc. 1535 (2013).

[193] P. Smith, *Electronic applications of the Smith Chart: in waveguide, circuit, and component analysis*, Classic (Noble Publishing Corporation) (1995).

Declaration of Pre-released Extracts

The following publication and internal note of the Pierre Auger Collaboration contain pre-released extracts of this work.

- Reference [148], P. Abreu *et al.*, *Antennas for the Detection of Radio Emission Pulses from Cosmic-Ray induced Air Showers at the Pierre Auger Observatory*, JINST **7**, P10011 (2012).
  The author contributed to this paper with the development, construction, excecution and analysis of the antenna calibration measurements presented therein. The data of the calibration measurements presented in Fig. 9 - Fig. 12 of the above paper are scope of Ch. 10.1.2 of this thesis. The data was also used in Reference [159].
- Reference [134], K. Weidenhaupt *et al.*, *A Survey of Narrowband and Broadband Radio-frequency Interference at AERA*, Internal note of the Pierre Auger Collaboration, GAP-2011-062 (2011).
  This internal note contains Fig. 6.4 of this thesis.

The following conference proceeding by the author is currently under review and will contain Fig. 6.1, Fig. 9.3 and Fig. 10.7 (right) of this thesis

- K. Weidenhaupt for the Pierre Auger Collaboration, *Radio Detection of Cosmic Rays at the Auger Engineering Radio Array*, Proceeding of the TIPP2014 conference, Amsterdam, The Netherlands (2014), to be published in Proceedings of Science.

Acknowledgements

At this point it is a special pleasure to thank those people who contributed to the work presented in this thesis.

I would like to express my gratitude to my adviser Prof. Dr. Martin Erdmann. He provided unique opportunities to pursue my research interests and valuable guidance throughout my work in the last years. The chance to perform a year of field work in Argentina during my PhD research was an outstanding experience.

For co-refereeing my thesis I am thankful to Prof. Dr. Christopher Wiebusch.

I would also like to thank Prof. Dr. Thomas Hebbeker for discussions in meetings of the Aachen Auger group.

I had the pleasure to be part of the vital Aachen Auger research group. A great deal of the work presented in this thesis would not have been possible without the strong support of colleagues from this group.
Right from the beginning Raphael Krause contributed to the development of the Octocopter setup and participated in all of the Octocopter measurements presented in this thesis. Raphaels passionate commitment during his Master and PhD thesis and his hardware skills were indispensable for the success of the Octocopter project. Many thanks also to Julian Grothoff who joined our small Octocopter team as an undergraduate student.
Large parts of the energy and polarization analysis presented in this thesis have been conducted in collaboration with Christian Glaser. With his outstanding analytical skills and understanding of radio detection he certainly pushed this work.
Dr. Stefan Fliescher strongly contributed to the execution and analysis of the balloon calibration measurements. I feel that a large part of my theoretical understanding of antennas is due to the collaboration and discussions with Stefan. Many thanks also to Lars Mohrmann who developed the data acquisition software for the antenna measurements and accompanied the balloon calibration campaign.

As a member of the AERA group I could benefit from the friendly and productive working atmosphere of this international team. I would especially like to thank Dr. Didier Charrier for fruitful discussions about antenna theory and antenna simulations.

The development and construction of the AERA radio antennas and several measurement setups would not have been possible without the work of the institute's workshop in Aachen. The workshop members always found a way to realize the 'crazy ideas' of the physicists in time. Barthel Philipps developed the CAD design of both AERA antennas. Günther Hilgers contributed to the antenna development with his extensive experience. Franz Zantis and Franz Adamczyk accompanied the electrical engineering of the antenna measurement setups. The production of the AERA antennas is due to the fine work of Josef Grooten, Ralf Kupper, Hans Frohn and Achim Paulus.

For true friendship and countless (physics) discussions during our studies and PhD time I would like to thank Maurice Stephan. I can not imagine the last years without you!
For introducing me to a different culture and giving me a great time in Argentina I wish to sent 'muchas gracias' to Pepe, Rosa, Nata and Ricardo and his team.
And I want to thank my other friends who had no direct impact on this thesis but certainly indirectly by showing me a great time.

Last but not least I would like to thank my family for their outstanding support and my sister Mona for being an inspiration throughout my live.